Gravitational Instabilities in a Protosolar-like Disc

Marc Graham Evans

School of Physics and Astronomy

University of Leeds

Submitted in accordance with
the requirements for the degree of
Doctor of Philosophy

February 2018

The candidate confirms that the work submitted is his own, except where work which has formed part of jointly authored publications has been included. The contribution of the candidate and the other authors to this work has been explicitly indicated. The candidate confirms that appropriate credit has been given within the thesis where reference has been made to the work of others.

This copy has been supplied on the understanding that it is copyright material and that no quotation from the thesis may be published without proper acknowledgement.

Preface

The chapters in this thesis are based on work presented in the following jointly authored publications:

i. Gravitational instabilities in a protosolar-like disc I: dynamics and chemistry, **M. G. Evans**, J. D. Ilee, A. C. Boley, P. Caselli, R. H. Durisen, T. W. Hartquist, J. M. C. Rawlings, 2015, MN-RAS, 453, 1147.

ii. Gravitational instabilities in a protosolar-like disc II: continuum emission and mass estimates, **M. G. Evans**, J. D. Ilee, T. W. Hartquist, P. Caselli, L. Szűcs, S. J. D. Purser, A. C. Boley, R. H. Durisen, J. M. C. Rawlings, 2017, MNRAS, 470, 1828.

iii. Gravitational instabilities in a protosolar-like disc III: sensitivities required for line absorption detection, **M. G. Evans**, T. W. Hartquist, P. Caselli, A. C. Boley, J. D. Ilee, J. M. C. Rawlings, in prep.

Paper I forms the basis of Chapter 2. The primary author (M. G. Evans) was responsible for running the hydrodynamic simulation of a gravitationally unstable, protosolar-like disc, provided by A. C. Boley, through a chemical code, provided by J. D. Ilee based on the work of J. M. C. Rawlings. The primary author improved the chemical code by adding a recursive feature that enabled much more successful treatment of rapid variations in density and temperature. The evolution of the chemistry over a short period of disc evolution was investigated, and the chemistry at certain epochs was also compared to those derived from a larger-mass disc simulation. The primary author wrote the initial draft of the publication, and then incorporated comments from co-authors into the final draft.

Paper II forms the basis of Chapter 3. The primary author (M. G. Evans) used a radiative transfer code (LIME) to produce continuum

flux images of the disc model from Paper I, including an exploration into improving the accuracy of the images obtained. The agreement between different radiative transfer codes was explored by comparing the LIME continuum images to consistent continuum images produced by L. Szűcs using RADMC-3D. Observations of the original continuum flux images were synthesised with CASA by the primary author, with guidance from S. J. D. Purser. Protoplanetary disc masses were derived from these observations using a technique that is widely adopted for real observations, and then compared with the actual disc mass. The primary author wrote the initial draft of the publication, and then incorporated comments from co-authors into the final draft.

Paper III forms the basis of Chapter 4. The primary author (M. G. Evans) used a radiative transfer code (LIME) to produce line flux images of the disc model from Paper I, including an exploration into improving the accuracy of the images obtained, which used the findings of Paper II as a launching point. The primary author synthesised observations of the line flux images and calculated the sensitivities required for detection of the spiral features. The primary author also extracted line spectra and produced PV diagrams in order to determine if non-axisymmetric structure could be parsed from line transition observations. The PV diagrams were also used to derive protostellar masses that were then compared to the actual protostellar mass. The primary author wrote the initial draft of the publication.

Acknowledgements

I would first like to thank Paola Caselli and Tom Hartquist for their expert guidance and supervision throughout the duration of my PhD, and John Ilee for effectively being an extra supervisor who has been an invaluable source of encouragement and inspiration. I would also like to thank the entire Astrophysics staff for making the department a very welcoming place to work. Moreover, I would like to thank Catherine Walsh and Tom Millar for taking the time to read and examine my thesis and for making my viva a positive and valuable experience.

Thanks to all of my officemates and fellow PhD students, past and present, for filling the last four years with lots of enjoyment and cherished memories. In particular, cheers to Si, Rob and Harry for being brilliant mates with great senses of humour, and for generally just being such morally upstanding people that I wholeheartedly respect.

Heartfelt thanks go to the people that have been especially close to me during my PhD, who have provided an endless source of solace and motivation without which I highly doubt I would have made it beyond even the first year- you know who you are. And sincere thanks to Catherine for giving me the love and support I needed in the last few months to get over the line.

And finally, special thanks to my entire family for always believing in and supporting me; especially to my Mum and Dad who have always been willing to let me drone on about my work and pick me

up whenever I've needed it. You've given me so much in life - I can only hope to repay a fraction of it all.

Abstract

This thesis presents a study of protoplanetary discs around young, low mass protostars. Such discs are believed to be massive enough to develop gravitational instabilities, which subsequently form spiral structures. The dynamical and chemical evolutions of a protosolar-like, gravitationally unstable disc are explored and the spiral structure in the disc is found to shock-heat material. This affects the chemical composition via enhanced desorption rates and endothermic reaction rates and through global mixing of the disc. As a result, the gravitational instability in the model disc leads to transient and permanent changes in the disc chemistry, and also provides a chemically-rich midplane in contrast to simulations of more evolved discs.

Secondly, radiative transfer calculations are performed for the dust continuum, and model-tailored grid construction is found to improve the accuracy of the resultant flux images. Continuum observations of the model disc are synthesised and the spiral structure (driven by the gravitational instability) is shown to be readily detectable with ALMA across a range of frequencies, disc inclinations and dust opacities. The derivation of disc mass from the observed flux densities is explored but the method commonly utilised is found to be unreliable and underestimate the disc mass. Therefore, it is concluded that gravitational instabilities could be retrospectively validated in discs previously thought not massive enough to be self-gravitating.

Finally, radiative transfer calculations are performed for molecular line transitions. Methods for improving the accuracy of line flux images are explored and the validity of assuming local thermodynamic

equilibrium is assessed. Observations of the line fluxes are synthesised without noise and the spiral structure is found to be traced to an extent by all transitions considered, which is not necessarily congruent with the underlying distribution of the molecular species. The disc is seen in absorption in all transitions considered, due to the global mixing of the disc, which suggests absorption features could be a signature of gravitational instability in young protoplanetary discs. The sensitivities required to detect flux originating in spiral features are determined and it is found that a dedicated observation with ALMA should be capable of spatially resolving spiral structure in a Class 0 disc. Whether the spiral structure can be also be determined from spectral features is explored, which is shown to only be reliable with PV diagrams of nearly edge-on discs. The derivation of protostellar mass from PV diagrams is also explored and found to most likely be unreliable for gravitationally unstable discs.

Contents

CONTENTS

Abbreviations

ACA	Atacama Compact Array
ALI	Accelerated Lambda Iteration
ALMA	Atacama Large Millimeter/submillimeter Array
arcsec	Second of arc
au	Astronomical unit
FUV	Far-ultraviolet
FWHM	Full width at half maximum
GI	Gravitational instability
GMC	Giant molecular cloud
ISM	Interstellar medium
KIDA	Kinetic Database for Astrochemistry
LTE	Local thermodynamic equilibrium
LVG	Large Velocity Gradient
MC	Monte Carlo
MHD	Magnetohydrodynamics
MRI	Magnetorotational instability
ORP	Outer rotational period
PAH	Polycylic aromatic hydrocarbon
pc	Parsec
PV	Position-velocity
PWV	Precipitable water vapour

ABBREVIATIONS

SED   Spectral energy distribution

SNR   Signal-to-noise ratio

SPH   Smoothed-particle hydrodynamics

UDfA   UMIST Database for Astrochemistry

UV   Ultraviolet

WOSHO   Without shocks, high-order

WOSLO   Without shocks, low-order

WS   With shocks

YSO   Young stellar object

ZAMS   Zero-age main sequence

List of Figures

LIST OF FIGURES

List of Tables

Chapter 1

Introduction

1.1   Star formation

The formation of stars is a fundamental macroscopic process that is relevant to many aspects of astrophysics, from the evolution of entire galaxies to the creation of individual planetary systems. This process occurs in molecular gas, which is typically concentrated in the spiral arms of galaxies, and involves dynamical and chemical evolution on a wide range of scales. These include the large scales of the gas clouds themselves, typically referred to as giant molecular clouds (GMCs), the small scales of dense regions, known as filaments and clumps, and even smaller scales of gravitationally bound regions, known as cores. The physical and chemical processes responsible for the formation of stars across this wide range of scales are summarised in the classic review by Shu *et al.* (1987), and can be separated into two distinct phases: the formation and evolution of clouds, clumps and cores; and the collapse, and subsequent protostar formation, of cores.

1.1.1   Clouds, filaments and cores

The definition of GMCs is not entirely strict, but essentially they are dense condensations within a more vast, mostly atomic gas, with masses and sizes ranging from 10^3–10^7 $M_\odot$ and 5–200 pc, respectively (Murray, 2011). Due to the fact that

1. INTRODUCTION

most GMCs are actively forming stars, and the range of ages of associated stars and clusters is comparable to the crossing times of molecular clouds, there cannot be any significant 'dead time' between the formation of a massive dense molecular cloud and the subsequent onset of star formation (Larson, 2003). With this restriction in mind, GMCs are believed to be formed in one of two scenarios. In the first scenario, GMCs form via condensation out of the interstellar medium (ISM) due to self-gravity. Their subsequent evolution is affected by turbulence that is converted from gravitational collapse and continuously driven by stellar feedback (e.g Lada & Kylafis, 1999). As a result, in this scenario, GMCs are in quasi-equilibrium, evolve slowly and are then destroyed by newly-formed stars within a few dynamical times. On the other hand, in the alternate scenario, GMCs are dynamic, transient structures formed by large-scale colliding gas flows that dissipate on the order of the crossing time (e.g Ballesteros-Paredes *et al.*, 2007). In truth, different physical processes likely dictate cloud evolution at different epochs, depending on the cloud environment (see Dobbs *et al.*, 2014, for a review).

Filamentary structure, where a filament is a high-aspect ratio (5–10) object with a significant density contrast to the surrounding environment, has been confirmed to be ubiquitous within molecular clouds in our Galaxy (André *et al.*, 2014). As this includes starless objects, such as the Polaris translucent cloud (Ward-Thompson *et al.*, 2010), and more than 70 per cent of the prestellar cores identified with *Herschel* appear to lie within filaments, the current consensus is that filament formation precedes star formation. As with GMCs, the mechanisms responsible for this formation are not entirely understood, but recent simulations have shown that colliding flows reproduce observed filamentary structure (e.g Gómez & Vázquez-Semadeni, 2014), which adds credence to the transient GMC theory. As a result, filaments probably occur where streams of cold gas collide

and dissipate energy, followed by subsequent accretion onto smaller structures within the filaments.

The gravitational collapse of sub-structure within filaments occurs when a region exceeds the Jeans mass

$$M_{\mathrm{J}} = \left(\frac{\pi k_{\mathrm{B}} T}{mG} \right)^{3/2} \rho^{-1/2}, \tag{1.1}$$

where k_{B} is the Boltzmann constant, G is the Gravitational constant, m is the average particle mass, T is a constant temperature fixed by radiative processes, and ρ is the mass density of the cloud. Whilst the prescription of the Jeans mass is mathematically inconsistent, as the background medium collapse is not incorporated, it provides a reasonable approximation for the threshold mass before collapse ensues, regardless of the geometry, equation of state or degree of equilibrium within the cloud.

It should also be noted that the Jeans mass is only strictly appropriate if thermal pressure is the stabilising force against self-gravity. However, molecular clouds are known to harbour complex internal motions as observed line spectra are often broad and complex, which implies that these objects are also turbulent. Moreover, many clouds are known to possess magnetic fields (Kazes & Crutcher, 1986), which could also offer support against gravity via static magnetic fields and slowly-dissipating magnetohydrodynamic turbulence (Myers & Goodman, 1988). Whilst the relative importance of self-gravity, turbulence and magnetic fields is not yet completely understood, gravitational forces are expected to dominate. Hence, the Jeans mass provides an adequate estimate for the threshold of core collapse.

1.1.2   Core collapse

As the process of molecular cloud collapse (and the resultant structure within molecular clouds) is very hierarchical, it becomes prudent to now focus on a region of gas, known as a prestellar core, that will proceed to form a star. The collapse of a uniform sphere, without a pressure gradient, occurs in a free-fall time

$$t_{\text{ff}} = \left(\frac{3\pi}{32G\rho} \right)^{1/2},$$
(1.2)

where ρ is the average mass density of the material, which is defined as the time taken to collapse to infinite density from a state of rest (Spitzer & Arny, 1978). This is for an assumed isothermal collapse, as the core is optically thin to thermal dust emission for H_2 densities below about $10^{10}\,\text{cm}^{-3}$. However, even if the equation of state is not precisely isothermal, and instead is polytropic, similar results are found (Larson, 1969). The free-fall time implies, then, that the denser inner regions always collapse faster than the less dense outer regions, i.e. the collapse is 'inside-out'. This results in an increasingly centrally peaked density distribution (Larson, 1973; Tohline, 1982). Therefore, only a very small fraction of the core mass reaches densities high enough to become optically thick. Once this density threshold is reached, the temperature in the centre of the collapsing core begins to rise because thermal dust radiation can no longer escape effectively. As a result, thermal pressure increases faster than gravity and the collapse decelerates. A central region, known as the first hydrostatic core, then forms, which is in rough hydrostatic equilibrium.

The first core continues to grow as material from the surrounding, still-collapsing envelope falls onto its surface through an accretion shock (Larson, 1969). Many simulations have predicted physical properties of the first hydro-static core across large parameter spaces (see Bate *et al.*, 2014; Joos *et al.*, 2013;

Matsumoto & Hanawa, 2011; Tomida *et al.*, 2015, and references therein), but because of the large optical depths, observational confirmation of their existence has remained elusive. Recently, however, due to the continual advancement in interferometric instruments, detections have been made that are the most convincing to date (e.g. Maureira *et al.*, 2017). Hence, a bona fide observation of a hydrostatic core is likely only a matter of time.

After formation, the temperature within the first hydrostatic core rises adiabatically until it exceeds 2000 K. At this point, hydrogen molecules begin to dissociate and the core becomes dynamically unstable. Another phase of collapse commences; it is isothermal like the first phase because here the released gravitational energy is absorbed by the dissociated hydrogen molecules. Once all the hydrogen is dissociated, the ratio of specific heats reaches the value required for stability and a second hydrostatic core is formed. At this stage the core is commonly refereed to as a protostar, as this is the region that will, after a period of accreting surrounding material, initiate nuclear fusion and become a pre-main sequence star.

The timescale for gravitational collapse of a core to the point just before nuclear fusion commences can be estimated with the Kelvin-Helmholtz timescale

$$t_{\mathrm{KH}} \approx \frac{G M_{\mathrm{s}}^2}{R_{\mathrm{s}} L_{\mathrm{s}}}, \tag{1.3}$$

where M_{s}, R_{s} and L_{s} are the mass, radius and luminosity (assumed constant) of the star. If this timescale is shorter than the free-fall time previously defined, then the protostar will ignite before core collapse has completed and protostellar radiation will have a significant impact on the evolving object. The boundary between these two regimes, which is located at $M_{\mathrm{s}} \approx 8\,\mathrm{M}_{\odot}$, is therefore used to define low-mass star formation and high-mass star formation.

1.1.3   Low mass

Low mass stellar systems (protostar and surrounding envelope) are classified as young stellar objects (YSOs) that were split into three groups: Class I, II and III by Lada (1987), and later expanded to include a Class 0 by André *et al.* (1993). These classes are believed to represent an evolutionary sequence, though observational ambiguities (e.g., projection effects and episodic accretion) can blur this picture somewhat (Dunham *et al.*, 2010; Robitaille *et al.*, 2006). Their determination relies on the observed appearance of the system, or on the spectral index of the spectral energy distribution (SED). This spectral index, which is calculated at $\lambda = 2.2$–$25\,\mu$m because the radiation emitted by the central protostar and the accretion shock is re-emitted by the surrounding dust at infrared wavelengths, is defined as

$$a_{\mathrm{IR}} = \frac{d\log(\lambda\mathrm{F}_\lambda)}{d\log\lambda}\,, \tag{1.4}$$

where λ is the wavelength and F_λ is the flux at the corresponding wavelength. Figure 1.1 shows a schematic of the traditional evolutionary sequence of a YSO with the expected SED, physical properties and observational characteristics for each class.

A Class 0 source represents some of the youngest YSOs and possesses an envelope that contains more than 50 per cent of the total system mass; due to this Class 0 sources are synonymous with the aforementioned second hydrostatic core. They are typically defined by their bolometric temperature (Chen *et al.*, 1995), by the ratio of their bolometric to submillimetre ($\lambda > 350\,\mu$m) luminosity (André *et al.*, 1993) or by the fact that, due to their highly embedded nature, their SED is undetected at $\lambda \leq 10\,\mu$m and represents a blackbody at a temperature $T \leq 30$ K. These objects also harbour molecular outflows (Bourke *et al.*, 2005; Hirano *et al.*, 2010; Lee *et al.*, 2000; Loinard *et al.*, 2013), although the exact
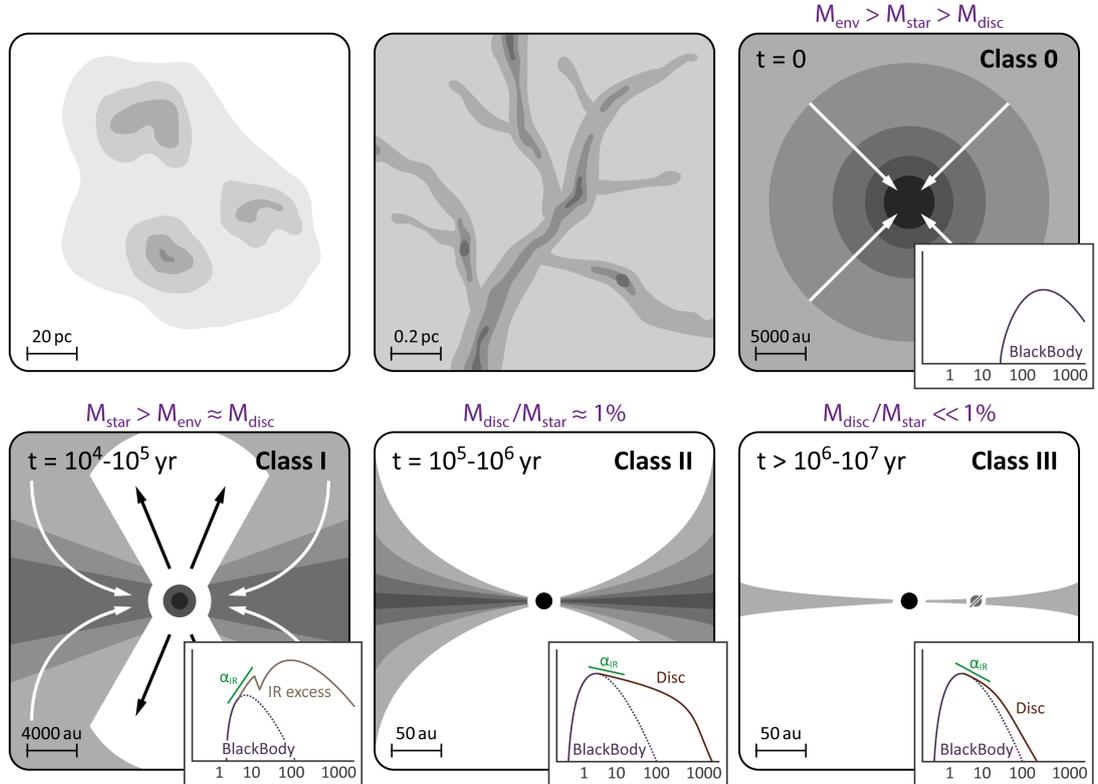
Figure 1.1: Schematic of low mass star formation from molecular cloud to planetary disc, based on the theoretical framework of Shu *et al.* (1987) and André *et al.* (1993), with the inclusion of the filamentary structure now believed to occur within GMCs (see e.g. André *et al.*, 2014). Labels show sizes, evolutionary classes, and typical formation times after cloud collapse ensues. Insets display a theoretical SED for each class, separated into components, along with the typical slope of the spectral index, α_{IR}. Adapted from Jonkheid (2006).

formation mechanisms are not fully understood yet, but outflows are not unique to Class 0 sources and hence cannot be used as a definitive distinction.

Once the stellar mass exceeds the envelope mass, which typically occurs after a few times 10^4 years of envelope dispersion, the Class I stage is reached. At this point, the associated SED is no longer defined by a single-temperature blackbody. Instead, the peak of the SED transitions to the far-infrared regime as the remaining inner envelope is heated to approximately $100\,\mathrm{K}$. Consequently, Class I

sources are characterised by a spectral index, $a_{IR} > 0.3$. Moreover, an additional SED component is seen at shorter, mid-infrared wavelengths, which is caused by the observation of a circumstellar, or protoplanetary, disc (see Section 1.2). There is also a clear dip seen in the disc-portion of the SED, which is caused by $10\,\mu m$ silicate absorption. As with Class 0 sources, Class I sources are associated with jets and outflows which are typically traced in H_2, CO, and SiO (see Bally *et al.*, 2007, and references therein).

When the envelope has been mostly dispersed through outflow and accretion, which typically takes a few times 10^5 years, the Class II stage is reached. At this point the system is visible at optical wavelengths and the SED is well represented by the spectrum of a blackbody at protostellar temperatures with an additional, cooler, disc component. Moreover, an ultraviolet component may be visible; it is generated by the magnetically-driven accretion shocks at the protostellar surface. For Class II sources, $-1.6 > a_{IR} > -0.3$ (there are 'flat-spectrum' sources, introduced by Greene *et al.* (1994), that bridge the spectral index gap between Class I and II YSOs), and these sources correspond to classical T Tauri stars that possess significant circumstellar dust. Planet formation is typically considered to occur at this stage, with massive gaseous planets forming from the large gas reservoirs in the disc. However, recent observations have suggested planet formation may begin at even earlier phases of YSO evolution (Carrasco-González *et al.*, 2016; Quanz *et al.*, 2015).

After a few times 10^6 years, the Class III stage is reached once the disc has mostly been dispersed by various mechanisms, such as accretion, photoevaporation, stellar winds, stellar encounters or (proto)planetary formation. As a result, Class III SEDs are similar to Class II SEDs, but with a much fainter disc contribution, resulting in $a_{IR} < -1.6$. Class III sources correspond to weak-line T Tauri stars, and moreover, as the dust within such systems is most likely gener-

ated by collisions between planetessimals, these objects are also known as debris discs. Once this final stage completes, the star approaches the main sequence as a zero-age main sequence (ZAMS) object.

1.2 Disc formation and evolution

Disc structures are crucial to many astrophysical processes, ranging from the formation and evolution of entire galaxies, to the comparatively minuscule rings around individual planets. During star formation, a disc forms from a collapsing core of dust and gas because, as these objects are rotating (Phillips, 1999), the constituent particles have a total non-zero angular momentum that has a preferred direction (and a set of preferred planes perpendicular to this direction). Collisions between particles become more frequent as the cloud collapses, which causes an increasing number of particles to be aligned with the average angular momentum direction. As a result, over time the system relaxes into a disc-like state.

The conservation of angular momentum also explains why protoplanetary discs must form around collapsing stars, due to the 'angular momentum problem'. To illustrate this, consider a core with a typical radius, $r_c = 0.05\,\mathrm{pc}$ (Caselli *et al.*, 2002), and typical angular velocity, $\Omega_{\mathrm{c}} = 10^{-14}\,\mathrm{s}^{-1}$ (Lodato, 2008). The specific angular momentum of such an object is

$$j_{\mathrm{c}} = \Omega_{\mathrm{c}} r_{\mathrm{c}}^2 = 2 \times 10^{20}\,\mathrm{cm}^2\,\mathrm{s}^{-1}. \tag{1.5}$$

If this core collapses to form a protostar, as most cores seem to, then, assuming a Solar-type star is eventually formed, the break up angular velocity can be calculated by equating centrifugal and gravitational forces,

$$\Omega_{\mathrm{c}}^2 r_{\mathrm{s}} = \frac{GM_{\mathrm{s}}}{r_{\mathrm{s}}^2}. \tag{1.6}$$

Therefore the specific angular momentum of a Solar-type star formed from this collapsing core at break up angular velocity is

$$j_{\mathrm{b}} = \Omega_{\mathrm{b}} r_{\mathrm{s}}^2 = 3 \times 10^{18} \, \mathrm{cm}^2 \, \mathrm{s}^{-1}. \tag{1.7}$$

As $j_{\mathrm{b}} \ll j_{\mathrm{c}}$, and the fact that disc structures seem ubiquitous in star forming regions, this means that angular momentum must be removed from the system during collapse before a star can form.

1.2.1 α-discs

A protoplanetary disc removes angular momentum from the collapsing core if the disc itself is viscous or some mechanism creates an effective viscosity. Essentially, in this scenario, concentric annuli are coupled together due to the Keplerian-like rotation of the disc, so that a torque acts between slower rotating outer material and faster rotating inner material. The result is that the outer material speeds up and moves outwards, and the inner material slows down and moves inwards, which results in a net transport of the angular momentum outwards via friction (Balbus, 2003). As the source of this viscosity is likely a combination of processes (that are explored in Sections 1.2.2, 1.2.3 and 1.2.4), which require significant amounts of computational resources, simulations have typically used the simplified α-disc prescription for the effective kinematic viscosity (Shakura & Sunyaev, 1973),

$$\nu = \alpha c_{\mathrm{s}} H_{\mathrm{p}}, \tag{1.8}$$

where c_{s} is the disc material sound speed, H_{p} is the pressure scale height, and α is a dimensionless parameter. A larger value of α corresponds to a more viscous disc, and typically in simulations $\alpha = 0.001$–0.1 is assumed.

Molecular viscosity does not contribute significantly to the disc viscosity because the timescale for accretion approaches the age of the Universe for typical

disc parameters. Instead, hydrodynamic, magnetic and/or gravitational forces are likely responsible for transporting angular momentum on both small and large scales within the disc.

1.2.2 Hydrodynamic instabilities

Initially it was believed that hydrodynamic turbulence could replace molecular viscosity in explaining the viscous nature of discs. However, several authors have found that convective turbulence produced inward angular momentum transport rather than outwards (e.g. Quataert & Chiang, 2000; Stone & Balbus, 1996; Stone *et al.*, 2000). Moreover, Hawley *et al.* (1999) found that a Keplerian flow possesses a Reynolds stress (essentially the component of the stress tensor that accounts for turbulent fluctuations in fluid momentum) that cannot by itself sustain turbulence. This is despite the differential rotation that could, in principle, maintain the turbulence because Coriolis forces induce epicyclic, oscillatory motions that quell turbulent motions (Ji *et al.*, 2006). Hence, Keplerian systems are most likely locally hydrodynamically stable, both linearly and non-linearly, which means an alternate source of viscosity is required.

1.2.3 Magnetorotational instabilities

Many molecular clouds are known to be threaded by magnetic fields (see e.g. Crutcher, 1999; Ward-Thompson *et al.*, 2000), which implies that some discs forming in such clouds are also magnetically threaded. Consequently, magnetorotational instabilities (MRIs), which are sometimes referred to as Balbus-Hawley instabilities (see Balbus & Hawley, 1991), seem to offer a promising explanation for disc viscosity in many scenarios because a weak magnetic field in conjunction with differential rotation is sufficient to overcome the issues with hydrodynamic instabilities. MRIs can be understood by considering two particles in the rotat-

ing disc connected by a spring. Even though there is an attractive force between the particles, the differential rotation causes the particles to move apart. Hence the outer particle gains angular momentum from the inner particle, causing the outer particle to move outward and the inner particle to move inward. This leads to an even larger difference in the angular frequencies. In a protoplanetary disc these particles are fluid elements connected by a magnetic field line, and the magnetic tension acts as the spring. Linearly there is an instability driven by an exponentially increasing separation of the fluid elements, followed by a non-linear instability as fluid elements from different regions of the disc mix together. MRIs therefore are efficient at transporting angular momentum outwards.

However, in the ideal magnetohydrodynamics (MHD) regime, angular momentum transport can be so efficient that disc formation is suppressed in simulations. For example, Allen *et al.* (2003) and Hennebelle & Fromang (2008) found that, in 2D and 3D simulations respectively, rotationally-supported discs were not formed in dense cores magnetised to realistic levels. This is because, as material accretes onto the central protostar, the magnetic field lines become 'pinched' (as shown in Figure 1.2), which produces a magnetic split monopole with field lines fanning out radially (Galli *et al.*, 2006). Hence, the magnetic energy density surpasses that of the accretion flow, meaning infalling material is dominated by the magnetic field and loses all of its angular momentum.

To alleviate this issue, known as the 'magnetic braking problem', and because there most likely is not a perfect coupling between material and field lines as is the case in ideal MHD, non-ideal MHD processes such as ambipolar diffusion, the Hall effect and Ohmic resistivity have been investigated. Ambipolar diffusion allows the field lines that are coupled to the ions to drift relative to the bulk neutral material. As a result, the pinching of the magnetic fields that suppresses disc formation is lessened because diffusion reduces the twisting of field lines caused
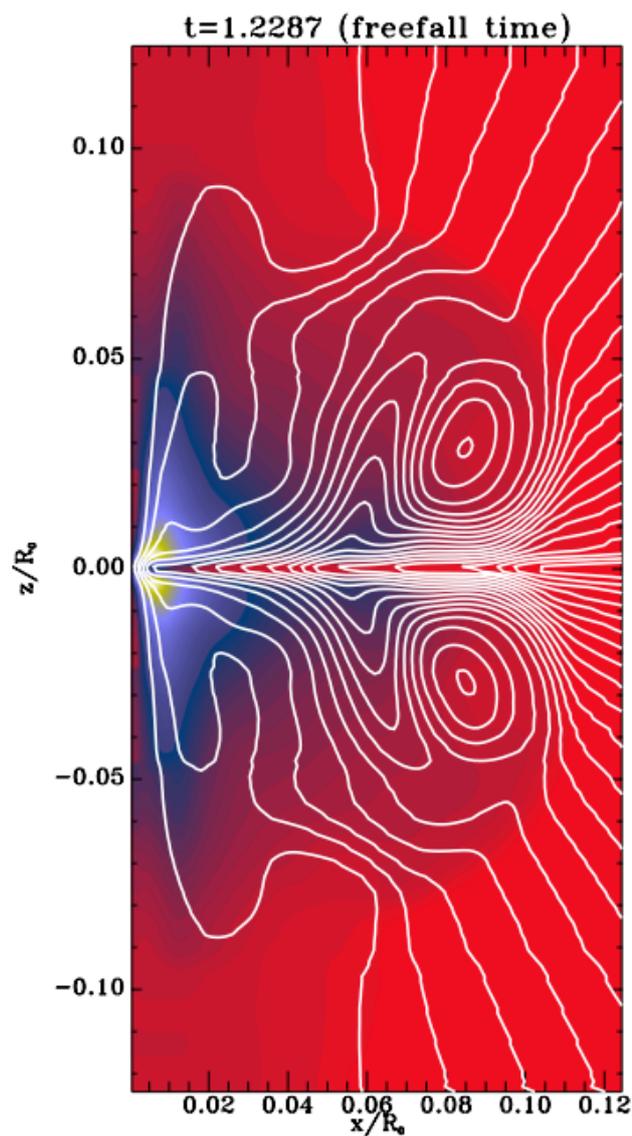
Figure 1.2: Structure of the azimuthally averaged magnetic field in a protoplanetary disc model demonstrating how field lines can become twisted and pinched. The solid lines display the poloidal magnetic field lines and the colour scale shows the toroidal magnetic field strength. Taken from Hennebelle & Fromang (2008).

by the rotation of neutrals. However, this is probably not to a sufficient extent given realistic field strengths and cosmic ray ionisation rates (e.g Mellon & Li, 2009). Moreover, in some simulations the suppression is even enhanced because of the formation of an accretion shock that traps a strong magnetic field near the central protostar, leading to efficient magnetic braking of the post-shock material (Li *et al.*, 2011). The Hall effect, where the electrons are coupled to the field whilst the ions are coupled to the bulk neutral material, becomes more important as the density increases, with the exact dependence reliant on the dust grain size distribution. Krasnopolsky *et al.* (2011) found that this phenomenon can actively spin-up the inner part of the collapsing, magnetised flow, but Li *et al.* (2011) found that the Hall effect is incapable of forming a rotationally supported disc under typical dense core conditions. Ohmic dissipation, which converts electrical energy into heat through resistive forces, dominates at the highest densities. Li *et al.* (2011) found that Ohmic dissipation could not enable the formation of a rotationally supported disc, either by itself or in conjunction with ambipolar diffusion. However, Machida & Matsumoto (2011) and Tomida *et al.* (2015) both found that Ohmic dissipation did enable the formation of a protoplanetary disc. Therefore, although the exact mechanisms by which rotationally supported discs form are not fully understood, the general consensus is that some combination of non-ideal MHD effects, as well as the magnetic interchange instability (akin to a magnetic Rayleigh-Taylor type instability; see e.g. Krasnopolsky *et al.*, 2012), misalignment between the magnetic field and rotation axis (see e.g. Joos *et al.*, 2012), and dust evolution (see e.g. Zhao *et al.*, 2016, 2018), act to reduce the suppression of disc formation in magnetised cores.

1.2.4 Gravitational instabilities

A protoplanetary disc can become unstable if gravitational forces overcome pressure and shear forces. This criterion is characterised by the Toomre parameter (Toomre, 1964)

$$Q = \frac{c_{\mathrm{s}}\kappa}{\pi G \Sigma}, \tag{1.9}$$

where c_{s} is the sound speed, κ is the epicyclic frequency at which a fluid element oscillates when perturbed from circular motion, G is the gravitational constant and Σ is the surface density. For axisymmetric disturbances the criterion for gravitational collapse is $Q < 1$. However, for non-axisymmetric disturbances, which develop as spiral arms (as shown in Figure 1.3), the criterion is $Q \lesssim 1.5$ (Durisen $et\ al.$, 2003; Papaloizou & Savonije, 1991). The instability is initially linear and also dynamic, so small perturbations grow exponentially on the time scale of a rotation period $P_{\mathrm{rot}} = 2\pi/\Omega$, where Ω is approximately equivalent to the epicyclic frequency in a near-Keplerian disc (Durisen $et\ al.$, 2007). As the spiral waves grow, they can develop into shocks that produce strong localised heating (e.g Pickett $et\ al.$, 1998). This can then lead to rapid vertical expansions that resemble hydraulic jumps (Boley & Durisen, 2006). Disc material is also heated by compression and mass transport driven by gravitational torques, irradiation by the central protostar (and possibly external sources), and accretion heating from the surrounding envelope (e.g. D'Alessio $et\ al.$, 1997). Due to the form of Equation 1.9, it is the disc temperature that dictates if a disc is gravitationally unstable once the disc mass distribution and stellar mass (which governs most of κ) have been specified. Therefore, the key distinction between a gravitationally stable and unstable disc is whether the cooling time is short enough to effectively dissipate the heat produced.
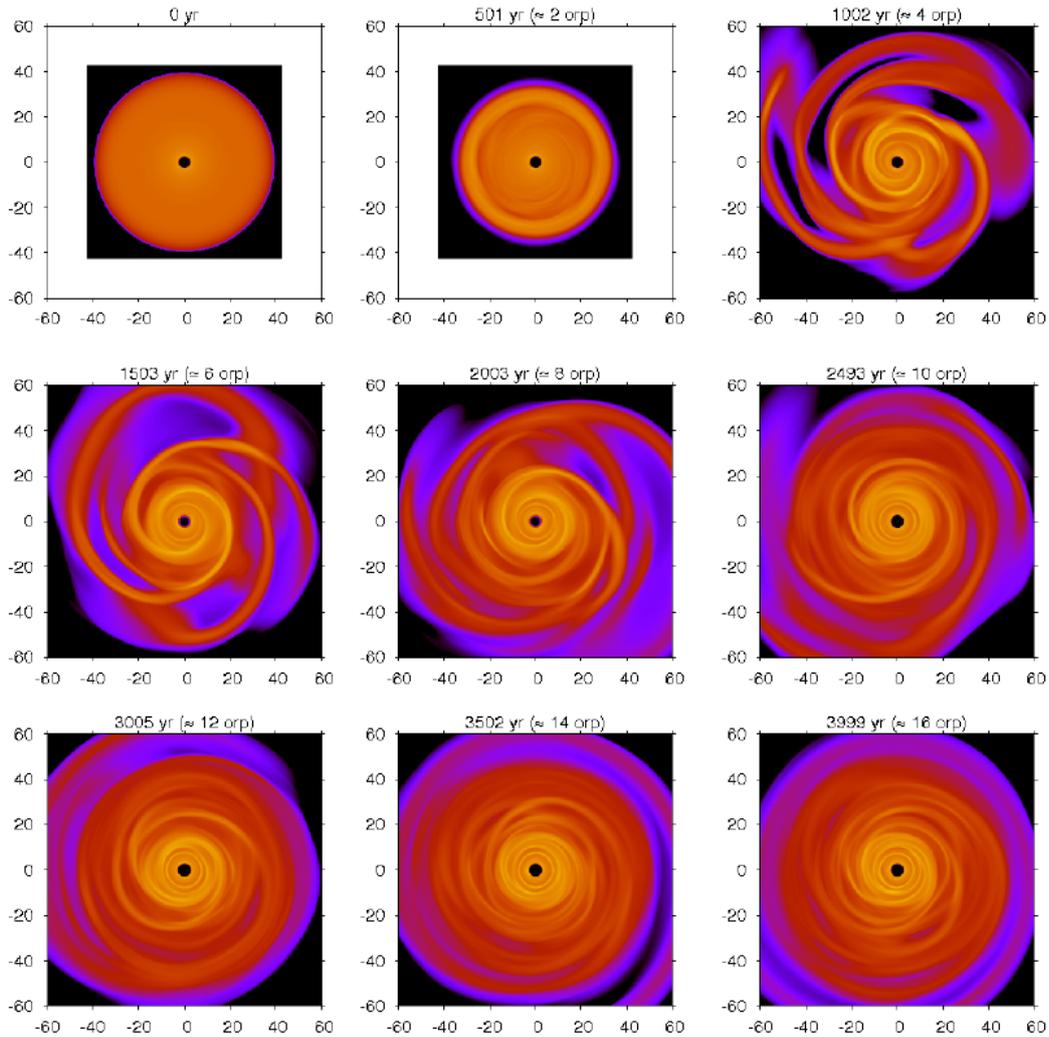
Figure 1.3: Evolution of a gravitationally unstable disc indicating the development of spiral structure. Taken from Boley (2007).

Considering the approximations that $H \approx c_{\mathrm{s}}/\Omega$, $\Omega^2 \approx GM_{\mathrm{s}}/r^3$ and $M_{\mathrm{d}} \approx \pi\Sigma r^2$, the Toomre criterion given in Equation 1.9 can be re-written as

$$Q \;\propto\; \frac{M_{\mathrm{s}}}{M_{\mathrm{d}}}\frac{H}{r}, \tag{1.10}$$

where M_{s} is the mass of the central protostar, M_{d} is the protoplanetary disc mass, H is the disc scale height, which is the vertical distance necessary for the density and pressure to fall by a factor of $1/\mathrm{e}$, and r is the radius. Typically protoplanetary discs have $H/r \approx 0.1$ (e.g. Andrews et $al.$, 2010), which means that non-axisymmetric instabilities will set in for a disc when

$$\frac{M_{\mathrm{d}}}{M_{\mathrm{s}}} \;\gtrsim\; 0.07. \tag{1.11}$$

In the very early stages of stellar formation, simulations have shown that the surrounding protoplanetary disc is likely to contain a mass comparable to that of the central protostar (e.g. Bate, 2010; Gerin et $al.$, 2017; Machida & Matsumoto, 2011). This implies, then, that young protoplanetary discs should be prone to developing gravitational instabilities (GIs), which has been verified in simulations (Dong et $al.$, 2016; Tsukamoto et $al.$, 2013; Vorobyov & Basu, 2005; Vorobyov & Pavlyuchenkov, 2017).

Several authors have investigated whether the previously mentioned α parameter is applicable to such global transport in GI-driven discs, albeit usually their main aim has been to investigate the fragmentation of the disc (e.g. Boley & Durisen, 2006; Boss, 2004; Cai et $al.$, 2006; Lodato & Rice, 2004; Mayer et $al.$, 2007). The general consensus is that even though the mass transport is dominated by global modes, with large fluctuations in the mass fluxes, an α-disc prescription is broadly applicable, as predicted by Gammie (2001). However, due to the global nature of gravitational torques, Boley et $al.$ (2007a) showed that pure flux-limited diffusion, which is commonly used in simulations, is inaccurate.

Rather, a fully three-dimensional ray tracing method would be more realistic and likely would lead to smaller amplitude GIs than have been reported.

1.2.5 Outflows and multiplicity

Winds provide a means of removing angular momentum that does not concern instabilities directly, and such outflows are often collimated to form jets (Ray, 2012). These are known to exist in T Tauri stars and are believed to carry away angular momentum at a range of disc radii, with highly collimated jets capable of removing angular momenta close to the protostar (Lee *et al.*, 2017). However, winds emanating from the innermost disc must rely on another source of angular momentum removal to actually drive them.

Another pathway for angular momentum redistribution is via stellar companions because stars typically form in binary or multiple systems. Tidal interactions between tightly bound systems can transfer angular momentum from the orbiting material around the forming stars to the orbital motions of companion stars (Larson, 2002). Interactions with passing stars in a cluster can also remove angular momentum from the collapsing core, causing some material to be directly accreted onto the star (e.g. Bate *et al.*, 2003). Moreover, in most simulations, multiple systems tend to decay and eject stars that carry angular momentum away with them (Bate *et al.*, 2003; Delgado-Donate *et al.*, 2004, e.g.), eventually ending up in the random motions of field stars.

Whilst outflows and interactions between stars can indeed remove angular momentum, it is highly unlikely that these mechanisms are responsible for the entirety of angular momentum removal. Instead, it is probable that several of the previously mentioned processes interact in complicated ways, ensuring that disc formation is a complex and chaotic process. Simplifications can be made, however, in order to assist hydrodynamic simulations. For example, in the bulk of an

isolated, embedded disc, one can assume that outflows and tidal interactions are negligible, and that the MRI is ineffective due to low ionisation rates (Fromang *et al.*, 2002; Gammie, 1996). In this scenario, GI should indeed be a very important mechanism for angular momentum transport. Even if this MRI assumption is relaxed, GI should still play an important role because dense, gravitationally unstable rings are expected to form, likely leading to disc outbursts related to FU Orionis events (Armitage *et al.*, 2001) and the formation of chondrules (small, rounded particles embedded in stony meteorites known as chondrites) (Boley & Durisen, 2008). Therefore, understanding the significance of GI in the early stages of disc formation is a very important avenue of research that warrants exploration.

1.3   Disc chemistry

To date, around 200 molecules have been detected in the ISM or circumstellar environments, with the largest being fullerenes C_{60} and C_{70}[1]. A whole host of reactions are responsible for the formation of these molecules, of which the main gas-phase processes are shown in Table 1.1.

In dense, shielded regions, the thermal energy and the number of photons available for reactions is low, so in this case cosmic-ray ionisation dominates. The cosmic-ray ionisation of H_2 occurs at a rate dependent on ζ, which is typically $1 \times 10^{-17}\,\mathrm{s}^{-1}$ (van der Tak & van Dishoeck, 2000), and 97% of the time produces H_2^+ (H^+ is produced the other 3% of the time). Other atomic species are also ionised via cosmic-rays, but at slower rates due to the abundance deficit compared to H_2. After formation, H_2^+ reacts quickly with H_2 via the reaction

$$H_2^+ + H_2 \rightarrow H_3^+ + H. \tag{1.12}$$

---

[1]http://www.astro.uni-koeln.de/cdms/molecules

Table 1.1: Important gas-phase reactions in astrophysical environments. Photoabsorption rates are given assuming no extinction and are typically negligible in dense, shielded regions. Adapted from Caselli (2005).

Reaction	Process	Rate Coefficient [s^{-1}]
Neutral-neutral	$A + B \rightarrow C + D$	10^{-12}–$10^{-10}\,cm^3$
Ion-neutral	$A^+ + B \rightarrow C^+ + D$	$10^{-9}\,cm^3$
Three-body	$A + B + M \rightarrow C + D + M$	$\lesssim 10^{-26}\,cm^6$
Radiative association	$A + B \rightarrow AB + h\nu$	10^{-16}–$10^{-13}\,cm^3$
Dissociative recombination	$AB^+ + e^- \rightarrow A + B$	$10^{-6}\,cm^3$
Charge transfer	$A^+ + B \rightarrow A + B^+$	$10^{-9}\,cm^3$
Photodissociation	$AB + h\nu \rightarrow A + B$	10^{-11}
Photoionisation	$A + h\nu \rightarrow A^+ + e^-$	10^{-11}
Cosmic-ray ionisation	$A + \gamma_{CR} \rightarrow A^+ + e^-$	10^{-19}–10^{-17}

Typically, only ion-neutral reactions considering H_2 are important because the reaction rate is proportional to the abundance of reactants and H_2 is at least three orders of magnitude more abundant than other species. The exception to this is when a reactant, such as He^+, undergoes a very slow reaction, with a rate coefficient significantly below $10^{-12}\,cm^3\,s^{-1}$.

H_3^+ is one of the most important molecular ions in astrochemistry because it facilitates the formation of a significant number of species, as shown in Figure 1.4. H_3^+ does not react with H_2 but can produce species such as OH^+ and CH^+ via proton transfer with atomic O and C, respectively. These molecular ions undergo hydrogen abstraction until CH_3^+ and H_3O^+ are formed. Dissociative recombination then proceeds, with the outcome dependent on the branching ratio. Finally, the products of this sequence react with atomic oxygen or carbon to produce HCO^+, which, via dissociative recombination, forms the second most abundant molecule in dark clouds, CO.

Rather than the hydrogen abstraction sequence followed by dissociative recombination that dominates for O and C, neutral-neutral reactions are more
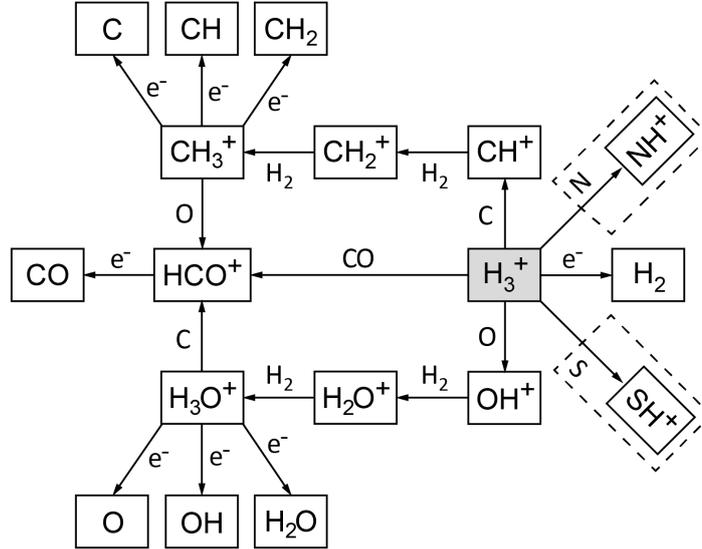
Figure 1.4: Depiction of the main ion-neutral reactions initiated by H_3^+. Rather than the hydrogen abstraction sequence followed by dissociative recombination that dominates for O and C, the dashed boxes indicate that neutral-neutral reactions are more important for N and S (at low temperatures). Adapted from Ilee (2013).

important for N and S (at low temperatures), which is indicated by the dashed lines in Figure 1.4. This is because the hydrogen abstraction reactions that would produce SH_3^+ are endothermic, meaning SH^+ dissociatively recombines with electrons to re-form S, and the proton transfer reaction of N with H_3^+ is particularly slow. Instead, the following reactions occur

$$N + CH \rightarrow CN + H, \tag{1.13}$$

$$S + OH \rightarrow SO + H. \tag{1.14}$$

N_2 is produced after CN has formed via Equation 1.13 and subsequently reacted with N (or also after NO reacts with N). N_2 can then react with H_3^+ to form N_2H^+, which has been observed in interstellar clouds. N_2 can also react with He^+ to produce N^+, followed by successive hydrogenation until the saturated ion,
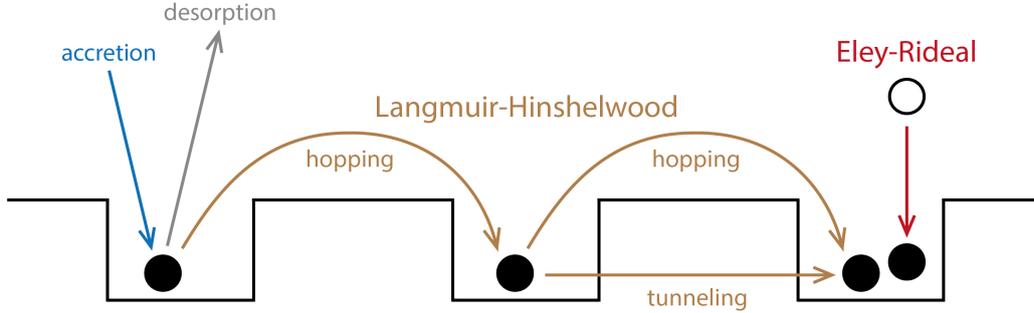
Figure 1.5: Mechanisms for surface reactions on grain surfaces: Langmuir-Hinshelwood (diffusive) and Eley-Rideal. An open circle represents a non-thermalised species, whereas a closed circle represents a thermalised species. Surface reactions can occur when two species are in the same potential well. Adapted from Ioppolo (2010).

NH_4^+, is formed. NH_3 is then produced via dissociative recombination, which, like N_2H^+, has been observed in molecular cloud cores (see e.g. Bergin, 2014, and references within).

The gas phase compositions observed in hot cores and corinos are not congruent with gas-phase chemistry by itself. Indeed, dust grain surface chemistry (specifically hydrogenation) is needed to offset the photodissociation of H_2 in diffuse clouds (Gould & Salpeter, 1963). Moreover, now the topic of grain-surface chemistry is known to be very important in explaining: the large abundances of complex organic molecules, which are typically carbon-containing molecules containing six or more atoms (see e.g. Herbst & van Dishoeck, 2009); the complex icy dust grain mantles deduced from observations; and the large amount of deuterium fractionation observed in low mass star forming regions (Caselli, 2005).

Molecules in the gas-phase are affixed to the surfaces of dust grains via adsorption, which occurs through two different mechanisms: physisorption via weak van der Waals forces and chemisorption via chemical valence bonds. Reactions involving adsorbed species can then proceed via the Langmuir-Hinshelwood or Eley-Rideal mechanisms, as illustrated by Figure 1.5. In the case of the Langmuir-

Hinshelwood mechanism, light species can diffuse across the grain surface and overcome energetic barriers via thermal hopping or quantum tunneling, depending on the dust temperature. In the case of the Eley-Rideal mechanism, a gas-phase molecule interacts more or less directly with a surface-adsorbed species; this mechanism can be the dominant pathway for surface reactions if a large potential barrier exists that rules out the Langmuir-Hinshelwood mechanism. Diffusive processes in particular enable the production of heavier species on grain surfaces, and these species tend to be saturated because H is capable of diffusing very quickly and is a very efficient reactant on surfaces. For example, water-ice, ammonia-ice and methane-ice are formed via the hydrogenation of O, N and C atoms, respectively, landing on dust grains (Herbst & van Dishoeck, 2009). Moreover, the complex organic molecule methanol is formed via hydrogenation of adsorbed CO (Charnley et $al.$, 1997), and further reactions with C and H atoms can create molecules that are even more complex, such as CH_3COH and C_2H_5OH (Charnley et $al.$, 2001). This multitude of reactions then leads to the build up of complex ice mixtures on dust grain surfaces, which can subsequently affect the evolution of dust grains by altering the efficiency of coagulation (e.g. Musiolik et $al.$, 2016).

After a species has been adsorbed, desorption can occur and return the surface species to the gas-phase. This proceeds either by thermal evaporation (sublimation) for very light species or by non-thermal mechanisms such as photodesportion, cosmic-ray bombardment and excess energy from surface reactions. Thermal desorption is dependent on the dust temperature, so in low temperature, shielded environments only light species such as H and D can evaporate at significant rates (Millar, 2015); a dust temperature of $\approx 150\,K$ is needed to thermally evaporate H_2O. Therefore, the abundances of water and other saturated species are indicators of the local conditions in star forming regions.

Protoplanetary discs harbour significantly different conditions than those of the ISM, with number densities and temperatures of $n \approx 10^9$–$10^{14}\,\mathrm{cm}^{-3}$ and $T \approx$ 20-2000 K, respectively, compared to $n \approx 10^4$–$10^5\,\mathrm{cm}^{-3}$ and $T \approx 10\,\mathrm{K}$ in star forming cores. Consequently, the chemistry contained within a disc can be significantly different and resemble that of some hydrogenated planetary atmospheres. For example, at high densities three-body reactions become important, with the third body reactant being the most abundant molecule, H_2.

1.3.1 Rate equations

Chemical kinetic models compute the solutions of a network of coupled ordinary differential equations (ODEs). These ODEs describe how the number density of each species changes as a function of time, due to the chemical reactions taking place. For example, if a species, X, is created and destroyed by the following bimolecular reactions

$$A + B \rightarrow X + C \tag{1.15}$$

$$X + D \rightarrow E + F \tag{1.16}$$
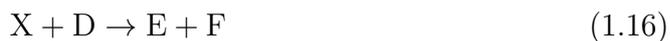
then the rate equation for species X is

$$\frac{dn_X}{dt} = k_{AB} n_A n_B - k_{XD} n_X n_D, \tag{1.17}$$

where k_{AB} and k_{XD} are the rate (or kinetic) coefficients for the appropriate reactions. There exist several publicly accessible databases that provide rate coefficients, such as the UMIST Database for Astrochemistry (UDfA[1]; McElroy *et al.*, 2013; Millar *et al.*, 1997; Woodall *et al.*, 2007), the Ohio State University networks[2] and the Kinetic Database for Astrochemistry (KIDA[3]; Wakelam *et al.*,

---

[1]http://udfa.ajmarkwick.net/
[2]http://faculty.virginia.edu/ericherb/research.html
[3]http://kida.obs.u-bordeaux1.fr/

2012). The reaction rate coefficients are not necessarily constants however, as there can be a strong dependence on temperature. For this reason the rate coefficients are usually given in the Arrhenius-Kooij form (Arrhenius, 1889; Kooij, 1893)

$$k = \alpha \left(\frac{T}{300} \right)^{\beta} \exp \left(-\frac{\gamma}{T} \right),$$ (1.18)

where T is the temperature of the material, α is the room temperature rate coefficient of the reaction, β is a constant and γ is the activation energy of the reaction.

The complexity of the chemical network can be increased by adding more species and by adding more types of reactions, such as photoabsorption, cosmic-ray ionisation, adsorption and desorption and surface reactions. However, the nature of this complexity ensures that the study of sophisticated chemical models is computationally challenging. For instance, rate equations used to describe gas-phase chemical kinetics may not be appropriate for surface chemistry because using average concentrations bears no meaning when the average number of reactive species is less than one per grain. Instead, stochastic methods can be implemented, but often with several approximations in place to speed up calculations (see e.g. Millar, 2015).

1.4   Radiative transfer

The transport of radiation within protoplanetary discs is fundamental in governing the heating and cooling mechanisms, the dust temperature, the radiation pressure, opacity and emissivity and the appearance of observations. It is de-

scribed by the equation of radiative transfer

$$\frac{dI_\nu}{ds} = -\alpha_\nu I_\nu + j_\nu, \tag{1.19}$$

where I_ν, α_ν and j_ν are the specific intensity, absorption coefficient and emission coefficient, respectively, at a particular frequency, ν. Essentially, the intensity along the line-of-sight through a medium is reduced by absorbing material and bolstered by emitting material. Equation 1.19 can be rewritten in the form

$$\frac{d}{ds}\left(I_\nu \exp\left[\int_0^s \alpha_\nu(s')ds'\right]\right) = j_\nu \exp\left[\int_0^s \alpha_\nu(s')ds'\right] \tag{1.20}$$

so that integration from s = 0 to s = Δs yields the general solution

$$I_\nu = I_{\nu_0} \exp\left[-\int_0^{\Delta s} \alpha_\nu(s')ds'\right] + \int_0^{\Delta s} ds' j_\nu(s') \exp\left[-\int_{s'}^{\Delta s} \alpha_\nu(s'')ds''\right]. \tag{1.21}$$

If α_ν and j_ν are spatially constant, Equation 1.21 simplifies to

$$I_\nu = I_{\nu_0} e^{-\alpha_\nu \Delta s} + \frac{j_\nu}{\alpha_\nu}\left(1 - e^{-\alpha_\nu \Delta s}\right), \tag{1.22}$$

which is equivalent to

$$I_\nu = I_{\nu_0} e^{-\tau_\nu} + S_\nu \left(1 - e^{-\tau_\nu}\right) \tag{1.23}$$

where S_ν is the source function and τ_ν is the optical depth, at a particular frequency. Essentially, Equation 1.23 means that the emergent intensity is defined as the summation of the background intensity attenuated by the entire absorbing medium, and the emission that is attenuated by the absorbing medium up to the point of emission.

In the case of continuum radiation, α_ν and j_ν depend only on the density and opacity (which is dependent on temperature and dust grain composition) of the

material, which affords a relatively simple solution to Equation 1.23

$$I_\nu = I_{\nu_0} e^{-\tau_\nu} + B_\nu(T_\mathrm{d}) \left(1 - e^{-\tau_\nu}\right),$$
(1.24)

where $B_\nu(T_\mathrm{d})$ is the Planck function that is easily calculated at the dust tempera-
ture, T_d. To explore how a solution is found for line radiation, consider the simple
case of a two level atom. The emission and absorption coefficients are defined as

$$j_\nu = \frac{h\nu}{4\pi} n_\mathrm{u} A_\mathrm{ul} \, \phi_\nu$$
(1.25)

$$\alpha_\nu = \frac{h\nu}{4\pi} \left(n_\mathrm{l} B_\mathrm{lu} - n_\mathrm{u} B_\mathrm{ul}\right) \phi_\nu,$$
(1.26)

where n_u and n_l are the populations of the upper and lower levels, respectively,
A_ul, B_ul and B_lu are the Einstein coefficients for spontaneous emission, stimulated
emission and spontaneous absorption, respectively, and ϕ_ν is the line profile func-
tion (Stahler & Palla, 2005, Appendix C). The line profile essentially describes
how likely a photon at a particular frequency is to excite/de-excite the atom or
molecule and is normalised so that $\int \phi_\nu d\nu = 1$.

The level populations obey the equation of statistical equilibrium,

$$\frac{dn_\mathrm{u}}{dt} = \left(n_\mathrm{l} B_\mathrm{lu} \bar{J} + \sum_k n_\mathrm{c}{}^k \gamma_\mathrm{lu}{}^k\right) - \left(n_\mathrm{u} A_\mathrm{ul} + n_\mathrm{u} B_\mathrm{ul} \bar{J} + \sum_k n_\mathrm{c}{}^k \gamma_\mathrm{ul}{}^k\right) = 0$$
(1.27)

where n_c, γ_ul and γ_lu are the number density, collisional de-excitation and colli-
sional excitation coefficients, respectively, for the collisional partner k, and $\bar{J}$ is
the mean intensity. As $\bar{J}$ is related to the specific intensity via

$$\bar{J} \equiv \int_0^\infty J_\nu \phi(\nu) d\nu \equiv \frac{1}{4\pi} \oint I_\nu d_\Omega \,,$$
(1.28)

it is clear to see that the emission and absorption coefficients depend on the
level populations, which in turn depend on the specific intensity, which itself

depends on the absorption and emission coefficients. Therefore, in the case of line radiation, an analytic solution to Equation 1.23 cannot be found and instead, numerical methods must be used to iterate towards a converged solution.

A significant simplification can be made to reduce the complexity of radiative transfer calculations if the density of collisional partners, such as H_2 or e^-, is high enough. This is characterised by a critical density, which is defined in the optically thin limit as

$$n_{\text{crit}}{}^k = \frac{A_{\text{ul}}}{\gamma_{\text{ul}}{}^k} \,. \tag{1.29}$$

Inserting this expression into Equation 1.27 results in

$$\frac{n_{\text{u}}}{n_{\text{l}}} = \frac{n_{\text{c}}{}^k \, \gamma_{\text{lu}}{}^k}{n_{\text{crit}}{}^k \, \gamma_{\text{ul}}{}^k + n_{\text{c}}{}^k \, \gamma_{\text{ul}}{}^k} \,, \tag{1.30}$$

where it is assumed that $B_{ul}\bar{J}$ and $B_{lu}\bar{J}$ are negligible due to the previously mentioned optically thin constraint. The collisional excitation and de-excitation coefficients are related by

$$\gamma_{\text{lu}}{}^k = \frac{g_{\text{u}}}{g_{\text{l}}} \gamma_{\text{ul}}{}^k \exp\left(-\frac{\Delta E}{k_{\text{B}} T_{\text{kin}}}\right) \,, \tag{1.31}$$

where g_{u} and g_{l} are the degeneracies of the upper and lower levels, respectively, k_{B} is the Boltzmann constant and T_{kin} is the kinetic temperature of the collision partners. Use of Equations 1.30 and 1.31 yields

$$\frac{n_{\text{u}}}{n_{\text{l}}} = \frac{g_{\text{u}}}{g_{\text{l}}} \exp\left(-\frac{\Delta E}{k_{\text{B}} T_{\text{kin}}}\right) \left[\frac{n_{\text{crit}}{}^k}{n_{\text{c}}{}^k} + 1\right]^{-1} \,. \tag{1.32}$$

When the density of collisional partners is high, i.e. $n_{\text{c}}{}^k \gg n_{\text{crit}}{}^k$ then the distribution given by Equation 1.32 approaches the Boltzmann distribution. Essentially, collisions are fast enough to transfer the net absorbed or emitted radiative energy into kinetic energy. In this case the gas is in local thermodynamic

equilibrium (LTE) for this transition, and the population distribution is said to be thermalised. Moreover, the population distribution can be calculated without prior knowledge of the radiation field. It is worth mentioning, however, that LTE only holds for this particular transition, and hence the general simplification of LTE may not be appropriate for all transitions in a multi-level atom or molecule. When LTE can not be assumed, Equation 1.32 shows that the upper level is less populated than in the LTE solution. In this case the population is subthermal.

Equation 1.32 was derived for an assumed optically thin medium. If the optical depth is non-negligible, however, the reabsorption of emitted photons, known as radiative trapping, must be taken into account. An accurate calculation of radiative trapping is complex because the process is non-local, i.e. photons emitted from one point in the medium can affect the level populations in entirely different regions of the medium. However, an approximation can be made by assuming emitted photons are either absorbed locally (i.e. near the emission site) or escape, with an escape probability defined as

$$\beta(\boldsymbol{r}) \equiv \frac{1}{4\pi} \int \int e^{-\tau_\nu(\hat{\boldsymbol{n}},\boldsymbol{r})} \phi_\nu \, d\nu d\Omega, \tag{1.33}$$

where ν is frequency, $\boldsymbol{r}$ is the emitting position, $\hat{\boldsymbol{n}}$ the direction and ϕ is the normalised line profile (Draine, 2011). If collisions are ignored then the number of photons absorbed, $n_\mathrm{l} B_\mathrm{lu} \bar{J}$, minus the number of photons produced by stimulated emission, $n_\mathrm{u} B_\mathrm{ul} \bar{J}$, must balance the number of photons that are spontaneously emitted and do not escape, $(1 - \beta) n_\mathrm{u} A_\mathrm{ul}$ (Klessen & Glover, 2016). Therefore Equation 1.27 can be rewritten as

$$\gamma_\mathrm{lu}{}^k n_\mathrm{c}{}^k n_\mathrm{l} = (\gamma_\mathrm{ul}{}^k n_\mathrm{c}{}^k + \beta A_\mathrm{ul}) n_\mathrm{u}. \tag{1.34}$$

This is equivalent to the optically thin equation without radiative trapping, i.e. when stimulated emission and absorption are neglected, but with A_ul replaced

by βA_{ul}. As $n_{\mathrm{crit}}{}^{k} \propto A_{\mathrm{ul}}$ (see Equation 1.29), the effect of radiative trapping is to reduce the critical density for collisional partner k.

The calculation of β is not straightforward due to the dependence on the optical depth along the line-of-sight, which in turn is defined by the geometry and kinematics of the medium. Therefore, the geometry is often simplified to speed up calculation, but real molecular clouds are complex and highly inhomogeneous structures so the approximations can be inaccurate. A more sophisticated approximation is the Large Velocity Gradient (LVG), or Sobolev approximation (Sobolev, 1957), in which the probability of escape is assumed to be high for fast moving gas due to Doppler shifting. The use of the LVG approximation appears to be justified for many turbulent molecular clouds of interest (Ossenkopf, 1997, 2002), and hence it is used in several radiative transfer codes when non-LTE line emission is calculated.

Typically, radiative transfer codes use Monte Carlo (MC) and Accelerated Lambda Iteration (ALI) to solve Equation 1.19. The Monte Carlo method is implemented with computational algorithms that are based on random sampling. In radiative transfer this is achieved by sampling the radiation field in random directions, or by sampling the radiation field from discrete propagated photons. The Accelerated Lambda Iteration is a variant of the normal Lambda Iteration method, in which an initial solution is assumed and then iterative evaluations are made until the system reaches a level of convergence. In the case of radiative transfer, a matrix operator connecting all the points and energy levels is introduced into the calculation of the mean intensity field, i.e. $\bar{J} = \lambda\,[\mathrm{S}]$. However, when using this method (normal Lambda Iteration) the time taken to reach convergence is very large at high optical depths, which can lead to false convergences. The ALI algorithm therefore pre-conditions the equations that are evaluated to speed-up convergence. For radiative transfer codes this is achieved by splitting

the calculation of the mean intensity field into local and non-local parts. The local part is straightforward to calculate, and, crucially, dominates in optically thick regions. Hence, the time taken to reach converged level populations in optically thick regions is significantly reduced.

Line Modelling Engine (LIME) is an example of a radiative transfer code that uses Monte Carlo and an ALI-like iteration method, and it is used to obtain continuum and line images in Chapters 3 and 4.

1.5 This thesis

This thesis features a study on the chemical modelling and observability of a gravitationally unstable disc. Chapter 2 presents a model of a gravitationally unstable, proto-Solar like disc, akin to the discs expected to exist in young, low mass systems. A chemical code is used to explore the evolution of the disc composition and the results indicate that GI-driven spiral waves periodically shock and heat disc material. Consequently, the rate of desorption is greatly enhanced, which leads to both transient and permanent changes in the disc composition. As the spiral density waves transport disc material globally, GI is found to produce a warm, chemically-rich midplane, which is in stark contrast to the studies of more evolved, axisymmetric discs.

Chapter 3 presents an analysis of the accuracy of continuum images produced using the radiative transfer code LIME. It is found that the default weighting algorithm implemented in LIME can be improved for the gravitationally unstable disc model introduced in Chapter 2, which suggests that weighting schemes should be specially tailored. It is also found that the efficiency of the sampling routine can be improved by the omission of points in optically thick regions as the calculations of negligible intensity contributions are avoided. Averaging of multiple LIME runs is also found to improve the resultant continuum images. Synthetic

observations of the continuum images are then presented, which show that spiral structure should be observable with ALMA. Disc masses derived from these observations are found to be unreliable because characterising the spiral structure by one value for the dust temperature and one value for the dust opacity, both of which are poorly constrained in young, embedded systems, is misrepresentative. Moreover, the disc model is found to be optically thick at all frequencies considered (90–850 GHz), and hence the disc masses are inherently underestimated.

In Chapter 4 the improvements developed in Chapter 3 for the continuum radiative transfer are applied to the production of line images. Using an abundance density weighting algorithm and a custom sampling routine that restricts grid points to optically thin regions leads to the decrease in the residual flux between congruent images. This suggests that the sampling algorithm should be specially formulated for a particular model. Noiseless observations are produced so that the sensitivity required for detecting flux originating within spiral features can be determined. This is done for a selection of molecular transitions that are of interest in protoplanetary discs. Spatially resolving the spiral structure is found to be challenging, but potentially possible for the strongest emitting transitions. Spectrally resolving the spiral flux is more straightforward, but attributing this flux to GI is tenuous. PV diagrams are found to perhaps offer the most promising means of confirming GI-driven spiral structure in young discs, although only for near edge-on inclinations. Protostellar masses are also derived from PV diagrams, but it is found that the method commonly used may not be particularly reliable for GI-active discs. Finally, all of the molecular transitions recover flux in absorption. This suggests that absorption could be a signature of gravitational instability in Class 0 sources, even if the spiral structure can not be resolved.

Chapter 5 contains a summary of the thesis along with a discussion of potential future work.

Chapter 2

A simulation of dynamics and chemistry

2.1 Introduction

Understanding the mechanisms governing the formation and evolution of young protoplanetary discs is crucial for explaining how the later periods of disc lifetimes unfold. Processes such as disc dispersal, outflow and planet formation all play important roles. However, because these objects are optically obscured, particularly at early ages, the information that can be obtained with most observational facilities is currently limited. Recently, the Atacama Large Millimeter/submillimeter Array (ALMA) has been providing important observational results, with detections of ringed structure in HL Tauri (ALMA Partnership *et al.*, 2015), centrifugal barrier emission (Sakai *et al.*, 2017) and spiral structure in an embedded Class 0 source (Tobin *et al.*, 2016). However, because observational availability and sensitivity impose strict limits on potential candidates, simulations are important for determining parameters and targets for future observations.

Many authors have investigated the chemical properties and evolution of protoplanetary discs (see Henning & Semenov, 2013, Section 3.4 for an extensive review), but because the inclusion of a complex chemical network in a model

can be computationally intensive, most astrochemical models are decoupled from the disc dynamics. The typical setup consists of a steady-state, axisymmetric thin disc, in which the temperature and density are calculated in the radial and vertical directions independently, usually under the assumption of vertical hydrostatic equilibrium. Most models are based on the assumption that the gas and dust are thermally coupled in order to simplify the thermal balance calculations. However, in recent years simulations have become increasingly sophisticated and more detailed descriptions of the heating and cooling processes have been developed. Some examples include photoelectric heating of the gas by FUV-irradiated dust and polycyclic aromatic hydrocarbons (PAHs), gas-grain collisions and fine-structure line cooling via atomic species.

Dust grains are usually assumed to be of uniform size, or to have a size distribution described by a simple power-law with minimum and maximum cutoff sizes. Grains are known to have grown to approximately $1\,\text{mm}$ sizes by the Class II stage (Ricci *et al.*, 2010), but whether this growth occurs at earlier stages is currently unknown. Recently, there have been studies that suggest grain growth can occur in earlier phases of YSO evolution (e.g Hasegawa *et al.*, 2017; Miotello *et al.*, 2014), but this evidence is tentative and more study is needed.

Generally, the results from simulations match observations of real objects satisfactorily, implying that the descriptions of the physical and chemical processes in these models are consistent with nature. This has therefore led to the picture of a disc composed of a cold midplane surrounded by heated surface layers (see e.g. Akiyama *et al.*, 2013; Bergin *et al.*, 2013; Walsh *et al.*, 2010; Walsh *et al.*, 2012, 2014), as depicted in Figure 2.1. The surface layer is heavily irradiated and only simple light hydrocarbons, their ions, and other radicals such as CCH and CN are able to survive. Photochemical processes and dissociative recombination dominate over relatively short timescales ($\approx 100\,\text{yr}$). The intermediate
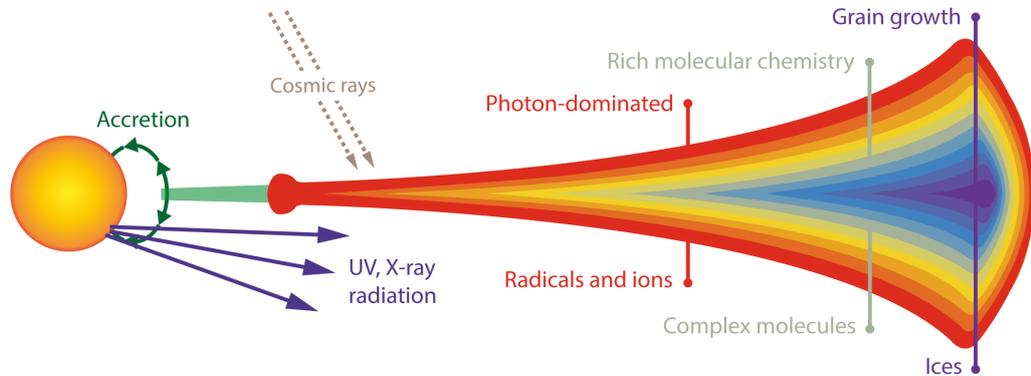
Figure 2.1: Physical and chemical structure of a 1–5 Myr old protoplanetary disk around a low mass star. Adapted from Semenov & Wiebe (2011) and Henning & Semenov (2013).

layer possesses chemistry akin to dense clouds due to the appreciable extinction afforded by the surface material. Here, the chemistry is rich and abundances of most molecules reach maximal values, resulting in the excitation of numerous molecular lines that can be observed. The midplane layer is optically thick to stellar, UV and X-ray radiation, and hence possesses low temperatures. Consequently, freeze-out reduces gas-phase abundances and, as the densities are very high ($\gtrsim 10^{10}\,\mathrm{cm}^{-3}$), grain growth is expected to occur. The midplane layer is usually in a chemical steady-state in most of these simulations, which allows simple desorption/adsorption thermodynamic modelling.

However, this is only true for Class II and late Class I objects. In deeply embedded Class 0 objects, gravitational instabilities are expected to form as the disc mass can be comparable to the protostellar mass. Gravitational instabilities formed in the disc produce spiral density waves that efficiently drive angular momentum transport outwards and mass accretion inwards. As these spiral waves grow, they can produce shocks that heat the disc material locally (e.g. Bae *et al.*, 2014; Boley & Durisen, 2008; Harker & Desch, 2002). In this case one might expect the chemistry to approach that of ejected material experiencing C-type

2. A SIMULATION OF DYNAMICS AND CHEMISTRY

shocks. Namely, within the shocks, important endothermic reactions, such as the conversion of oxygen to water and sulfur to sulfur monoxide and sulfur dioxide, occur at significant rates. Moreover, the high temperatures release adsorbed species back into the gas-phase over a timescale dependent on the shock temperature. However, this increase in gas-phase abundances is only temporary as the efficient cooling of H_2, CO and H_2O reduces the temperature to pre-shock values in a few hundred years (e.g. Kaufman & Neufeld, 1996). Subsequently, the gas-phase material will again freeze-out (e.g. Bergin *et al.*, 1998). This episodic heating can enhance the rates of desorption and chemical reactions with high activation energies, which may significantly affect the chemical composition of discs.

Nearly all of the simulations to date have been of axisymmetric α-disc models, with a quiescent disc or $\alpha = 0.005$–0.03 (see Henning & Semenov (2013, Table 3) and Akimkin *et al.* (2013); Cleeves *et al.* (2015); Drozdovskaya *et al.* (2014, 2016); Molyarova *et al.* (2017); Walsh *et al.* (2014)), in which the mass is transported locally. In a GI-driven disc, however, the mass transport is global and the disc structure becomes non-axisymmetric. This implies, therefore, that the commonly used prescription is inappropriate for such systems and, consequently, that there are few simulations that address the chemistry in the earliest phases of protoplanetary disc evolution - a phase that may be pivotal in establishing the evolution of more dispersed discs. Indeed, simulations of gravitationally unstable Class 0 sources are crucial for furthering our understanding because, if gravitational instabilities are seen in simulations but not in observations of real objects, then the model parameters can be refined until GIs can be satisfactorily excluded as a possibility in young systems, or the simulations can be improved to identify actual observable signatures.

Ilee *et al.* (2011), hereafter I2011, simulated a massive protoplanetary disc

throughout an evolutionary phase during which FU Orionis outbursts may occur (Hartmann & Kenyon, 1996). The system represents a Class 0/early Class I object and the relatively massive $(0.39\,\mathrm{M_\odot})$ disc is appropriate for a protostar that will likely become an F star $(\approx 1.4\,\mathrm{M_\odot})$ at the end of the accretion phase. The authors found that shock heating within the disc induced temperature peaks that desorbed various chemical species from the surface of dust grains and enhanced the rates of reactions that were otherwise not energetically favourable, therefore increasing some gas-phase abundances. They found that, in contrast to simulations of more evolved, less dynamic systems, the midplane is the hottest region and therefore rich in chemistry. All species that they consider are tracers of the spiral shocks, and Douglas *et al.* (2013) showed that these gas-phase tracers of disc dynamics may be detectable with ALMA at a distance of 100 pc. Furthermore, Dipierro *et al.* (2014) have recently shown that ALMA can readily detect spiral structure in continuum emission, within Class 0/I systems located at distances comparable to those of the TW Hydrae, Taurus-Auriga and Ophiucus star-forming regions. Hence, the empirical assessment of whether young protoplanetary discs around intermediate mass stars are indeed gravitationally unstable seems possible.

In this chapter the results from a chemical model of a GI-driven, young, protoplanetary disc are presented. Section 2.2 outlines the physical and chemical model used and how it differs from the more massive I2011 disc. Section 2.3 contains results for time-dependent fractional gas-phase abundances determined for individual fluid elements, along with column density maps of the entire disc, in order to assess the differences in composition between the more massive disc, the lower mass disc at different times, and discs featured in other published works. Finally, Section 2.4 presents conclusions based on the results and a forward look to future research.

2.2 Models

2.2.1 Dynamical simulation

A radiation hydrodynamics simulation of a $0.17\,M_\odot$ protoplanetary disc is run over a period of approximately $2000\,yr$ and used as the input into a chemical model. The disc surrounds a central protostar of $0.8\,M_\odot$, which will likely evolve into a Solar-like star. The majority of the mass in the disc initially lies between $r \approx 6$–$41\,au$ from the central protostar, but spreads partially during its evolution as a consequence of angular momentum transport and accretion, resulting in a disc that spans $r \approx 5$–$54\,au$ at the end of evolution. The system represents a Class 0 or early Class I object that potentially resembles the early Solar System.

The physical simulation is performed using CHYMERA (Boley, 2007), which solves the equations of hydrodynamics on a regularly spaced cylindrical grid. Outflow boundaries are used at the inner, outer, and top grid edges and mirror symmetry is assumed along the midplane of the disc. Self-gravity is calculated directly through cyclic reduction, which is a numerical method for solving large linear systems by repeatedly splitting the problem, with the boundary potential determined by a spherical harmonics expansion. An indirect potential is used for capturing the star-disc interactions (e.g. Michael & Durisen, 2010) and the Boley *et al.* (2007b) equation of state is used for a fixed H_2 ortho-para ratio of 3:1 in a Solar mixture gas. Use is made of the Boley *et al.* (2007a) 3D radiative transfer algorithm, which combines flux-limited diffusion with ray tracing in the vertical direction. The radiative routine calculates a separate radiative time step, and subcycles in the event that the hydrodynamics time step becomes much larger than the radiative step. A maximum iteration of 8 sub cycles is used. If this limit is reached, then one last step is used to synchronize the hydrodynamics and radiative times. To ensure stability, energy is not allowed to change in any

one cell by more than 10 per cent (see Boley & Durisen, 2006); such limiters are typically only necessary in very low-density regions. The heating and cooling mechanisms consist of radiative energy losses, PdV work, viscous dissipation and irradiation by the central protostar with a background temperature profile

$$T_{\mathrm{irr}}^4 = \left(150\,\mathrm{K}(r/\mathrm{au})^{0.5}\right)^4 + (3\,\mathrm{K})^4, \tag{2.1}$$

where r is the radius from the protostar.

The disc is initialized with a flat Toomre parameter profile, $Q \approx 1.2$, and a temperature profile following $T \propto r^{-0.5}$, which gives a surface density profile $\Sigma \propto r^{-1.75}$ for a Keplerian disc. The disc is seeded with a random density perturbation to promote the growth of gravitational instabilities. The initial Q value is low enough to guarantee a very rapid onset of spiral structure, but not so low as to overshoot the instability regime severely. While the I2011 calculations were performed in the context of a massive disc undergoing an outburst of GIs, the simulations here are intended to explore a more protracted phase of instability in a lower mass disc. As such, the new disc is evolved past the outburst phase of unstable discs (Mejía *et al.*, 2005) before the fluid elements are traced. After about 1290 yr of evolution (about 5 orbits at 40 au), 2000 fluid elements are placed randomly in the disc, but weighted by mass to reflect the actual distribution of material. This is twice as many fluid elements as used in I2011. The fluid elements are evolved by interpolating the gas flow from the surrounding cells to a given position and integrated directly. Local disc conditions, such as pressure, density, and temperature are also interpolated to the position of the fluid element, allowing the thermodynamic history of the gas to be traced. Of the 2000 fluid elements evolved in the simulation, nine are lost through a grid boundary and therefore not included in the following analysis.
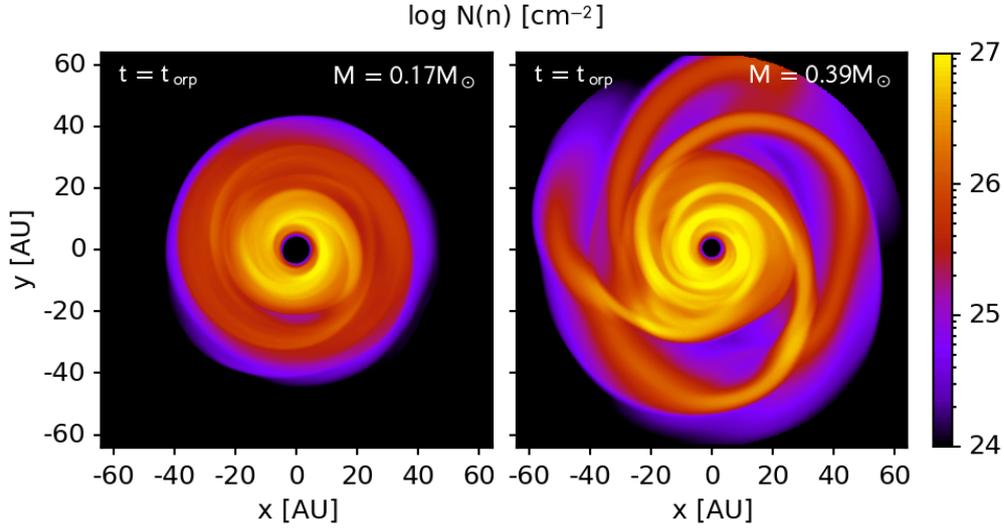
Figure 2.2: Nuclei column density at $t = t_{\mathrm{orp}}$ for the $0.17\,\mathrm{M}_\odot$ (left) and $0.39\,\mathrm{M}_\odot$ (right) discs as viewed from above. The more massive disc (right) undergoes a violent instability, while the lower mass disc (left) shows a more protracted phase of instability.
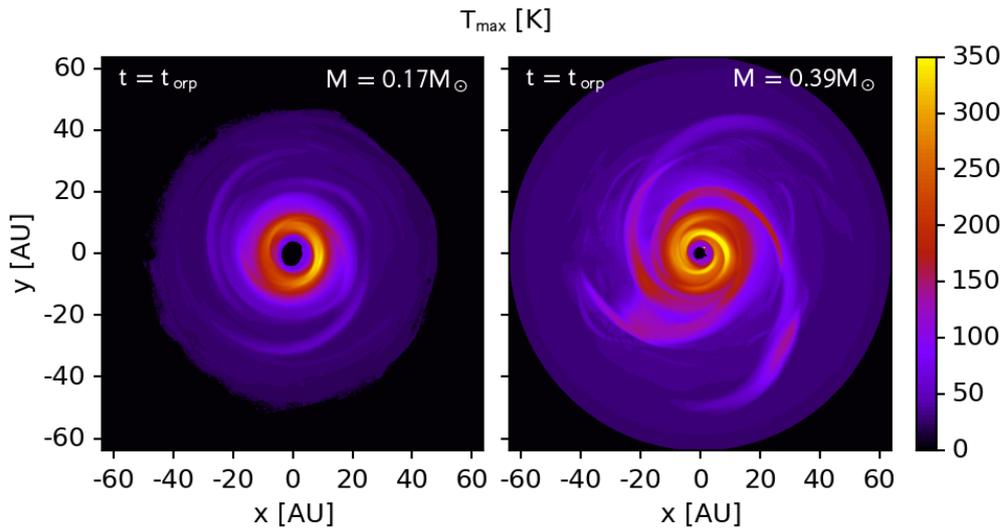
Figure 2.3: As in Figure 2.2, but showing the maximum line-of-sight temperature.

2.2.2 Comparison with a more massive disc

The more massive disc featured in I2011 was simulated for 389 yr, and because of this short duration the hydrodynamical results were repeated for ten chemical cycles, i.e. using the final abundances after 389 yr as initial abundances for the next run, in order to achieve a well mixed chemical distribution. This introduced unrealistic discontinuities into their chemical calculations. Here, the new simulation is run continuously for 2047 yr with fluid element tracers present, which means the behaviour of the lower mass disc can be followed over a longer period without artificial cycling, allowing for a more self-consistent analysis.

The more massive disc was initialised with a $Q \approx 1$ profile for most of the disc and a $T_{\mathrm{irr}} = 140(r/\mathrm{au})^{0.5} + 10\,\mathrm{K}$ radiation field, requiring a surface density profile $\Sigma \propto r^{-1.75}$. Although these parameter initialisations are similar to the lower mass disc setup, these discs are not directly comparable because they trace different potential phases of protoplanetary disc evolution; the higher mass disc is more applicable to a violent burst in activity, whereas the lower mass disc undergoes a more quiescent and protracted period of evolution. However, the discs can be compared after a consistent number of outer rotational periods (ORPs), which defines the time since the inclusion of tracers at a particular radii. At 30 au the ORP is approximately 140 yr in the more massive disc and 165 yr in the less massive disc. By the end of the simulation, $t = 389\,\mathrm{yr}$, the more massive disc has completed 2.7 ORPs at 30 au. The lower mass disc completes the same number of ORPs at the same radius after approximately $t = 440\,\mathrm{yr}$. Hence, the discs are roughly comparable dynamically at these respective times, which is denoted as $t = t_{\mathrm{orp}}$ for both discs and used as the basis for comparison.

Figures 2.2 and 2.3 show the column density of total nuclei and maximum line-of-sight temperature, respectively, within the featured discs at $t = t_{\mathrm{orp}}$, as viewed from above. At this time, the maximum temperature and number density
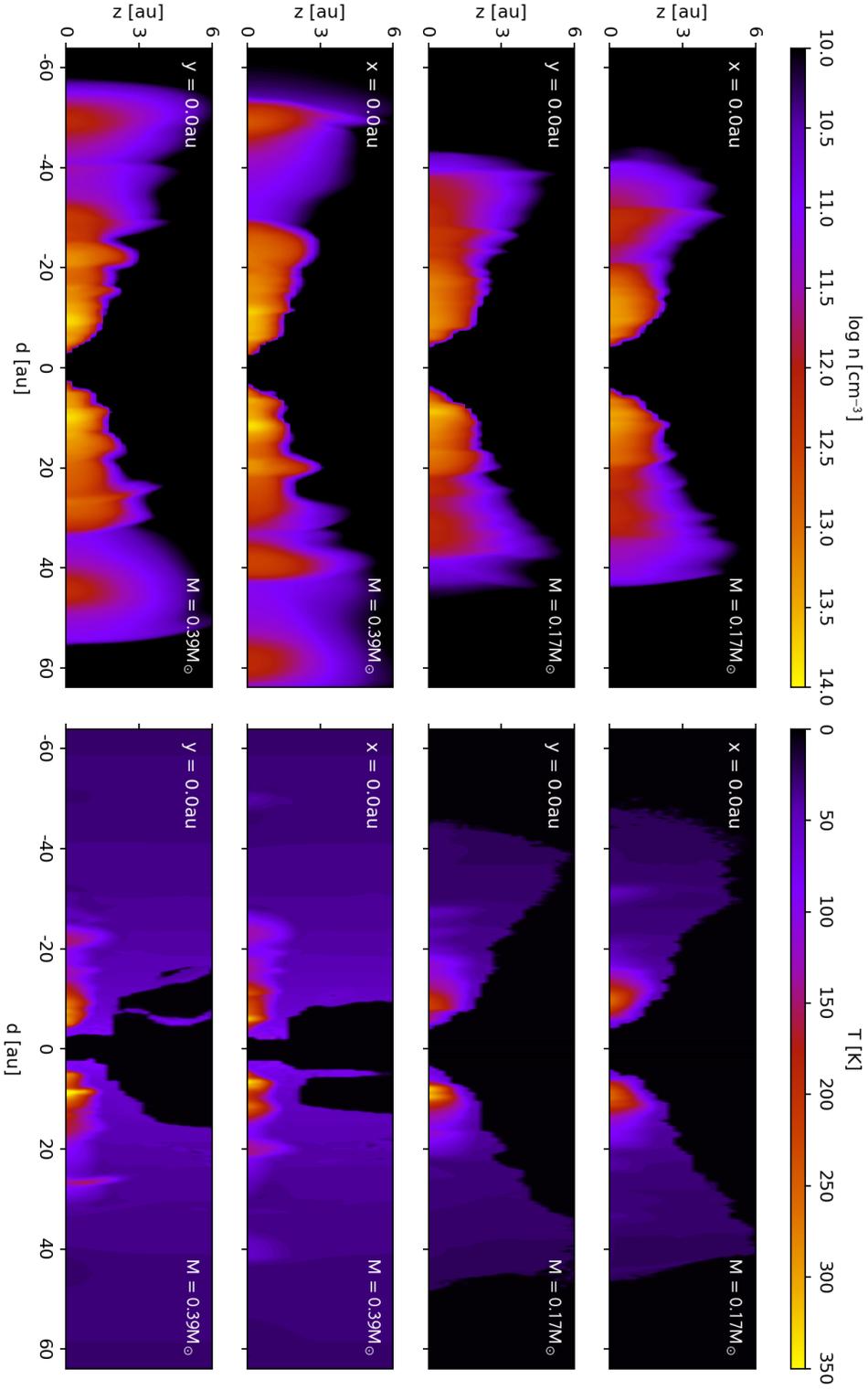
Figure 2.4: Nuclei number densities and temperatures within slices of the disc interior at $t = t_{\rm orp}$ for the $0.17\,{\rm M}_\odot$ (top four panels) and $0.39\,{\rm M}_\odot$ (bottom four panels) discs. Slices are taken at the specified location and d denotes the distance from the disc centre along the appropriate orthogonal axis.

within the more massive disc are $400\,\mathrm{K}$ and $8 \times 10^{13}\,\mathrm{cm}^{-3}$, respectively, which are 1.2 times hotter and 1.4 times denser than within the less massive disc. Both figures show that prominent spiral features have formed in each disc, but the more massive disc is significantly more flocculent due to the stronger gravitational instabilities and evolutionary phase.

Figure 2.4 shows slices of the disc interior along the x = 0 au and y = 0 au axes within the less massive and more massive discs at $t = t_{\mathrm{orp}}$. Overall the interior structures are similar; both discs show a flared morphology, with the hottest and densest material located in a ring-like structure approximately 10 au from the protostar, and possess uneven surfaces resulting from the shocks (Boley & Durisen, 2006). However, the more massive disc is also clearly more extended and features enhanced temperatures at large radii, compared to the lower mass disc. Moreover, there is a higher ambient temperature because of the more massive central protostar and disc. These differences in outer disc temperature structure in particular may have a prominent effect on the chemistry as more energy is available for chemical processes and reactions at larger radii.

The number densities and temperatures of fluid elements tracked throughout the disc simulation are used as the input for the chemical model. Figure 2.5 shows the trajectories of a fluid element in the outer regions of each disc, which is only intended to be illustrative of the types of trajectories that fluid elements can follow. Both fluid elements are initially roughly 30 au from the centre and orbit on trajectories that first radially expand and then contract. I identify the collisional shocks experienced by each fluid element from the concurrent peaks of temperature and number density, seen in Figure 2.6, and pressure (not shown). The shocks cause the fluid elements to be displaced vertically upwards in the discs before falling back towards the midplane. This is an effect seen in gravitationally unstable disc simulations as the strong spiral waves in a vertically stratified disc
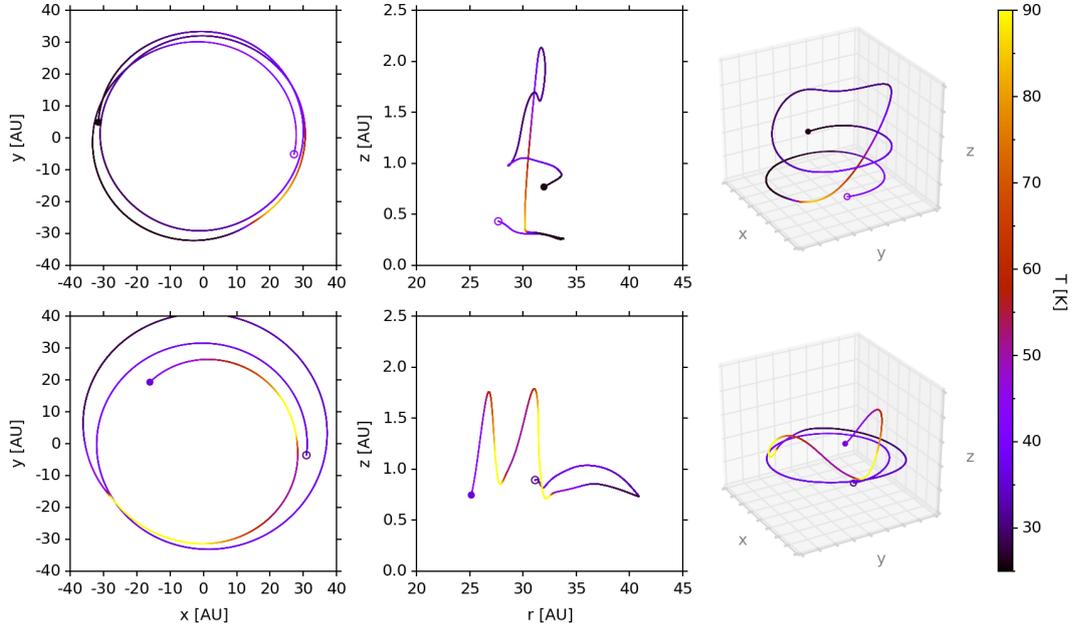
Figure 2.5: Positions and corresponding temperatures of fluid elements extracted from the $0.17\,M_\odot$ (top) and $0.39\,M_\odot$ (bottom) discs that demonstrate similar orbital behaviour within $2.7\,\mathrm{ORPs}$ at $30\,\mathrm{au}$ in each disc. The open circles denote $t = 0$ and the closed circles denote $t = t_{\mathrm{orp}}$.
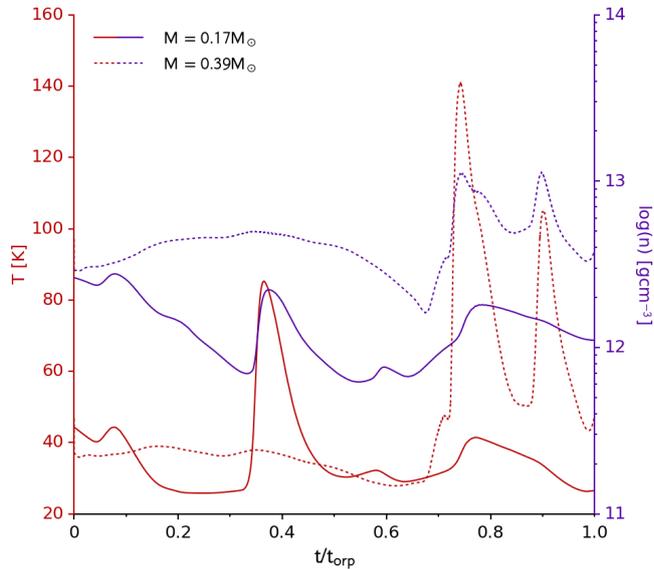
Figure 2.6: Temperature and number density histories of fluid elements extracted from the $0.17\,M_\odot$ and $0.39\,M_\odot$ discs that follow similar trajectories within $2.7\,\mathrm{ORPs}$ at $30\,\mathrm{au}$ in each disc (see Figure 2.5).

drive shocks that act as hydraulic jumps (e.g. Boley & Durisen, 2006). The velocities of the shock waves in the disc are relatively low (a usual Mach number is 2, implying a shock velocity of a few km s^{-1}). Such low Mach numbers are due, in part, to the shallow pitch angles of the spiral arms, which significantly reduce the speed of a fluid element normal to the spiral shock (see Boley & Durisen, 2008, for a detailed discussion).

2.2.3   Evolution of the lower mass disc

Figures 2.7 and 2.8 show the nuclei column density and maximum line-of-sight temperature, respectively, within the $0.17\,\mathrm{M}_\odot$ disc at $t = t_{\rm orp}$ ($t = 440\,\mathrm{yr}$) and at the end of the simulation $t = t_{\rm fin}$ ($t = 2043\,\mathrm{yr}$), as viewed from above. Over the duration of the simulation the average mass flux through the disc is $10^{-6}\,\mathrm{M}_\odot\,\mathrm{yr}^{-1}$. By the end of the simulation the disc is clearly more flocculent as the gravitational instabilities have driven progressively denser spiral waves (see Appendix A).
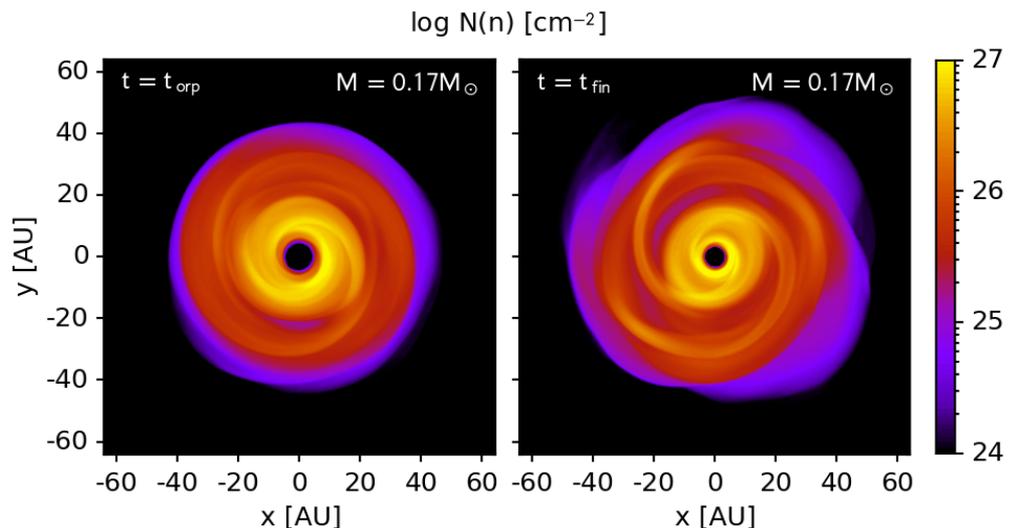
Figure 2.7: Nuclei column density at $t = t_{\rm orp}$ (left) and $t = t_{\rm fin}$ (right) for the $0.17\,\mathrm{M}_\odot$ disc as viewed from above. As the disc evolves dynamically, the spiral structure becomes much more flocculent.
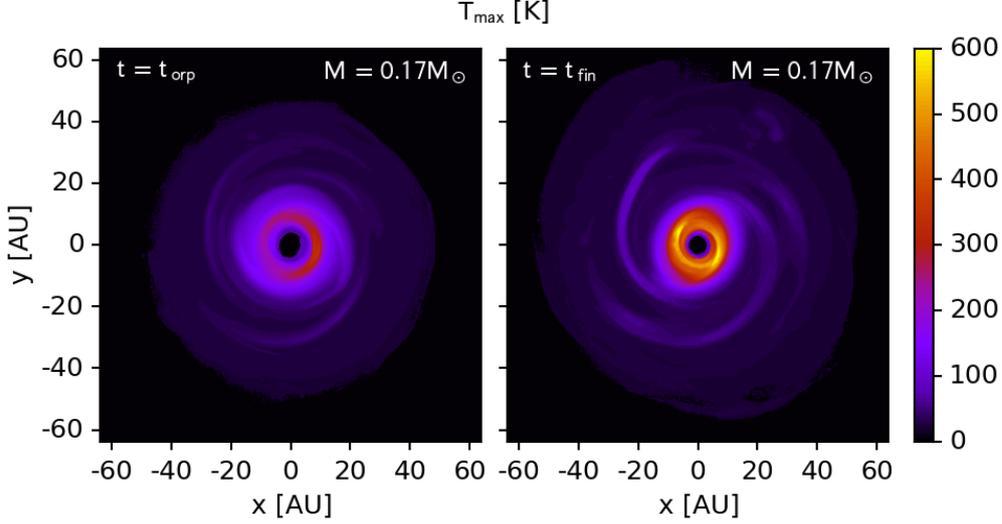
Figure 2.8: As in Figure 2.7, but showing maximum line-of-sight temperature. The maximum temperature reached is approximately 600 K.

Figure 2.9 shows the trajectories of two fluid elements located within the inner and outer regions of the lower mass disc, throughout the entire duration of the simulation. The temperature and number density histories of these fluid elements are shown in Figure 2.10, and the outer disc temperature and number density evolution displayed is for the same fluid element as featured in Figures 2.5 and 2.6. In the outer disc, the temperature profile is determined primarily by the stellar irradiation, with significant variations due to spiral shock heating. As a result, over the duration of the entire simulation, the temperature and number density of the outer disc fluid element appear periodic. This period is approximately 100 yr, which means that the spiral waves propagate faster than the outer disc rotates; the average corotation of the spiral structure appears to be at about 17 au based on the average mass flux profile. The inner disc fluid element, however, exhibits significantly different behaviour. The much faster rotation of this fluid element, roughly 10 yr per orbit, results in much more frequent shock encounters, which produces the markedly faster variations in temperature and number den-

sity. Moreover, there are substantial increases in the average temperature and number density for the inner disc fluid element after about $t = 400\,\mathrm{yr}$. This is due to the gravitational instabilities driving mass transport and shock heating. Furthermore, within $\approx 20\,\mathrm{au}$, the radiative cooling becomes very inefficient because the densest, inner disc regions are more optically thick than the outer disc. In the inner disc fluid element, the approximately decennial variations in temperature and number density reflect passage through spiral structure. The longer term changes, however, spanning over $100\,\mathrm{yr}$ or more, reflect motion through different regions of the inner disc that are in rough pressure equilibrium, i.e. cool and dense regions, or hot and rarefied regions.
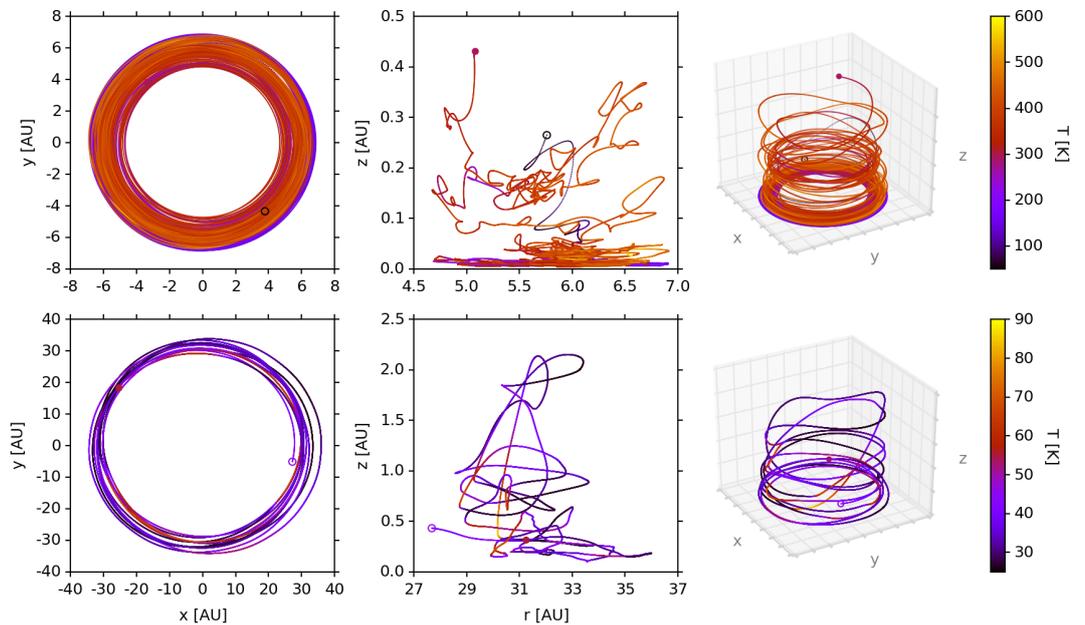
Figure 2.9: Orbital positions and corresponding temperatures of fluid elements extracted from the inner (top) and outer (bottom) regions of the $0.17\,\mathrm{M_\odot}$ disc. The open circles denote $t = 0$ and the closed circles denote $t = t_{\mathrm{fin}}$.
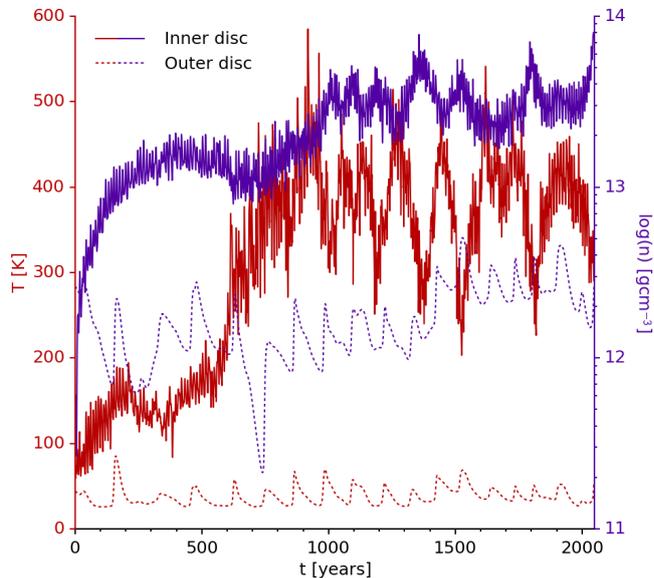
Figure 2.10: Temperature and number density of fluid elements extracted from the outer and inner regions of the $0.17\,\mathrm{M_\odot}$ disc (see Figure 2.9). The rapid variations in temperature and number density are a consequence of collisional shocks, which are much less frequent in the outer disc. The longer term changes seen only in the inner disc are a result of the fluid element passing through cooler and denser, or more rarefied and hotter regions of the inner disc that are in rough pressure equilibrium.

2.2.4 Chemical model

I use the chemical evolution code developed in I2011, which consists of a network of 125 species and 1334 reactions. These reactions are selected from a subset of the UMIST95 network (Millar *et al.*, 1997), in which the rate coefficients have been updated using data from KIDA[1](Wakelam *et al.*, 2012). The reactions include: positive ion-neutral reactions, ionisation by cosmic rays, charge transfer, proton transfer, hydrogen abstraction, radiative and dissociative recombination with electrons, radiative association, neutral exchange, photodissociation and photoionisation, recombination of ions with negative grains, and adsorption and desorption. The code interpolates temperature and number densities extracted

[1]http://kida.obs.u-bordeaux1.fr/

from the fluid elements to a higher resolution chemical timescale using cubic spline fits. The DVODE package (Brown *et al.*, 1989) is then used to integrate the rate equations for each included species, outputting fractional gas-phase abundances, $X_i = n_i/n$, where $n = n_{\text{H}} + n_{\text{He}} + n_{\text{Z}}$ (see I2011, equation 1).

For each species, i, in the chemical code, its rate equation is given by

$$
\begin{aligned}
\frac{dX_i}{dt} = {} & \sum_{jlm} k_j X_l X_m\, n - \sum_{j'm} k_{j'} X_i X_m\, n - 2 \sum_{j''} k_{j''} X_i^2\, n \\
& + \sum_{jlm} k_j X_l X_m X_{\text{H}_2}\, n^2 - \sum_{j'm} k_{j'} X_i X_m X_{\text{H}_2}\, n^2 - 2 \sum_{j''} k_{j''} X_i^2 X_{\text{H}_2}\, n^2 \\
& + \sum_{jl} \Gamma_{\text{cr, j}}\, X_l - \sum_{j'} \Gamma_{\text{cr, j}'}\, X_i + \sum_{jl} \Gamma_j\, X_l - \sum_{j'} \Gamma_{j'}\, X_i + R_{\text{d, i}} - R_{\text{a, i}}
\end{aligned} \tag{2.2}
$$

where k_j is the rate coefficient of the jth reaction and summations are restricted so that only reactions involved in forming or destroying the ith species are included. The rate coefficient for the formation or destruction of the ith species directly due to cosmic rays is represented by $\Gamma_{\text{cr,j}}$ and $\Gamma_{\text{cr,j}'}$ respectively, and is dependent on the cosmic ray ionisation rate, ζ, which is taken to be $10^{-17}\,\text{s}^{-1}$. The rate coefficient for each photon-induced reaction that forms or destroys the ith species is represented by Γ_j and $\Gamma_{j'}$ respectively, which is given by

$$
\Gamma_j = \alpha_j\, e^{-\beta_j\, A_{\text{V}}} + \frac{\zeta P_j}{1 - A}\,, \tag{2.3}
$$

where a_j and P_j are constants, A is the dust grain albedo, taken to be 0.5, and A_V is the extinction coefficient. The left side of Equation 2.3 represents direct photodissociation and photoionisation processes, whereas the right side represents photoemission resulting from collisions of molecular hydrogen with energetic electrons produced as a by-product of cosmic ray ionisation. The rate equation calculations are performed under the assumption that the disc environments of Class 0 or early Class I objects are well shielded from sources of stellar

2. A SIMULATION OF DYNAMICS AND CHEMISTRY

and interstellar radiation. This is likely to be an appropriate assumption because the omission of UV photons at $A_V > 4$ is valid (McKee, 1989). Therefore, only a relatively small amount of obscuring material is needed to limit the illumination of the upper layers of young discs by the protostellar and interstellar UV field, which may be provided by the combination of powerful outflows and envelope infall as the disc develops (see, e.g., Machida & Hosokawa, 2013). Incidentally, a visual extinction $A_V = 100$ mag is adopted, which ensures only cosmic ray induced photoreactions are significant. Note that no attenuation of cosmic rays is assumed in the chemical model. This is perhaps inappropriate as the attenuation length of cosmic rays is ≈ 120 g cm^{-3}(Kataoka & Sato, 2016), which is reached in the spiral arms and inner disc at approximately $z = 1$–2 au; hence the cosmic ray ionisation rate in the spirals and inner disc may be overestimated.

In Equation 2.2, $R_{\mathrm{d},i}$ represents the contribution to the abundance of the ith species due to thermal desorption, which is treated in the same way as Visser *et al.* (2009) and given by

$$R_{\mathrm{d},i} = 1.26 \times 10^{-21} \left(\frac{\sigma}{\mathrm{cm}^{-2}} \right) f_i \, v_{0,i} \, \exp \left(-\frac{E_{\mathrm{b},i}}{k_{\mathrm{B}} T_{\mathrm{d}}} \right), \qquad (2.4)$$

where σ is the surface density of binding sites, which is taken to be 1.5×10^{15} cm^{-2} and $E_{\mathrm{b},i}$ is the binding energy of the ith species to the dust grain surface, taken from the Ohio State University database[1] and Hollenbach *et al.* (2009) and references within. T_{d} is the dust grain temperature, which is assumed to be equal to the gas temperature, and f_i is the fraction of the dust grain surface covered by the ith species, given by

$$f_i = min \left(1, \frac{X_{\mathrm{s},i}}{\eta N_b} \right), \qquad (2.5)$$

where $X_{\mathrm{s},i}$ is the solid fractional abundance of the ith species (i.e. frozen-out

---

[1]http://faculty.virginia.edu/ericherb/research.html

abundance), η is the ratio of dust grain number density to nuclei number density, which is taken to be 3.3×10^{-12} (as is appropriate for a dust grain radius of $a = 0.1\,\mu\text{m}$ and gas-to-dust ratio of 100), and N_b is the typical number of binding sites per grain, taken to be 10^6 (Hasegawa $et~al.$, 1992). The characteristic vibrational frequency of the desorbing species is given by

$$\nu_{0,\,i} = \sqrt{\frac{2\sigma E_{\text{b},\,i}}{\pi^2 m_i}} \tag{2.6}$$

where m_i is the mass of the ith species (Tielens & Allamandola, 1987).

The rate of adsorption, $R_{\text{a},\,i}$ in Equation 2.2 can be calculated by evaluating the product of the species geometrical dust-grain cross-section, sticking probability, thermal velocity and concentration. Algebraically this is given by

$$R_{\text{a},\,\text{i}} = \pi a^2 S_i\,\eta \sqrt{\frac{8k_\text{B}T_\text{g}}{\pi\mu m_\text{H}}} X_i\,n, \tag{2.7}$$

where S_i is the sticking probability, which is assumed to be 1.0, T_g is the gas temperature, k_B is the Boltzmann constant, μ is the molecular mass in atomic mass units and m_H is the mass of a hydrogen atom. It is assumed that species are only physisorbed onto dust grains and that only simple surface chemistry (i.e. charge neutralisation of positive ions and hydrogenation) occurs after adsorption. Hydrogenation is treated as an instantaneous process that also includes desorption of the product into the gas-phase. Note that the atomic hydrogen abundance is not conserved during this reaction. Instead, a separate reservoir of H is assumed to exist on the dust grain surfaces that facilitates the hydrogenation process.

The initial abundances are taken to be representative of observations of cometary ice abundances (see Ehrenfreund & Charnley, 2000, Table 2) and are given in Table 2.1. There is no N_2 present initially, which results as a consequence of the particularly high volatility of N_2; hence N_2 may not persist in cometary bodies

and is therefore absent in observed abundances. However, NH_3, which *is* included initially in this work, is expected to be the dominant reservoir of elemental nitrogen in interstellar cloud conditions, and therefore the absence of N_2 should only result in a small (≈ 20 per cent) difference in the total abundance of elemental nitrogen. However, the N/H abundance ratio in Table 2.1 is 1.0×10^{-6} whereas the values reported in the ISM and the η Oph cloud are 7.5×10^{-5} (Przybilla *et al.*, 2008) and 2.1×10^{-5} (Graedel *et al.*, 1982), respectively. These large discrepancies are therefore likely to be caused by the imperfect persistence of cometary abundances, i.e. although there is some consistency between cometary and interstellar ices, it is not known whether comets undergo significant chemical processing that affects the accurate preservation of the initial elemental compositions within young systems (see Caselli & Ceccarelli, 2012, Chapter 7).

As mentioned previously, the velocities of the shock waves in the disc are relatively low (a few $\mathrm{km\,s^{-1}}$). Hence, these shocks are not expected to cause effects such as the disruption of dust grain cores or grain mantle sputtering, which typically require shock speeds of at least $10\,\mathrm{km\,s^{-1}}$ (e.g. Caselli *et al.*, 1997; Van Loo *et al.*, 2013). Rather, this chapter focuses on how thermal desorption of the ices from the icy mantles of dust grains is affected by shocks.

Modifications

The chemical evolution code used here was first presented in I2011. However, I make some alterations in order to improve its efficiency and success rate. Originally the code used a logarithmic time step in order to capture the fastest initial chemical reactions at a sufficient resolution. This was necessary because the fluid element temperature and density histories in the more massive disc were cycled to compensate for the short timescale of the physical disc evolution. However, this introduced artificial numerical discontinuities into the chemical analysis that

Table 2.1: Initial fractional abundances $X(i) = n_i/n$. Note that a(b) represents a x 10^b.

Species	Abundance
He	1.00(-1)
H_2CO	1.83(-6)
CO_2	3.67(-5)
CO	3.66(-5)
HCN	4.59(-7)
CH_4	1.10(-6)
HNC	7.34(-8)
S	1.62(-5)
NH_3	3.30(-6)
H_2S	2.75(-6)
SO	1.47(-6)
H_2O	1.83(-4)
SO_2	1.84(-7)
OCS	3.30(-6)

caused the chemical integrator to fail for a selection of fluid elements. The less massive disc, on the other hand, is simulated for a considerably longer time, so there is no need to cycle the chemical abundances. Therefore, I change the time step to be additive, with a time step of 1000 s so that fast reactions are followed with sufficient resolution throughout the entire disc evolution. The resulting abundances are recorded every 0.05 yr. Recursion is also incorporated into the chemical code so that a failed integration step is re-attempted in a dichotomy paradox fashion, i.e. continually halving the time step, until the integration succeeds or the step size becomes zero and the run fails. These two adaptations make the code much more robust against rapid changes in temperature and density, which a significant number of inner disc fluid elements possess.

2.3 Chemical results

Understanding how gravitational instabilities affect the chemical evolution of the lower mass disc, and how this differs from what occurs in the more massive disc, is necessary for understanding the potential diversity and observational signatures of such discs. This allows the determination of what tests are the most likely to detect or exclude active instability in any given Class 0 or I source.

Figures 2.11 and 2.12 show the fractional gas-phase abundance for 20 species (CO, CO_2, SO, SO_2, NH_3, H_2O, H_2S, H_2CO, OCS, O_2, HCO, HCO^+, HNO, CS, HCS, HCS^+, HCN, HNC, CN and OCN) as a function of t_{orp} for both discs. The abundances are shown for the same fluid elements featured in Figures 2.5 and 2.6, which as discussed orbit at approximately 30 au. I have included three species, CO_2, CN and H_2CO, in addition to those that are featured in I2011 because these are significant species that have recently been detected in protoplanetary discs (e.g. Bast *et al.*, 2013; Chapillon *et al.*, 2012; Qi *et al.*, 2013).

The gas-phase fractional abundances of the species in the upper right panels (CO, SO, OCS, NH_3, H_2O and H_2S) are only significantly affected by adsorption and desorption processes because their total abundance, comprised of gas-phase, $X(i)$, and grain abundance, $N_g(i)\eta$, is approximately constant during the disc evolution. Here, η is the ratio of the number density of dust grains to the number density of nuclei, and is taken to be $\eta = 3.3 \times 10^{-12}$, while $N_g(i)$ is the average number of molecules of the ith species adsorbed on to a grain. However, gas-phase chemical reactions do still occur for these species. For example, the dominant formation reaction at low temperatures for SO is O combining with HS. But at low temperatures ($\approx$,30 K) SO is almost entirely frozen-out, which means the grain abundance dominates, and given the relatively large initial ice abundance (see Table 2.1), the effect of this chemical reaction is insignificant for the total SO
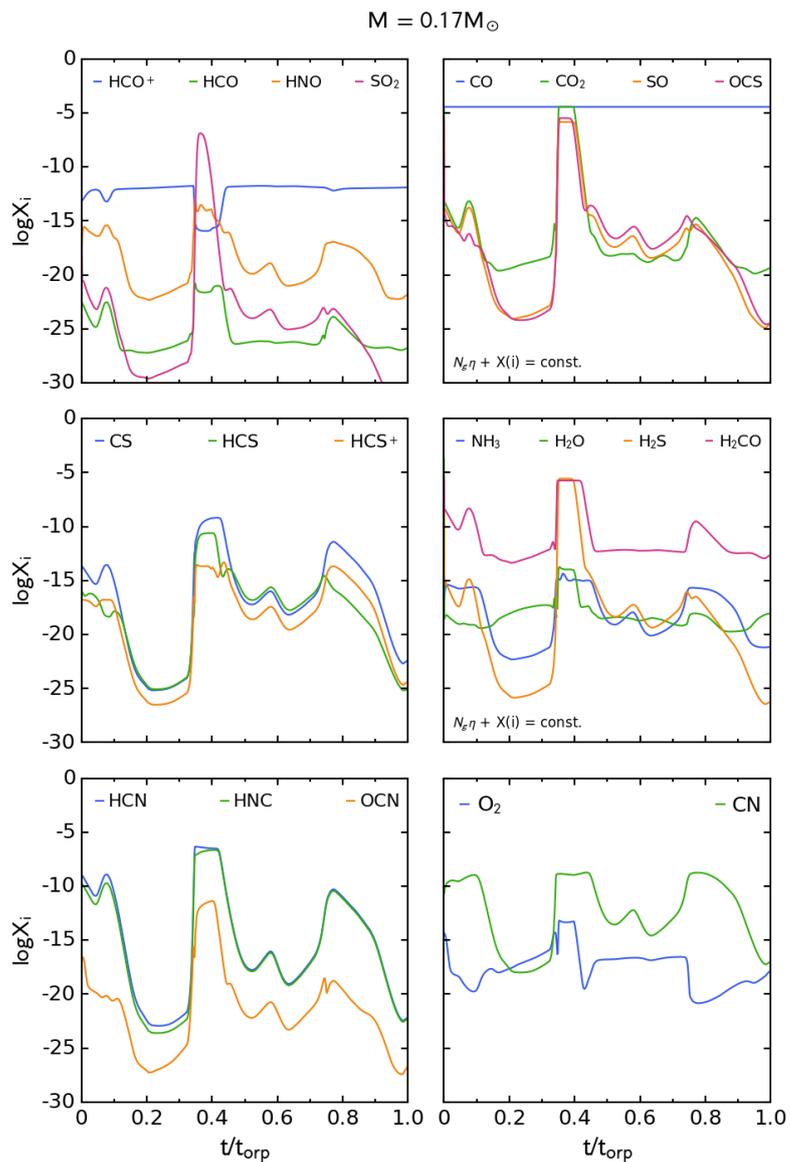
Figure 2.11: Gas-phase fractional abundances of a fluid element extracted from the $0.17\,\mathrm{M}_\odot$ disc (see Figure 2.5). The upper two panels feature species with total abundances, comprised of the number of molecules on grains and in the gas-phase, that are constant over the duration of the simulation.
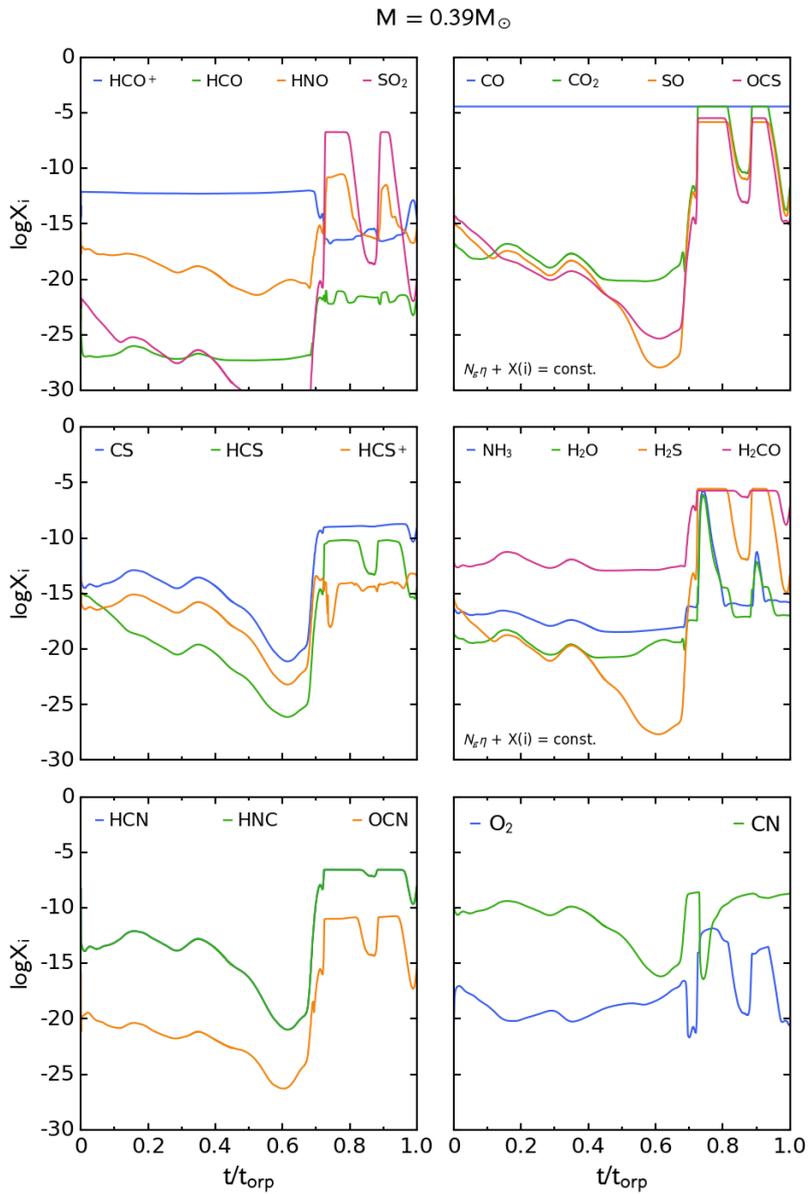
Figure 2.12: Same as Figure 2.11 but for a fluid element extracted from the $0.39\,\mathrm{M_\odot}$ disc model that follows a similar trajectory (see Figure 2.5).

Table 2.2: Desorption temperatures of the neutral molecular species featured in this work, calculated at the typical density ($n = 5 \times 10^{12}\,\mathrm{cm}^{-3}$) and temperature ($T_\mathrm{g} = 80\,\mathrm{K}$) of the spiral arms in the disc model.

Species	Binding Energy [K]	T_des [K]
CO	855	24
CO_2	2575	70
SO	2600	69
SO_2	3405	90
NH_3	5534	145
H_2O	5773	158
H_2CO	2050	54
H_2S	2743	72
HCN	2050	54
HNC	2050	54
OCS	2888	76
HCO	1600	42
HNO	2050	54
CS	1900	50
HCS	2350	62
OCN	2400	63
O_2	1200	32
CN	1600	42

abundance. Likewise, CO is only frozen-out on to grains below $20\,\mathrm{K}$ and hence it is so abundant in the gas-phase that the effect of the shocks appears negligible. Indeed for species with total fractional abundances above approximately 10^{-7}, which are most of the species injected into the disc at initialisation, gas-phase reactions enhanced by shocks are too slow to significantly affect the evolution of the abundances. However, although the total fractional abundance of some species does not depend on shocks, the distribution of gas-phase material is still affected by the spiral arms.

Table 2.3: Maximum fractional gas-phase abundances within the $0.39\,M_\odot$ disc at $t = t_\mathrm{orp}$, $0.17\,M_\odot$ disc at $t = t_\mathrm{orp}$ and $0.17\,M_\odot$ disc at $t = t_\mathrm{fin}$.

Species	Maximum $\log X(i)$		
i	$0.39\,M_\odot$	$0.17\,M_\odot$	$0.17\,M_\odot$
	$t = t_\mathrm{orp}$	$t = t_\mathrm{orp}$	$t = t_\mathrm{fin}$
CO	-4.4	-4.4	-4.4
CO_2	-4.4	-4.4	-4.4
SO	-5.8	-5.8	-5.8
SO_2	-6.5	-6.6	-6.3
NH_3	-5.5	-5.5	-5.5
H_2O	-3.7	-3.7	-3.7
H_2CO	-5.7	-5.7	-5.7
H_2S	-5.6	-5.6	-5.6
HCN	-6.4	-6.3	-6.4
HNC	-6.6	-6.6	-6.6
OCS	-5.5	-5.5	-5.5
HCO^+	-10.8	-11.2	-10.9
HCO	-20.8	-20.8	-20.3
HNO	-7.9	-8.1	-7.5
CS	-8.0	-8.1	-7.5
HCS	-9.6	-10.3	-9.2
HCS^+	-12.6	-12.8	-12.1
OCN	-10.2	-10.3	-9.9
O_2	-10.8	-11.2	-11.2
CN	-7.9	-7.7	-7.2

2.3.1 Comparison with the more massive disc

Most of the gas-phase species reach the same maximum abundances in both fluid elements during their respective shocks. This is because, despite the contribution from gas-phase chemical reactions, desorption dominates the formation rates near the desorption temperatures (given in Table 2.2), which are exceeded for most species during the evolution of both fluid elements. Although the selected fluid elements trace the outer regions of both discs, this result is consistent across the entirety of both discs. Table 2.3 shows the maximum gas-phase fractional abundances for the 20 species selected at $t = t_{\text{orp}}$, and most species show negligible differences between the lower mass and higher mass discs. Therefore, these results suggest that the difference in disc mass and instability strength does not significantly affect the chemistry. Rather, the chemistry is affected merely by the presence of shocks, and perhaps only on short timescales.

In order to understand the features expected to exist in observed gravitationally unstable discs, I generate column density maps for the species discussed at $t = t_{\text{orp}}$. A particular aim of this section is to characterise the effect of system mass on chemical diversity, so these maps are comparable to Figures 7 and 8 featured in I2011.

The column density of the ith species is defined as

$$N_i\,(x, y) = \int n\,(x, y, z)\, X_i\,(x, y, z)\, dz. \tag{2.8}$$

The number density is obtained at each x, y, z position using the full hydrodynamics simulation as this affords the highest resolution possible. I then interpolate the fluid element abundances to the same grid using the `griddata` and `simps` modules in PYTHON. To obtain results for the full vertical extent of such a disc, it is assumed that number density and abundances are even functions

2. A SIMULATION OF DYNAMICS AND CHEMISTRY

of disc height (e.g. mirrored about the z = 0 plane).

Figures 2.13 and 2.14 show the column density maps for the selected species at $t = t_{\mathrm{orp}}$, separated by the significance of gas-phase chemical reactions as discussed. Figure 2.13 features the species only affected by adsorption and desorption processes due to their high initial abundances. I have included HCN, HNC and SO_2 in this figure because the most dominant reactions, electronic recombination of $HCNH^+$ and SO combining with O or OH, are only prevalent at the lowest temperatures and hence only have a marginal effect on the total abundance. Figure 2.14 shows the species having abundances that are significantly affected by chemical reactions during the disc evolution.

The spatial distribution of gas-phase CO is the most extensive of the gas-phase species discussed here. This is expected because the freeze-out temperature is around $20\,\mathrm{K}$, which only occurs in the outermost regions of the disc ($> 45\,\mathrm{au}$). The relatively abrupt edges seen in this map are primarily due to the limited extent of the fluid elements, as the size of the full simulation is significantly larger than the volume defined by the fluid elements followed throughout the disc. I chose to avoid extrapolating the abundances of species beyond the maximum radial extent of the fluid parcels because the reliability of the chemical results in this regime can not be assured.

The spatial distribution of gas-phase H_2O is the most confined of the gas-phase species considered here because water possesses the highest binding energy to grains. Hence, water requires the most energy to be efficiently desorbed into the gas-phase, requiring a temperature greater than $150\,\mathrm{K}$ at the pressures in the disc model. As can be seen in Figure 2.3, this only occurs for the torus of material approximately $10\,\mathrm{au}$ from the centre.

The remaining species with the highest abundances and therefore highest column densities have maps that trace regions of the disc in between these two
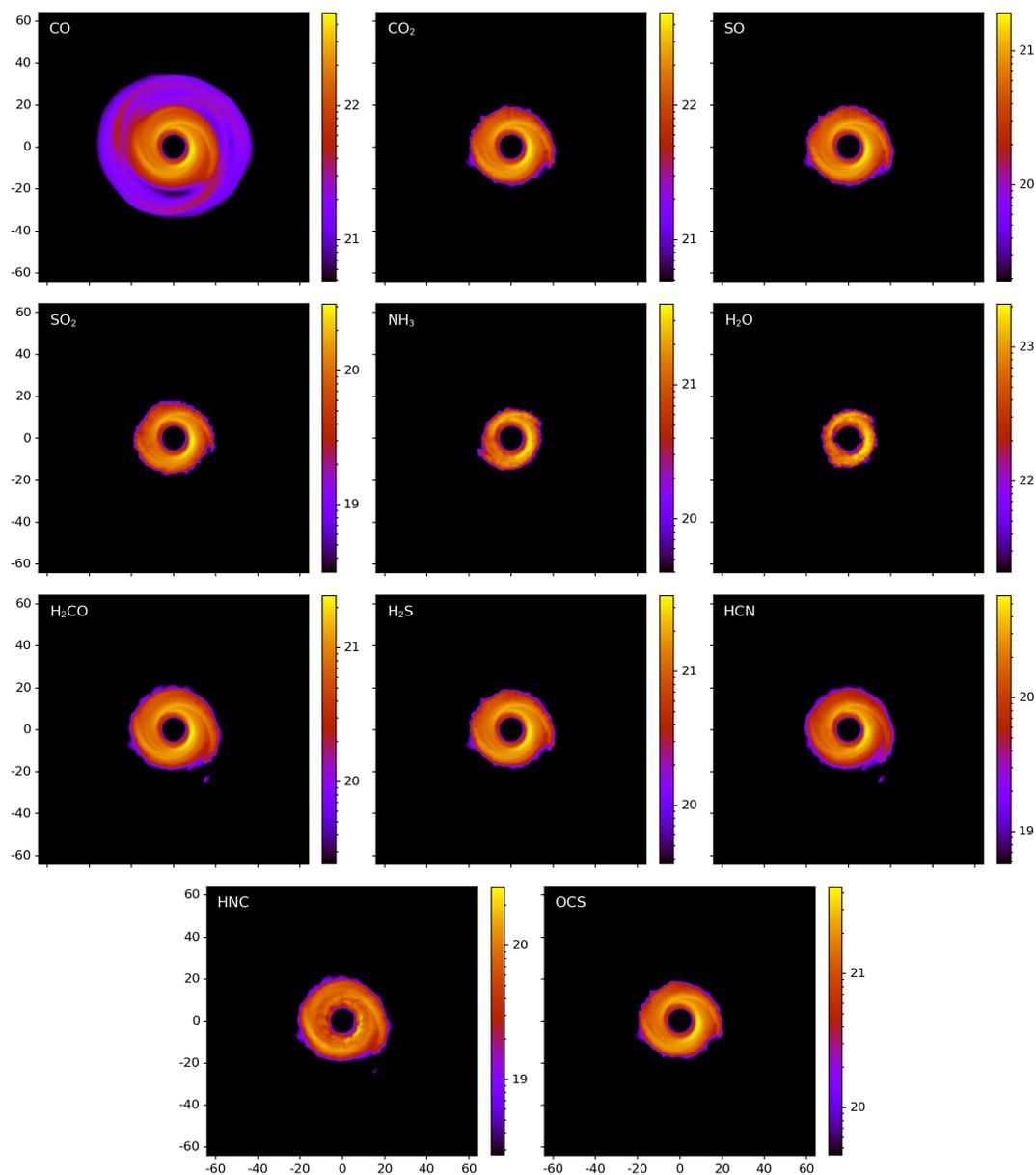
Figure 2.13: Logarithmic gas-phase column densities (in cm^{-2}) of species at $t = t_{\mathrm{orp}}$ with gas-phase fractional abundances determined primarily by thermal adsorption and desorption processes. Distances from the centre are in au.
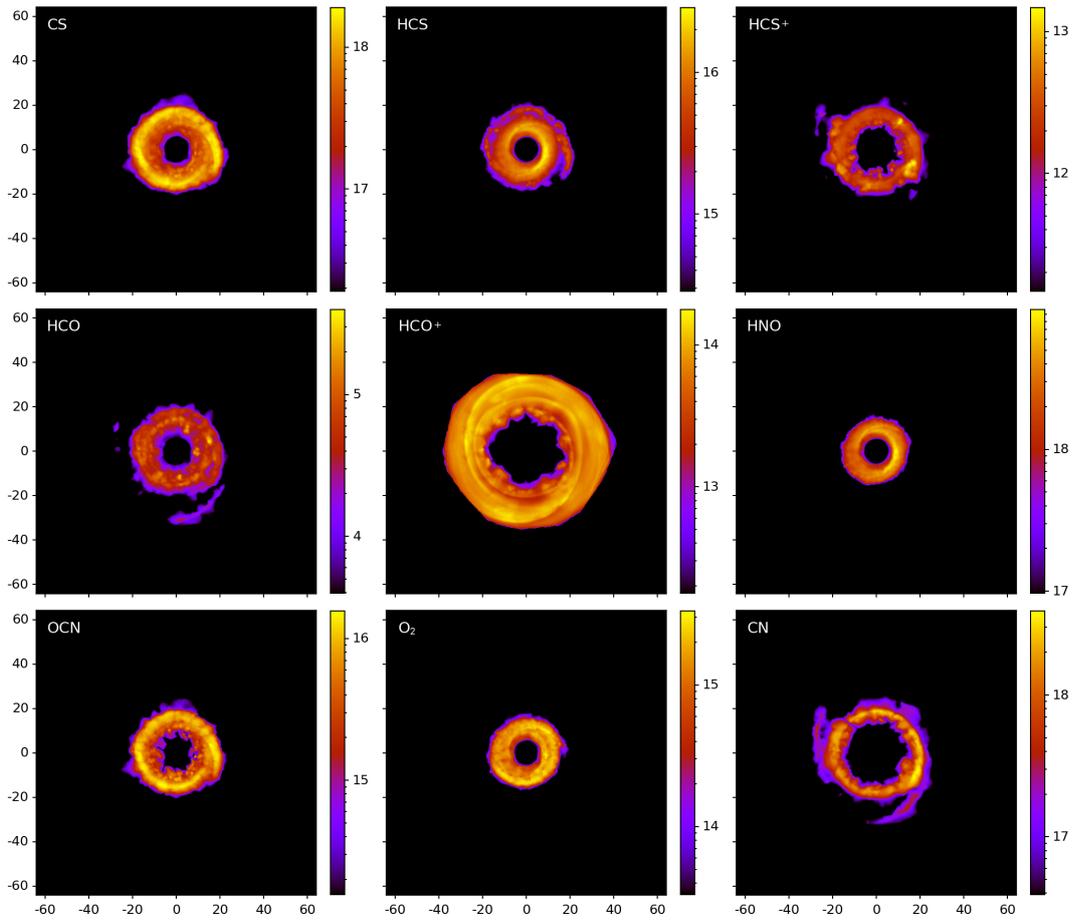
Figure 2.14: Logarithmic gas-phase column densities (in cm^{-2}) of species at t = t_{orp} with gas-phase fractional abundances significantly affected by chemical reactions. Distances from the centre are in au.

extremes, dependent on their desorption temperatures. As the highest abundances for most of these species exist in the hottest regions nearest the protostar, the edges of the column density maps effectively define the midplane snow lines in the x-y plane. Hence, simulating the molecular emission from the disc chemistry and comparing to observations could provide an indicator of the reliability for the disc model used.

The column density maps in Figure 2.14, for the species that are significantly affected by gas-phase reactions, show some different features compared with the maps shown in Figure 2.13. Firstly, all of the maximum column densities are much lower. Secondly, CS and OCN appear to have similar extents and structures as species such as CO_2 and SO. However, their maximum column densities occur in a torus at approximately $20\,\mathrm{au}$ from the centre. Furthermore, the HCO^+ map spans the entire fluid element distribution but possesses a large inner hole. This is due to HCO^+ being primarily formed through a reaction with CO, but destroyed at moderate to high temperatures ($\gtrsim 80\,\mathrm{K}$) through proton transfer with H_2O and reactions with HCN and HNC, all of which are most abundant in the inner disc region. HCS^+ is also removed by proton transfer with H_2O but is dependent on the distribution of CS rather than CO, and hence is not as extensive. Aside from HCO^+, CN is one of the only species to show clear evidence of spiral structure. CN is initially formed in the gas via cosmic-ray induced photodissociation of HCN and HNC (see, e.g., Gredel *et al.*, 1989). The desorption temperature of CN is around $42\,\mathrm{K}$, which is reached in the spiral features due to the shock heating. At higher temperatures the reaction $CN + NH_3 \rightarrow HCN + NH_2$ destroys the molecule, thereby producing a very large inner hole. As CN maps areas of moderate temperatures, it could be an ideal tracer for transient heating events in protoplanetary discs, potentially driven by gravitational instabilities.

Although the less massive and more massive discs represent different strengths

of GI activity, comparisons can be drawn by using a comparable dynamical age in both systems, defined as $t = t_{\mathrm{orp}}$ (2.7 ORPs at 30 au). Figures 7 and 8 in I2011 show column density maps for the same species that I have included in this chapter, except for CN and CO_2. All of the maps included in I2011 show much more defined spiral structure, but this is due to the more massive system driving stronger density waves than occur in the less massive disc. Despite this, there are very few notable differences between the sets of column density maps; the proportional extent of species in relation to the total disc size is comparable and the maximum column densities are largely coincident. For example, the CO column density maps show much less spiral structure in the lower mass disc at $t = t_{\mathrm{orp}}$, but this is purely a consequence of the differences in mass and instability strength between the discs; the maximum CO abundance is identical in both discs due to the consistent initial conditions and low freeze-out temperature (see Table 2.3). There are, however, some distinct differences in the column density maps of HCO^+.

There is a 2.5 times lower peak HCO^+ abundance in the lower mass disc, which also manifests itself in the column density maps. This is a consequence of the stronger spiral density waves and larger radius of the more massive disc. HCO^+ is formed through a reaction involving CO, which proceeds at the fastest rate in low to moderate temperatures (below approximately 150 K). The destructive reactions $HCO^+ + HNC \rightarrow HCNH^+ + CO$, and more notably, $HCO^+ + HCN \rightarrow HCNH^+ + CO$ become significant at temperatures around 40-60 K. In the outer regions of the lower mass disc these reactions are prevalent due to the weak shock strength. However, the shocks are stronger in the higher mass disc, and hence, in the outer regions, these destructive reactions are much less significant. This results in a higher peak HCO^+ abundance.

Moreover, the different masses of the discs appear to affect the size of the
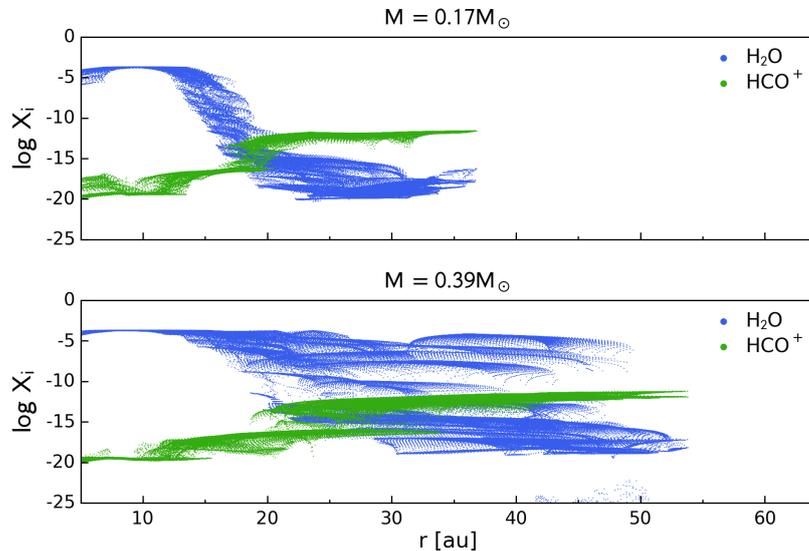
Figure 2.15: Radial extent of H_2O and HCO^+ fractional gas-phase abundances in the midplane of the $0.17\,M_\odot$ (top) and $0.39\,M_\odot$ (bottom) discs at $t = t_{orp}$. There is a wide range in abundance values at each radii because of the shock heating and non-axisymmetric nature of the discs.

HCO^+ inner hole. At the higher temperatures occurring in the inner disc, H_2O destroys HCO^+ at a dominant rate, producing an inner hole depleted of the cation. After 2.7 ORPs, the maximum temperature in the more massive disc is 15 per cent hotter than in the lower mass disc and the extent of the high-temperature region in the inner disc is larger. Therefore, in the lower mass disc, HCO^+ is suppressed significantly at a radii approximately 1.4 times smaller than in the massive disc, which is shown in Figure 2.15. This result suggests that HCO^+ could potentially be used to characterise the disc mass and the strength of gravitational instability in young systems.

The most striking difference, in terms of tracing spiral structure, between these column density maps and those featured in I2011 occurs for HCS. HCS only traces the innermost disc regions in the lower mass disc, whereas, in the more massive disc, HCS also maps the strongest spiral features. More importantly, however, the

HCS abundance in these strongly shocked, outer disc regions is equivalent to the peak abundance in the innermost disc; a significant number of other species have distinctly lower abundances in the outer spiral structure. This is because HCS is desorbed above $62\,\text{K}$ (see Table 2.2), but once in the gas-phase, is not destroyed at significant rates. Hence, gas-phase HCS is preserved in shocked regions. As a result, HCS could be a useful tracer of spiral shocks in particularly massive systems. This is an encouraging avenue of future research as the first detection of HCS in interstellar space was very recently reported (Agúndez *et al.*, 2018).

2.3.2   Chemical evolution of the lower mass disc

The development of a gravitationally unstable system, which is potentially analogous to the early Solar System, can be investigated by simulating the $0.17\,\text{M}_\odot$ protoplanetary disc for multiple dynamical timescales. In addition to the changes in physical properties, such as enhanced maximum density and temperatures as discussed, it is interesting to observe the effects on the chemical evolution of the disc, and in particular characterise whether these are short-term results or can leave a lasting imprint on further chemical evolution.

Figures 2.16 and 2.17 show the evolution of the fractional gas-phase abundances of the same 20 species used in Section 2.3.1 for fluid elements in the outer and inner regions of the lower mass disc. The fluid elements are the same as featured in Figures 2.9 and 2.10 and orbit at approximately $30\,\text{au}$ and $6\,\text{au}$, respectively. The effects of the shocks on the outer disc fluid element are clearly seen throughout the entire duration of the abundance histories, except for CO due to its very low freeze-out temperature. The shock heating raises the temperature of the fluid element, affording more energy for species to desorb or overcome activation barriers. The exception to this trend is HCO^+, which as discussed is destroyed by high abundances of H_2O, HCN and HNC.
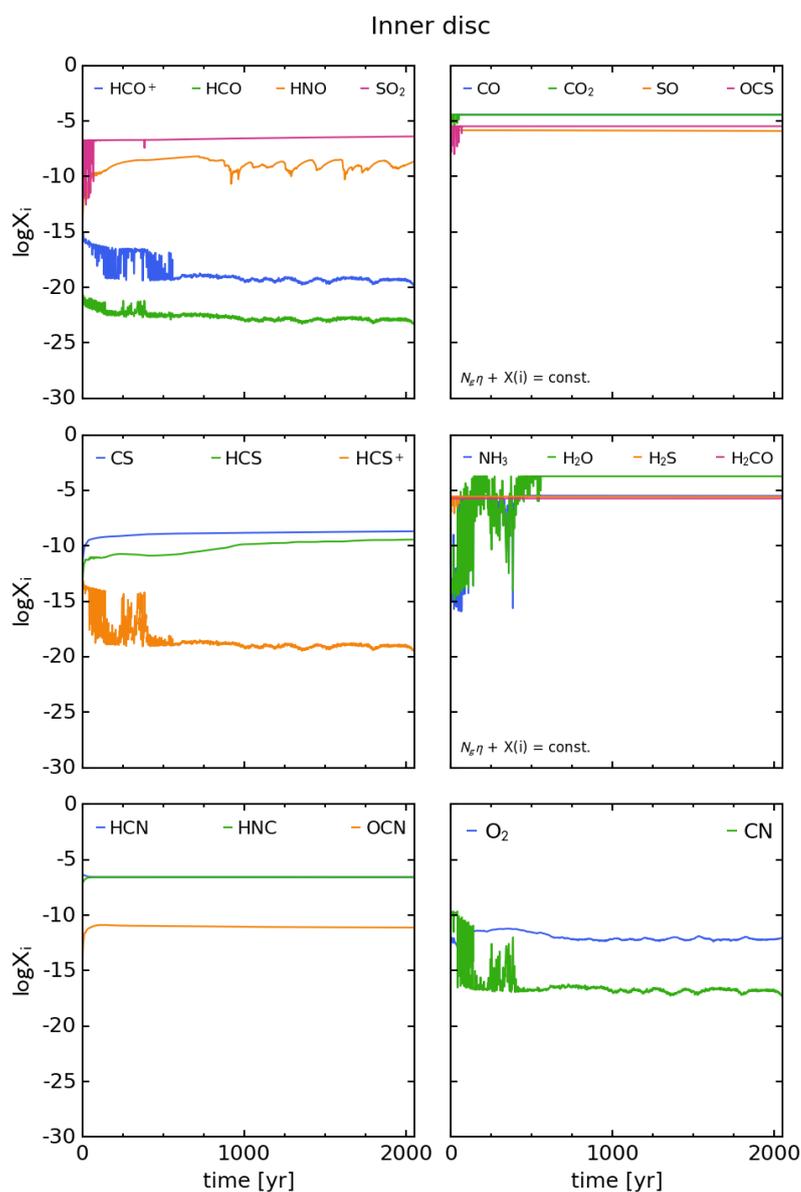
Figure 2.16: Gas-phase fractional abundances of a fluid element extracted from the inner region of the $0.17\,\mathrm{M}_\odot$ disc (see Figure 2.9). The upper two panels feature species whose total abundance, comprised of the number of molecules on grains and in the gas-phase, is constant over the duration of the simulation.
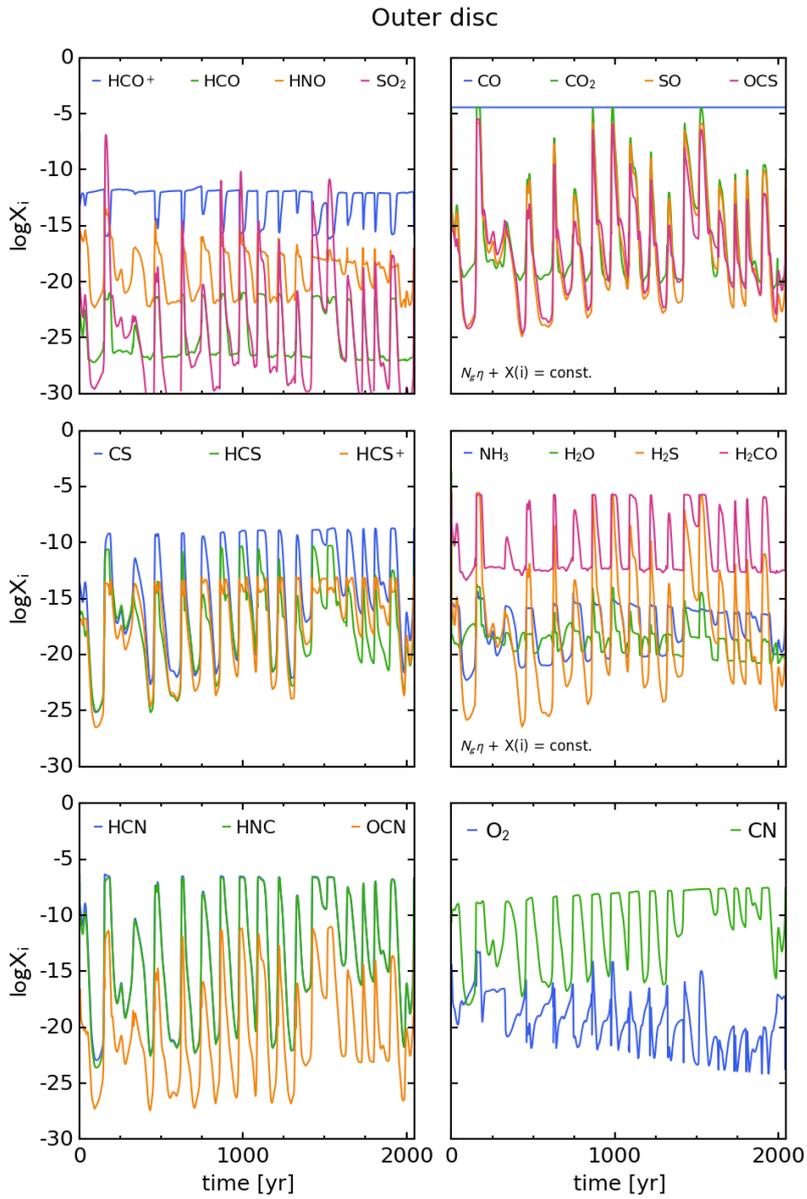
Figure 2.17: Same as Figure 2.16 but for a fluid element extracted from the outer region of the $0.17\,\mathrm{M_\odot}$ disc (see Figure 2.9).

The abundance histories of the inner disc fluid element appear significantly different but are entirely consistent with the outer disc abundances. Every species effectively reaches its maximum abundance once the temperature exceeds the energy required for desorption. This occurs at different temperatures, and hence at different times, for each species. For example, HCN and HNC are efficiently desorbed above $55\,K$, which is instantly reached upon initialisation for the inner disc fluid element. Hence, the fractional gas-phase abundances of HCN and HNC instantaneously reach maximal values and persist until the end of the simulation. H_2O, on the other hand, is desorbed above $160\,K$, which is only consistently exceeded after around $600\,yr$. Before this time, the shocks can be seen to affect the abundance as already discussed, and afterwards effectively all the water is in the gas-phase. The behaviour of CN is more complex, but has already been explained. CN is efficiently desorbed above $45\,K$ and hence reaches maximum gas-phase abundance nearly instantly. However, at high temperatures CN is formed through cosmic-ray induced photodissociation and destroyed by NH_3. Hence, once virtually all of the CN is in the gas-phase, chemical reactions occur at significant enough rates to affect the abundance.

There are more appreciable differences in species for which I have not displayed fractional abundances, but I have excluded these as they have not been observed in protoplanetary discs and/or have insignificantly low abundances. For example, OH has been detected in protoplanetary discs (e.g. Fedele *et al.*, 2012, 2013; Meeus *et al.*, 2012) but a peak OH abundance of only 10^{-14} is recovered in the disc model featured in this chapter, primarily because the disc model I use is assumed to be well shielded from UV photons. This corresponds to a peak column density of 10^{12} cm^{-2} that is likely undetectable. Furthermore, although reactions of atomic hydrogen can play a destructive role at temperatures greater than $300\,K$, the fractional abundance of atomic hydrogen in the gas phase is approximately

constant throughout the disc evolution at $\approx 10^{-11}$, which corresponds to a number density of approximately $1\,\mathrm{cm}^{-3}$. As such, this relatively small reservoir of H is quickly used up and is not available for further reactions. Other reactions involving O and C atoms play more dominant roles in the chemical evolution.

In order to further assess the implications of GIs on the chemical evolution of young, self-gravitating protoplanetary discs, I produce column density maps at $t = t_{\mathrm{fin}}$ for comparison with Figures 2.13 and 2.14. I also produce column density maps in the x-z plane which are shown in Figures 2.20 and 2.21. I use Equation 2.8 and the same procedure and presentation as discussed in Section 2.3.1. Every species shown in Figures 2.18, 2.19, 2.20 and 2.21 has a larger maximum column density compared to $t = t_{\mathrm{orp}}$, which can be attributed to a combination of enhanced maximum nuclei density and maximum temperature. This suggests, therefore, that despite the fact that some species are destroyed in the inner disc, higher column densities of all species is expected in a hotter and denser disc.

Investigating the structure of the column density maps at $t = t_{\mathrm{fin}}$ shows that CO is again the most extensively distributed species because of its highly volatile nature. However, due to the more flocculent structure evident in the nuclei column density map at the end of the simulation (see Figure 2.7), the spiral structure is much more prominent. This strengthening of spiral features is also observed in species with relatively low desorption temperatures, such as CO_2, H_2CO and CS, but species with the highest binding energy to grains, such as H_2O and NH_3 still only trace the innermost regions of the disc. CS in particular appears to be a useful molecule in tracing the spiral features expected in young, self-gravitating discs, but only after the spiral waves have fully developed. CN, on the other hand, could prove to be excellent in characterising instabilities in embedded discs as it traces non-axisymmetric features throughout the entire disc evolution with
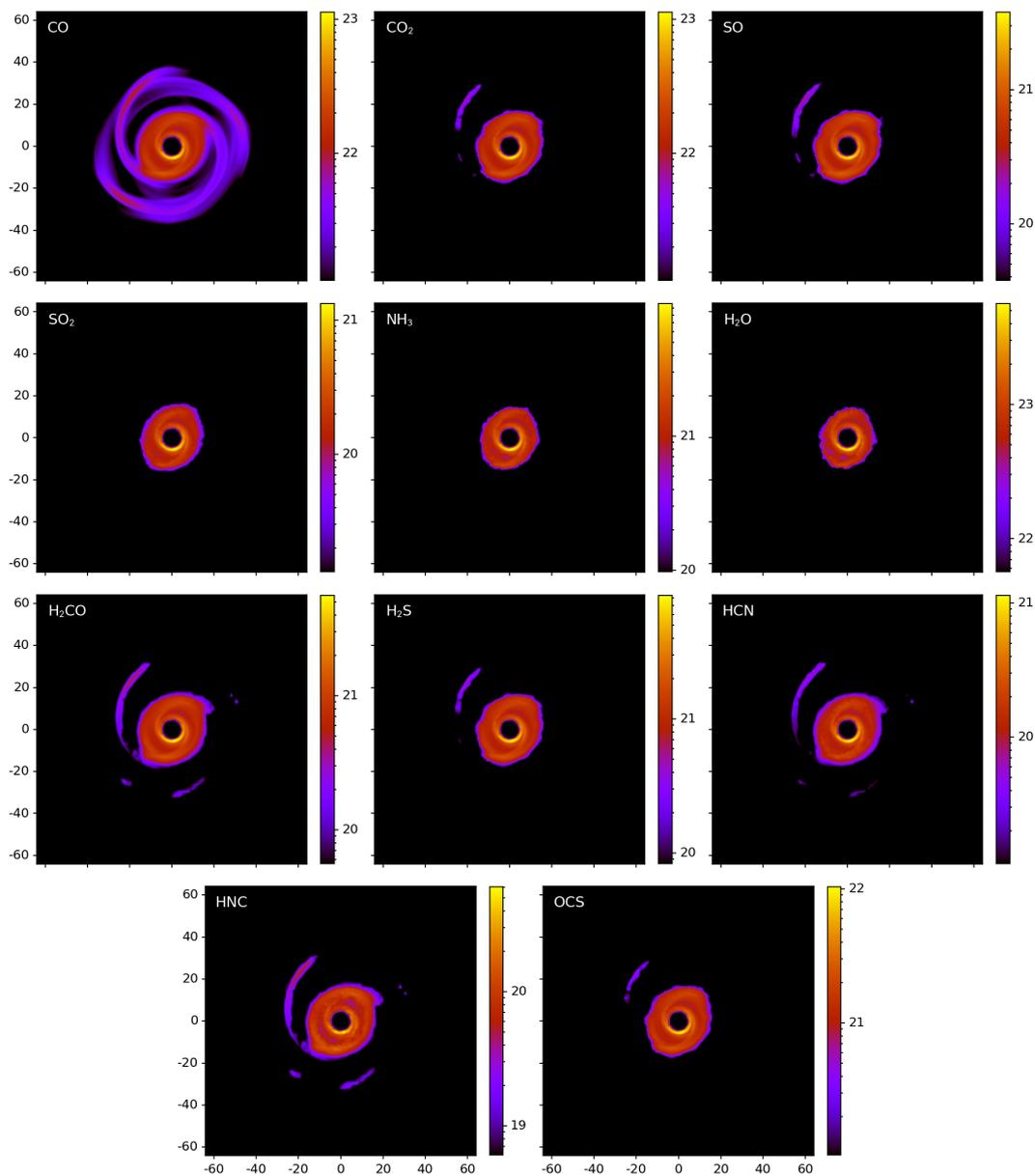
Figure 2.18: Logarithmic gas-phase x-y plane column densities (in cm^{-2}) of species at $t = t_{\rm fin}$ with gas-phase fractional abundances determined primarily by thermal adsorption and desorption processes. Distances from the centre are in au.
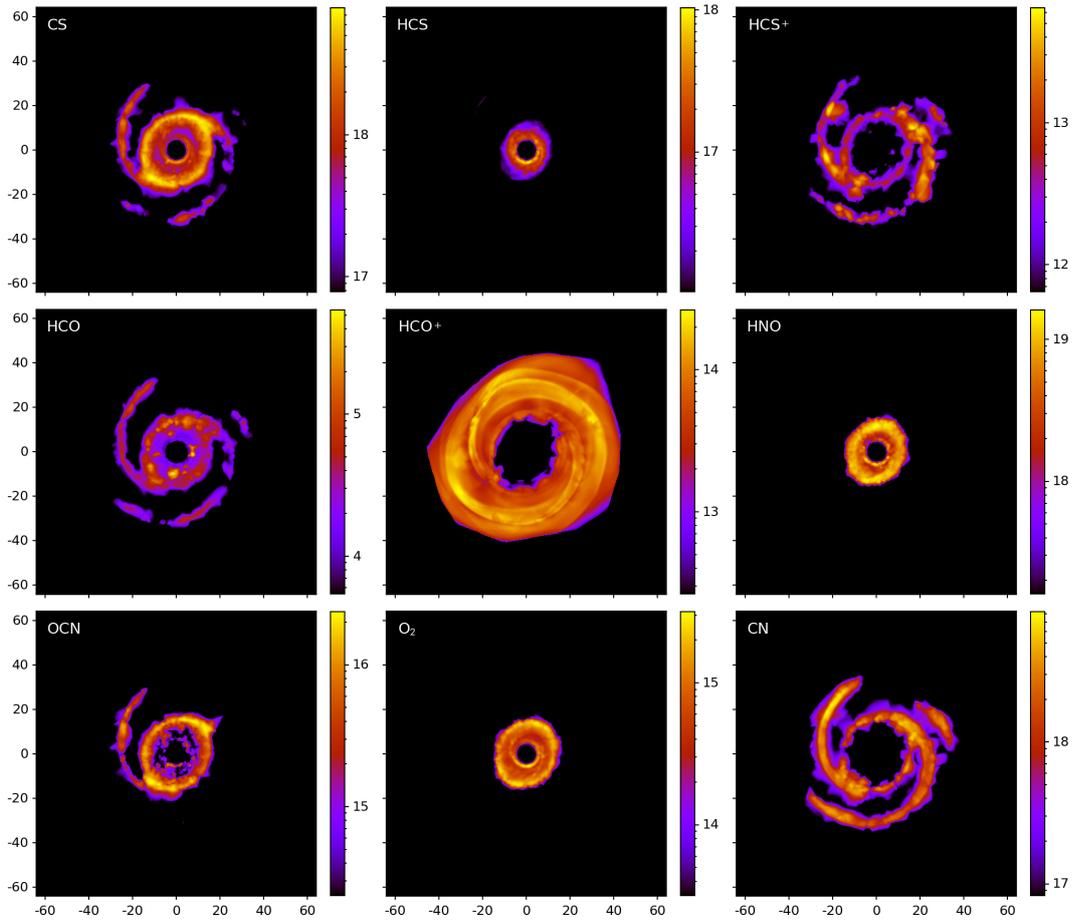
Figure 2.19: Logarithmic gas-phase x-y plane column densities (in cm^{-2}) of species at $t = t_{\mathrm{fin}}$ with gas-phase fractional abundances significantly affected by chemical reactions. Distances from the centre are in au.
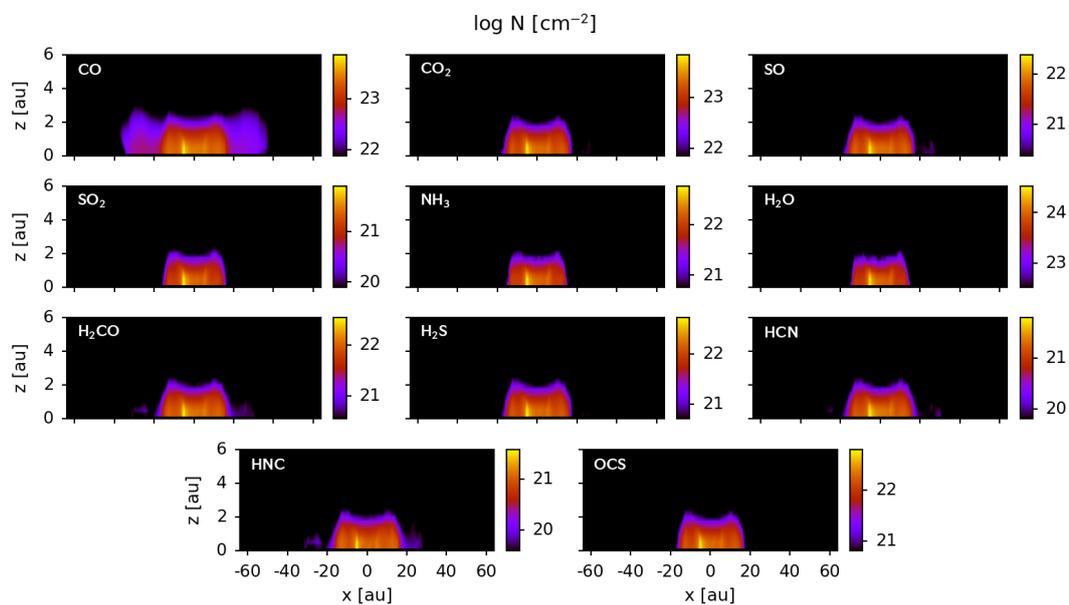
Figure 2.20: Logarithmic gas-phase x-z plane column densities (in cm^{-2}) of species at $t = t_{\mathrm{fin}}$ with gas-phase fractional abundances determined primarily by thermal adsorption and desorption processes.
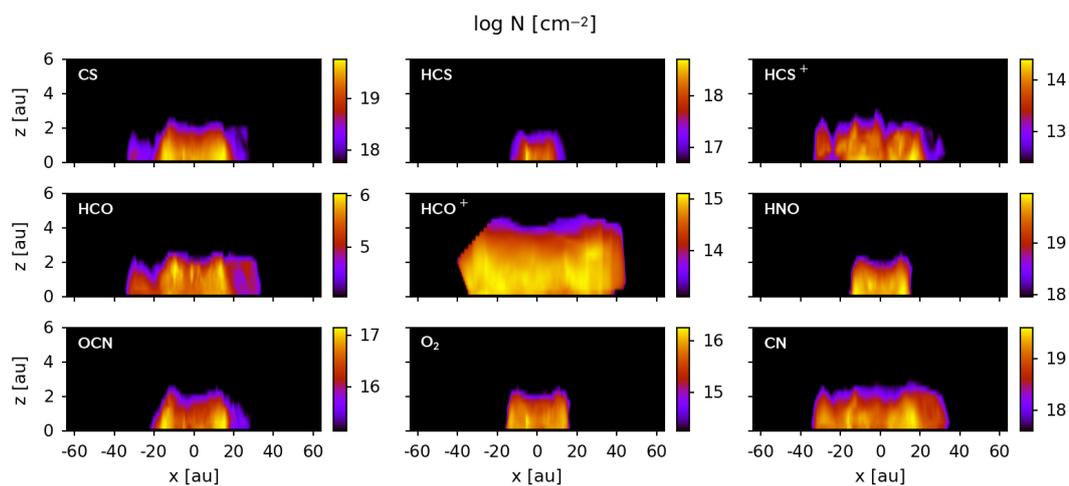
Figure 2.21: Logarithmic gas-phase x-z plane column densities (in cm^{-2}) of species at $t = t_{\mathrm{fin}}$ with gas-phase fractional abundances significantly affected by chemical reactions.

a relatively high column density, and, more importantly for current observational constraints, in the outer regions of the disc.

Persistent effects of shock heating

The shock heating in the disc clearly has an instantaneous effect on the chemistry, but it is worthwhile to investigate whether these effects persist. In the inner disc, once the desorption temperature is exceeded for a particular species, the abundance appears unaffected by further shocks. However, Table 2.3 shows that some species have enhanced maximum abundances at the end of the simulation despite the high temperatures and densities of the inner disc at $t = t_{\mathrm{orp}}$. This suggests that the enhanced densities and temperatures of the inner disc regions driven by GI in a young, massive disc can lead to persistent changes in the chemical composition, with the largest difference pertaining to an order of magnitude increase in the maximum abundance of HCS. However, the inner regions of discs (i.e. within roughly 20 au), particularly in young, embedded systems, are very challenging to observe.

In the more observationally accessible outer disc, the shocks have a continual effect on the chemical abundances due to the low ambient temperature. Although most species appear to reach the same abundances post-shock as pre-shock, I find evidence to suggest that consistent shock heating changes the chemical composition, at least over the short timescale of the disc simulation I have used. To do this, I take a fluid element in the outer disc and fit a low and high-order polynomial to binned minima of the temperature and number density, as Figure 2.22 demonstrates. I then use this polynomial to investigate the chemical evolution of an artificial fluid element more appropriate for a trajectory within a disc absent of shocks in the outer regions.

The abundances of most species are not affected significantly when shocks are

Table 2.4: Fractional gas-phase abundances at $t = 2000\,\mathrm{yr}$ for a fluid element in the outer disc with shocks (WS), and for the same fluid element without shocks via fitting a low-order (WOSLO) and high-order (WOSHO) polynomial to the temperature and number density minima. Note that results for $t = 2000\,\mathrm{yr}$ are presented because at the end of the simulation the fluid element is encountering a shock.

| Species | $\log X(i)$ | | |
i	WS	WOSLO	WOSHO
CO	-4.4	-4.4	-4.4
CO_2	-19.1	-17.3	-17.4
SO	-21.7	-19.7	-19.7
SO_2	-27.3	-24.5	-24.4
NH_3	-20.3	-24.8	-24.8
H_2O	-17.5	-16.2	-16.2
H_2CO	-12.9	-11.9	-11.9
H_2S	-23.1	-21.3	-21.4
HCN	-23.8	-24.1	-24.1
HNC	-23.7	-24.8	-24.9
OCS	-21.3	-20.1	-20.1
HCO^+	-11.8	-11.5	-11.5
HCO	-26.5	-25.0	-25.1
HNO	-21.2	-24.3	-24.2
CS	-22.5	-20.9	-21.0
HCS	-22.1	-20.8	-20.9
HCS^+	-23.6	-22.2	-22.3
OCN	-27.8	-28.3	-28.3
O_2	-18.0	-15.2	-15.2
CN	-18.0	-21.3	-21.3
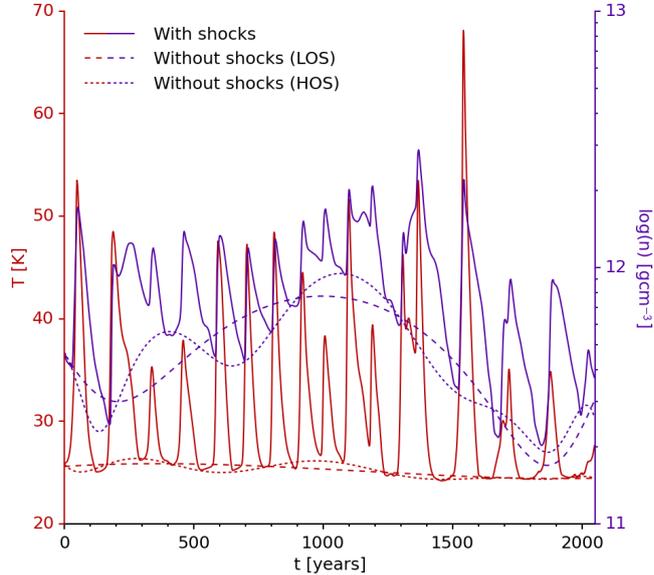
Figure 2.22: Temperature and number density history of a fluid element in the outer disc. Overplotted are polynomials of low and high-order fitted to the minima of temperature and density, representing the same fluid element history devoid of shocks.

removed because the abundances near the end of the simulation are comparable, as shown in Table 2.4. Hence, the chemical changes for most species are not persistent. However, HNO, CN and NH_3 have significantly higher abundances near the end of the simulation when the fluid element is consistently shock-heated in the outer disc. For example, devoid of shocks, HNO forms in the gas-phase via $NO + HCO \rightarrow HNO + CO$ at a rate of approximately $10^{-12}\,s^{-1}$, which is too slow to significantly affect the gas-phase abundance of HNO over the duration of the simulation ($\approx 2000\,yr$). However, in shock-heated regions the rate of this same reaction reaches a maximum of approximately $10^{-5}\,s^{-1}$. This results in a reaction timescale of roughly one day, which allows the reaction to proceed at a fast enough rate to increase the total amount of HNO in the gas-phase by a factor of 10^3 by the end of the simulation. As the $NO + HCO \rightarrow HNO + CO$ reaction is not temperature dependent in the chemical network used, the cause

76

of this enhanced reaction rate is the abundance enhancement of NO at higher temperatures. Similarly, the abundance of NH_3 is enhanced by a factor of 3×10^4, despite the fact the rate of the reaction $NH_3^+ + HCO \rightarrow HCO^+ + NH_3$ is also only weakly temperature dependent. In fact, a significant number of nitrogen-bearing species have enhanced abundances, and this is because persistent shock heating maintains a larger reservoir of nitrogen in the gas-phase for molecules to be formed from. CN is also found to be enhanced by a factor of 2×10^3, except in this case it is due, more straightforwardly, to the desorption temperature of CN being similar to that of the shocked disc material (see Table 2.2).

Shocks in a relatively low-mass, protosolar-like disc are seen to cause persistent changes in the abundances of some species. This has several implications for future studies of young protoplanetary discs. Firstly, whether this effect is independent of the initial conditions should be investigated, as subtle differences in early-phase composition may not be preserved through a short evolutionary period, resulting in similar abundances at the end of the GI phase across a variety of young systems. Secondly, if gravitational instability occurs over a significant phase of early disc evolution, researchers simulating more evolved systems should consider the processing of GI before setting their initial abundances, in order to account for the enhancement in some important species. This could be of particular importance for simulations of planets that may have been synthesised from fragments formed and chemically processed by GIs (see e.g. Ilee *et al.*, 2017). Ideally, models of protoplanetary disc chemistry should be based on a self-consistent approach concerning the molecular core collapse phase (e.g. Hincelin *et al.*, 2013; Visser *et al.*, 2011), followed by GI-driven evolution if the disc-to-star mass ratio is large enough. The resulting abundances can then be used as initial conditions for the simulation of a more evolved, low-viscosity or quiescent disc, at which point an axisymmetric α-disc prescription becomes appropriate.

Furthermore, the enhanced gas-phase abundances driven by shock heating suggest that observations of discs could still be used to characterise disc dynamics even if they cannot be resolved spatially, which is an important finding. This is because an observation of a species such as CN, that may otherwise be undetectable in the outer regions of a more quiescent disc, indicates an enhancement in temperature that could be produced by GI. Moreover, even if the effects of shock heating are short-lived for some species, the enhancement in abundance is very significant, e.g. up to a factor of 10^{20} for SO_2 (see Figures 2.16 and 2.17), Therefore, detections of transient species may still be indicative of GI. Further investigation is warranted in this area to determine how permanently gravitational instabilities affect disc composition over longer timescales.

2.3.3 Comparison with axisymmetric models

Comparing the results reported in this paper to other results in the literature is not straightforward due to the varying simulation dynamics, techniques and assumptions. I have used the chemical network developed in I2011, yet even a comparison with this work is complicated because the less massive and more massive discs represent different stages of GI activity and occupy different parameter spaces. Nevertheless, Table 2.5 shows maximum abundances taken from two recent studies, Walsh *et al.* (2010) (hereafter W2010) and Akimkin *et al.* (2013) (hereafter A2013), to provide a very rough comparison to the maximum abundances at the end of the lower mass disc simulation I have used.

I extract the peak abundances from W2010 by visually inspecting their 'fiducial' model between 10 au and 50 au, which introduces some uncertainty into the quoted values. Nevertheless, there are significant differences between the sets of results that arise from a multitude of factors. Firstly, W2010 modelled a 1 Myr old laminar model disc, which is more evolved than the system I consider and

Table 2.5: Maximum gas-phase abundances reported within this chapter, W2010 and A2013. A dash represents a missing reported value for that species in the corresponding work.

Species	Maximum log $X(i)$		
i	This work	W2010	A2013
CO	-4.4	-4	-4.0
CO_2	-4.4	-6	-
NH_3	-5.5	-	-4.7
H_2O	-3.7	-4	-5.0
H_2CO	-5.7	-9	-9.0
HCN	-6.4	-7	-8.5
HCO^+	-10.9	-6	-
CS	-7.5	-8	-
O_2	-11.2	-	-4.5
CN	-7.2	-7	-
C_2H	-9.9	-7	-
N_2H^+	-18.9	-11	-11.0
OH	-13.9	-4	-

features only local mass transport. As a result, their disc possesses the vertically inverted temperature structure observed in Class II YSOs due to the photon-dominated region near the disc surface. Therefore, the highest abundances for most species in W2010 occur in a 'transition' layer confined to $z/r \approx 0.3$, where UV and X-ray dissociation is pertinent, which explains their greatly enhanced OH abundance. If comparisons are drawn only within the midplane regions then a similar peak OH abundance is recovered. This is also true for the HCO^+ abundance, which is expected to be due to the ubiquity of gas-phase CO in both models. The midplane abundance of H_2CO in W2010 is much lower due to the more efficient freeze-out in their colder midplane and lower initial abundance; W2010 use significantly different initial abundances, focusing on oxygen-rich low-metallicity elements rather than cometary ices. Due to the strong dependence on initial abundances for some species, those that are only significantly affected

by adsorption and desorption processes, higher abundances are found at the end of the simulation. Furthermore, atomic N is not included initially in the chemical network I have used which results in a significantly lower N_2H^+ than W2010 found.

The maximum abundance values quoted for A2013 are determined from figures showing the abundances at $10\,au$ and $50\,au$ within their disc model. Initial abundances are different in the disc model I have used than in A2013, who use oxygen-rich low-metallicity abundances similar to W2010, which helps explain the enhanced values for H_2O, H_2CO and HCN. Contrary to A2013, I do not include N or N_2 in the initial conditions and furthermore, A2013 incorporate grain growth in their simulation, which they report enhances the abundance of nitrogen atoms in the midplane. Hence, I record a lower N_2H^+ abundance. Interestingly, however, A2013 report the same peak N_2H^+ abundance as W2010 despite the lack of grain growth treatment in the latter. The lower maximum abundance of O_2 is a consequence of the disc model I have used containing 1.3 times less elemental oxygen and the A2013 model including UV and X-rays that enhance the abundance of OH in the upper disc, which subsequently leads to synthesis of molecular oxygen via a neutral-neutral reaction with atomic oxygen. As the A2013 disc follows the classic α prescription with an array of photoprocesses incorporated into their chemical model, they recover a heated layer in the disc possessing the richest chemistry, similar to W2010, which is common of more passive discs.

Realistically, these comparisons are very weak because of the significantly different dynamics between the disc model I have used and other models in the literature. In essence, what they show is that in a more quiescent, axisymmetric α-disc, a photon-dominated, chemically rich layer sits above a shielded, cold, chemically sparse midplane. However, in a non-axisymmetric, gravitationally unstable disc, global instability and mass transport produce a hot midplane that

experiences a rich chemical evolution. Ideally, other 3D simulations of GI-driven discs need to be completed before appropriate comparisons can be made to the results presented in this paper.

2.4   Conclusions

This chapter features the physical and chemical evolution of a $0.17\,\mathrm{M_\odot}$ protoplanetary disc over a period of approximately $2000\,\mathrm{yr}$. The disc surrounds a $0.8\,\mathrm{M_\odot}$ protostar that will evolve into a Solar-like star. As a result, this work is relevant to the early dynamical and chemical evolution of our Solar System.

This chapter extends previous work that suggests gravitational instabilities significantly affect the chemistry in more massive systems. The main results that I have found from simulating a lower mass, protosolar disc are as follows:

- Spiral waves generated in the disc heat material through shocks that enhance the local temperature and increase the rates of desorption and some endothermic reactions. This subsequently increases the gas-phase abundance of most species across the entire disc, including the midplane.

- In the more massive disc, the majority of species trace distinct spiral structure in the column density maps after $2.7\,\mathrm{ORPs}$ at $30\,\mathrm{au}$ (defined as $t = t_{orp}$). After the same number of outer rotational periods in the lower mass disc, the majority of species do not trace much spiral structure because the spiral density waves are of lower amplitude.

- At the end of the simulation, spiral features driven by GI in a protosolar disc are traced by a significant number of important species; CN is a particularly strong tracer as it is most abundant in the outer disc regions and has a relatively high column density.

2. A SIMULATION OF DYNAMICS AND CHEMISTRY

- Comparing the less massive and more massive discs at $t = t_{orp}$ reveals that most species have reduced or enhanced peak abundances by a factor of only two to four times. Therefore, this suggests that the presence of gravitational instabilities in young, massive protoplanetary discs affects the chemical evolution more significantly than the mass differences of the discs.

- GIs, due to global transport of disc material, produce a chemically-rich midplane. This is in contrast to studies of more evolved, axisymmetric discs, which report peak abundances in heated layers above the cold 'gas-phase desert' midplanes, caused by photoprocesses and local transport of material.

- A rapid succession of shocks can lead to long-lasting changes in the inner disc composition. At small radii, the shock heating quickly increases the temperature beyond the desorption energy for all neutral species. Therefore abundances are recovered close to the protostar that are likely higher than in a more quiescent disc.

- In the outer disc, the effect of shock heating is easily distinguishable because of the lower ambient temperature. For most species this effect is short-lived. However, successive shock heating permanently alters the abundances of HNO, CN and NH_3 in the outer disc over the duration of the simulation. This has two major implications. Firstly, researchers performing chemical simulations of more evolved systems should perhaps consider the processing of GIs when setting initial conditions, if indeed GIs are present in the early phases of disc evolution. Secondly, observations of discs could still be used to characterise disc dynamics even if they can not be resolved spatially because shocks cause permanent as well as transient changes in gas-phase abundances.

- H_2O removes HCO^+ via a proton transfer interaction, creating a hole in the HCO^+ distribution of the inner disc. The extent of H_2O is predominantly

determined by the amplitude of the disturbance driven by the instability, which is characterised by disc mass. Therefore, observations and measurements of the HCO$^+$ inner holes in real systems could be used for characterising protoplanetary disc mass.

Envelope accretion or outflows are not incorporated in the disc model in order for the focus to be on the effects of gravitational instabilities on the chemical evolution of protoplanetary discs. This is appropriate as collimated outflows are assumed to have an insignificant effect on disc composition and a surrounding envelope would likely only enhance the molecular abundances in the outermost regions of the disc. Sakai *et al.* (2014) have found an enhancement of SO at the centrifugal barrier of a Class 0 object that may be produced in a weakly shocked region as envelope material accretes on to the disc whilst exceeding the Keplerian velocity. The results in this chapter support this theory as the gas-phase abundances of volatile species are enhanced through shock heating. However, as the authors find no significant SO abundance interior to the centrifugal barrier, the impact from this phenomenon on the results concerning gravitational instabilities may be unimportant.

Recent observational advancements, such as those made possible by ALMA, are beginning to, and will continue to, revolutionise the studies of protoplanetary discs, and open up the possibilities for investigating young, embedded objects. The attainable resolutions suggest that if the $0.17\,M_\odot$ disc were located within the Taurus-Auriga cloud complex, its spiral structure should be distinguishable, which is an exciting prospect for characterising gravitational instabilities in real systems. As a cautionary note, however, it is possible to have well defined spiral structure and not detect it, or for complicated spiral structure to give an incorrect appearance at low resolution. For example, CO appears to be the best species for directly observing spiral structure in real systems, but at low resolution the

image could appear as two rings, which would be incorrectly interpreted as a gap. Therefore, in Chapters 3 and 4, I perform radiative transfer calculations in order to assess the detectability and image fidelity of spiral structure in a lower mass disc, focusing on a combination of the species I have found to be encouraging tracers such as CN and CO.

Chapter 3

Continuum emission and mass estimates

3.1 Introduction

At the earliest stages of protoplanetary disc evolution, the disc may contain a mass comparable to that of the central protostar. In such a disc, the gravitational instability can develop and drive global spiral waves. As these spiral waves grow, they can produce shocks that heat the disc material locally (e.g. Bae *et al.*, 2014; Boley & Durisen, 2008; Harker & Desch, 2002), which has a significant effect on the chemical evolution of some species as shown in Chapter 2. As the dust emission within a disc depends on the temperature, the spiral shocks should produce a flux contrast between the arm and inter-arm regions. Therefore, continuum observations of young, embedded systems have the potential to reveal GI-induced spiral structure, which would have significant impact on the understanding of formation and evolution mechanisms within protoplanetary discs.

In recent years, the capabilities of observational instruments have been significantly improved and expanded upon, which has resulted in an unprecedented amount of protoplanetary disc images at millimetre wavelengths. However, be-

cause spatially resolving the youngest, most embedded sources (late Class 0/early Class I) at au scales (the expected size of GI-driven spirals) remains very challenging, most observations to date have been focused on more evolved discs (Class II). Spiral features have been detected in Class II discs (e.g. Benisty *et al.*, 2015; Muto *et al.*, 2012), but Dong *et al.* (2015) raise several important points that question if spiral arms in more evolved objects are driven by GIs. Firstly, derived disc masses are typically not high enough to induce gravitational instabilities. Secondly, the accretion rates in observed Class II objects do not appear consistent with the accretion rates in their simulations of gravitationally unstable discs. Thirdly, the observed features are probably beyond the critical radius where discs are believed to fragment. Dong *et al.* (2015) conclude by offering planet-disc interactions as a more credible origin for the spiral features, but it should be noted that there are counterarguments to each of the aforementioned points, and even planet-disc interactions may not explain observations to satisfaction (Richert *et al.*, 2015).

Since the Atacama Large Millimetre / submillimetre Array (ALMA) became operational, the sensitivity of millimetre observations has greatly increased, allowing us to peer deep into younger systems for the first time. As a result, Pérez *et al.* (2016) have detected spirals originating from the bulk of the disc surrounding Elias 2-27 that appear consistent with gravitational instabilities (Meru *et al.*, 2017; Tomida *et al.*, 2017). Moreover, Tobin *et al.* (2016), have detected spiral features in a Class 0 object that also appear likely to have originated due to gravitational instability, albeit in a fairly complex multiple star system where the spirals may be produced by gravitational interaction between the proximal young stellar objects.

In light of these recent discoveries, it is currently a very exciting time in protoplanetary disc observations. However, even though spirals are beginning to be detected in real discs, it remains important to simulate observations, where all

the properties are known *a priori*, in order to assess the validity of claims that structure seen in young discs arise due to GIs. Furthermore, simulated observations will allow the constraint of the observational parameters necessary for modern technologies such as ALMA to unequivocally detect GI-driven spiral features. Several authors have reported that GI-driven spirals should be detectable with ALMA in discs with a range of masses and sizes (e.g. Cossins *et al.*, 2010; Dipierro *et al.*, 2014; Douglas *et al.*, 2013). The current chapter builds upon this repository of results through the synthesis of observations of the hydrodynamic simulation used in Chapter 2. As this simulation is of a gravitationally unstable disc surrounding a $0.8\,\mathrm{M_\odot}$ protostar, the system it represents may be analogous to our early Solar System. Hence, the synthetic detection of spiral structure in this case would be of particular significance.

An important result derived from observations of protostar systems is the mass of the surrounding protoplanetary disc as it is a pivotal quantity in understanding disc formation and evolution. Estimates from observations of the nearby Taurus star-forming region have determined that Class II disc masses range between 0.0003–$0.06\,\mathrm{M_\odot}$ (Andrews *et al.*, 2013) and masses of Class 0 discs range between 0.000001–$0.0006\,\mathrm{M_\odot}$ (see Greaves & Rice, 2011, Table 1). These estimates are based on the assumptions of vertically isothermal disc structures and optically thin dust emission, which are perhaps appropriate for lower mass discs, although debatable given that masses derived from accretion rates tend to be higher. However, for younger and more embedded discs these assumptions are even less likely to be accurate for a number of reasons. Firstly, shocks driven by GIs heat and lift material from the midplane; hence the vertical structure is far from isothermal (see Boley & Durisen, 2006, Chapter 2). Secondly, due to the surrounding envelopes and high densities, Class 0/I discs are likely optically thick even at millimetre wavelengths (e.g. Miotello *et al.*, 2014). As a result, the

observed flux from very young systems is likely to only be tracing a fraction of the actual disc mass. This has implications for existing and future studies because if masses are greater than have been estimated, the GI may play roles in discs in which its importance has been erroneously discounted.

In this chapter, the radiative hydrodynamic model of a gravitationally unstable disc from Chapter 2 is used to investigate the observability of GI-driven spiral structure in dust continuum emission with ALMA. The optimal parameters with which to perform the LIME radiative transfer are established. I produce ALMA synthetic observations of the disc model at different frequencies and inclinations by implementing a range of dust opacities in the radiative transfer calculations. The aim here is to provide an insight into how sensitive the interpretations of observations of gravitationally unstable discs can be to the assumed dust opacities, because the values for young, embedded objects are poorly constrained. Observationally derived disc masses are compared with the actual disc mass, and assumed dust temperatures compared with the actual dust temperatures. There is also a comparison presented concerning the synthetic observations derived from LIME images and those derived from another existing radiative transfer code, RADMC-3D (Dullemond *et al.*, 2012), because it is important to ensure that there is consistency between different radiative transfer codes in the literature.

I briefly explain how LIME can be used to produce intensity maps in Section 3.2, and explore methods to improve upon the base LIME setup, which I refer to as 'vanilla' LIME. These methods include: changing the weighting parameters; changing the number of grid points; restricting grid point positioning based on the optical depth; and averaging multiple runs. I produce synthetic observations of the disc model across a large parameter space in Section 3.3 and then use the flux density to determine the disc mass for each combination of parameters. The observationally determined disc masses are then compared to the actual simu-

lation mass to assess the validity of this commonly used observational method. Finally, Section 3.4 presents conclusions and discusses future research.

3.2 Producing intensity maps with LIME

3.2.1 Disc model

The disc model used to produce continuum emission maps is a snapshot of the lower mass disc featured in Chapter 2, taken at the end of the simulation, $t \approx 2050\,\mathrm{yr}$, once the spiral features are fully developed and the disc is in a rough balance between heating and cooling processes, i.e. the disc is self-regulated and not fragmenting. Details of the hydrodynamic simulation can be found in Chapter 2.

The dust model adopted in the hydrodynamic simulation assumes D'Alessio *et al.* (2001) opacities with a grain size distribution $n = n_0\,a^{-3.5}$ and $\alpha_{max} = 1\,\mathrm{mm}$ to account for grain growth (D'Alessio *et al.*, 2006). A gas-to-dust mass ratio of 100 is used, which is typical of the ISM, and the dust grains are assumed to be thermally coupled and well mixed with the gas since significant dust settling is not expected in such turbulent systems. To assess the validity of this assumption I compute the Stokes number, which is given by

$$St = \frac{\pi a \rho_s}{2\Sigma_g} \qquad (3.1)$$

where a is the dust grain radius, ρ_s is the dust grain solid density and Σ_g is the gas surface density. The Stokes number for $1\,\mathrm{mm}$ dust grains is shown in the left panel of Figure 3.1, and as can be seen, $St < 1$ across the majority of the disc. Therefore, the assumption that dust grains are well coupled to the gas is justified. Note that this formulation of the Stokes number is based on the assumption that particles remain in the Epstein gas drag regime, which is
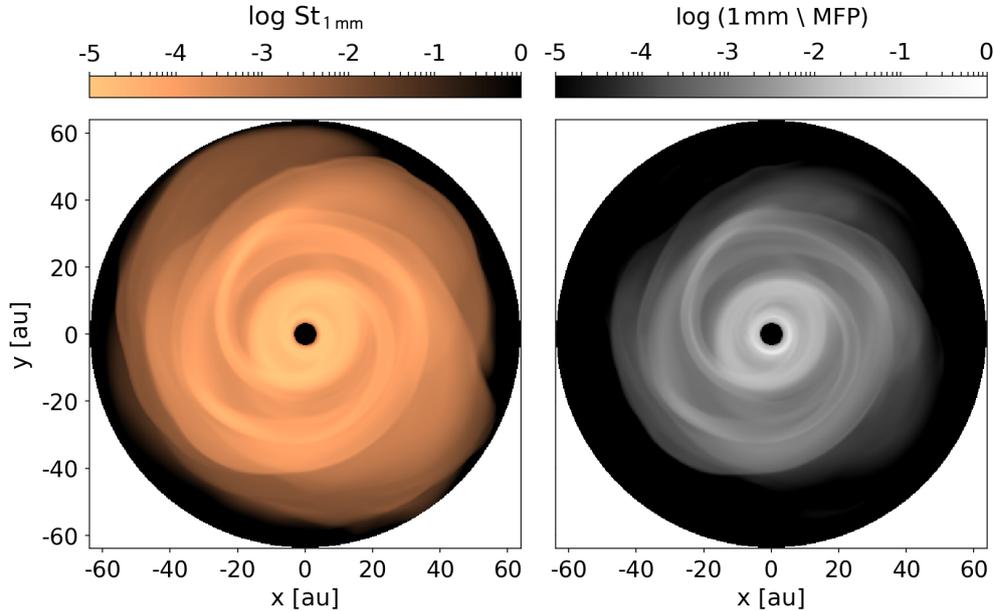
Figure 3.1: Stokes number for 1 mm dust grains across the disc model (left) and the logarithm of 1 mm divided by the mean free path of gas molecules in the disc midplane (right); the Epstein drag regime is valid where the mean free path is larger than the dust grain size.

appropriate here because $a < \frac{9}{4}\lambda_{\mathrm{mfp}}$ (Birnstiel *et al.*, 2010) for 1 mm sized dust grains, as is shown in the right panel of Figure 3.1.

There is no envelope integrated into the radiative hydrodynamic simulation as the focus is only on the detectability of GI-driven spiral structure. In reality, a surrounding envelope may shield the disc from external radiation that can otherwise diminish the spiral structure (e.g. Cai *et al.*, 2008; Kratter & Murray-Clay, 2011), but here it is assumed that the disc is already well-shielded, i.e. heating from the interstellar radiation field is neglected. Furthermore, infall from the envelope onto the disc can significantly affect the spiral structure (e.g. Harsono *et al.*, 2011). However, as the consequence appears to be an enhancement in the contrast between arm and inter-arm regions, the omission of this interaction will only be significant for the conclusions if GI-driven spirals are not detected.

In contrast, an envelope *is* incorporated into the radiative transfer step of the modelling when producing continuum emission maps. In order to appropriately describe the environment within which a young protoplanetary disc is embedded, this envelope is taken to be a $10\,\mathrm{M}_\odot$ contracting Bonnor-Ebert sphere (see Keto *et al.*, 2014). Moreover, whilst radiative transfer codes often self-consistently calculate the dust temperature, here the dust temperatures from the radiative hydrodynamics code are utilised in order to account for the viscous and shock heating in the model. As a result, only ray tracing needs to be performed on the disc model to obtain continuum emission maps.

3.2.2 'Vanilla' LIME

I use the Line Modelling Engine (LIME; Brinch & Hogerheijde, 2010), which calculates continuum emission and line intensities from a weighted Monte Carlo sampling of an input 3D model. Following is a summary of how LIME operates, but the reader is referred to Brinch & Hogerheijde (2010) for a more detailed description.

The input model contains density and temperature information, and also abundance and velocity information when line emission is considered. LIME then selects an x, y, z position randomly, and if a selection criterion is met, which is dependent on the density by default, this point is added to the grid. Once the grid is constructed, LIME calculates the appropriate parameter values at each point; the method used to achieve this, such as nearest point interpolation, linear interpolation, or something more advanced, is defined by the user in the model file. The constructed grid is then smoothed via Lloyd's algorithm (Lloyd 1982, Springel 2010) in order to ensure that the distance between points is comparable to the local separation expectation value whilst still maintaining the underlying model structure. Next, the smoothed grid points are connected by lines through
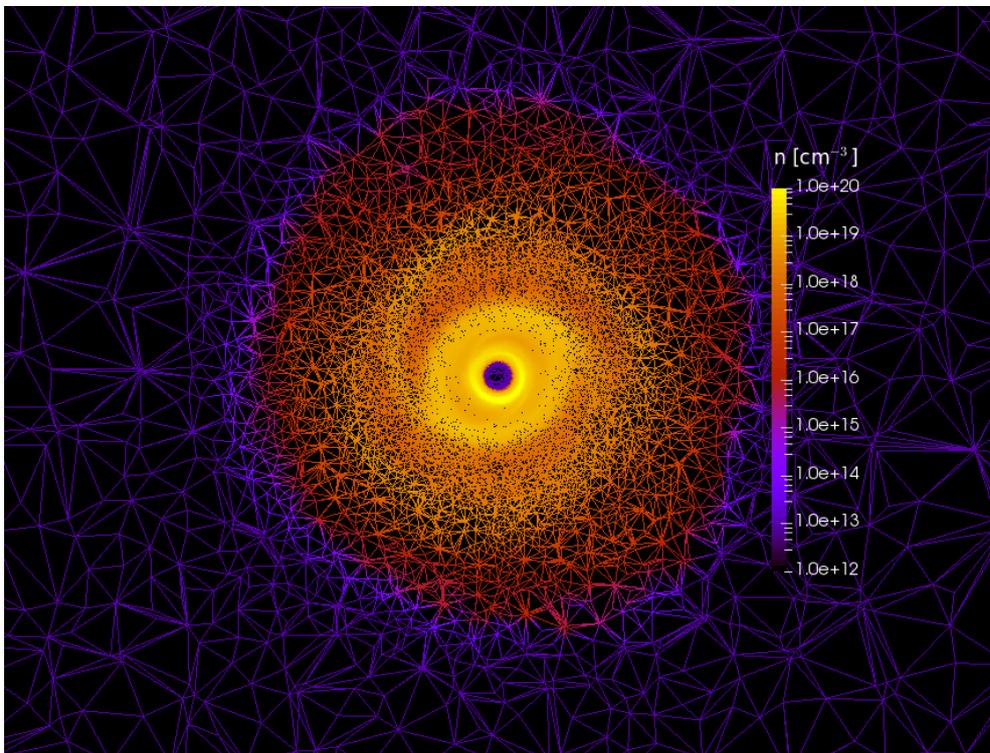
Figure 3.2: Delaunay triangulation of randomly sampled grid points in the x-y plane.

Delaunay triangulation, which is illustrated in Figure 3.2; note the comparison with the right panel of Figure 2.7 also illustrates how the process of random point selection samples the underlying model. If non-LTE line emission is being considered, photons are propagated along the Delaunay lines and the radiative transfer equation is solved at each grid point via an iterative process. Finally, once convergence is reached, or if only continuum emission is being considered, LIME ray traces lines of sight through the model in order to produce intensity maps.

LIME differs somewhat from other radiative transfer codes as instead of random sampling to construct a grid, most codes use a source model mapped to a grid of cells in Cartesian or cylindrical coordinates, with model properties (e.g. temperature, density and abundance) assumed constant over each cell. Moreover, the photon propagation in LIME is along the Delaunay lines, whereas typically photon packages are traced in random directions from random points of absorption in each cell. The difference in operation means that LIME can calculate full non-LTE radiative transfer in 3D space without the need for simplifications implemented in most codes, such as the LVG approximation currently implemented in RADMC-3D.

LIME is in continual development, has been hosted on GitHub since v1.3[1], and the available documentation is rapidly improving. At the time of writing, LIME offers the user the ability to specify a whole array of parameters that affect the resultant intensity maps. In order to investigate potential pitfalls, I ran LIME v1.6 as is, which I refer to as 'vanilla' LIME, for the disc model using 2.5×10^4 grid points; I use this number of grid points initially as the documentation recommends 'between a few thousands up to about one hundred thousand' and it is also the number of grid points used in Douglas *et al.* (2013).

---

[1]https://github.com/lime-rt/lime
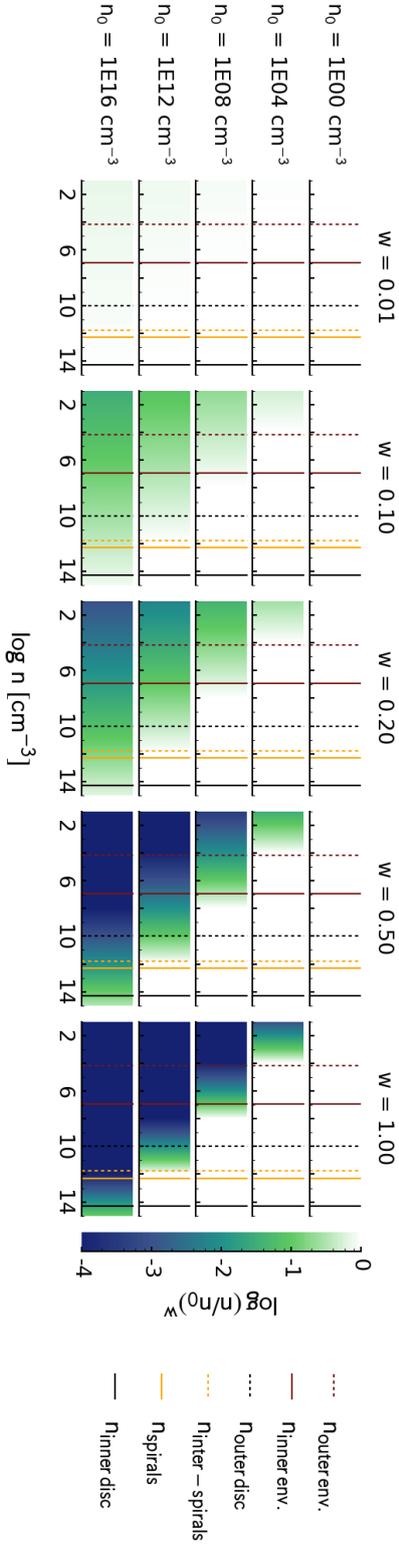
Figure 3.3: Probability of grid point selection as the density weighting parameters, n_0 and w, are varied. The vertical lines correspond to approximate number densities within various features of the disc model, as labelled.
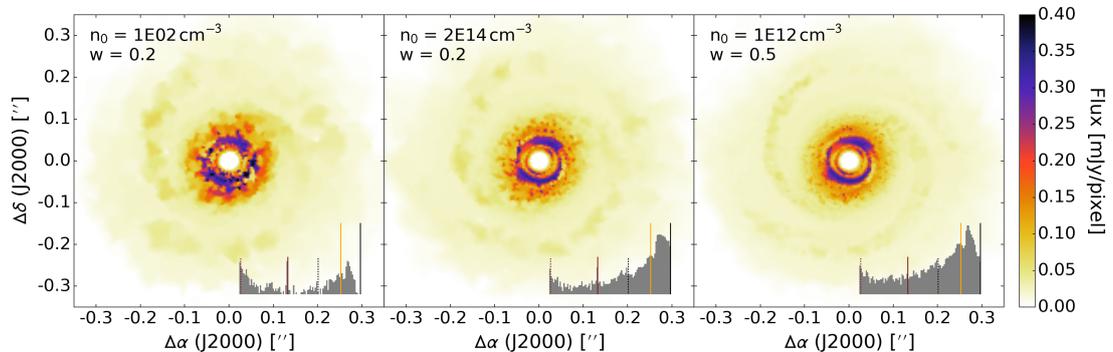
Figure 3.4: Comparison between 300 GHz flux images produced with LIME using varied n_0 and w parameters, demonstrating that LIME images are sensitive to the weighting imposed. The inset figures show the number density distributions of the grid points, confined within the disc region, that produce the corresponding image. The vertical lines corresponding to the key in Figure 3.3.

The leftmost panel of Figure 3.4 shows the 300 GHz continuum emission map for the disc model featured here (see Chapter 2) when using vanilla LIME, and comparing to Figure 2.2 it is immediately apparent that the non-axisymmetric structure is very poorly resolved. This is because the default weighting routine sets a normalisation density at the model inner boundary, which is within the inner hole of the disc model. This means that, essentially, any density weighting is being omitting when using vanilla LIME. Note, a frequency of 300 GHz is adopted for the rest of Section 3.2.

3.2.3 Weighting of grid points

In order to procure a more accurate flux image, the density weighting function must first be amended to be appropriate for the disc model. LIME randomly distributes points during the grid building routine and only selects the point if it passes the criterion

$$a < \left(\frac{n}{n_0}\right)^w, \tag{3.2}$$

95

where a is a random number generated between 0 and 1 each time a point is selected, n is the density of the grid point, n_0 is a normalisation density and w is an exponent. The normalisation density was fixed to the inner boundary density in LIME v1.5 and earlier, but since v1.6 the user should now set the parameter $n_0{}^w$ in the model file. If the user does not set this parameter then the old default is restored, which can be a poor selection criterion if, for example, the model has an inner hole or if the user would like to focus on features with a lower density than the central density. This effect is demonstrated in Figure 3.3, which shows the probability of point selection, $\log(n/n_0)^w$, as n_0 and w are varied, with features of the disc model overlaid.

As can be seen, if the reference density, n_0, is increased then the likelihood of point selection at low densities becomes increasingly small, and if the exponent, w, is increased then the range where points are likely to be selected contracts. For the purposes of this work, I want a high probability of point selection at typical spiral arm densities, indicated by the solid orange vertical lines in Figure 3.3, but also with a significant percentage of points extending to the densities of the outer disc, indicated approximately by the dotted dark gray lines in Figure 3.3. Therefore, Figure 3.3 indicates that $n_0 = 1 \times 10^{12}\,\mathrm{cm}^{-3}$ and $w = 0.5$ are optimal choices for the disc model. Note that this choice of parameters results in only a small fraction of points being positioned within the envelope. However, this is not an issue because the maximum envelope density is lower than the bulk of the disc model. As a result, the mean free path within the simplistic envelope model is ubiquitously larger than the envelope size; hence only a small fraction of points are required to treat the emission accurately. In reality, the innermost part of the envelope around embedded protoplanetary discs may be very dense, which could affect the conclusions in the outer disc regions.

I ran vanilla LIME for the disc model with $n_0 = 100\,\mathrm{cm}^{-3}$ and $w = 0.2$. I

then ran LIME using $n_0 = 2 \times 10^{14} \, \text{cm}^{-3}$ and $w = 0.2$ to simulate the behaviour of the default reference density value assignment. Finally, I ran LIME using n_0 $= 1 \times 10^{12} \, \text{cm}^{-3}$ and $w = 0.5$ that, as mentioned above, are determined from Figure 3.3. Figure 3.4 shows the flux image outputs of these runs and as can be seen, if n_0 is set much lower than the typical disc density then essentially no weighting is applied, apart from excluding the inner hole. In this case there is poor sampling of the densest features and a large percentage of points are positioned in regions of low density. If, on the other hand, n_0 is set to the highest density in the model, as shown in the middle panel, then density weighting is applied and the disc spirals and inner region are sampled much more thoroughly. However, comparing this result to the result in the right panel, where n_0 is set at the approximate spiral density, it is evident that using too high a reference density undersamples the spiral features comparatively. This is because, as Figure 3.3 shows, the probability of point selection at the density of the spiral arms is reduced as n_0 increases. Indeed the panel on the right, with $n_0 = 1 \times 10^{12} \, \text{cm}^{-3}$ and $w = 0.5$, showcases a type of 'Goldilocks' regime for the disc model, in which the spirals are sampled in an optimal manner. Note, though, that the trade-off is a smaller percentage of points at the highest densities, which corresponds to the innermost disc in the model I use, as indicated by the inset histogram in the right panel of Figure 3.4. Therefore, the optimal choice of n_0 is dependent on the features of interest in a particular model. Hereafter, for the disc model used in this chapter I use $n_0 = 1 \times 10^{12} \, \text{cm}^{-3}$ and $w = 0.5$, and refer to this setup as the standard sampling.

3.2.4   Number of grid points

Due to the Monte Carlo nature of the LIME gridding, two runs using identical inputs will likely produce differing images as the grid points will be positioned dif-
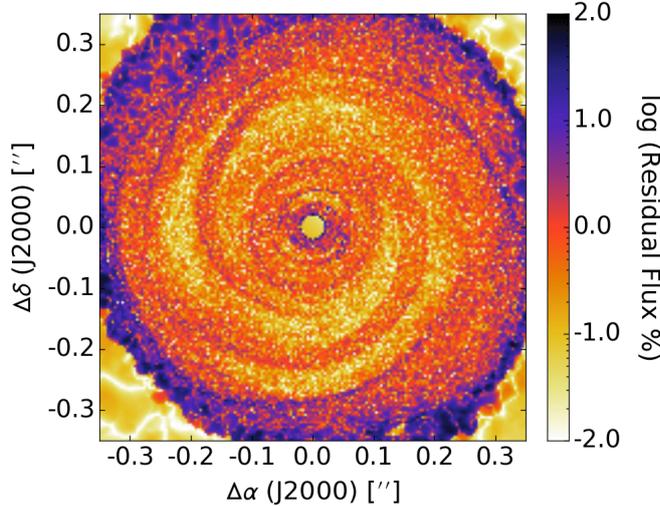
Figure 3.5: Residual flux between two LIME runs using identical inputs with 2×10^6 grid points and standard sampling. This residual is defined as $|(f_1\text{-}f_2)|/(f_1\text{+}f_2)$, where f denotes flux per pixel.

ferently. This effect obviously decreases as the number of grid points is increased, so in order to circumvent this issue, the user can simply use a large number of grid points. For continuum images this is not a particularly significant issue because the computational cost is relatively low. However, for line images, because each molecular energy level population must be computed for each grid point, the computational cost increases dramatically with the number of grid points. Therefore, even though this chapter focuses on continuum images, deducing the minimum number of grid points that can be used and still obtain accurate images in the continuum is a worthwhile endeavor because the results are applicable to line images, as is later shown in Chapter 4.

I adopt the weighting parameters discussed in Section 3.2.3 and produce continuum images with an increasing number of total grid points until the residual between two runs using identical inputs meets a sufficient level. This level is set to 5 per cent as it is smaller than the errors typically expected in observations. Moreover, as Figure 3.5 shows, the majority of the residual flux is smaller than
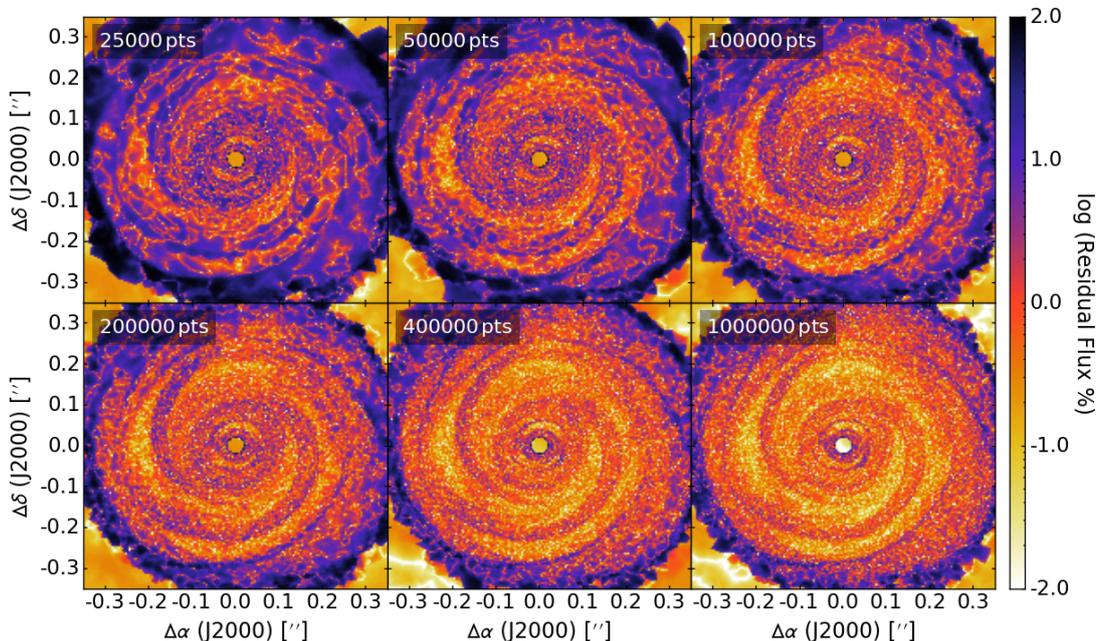
Figure 3.6: Residual flux between standard LIME runs using the indicated number of grid points and 2×10^6 grid points, with standard sampling. This residual is defined as $|(f_1\text{-}f_2)|/(f_1\text{+}f_2)$, where f denotes flux per pixel.

this threshold level when using 2×10^6 points. Note that the large residual differences seen towards the edges of Figure 3.5 are where the model transitions from the disc to the envelope and the abundance of points drops off sharply. However, as the focus is primarily on the spiral structure, this is not a concern and the disc-envelope regions are omitted in future analyses.

By comparing the images produced using fewer grid points with this 'canonical' result, Figure 3.6 shows that increasing the number of grid points reduces the residuals. This is obviously a trivial result, but more importantly, Figure 3.6 indicates that a sufficiently accurate image, which was defined prior as the majority of the disc having a residual flux lower than 5 per cent, can be produced using 2×10^5 grid points. This is a factor of ten lower than the 'canonical' result, and hence affords a significant reduction in computational cost when producing

continuum images. Not only is this a benefit in reducing computational time, but it also reduces memory consumption. This allows more instances of LIME to be run simultaneously, which is utilised in Section 3.2.6.

Although the results presented in Figure 3.6 are expected, it is important to understand precisely why an increase in grid points affords an improvement in the image accuracy. The emission of photons is governed by the mean free path, which is the average distance a photon will travel before interacting. If the grid point separation is larger than the local mean free path, then important photon interactions will be neglected; hence the resultant flux images will be inaccurate.

The mean free path is given by $l = 1/\alpha_\nu$, where α_ν is the absorption coefficient at a particular frequency. For dust-dominated continuum emission $\alpha_\nu = \kappa_\nu \rho_d$, where κ_ν is the dust opacity at a specific frequency and ρ_d is the dust mass density. The κ_ν value is known *a priori* as it is contained within a dust opacity file read by LIME, and the gas mass density information is contained within the hydrodynamic simulation, which is converted to the dust mass density using the adopted gas-dust mass ratio of 100. Using these quantities I calculate mean free path values throughout the disc model. The grid point separation information is obtained straightforwardly as LIME v1.6 has the ability to output the grid point positions and nearest neighbour distances. I then interpolate the nearest neighbour distances to a coordinate grid matching the mean free path data cube in order to compare both length scales.

Figure 3.7 shows the comparison between the mean free path and grid point separation across the x-y plane at $z = 0$ for each of the runs with results shown in Figure 3.6. As can be seen, by increasing the number of grid points, the disparity between these two length scales across the majority of the disc is reduced. However, even when using 1×10^6 points there is still an appreciable discrepancy between the mean free path and grid point separation within the spiral arms and
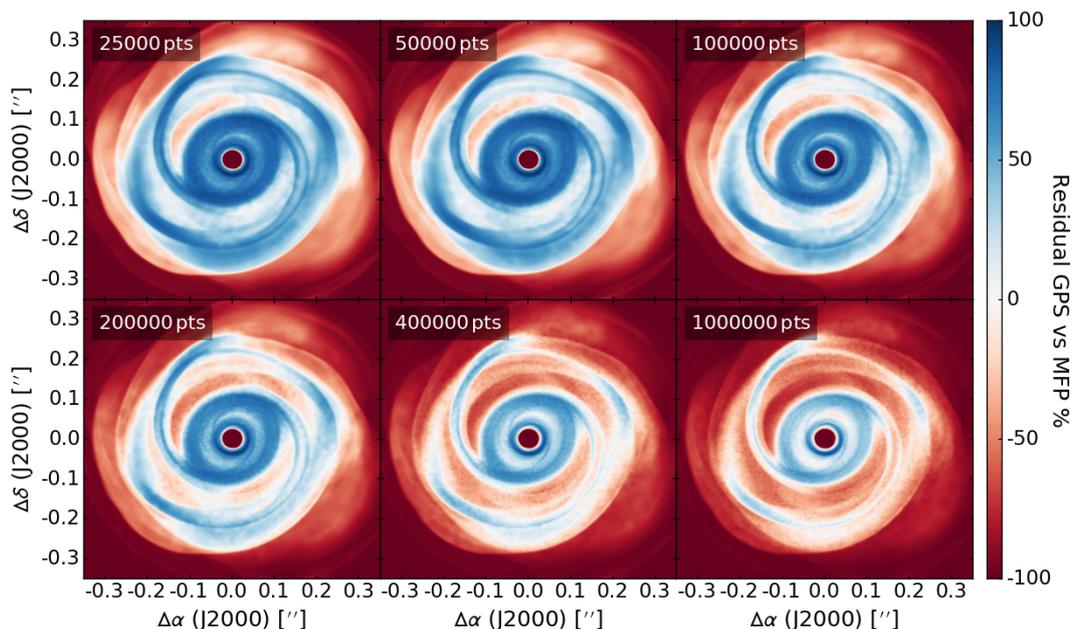
Figure 3.7: Residual of grid point separation (GPS), s, and mean free path (MFP), l, at the disc midplane for LIME runs using the indicated number of grid points and standard sampling. This residual is defined as (s-l)/(s+l).

inner disc regions. This is not surprising because these are the densest regions of the model disc, which therefore possess the smallest local mean free path values. Fortunately, this is not a particularly significant issue because the contribution to intensity in these densest, most optically thick regions is small. In fact, the sampling routine can be optimised further by accounting for this phenomenon.

3.2.5 Optical depth surface

In optically thick regions, such as those expected in embedded protoplanetary discs, the contribution to the observed intensity is low because the contribution of I_{ν_0} to the local intensity is reduced by $e^{-\tau}$, as can be seen in Equation 1.23. Therefore, as observational errors are expected to be on the order of 10 per cent, the background intensity can assumed to be negligible wherever $e^{-\tau} < 0.05$. This means that grid points should only be required at $\tau < -\ln(0.05) < 3$ in order

to produce an accurate image. Hence the $\tau = 3$ surface is used as a threshold, and is referred to as the 'optical depth surface' hereafter. For comparison, the photosphere of a star is defined at $\tau = 2/3$, and so the densest regions of the disc are likely still being over-sampled by adopting $\tau = 3$ for the optical depth surface. However, determining the minimum optical depth that can be used in grid point restriction and still obtain accurate images is dependent on dust opacity and frequency, which requires a dedicated study.

LIME is capable of outputting several different image types, such as brightness temperature, flux and optical depth along the line-of-sight, which the user can specify; I adapt the way LIME outputs images so that the user can now choose to have multiple image types output for one set of image parameters, which has been incorporated into LIME as of v1.7.2.

In order to implement the optical depth surface method, I add a new image output to LIME that allows the determination of where in a disc model this optical depth surface lies[1]. This is achieved via an addition to the ray tracing routine that records the z position for each propagated ray once the optical depth has surpassed the specified value. The optical depth is calculated via $d\tau = \kappa_\nu \rho_d ds$, where κ is the dust opacity at the specified frequency ($300\,\text{GHz}$), ρ_d is the dust density and ds is the distance between Voronoi cells after each iteration of the ray propagation. As the optical depth can jump significantly beyond the threshold value from one Voronoi cell to the next, I implement linear interpolation. This value is passed into an additional ray *struct* parameter and then averaged over the number of rays that pass through each pixel in the same manner as occurs for the existing flux and optical depth images. The resultant image displays the height beyond the midplane of the desired optical depth surface across the entire disc model.

---

[1]github.com/lolmevans/lime/tree/optical-depth-surface
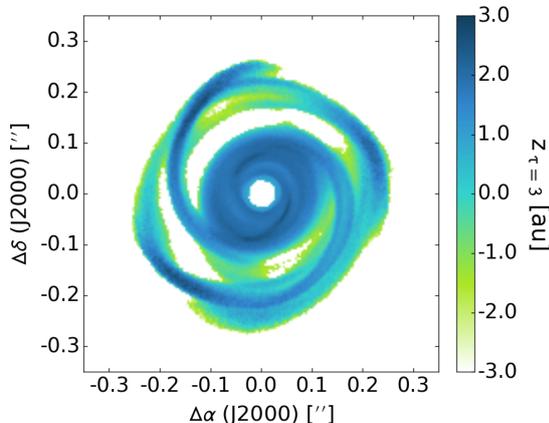
Figure 3.8: Height of the surface across the disc model where $\tau = 3$ when viewed from above at $300\,\mathrm{GHz}$. Below this surface, i.e. at $\tau > 3$, the contribution to intensity becomes insignificant. The surface is located at negative heights in the outer disc and inter-arm regions and at positive heights in the inner disc and spiral arm regions due to the differences in density; in the denser regions the material is more optically thick and hence less distance (originating at $z = \infty$) is required to reach $\tau = 3$ along each line of sight.

Figure 3.8 shows the $\tau = 3$ surface for the disc model when viewed from above. The optical depth surface is positioned at positive heights within the spiral arms due to the large column densities and the hydraulic jump nature of the shocks elongating the vertical distribution of material in the spirals (see e.g. Boley & Durisen, 2006). In the inter-arm regions, the optical depth surface lies below the midplane, i.e. at negative heights when the disc is viewed from above, which means significantly more of the disc material is being peered through.

As the contribution to the emission is negligible at $\tau > 3$, it becomes apparent in Figure 3.8 that, when viewing the disc from above, omission of grid points below $z \approx 3.0\,\mathrm{au}$ in the spirals, below $z \approx 2.0\,\mathrm{au}$ across the inner disc and below $z \approx -1.0\,\mathrm{au}$ in the inter-arm regions is reasonable. Rather than use these approximate values, however, I amend the LIME gridding function to read in the disc optical depth surface and use this as a look-up table for the minimum z position permissible during sampling. Therefore, if a point is selected with a
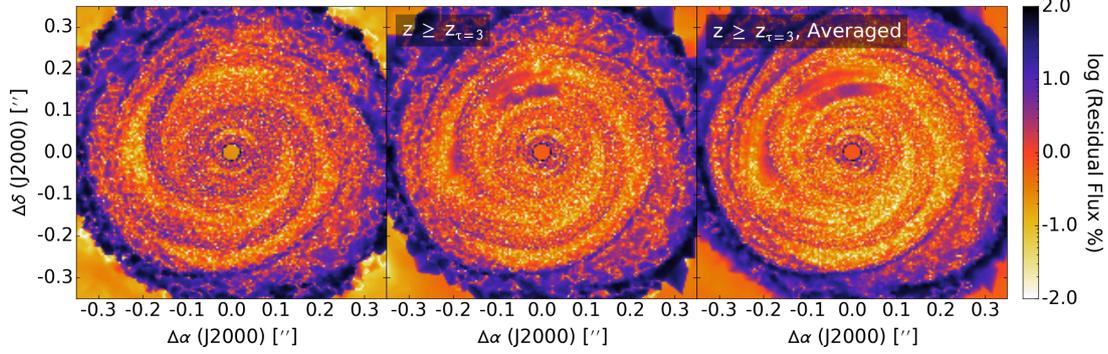
Figure 3.9: Residual between flux for LIME runs using 2×10^5 grid points and different sampling methods, f_1, and flux for 2×10^6 grid points with standard sampling, f_2. This residual is defined as $|(f_1\text{-}f_2)|/(f_1\text{+}f_2)|$, where f denotes flux per pixel. The panel on the left is the residual result for standard sampling seen in Figure 3.6. The middle panel shows the residual result when using an optical depth surface to constrain the positioning of grid points, which is referred to as optimal sampling. The right panel shows the residual result for an average of eight optimally sampled LIME runs using identical input parameters.

z position beyond the optical depth surface it is translated vertically to within the surface; the distance translated is proportional to the original distance from the midplane so that the focus of points is essentially moved from around the midplane to around the optical depth surface only.

This technique is used to reproduce the LIME image consisting of 2×10^5 grid points, calculate the residual from 2×10^6 points, and compare this to the bottom left panel of Figure 3.6. The results are shown in the left and middle panels of Figure 3.9 and as can be seen, limiting the grid points to regions where $\tau < 3$ affords an improvement in the image overall. In fact, when comparing to Figure 3.6 it can be seen that the effect is similar to doubling the number of grid points, but without the large increase in computational time; implementing this method has no significant effect on the runtime but doubling the number of grid points increases the runtime by 400 per cent. It should be noted that in order to implement the optical depth surface routine, LIME needs to be run

initially to generate the optical depth look-up table. Despite this, however, the optical depth surface method is still more efficient than producing a continuum image with double the number of grid points. Therefore, this result is a proof of concept that the omission of optically thick regions, which is referred to as 'optimal sampling' hereafter, can speed up radiative transfer calculations when using LIME.

Although there is a general improvement visible between the left and middle panels of Figure 3.9, there are also some regions where the residual has deteriorated. This is particularly evident in the prominent dark feature above the inner hole. However, the residual difference in this region is approximately 5 per cent, which is within the expected threshold of omitted emission when using the $\tau = 3$ surface to constrain point positions. Furthermore, this residual difference equates to an absolute difference of $2\,\mathrm{K}$ in the brightness temperature and is associated with a weakly emitting region. As a result, this rather visually striking difference is entirely insignificant, but a probable cause is that there is a particularly sharp density gradient that is difficult to sample sufficiently. This then implies that the density weighting employed by LIME is not entirely accurate for the disc model featured in this chapter, and a more precise weighting scheme could instead utilise the density gradient.

The reason this method produces a more accurate image is entirely consistent with the results from Section 3.2.4, where the grid point separation is reduced throughout the entire disc as the total number of grid points is increased. In this section, however, the number of grid points in the emitting regions is increased using selective positioning. Therefore, only the disparity between grid point separation and mean free path within the emitting regions, i.e. at $z \geq z_{\tau=3}$, is reduced.

3.2.6 Averaging runs

Multiple instances of LIME can be run simultaneously, limited only by the number of processor cores and memory available. The averaging of ten runs using identical inputs was performed by Douglas *et al.* (2013) (see their Figure 6), and found to reduce image artifacts and smooth their flux emission successfully. I adopt the same technique but use optimal sampling ($n_0 = 1 \times 10^{12} \, \mathrm{cm}^{-3}$, $w = 0.5$, 2×10^5 points, $z \geq z_{\tau=3}$) and only average eight runs due to computational memory constraints.

The comparison between a single run and the averaging of multiple runs using identical inputs is shown in the middle and right panels of Figure 3.9, and as can be seen, averaging affords an improvement to the output image. Due to the Monte Carlo nature of the LIME gridding, averaging multiple identical runs essentially increases the point coverage. This is practically identical in effect to increasing the number of grid points, which, as shown in Section 3.2.4, improves the image due to the disparity reduction between the grid point separation and mean free path. It is worth noting that the improvements seen between the middle and right panels of Figure 3.9 are small in magnitude and likely much less than observational errors. However, because multiple instances of LIME can be run simultaneously, which affords a significant reduction in computation time compared to increasing the number of grid points, there seems to be no strong argument against using the average of the outputted images for further analysis. Furthermore, although the focus is only on continuum images in this chapter, which have an approximately linear increase in computation time with increased grid points, for line images this relationship is non-linear if the iterative calculations of level populations are required. As a result, the benefit of averaging multiple runs using identical inputs should be emphasised when producing line emission images.

3.3 Synthetic observations

Tobin *et al.* (2016) detected spiral structure in a very young disc that hosts multiple protostars, which appears consistent with a gravitationally unstable disc that recently underwent fragmentation. Moreover, Pérez *et al.* (2016) detected spiral structure in a single-protostar circumstellar disc that appears consistent with GI-driven spiral arms (Meru *et al.*, 2017; Tomida *et al.*, 2017). However, confirmation of gravitational instabilities in these objects is tenuous due to the degenerate nature of spiral structure in protoplanetary discs. Therefore, simulations are crucial for resolving this degeneracy and critically assessing the validity of GIs in young, embedded discs. Moreover, synthesised observations of such simulations are pivotal in order to constrain properties and potential targets for real observations. Hence, here I produce synthetic continuum emission maps of the GI-active disc model used in Section 3.2.

I produce 270 LIME images of the model disc across a 3-dimensional parameter space, using 4×10^5 grid points. The optical depth surface method described in Section 3.2.5 is not implemented here as a $\tau = 3$ surface would need to be produced initially, and then LIME run again whilst implementing this surface. As only ray tracing needs to be performed for continuum emission, and because precomputed dust temperatures are being considered, the increase in image accuracy when adopting the optical depth surface model is offset by the significant increase in computational time from running LIME twice for each combination of dust opacity and frequency. Moreover, by comparing Figures 3.6 and 3.9, it can be seen that a single run of 4×10^5 points is comparable to the optimal averaged image (produced using the average of eight runs implementing the optical depth surface method). Therefore, for this large parameter space study, I opt to use double the number of grid points without implementing the optical depth surface method in the interest of efficiency, whilst still producing accurate images for

analysis. However, it is prudent to emphasise that the purpose of Sections 3.2.5 and 3.2.6 is to demonstrate that the gridding routine *can* be optimised for a particular model, which is more prevalent when producing line images as the computational time may no longer scale linearly with the number of points due to the necessity in calculating level populations. This is investigated in Chapter 4.

The parameter space consists of varying frequencies, inclinations and dust opacities. I use five different frequencies commonly employed in observations of protoplanetary discs, 90 GHz, 230 GHz, 300 GHz, 430 GHz and 850 GHz, equivalent to 3.33 mm, 1.30 mm, 1.00 mm, 0.70 mm and 0.35 mm, respectively, and the inclinations range from face-on (0°) to edge-on (90°) in 5° increments. Three dust grain models are assumed: coagulated grains with thin ice mantles (ThinIceCoag); coagulated grains without thin ice mantles (NoIceCoag); and non-coagulated grains with thin ice mantles (ThinIceNoCoag), all taken from Ossenkopf & Henning (1994). Here, 'coagulated' refers to a coagulation after 10^5 years for a gas density of $10^6 \, \mathrm{cm}^{-3}$ and 'thin' refers to an ice mantle volume that is 0.5 times the volume of the refractory components.

3.3.1 Dust opacities

The values of the dust opacities for the different dust models are shown in Table 3.1 at each frequency, alongside the D'Alessio *et al.* (2001) opacities used in the radiative hydrodynamic simulation. As can be seen, the 'NoIceCoag' dust model is consistent (within a factor of 1.3) of the D'Alessio *et al.* (2001) opacities across the observational frequency range used (90–850 GHz), whereas the 'ThinIceCoag' and 'ThinIceNoCoag' dust models diverge substantially at low frequencies. For this reason synthetic observations produced using 'ThinIceCoag' and 'ThinIceNoCoag' dust opacities are not entirely self-consistent with the disc

	Frequency [GHz]				
	90	230	300	430	850
Dust Grain Configuration	κ_ν [cm^2 g^{-1}]				
ThinIceNoCoag	0.112	0.509	0.782	1.488	5.827
ThinIceCoag	0.200	0.896	1.369	2.593	9.938
NoIceCoag	0.635	1.987	2.744	4.591	11.184
D'Alessio et al. (2001)	0.523	1.557	2.111	3.653	12.082

Table 3.1: Dust opacity values for different dust grain configurations across the frequency range used when deriving disc mass estimates.

simulation. However, these results are intended to serve as an exploration of the effects that dust opacity can have on the observability of spiral structure. In truth, the evolution of a gravitationally unstable disc is affected by the heating and cooling processes (see Kratter & Lodato, 2016), so repeating the radiative hydrodynamic simulation with, for example, the 'NoIceCoag' dust model would most likely change the spiral structure in the disc model. In this case, as Figure 3.10 shows, the 'NoIceCoag' opacities in Table 3.1 are higher than the D'Alessio *et al.* (2001) opacities at micron wavelengths, which would result in an increased cooling time. This suggests that the contrast between arm and inter-arm regions would be less pronounced (Cossins *et al.*, 2009), and hence the detection of spiral structure is expected to become more difficult. However, whilst self-consistently exploring the effects of dust opacity on the observability of spiral structure in a 3D radiative hydrodynamic simulation is an important topic of research, it is an extremely computationally expensive process that requires a detailed and focused study.

Even though the dust models in Table 3.1 do not follow a simple power law $\kappa_\nu \propto \nu^\beta$ across the frequency range used, β values can be extracted at specific frequencies to allow comparisons to values derived in the literature. For instance, $\beta_{230\,\mathrm{GHz}} = 2.02$, $\beta_{230\,\mathrm{GHz}} = 1.64$ and $\beta_{230\,\mathrm{GHz}} = 1.10$ for the 'ThinIceNoCoag',
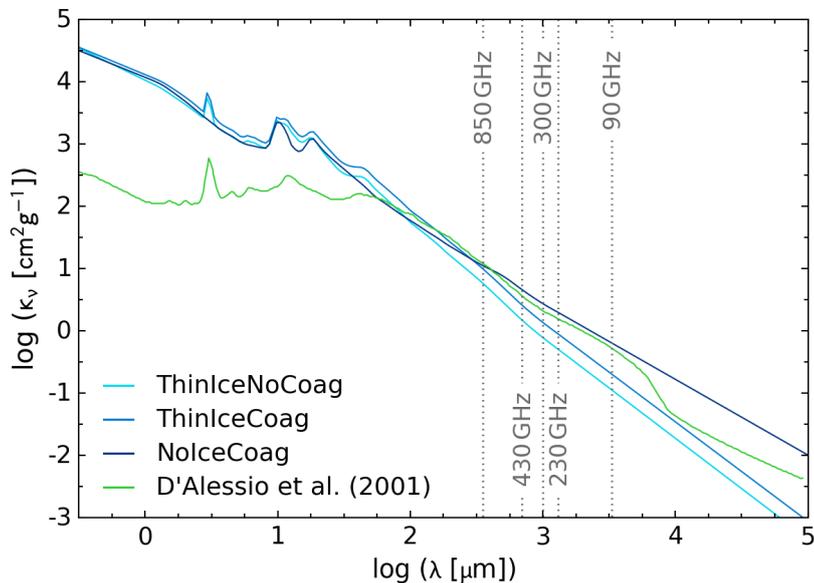
Figure 3.10: Dust opacity as a function of wavelength for the dust models used to produce synthetic observations of the disc model ('ThinIceNoCoag', 'Thinice-Coag', 'NoIceCoag'), and for the dust model used in the radiative hydrodynamic simulation (D'Alessio *et al.*, 2001).

'ThinIceCoag' and 'NoIceCoag' dust models respectively. Miotello *et al.* (2014) find $\beta \approx 0.5$–1.0 in Class I objects, which may suggest a higher level of grain growth than is considered here. However, the relative contribution of envelope and disc to this value is not clear, and the change in the dust grain population between the envelope and disc is not yet well characterised, especially in gravitationally unstable systems.

3.3.2 Detecting spiral structure

In order to investigate whether spiral structure can be distinguished across the parameter space, I synthesise observations of the LIME images using the Common Astronomy Software Applications package (CASA v4.5.0; McMullin *et al.*, 2007). The disc model is assumed to be located at a distance of 145 pc in order to examine the observability of self-gravitating discs in some of the nearest star

Table 3.2: Antenna configurations for Cycle 5 ALMA (C43-*) and a maximally extended, fully operational ALMA (out28) that are used to produce realistic synthetic observations. The Cycle 5 configurations use 43 antennas and the maximally extended, fully operational configuration uses 50 antennas.

Frequency [GHz]	Antenna Config.	Max. Baseline [km]	Angular Resolution [arcsec]	Sensitivity [µJy]	PWV [mm]
90	C43-10	16.2	0.042	11.1	5.186
	out28	16.2	0.042	9.6	
230	C43-10	16.2	0.018	15.6	1.796
	out28	16.2	0.018	13.4	
300	C43-8	8.5	0.028	24.9	1.796
	out28	16.2	0.015	21.4	
430	C43-7	3.6	0.046	92.3	0.913
	out28	16.2	0.011	79.3	
850	C43-7	3.6	0.024	581.3	0.658
	out28	16.2	0.005	499.1	

forming regions (e.g. ρ Ophiuchi). The inclination of the disc is varied from $0°$ to $90°$ to cover the range of orientations seen in observations of real systems such as IRAS 16243-2422, which is a protostellar binary with two sources, A and B separated by approximately 600 au, with near face-on and edge-on disc inclinations, respectively. I use two different antenna setups in order to simulate the capabilities of ALMA Cycle 5 and a fully extended, maximally operational ALMA. The configurations and observational properties of each antenna setup are shown in Table 3.2. An on-source observation time of 60 minutes is adopted using the `simobserve` routine in CASA, considering thermal noise with an ambient temperature of 270 K and a precipitable water vapour (PWV) given when selecting the 'automatic' option in the ALMA Sensitivity Calculator[1], which uses the specified frequency to calculate appropriate values. This observation time is

---

[1]https://almascience.nrao.edu/proposing/observing-tool
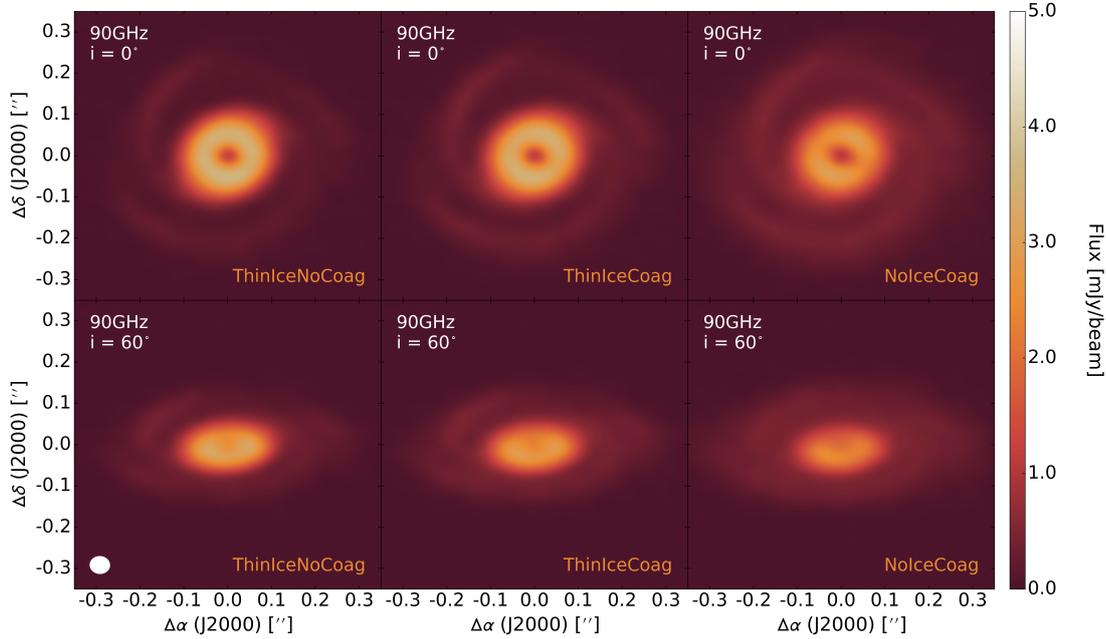
Figure 3.11: Continuum emission images of the disc model at $90\,\mathrm{GHz}$ for three different dust configurations and two different inclinations, synthesised using the ALMA Cycle 5 antenna configuration. The white ellipse in the lower left indicates the size of the beam, which is $0.046 \times 0.044\,\mathrm{arcsec}^2$ and is constant across all panels. The noise is approximately $11\,\mathrm{\mu Jy\,beam}^{-1}$ across the parameter space.

expected to be sufficient for detecting the dust continuum emission in the spiral features across the majority of the parameter space. Finally, the multiscale `clean` algorithm is used for deconvolution of the synthetic visibility data, in order to effectively recover the extended disc and spiral arm structure.

Here, the results when observing the disc model with an ALMA Cycle 5 antenna configuration, as seen in Figures 3.11–3.15, and when observing the disc model with a fully extended, maximally operational antenna configuration, as seen in Figures 3.16–3.18, are presented. Note that if the size of the observed source is large compared to the shortest baseline used, then the source can be partially resolved out, resulting in a loss of recovered flux. For the disc model and ALMA antenna configurations used in this chapter, this loss in flux is only
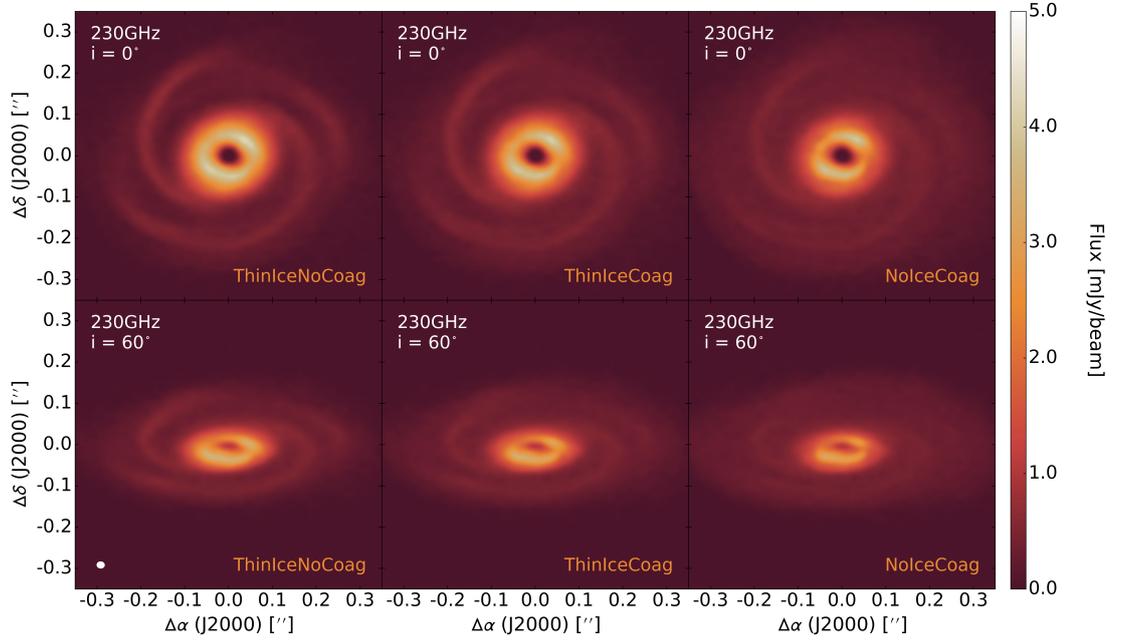
Figure 3.12: Same as Figure 3.11 but synthesised at $230\,\mathrm{GHz}$ with a beamsize of $0.019 \times 0.017\,\mathrm{arcsec}^2$ and a noise level of approximately $15\,\mathrm{\mu Jy\,beam^{-1}}$.
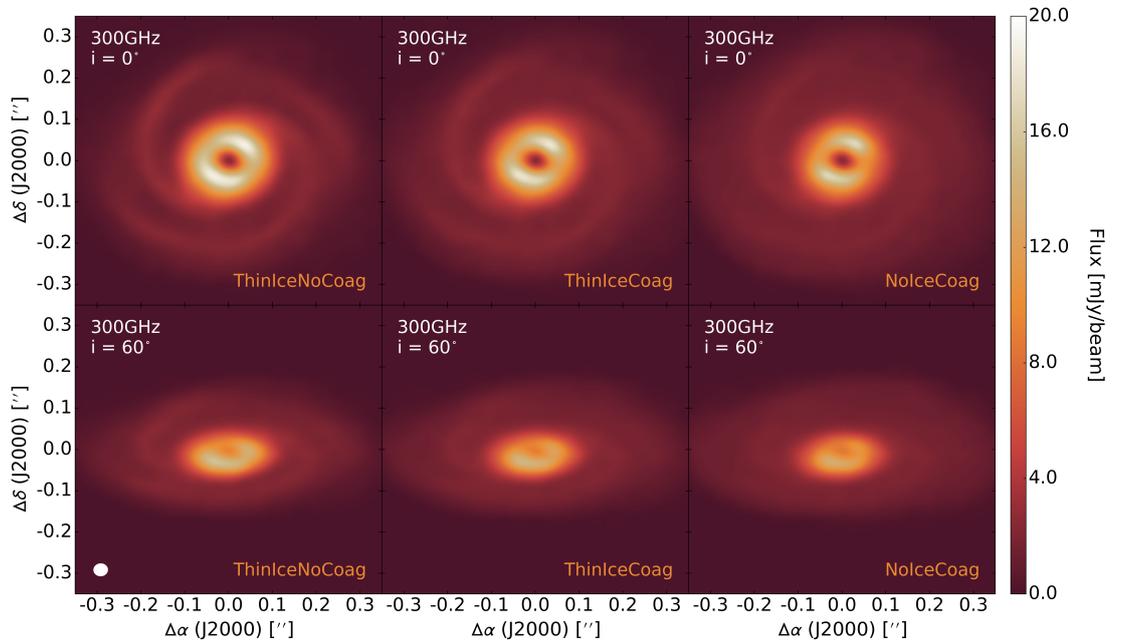
Figure 3.13: Same as Figure 3.11 but synthesised at $300\,\mathrm{GHz}$ with a beamsize of $0.033 \times 0.031\,\mathrm{arcsec}^2$ and a noise level of approximately $26\,\mathrm{\mu Jy\,beam^{-1}}$.

113
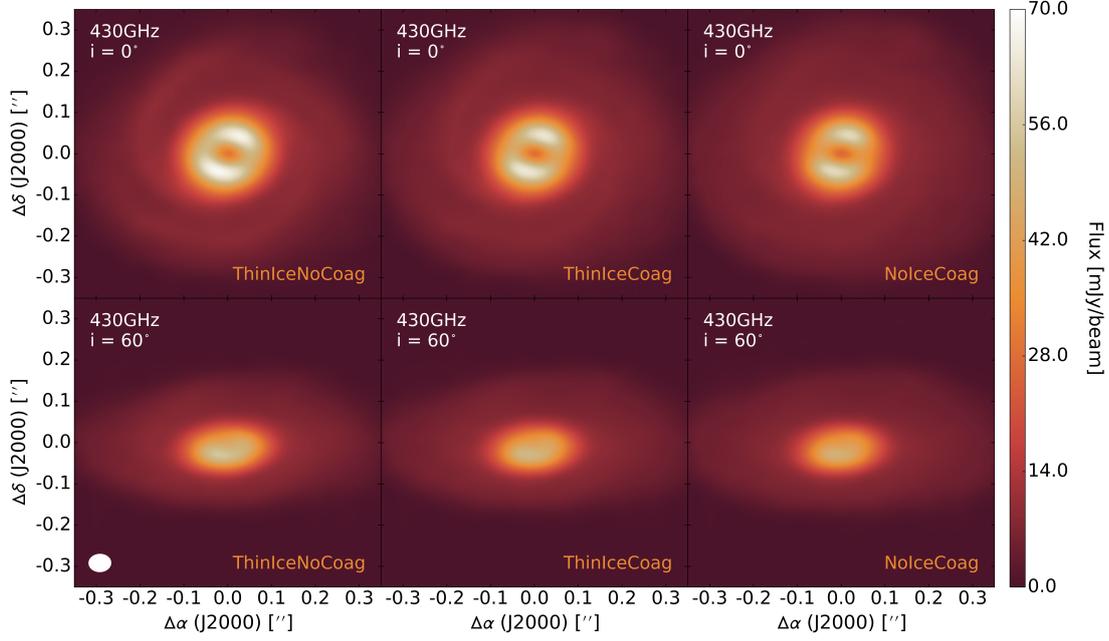
Figure 3.14: Same as Figure 3.11 but synthesised at $430\,\mathrm{GHz}$ with a beamsize of $0.052 \times 0.045\,\mathrm{arcsec}^2$ and a noise level of approximately $115\,\mathrm{\mu Jy\,beam}^{-1}$.
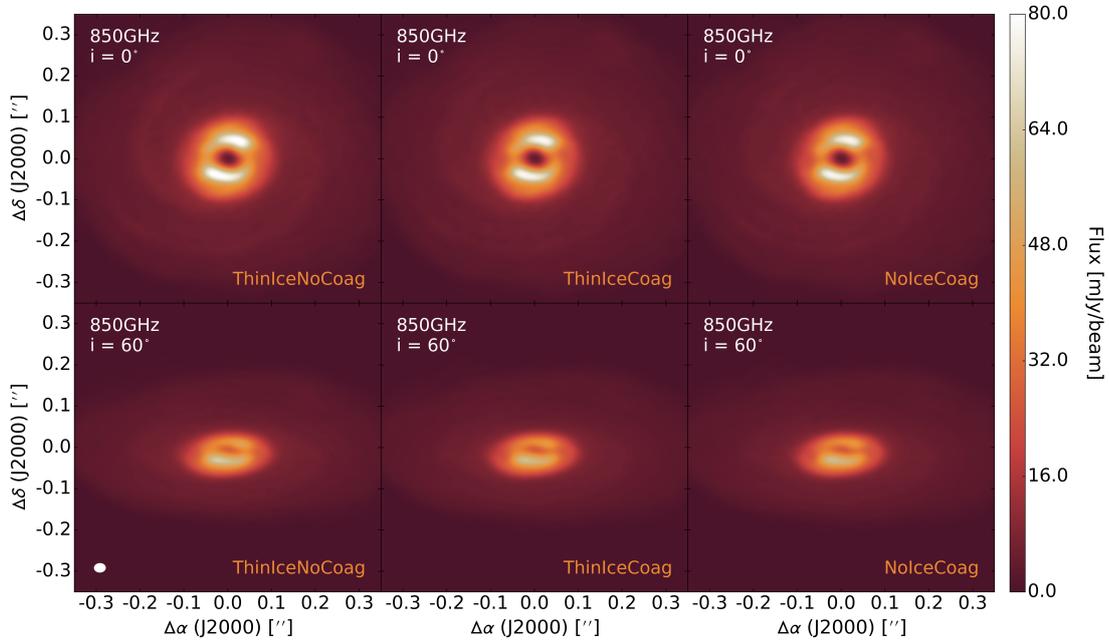
Figure 3.15: Same as Figure 3.11 but synthesised at $850\,\mathrm{GHz}$ with a beamsize of $0.027 \times 0.023\,\mathrm{arcsec}^2$ and a noise level of approximately $110\,\mathrm{\mu Jy\,beam}^{-1}$.
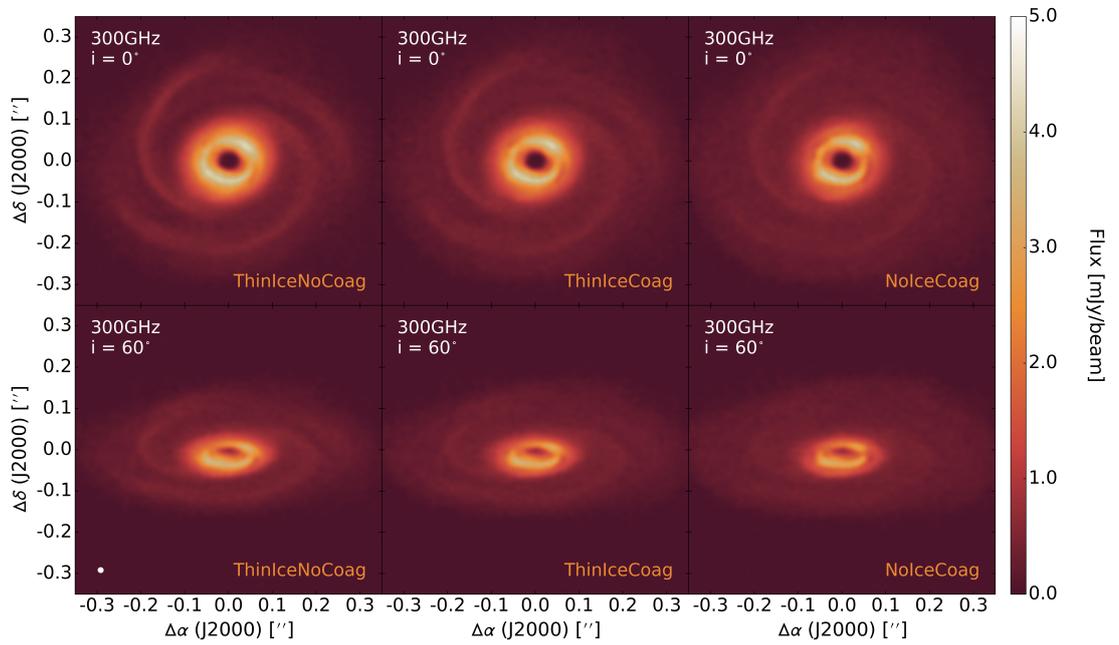
Figure 3.16: Continuum emission images of the disc model at 300 GHz for three different dust configurations and two different inclinations, synthesised using a fully extended, maximally operational ALMA antenna configuration. The white ellipse in the lower left indicates the size of the beam, which is $0.014 \times 0.014 \, \mathrm{arcsec}^2$ and is constant across all panels. The noise is approximately $20 \, \mu\mathrm{Jy \, beam}^{-1}$ across the parameter space.
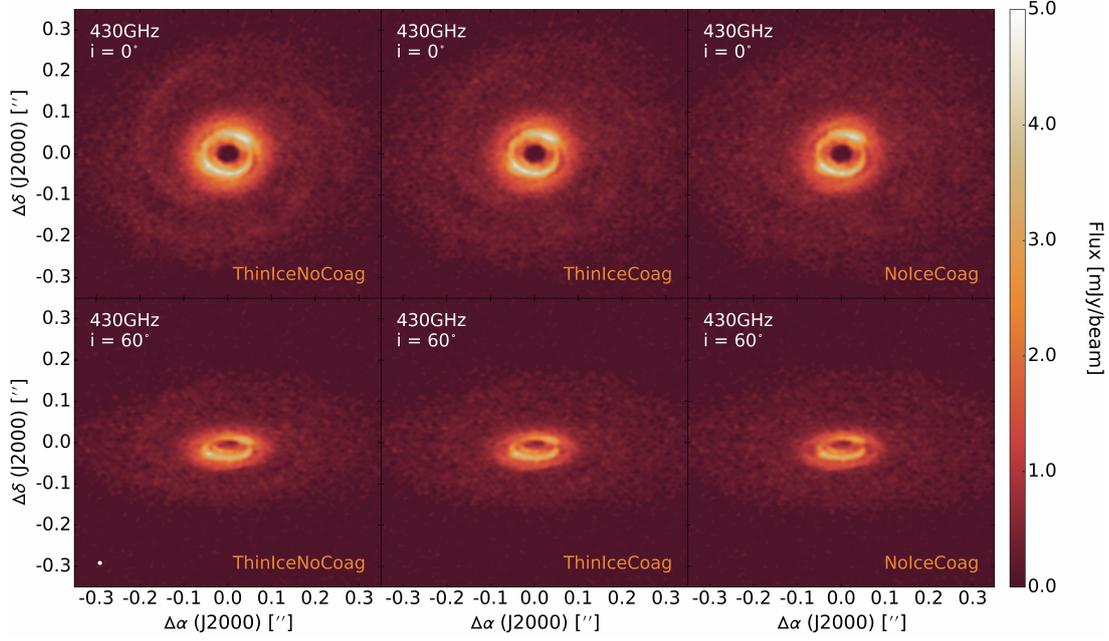
Figure 3.17: Same as Figure 3.16 but synthesised at $430\,\mathrm{GHz}$ with a beamsize of $0.010 \times 0.010\,\mathrm{arcsec}^2$ and a noise level of approximately $85\,\mathrm{\mu Jy\,beam}^{-1}$.
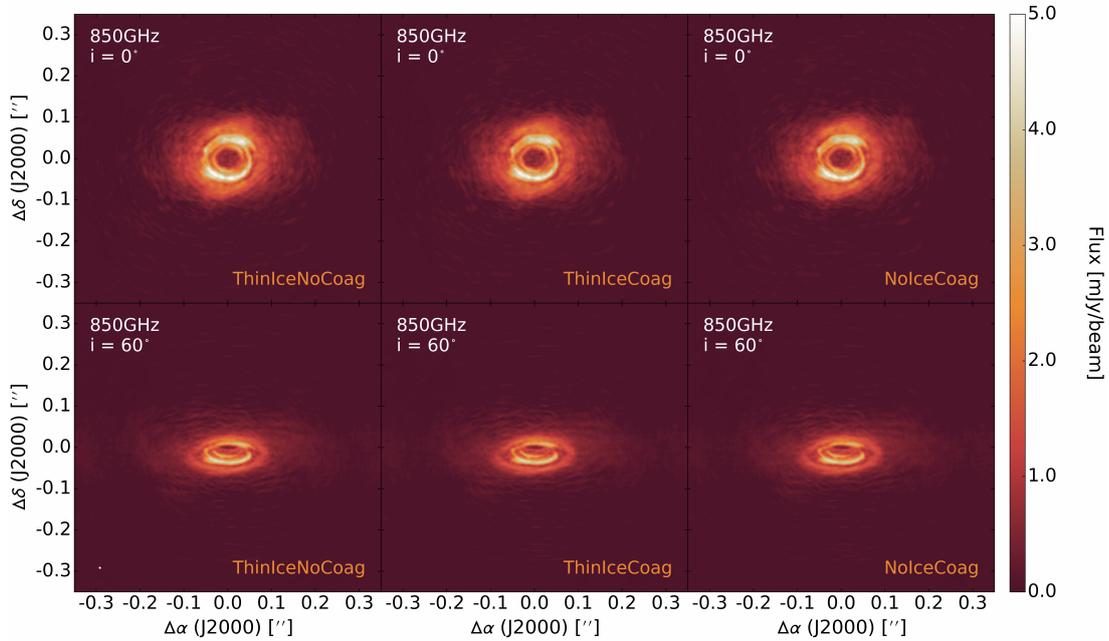
Figure 3.18: Same as Figure 3.16 but synthesised at $850\,\mathrm{GHz}$ with a beamsize of $0.005 \times 0.005\,\mathrm{arcsec}^2$ and a noise level of approximately $25\,\mathrm{\mu Jy\,beam}^{-1}$.

a few per cent across most of the parameter space used. However, at 850 GHz the difference in flux recovered from the LIME images and corresponding synthetic images reaches a maximum of 30 per cent when using a fully extended, maximally operational antenna configuration and a face-on disc inclination. This implies, then, that the issue of resolving out a source can become a prominent concern at high frequencies, particularly as the resultant loss in flux will lead to inherently underestimated disc masses (see also Dunham *et al.*, 2014). The severity of this issue can be reduced by using the Atacama Compact Array (ACA) in conjunction with ALMA in order to sample larger angular scales and recover more accurate flux values. However, this would significantly increase the overheads and therefore the on-source observing times required.

When a fully operational ALMA configuration is used, the spiral structure is very prominent at 300 GHz, with a signal-to-noise ratio (SNR) > 30, due to the beamsize reduction at higher frequencies. Unfortunately, the sensitivity is inversely proportional to the frequency, and so at 430 GHz the spirals are not as easily identified because noise becomes significant. In fact, because of this, the spirals are only distinguishable at 430 GHz when a very low dust opacity is assumed, and at 850 GHz the spirals are completely dominated by the noise. Note that observations at 90 GHz and 230 GHz are not shown because they are virtually identical to those performed using the ALMA Cycle 5 antenna configuration due to the fact that the maximum baseline is already at the fully operational limit for Band 3 and 6; the only difference is the number of antennas (43 for Cycle 5, 50 for fully operational ALMA).

When using Cycle 5 antenna configurations, the spiral structure is distinguishable in a face-on disc across all frequencies and dust opacities. At an inclination of 60° the spirals are only identifiable at 300 GHz or lower, and only convincingly when a lower dust opacity is assumed. The most detail is recovered at 230 GHz

because there is an optimal combination of angular resolution and sensitivity affording a SNR $\approx$ 30 within the resolved spirals; the noise level is calculated by taking the root mean square of regions within the residual maps free from disc emission or sidelobes.

By comparing the individual panels in Figures 3.11–3.18, it becomes apparent that the spiral structure is sensitive to the assumed dust opacities because the contrast between the arm and inter-arm regions is different between the panels. This is important because the state of grain growth is relatively unknown at such early stages of disc evolution. However, as the spiral structure is clearly visible within all panels of Figure 3.12, relatively short observations should be capable of detecting spiral structure in young, gravitationally unstable discs across a wide range of inclinations and possible dust grain opacities.

These synthetic observations are encouraging for future continuum observations as they show that ALMA can detect non-axisymmetric structure in young, embedded systems. As aforementioned, this has already been proven with recent observations. However, further conclusions can be drawn from these synthetic results in particular. Firstly, unlike real observations to date, the spiral features are known unequivocally to be driven by the GI in the disc model used here; hence these results have demonstrated that ALMA can successfully resolve GI-driven spirals. Secondly, an on-source observation time of only 60 minutes is sufficient to resolve the spiral structure at low frequencies across most of the parameter space considered in this chapter. If a longer observational time is adopted, then the spiral features would also become more prominent at higher frequencies, allowing the detection of spirals in a young, gravitationally unstable disc across multiple ALMA bands. This would permit determinations of the spectral index and give insight into the grain size distribution (e.g. Pérez *et al.*, 2012), shedding light on processes such as grain growth and dust trapping (e.g Dipierro *et al.*, 2015)

in embedded systems. Finally, the disc model I use represents a protosolar-like disc, which means ALMA should be able to resolve spiral features in a relatively low-mass disc that is possibly analogous to the disc in our early Solar System.

Comparison with other studies

The synthetic observations of the disc model I have investigated show that ALMA can detect non-axisymmetric structure in young, embedded systems across a range of frequencies, inclinations and dust opacities.

A first attempt at assessing the detectability of a spiral structure in the disc, based on the expected properties of the gravitational instability, has been made by Cossins et al. (2010), who found that spiral structures in compact self-gravitating discs are visible with ALMA over a wide range of wavelengths. This agrees with Dipierro *et al.* (2014) who extend the work of Cossins *et al.* (2010) and use a 3D smoothed-particle hydrodynamics (SPH) code (Lodato & Rice, 2004). The authors find that, like Cossins *et al.* (2010), for a gravitationally unstable disc located in the TaurusAuriga and Ophiucus star-forming regions (≈ 140 pc), the spiral structure is readily detectable with ALMA across a range of frequencies, inclinations and disc-to-star mass ratios. However, it should be noted that their model uses a cooling prescription that does not take into account the irradiation emitted by the central star, which implies that the amplitudes of their spiral perturbations are overestimated. Dipierro *et al.* (2014) do assume more grain growth has occurred than considered in this work, though, which may counter-act the effect of lower spiral wave amplitude as larger dust opacities reduce the detectability of spiral structure, as is demonstrated by the flux images presented in Section 3.3.2.

Dong *et al.* (2015) use a 3D SPH simulation augmented by a hybrid radiative transfer in order to model both global cooling and radiative transfer (Forgan

et al., 2009), which is comparable to the technique implemented here. They find that spiral arms should be detectable in near-infrared scattered light observations of systems with disc-to-star mass ratios of $q \geq 0.25$ (the disc model I use has $q = 0.21$), and also find that their high q models closely resemble real objects, though the validity of GIs operating in these objects is not clear. The comparison with Dong *et al.* (2015) is not like-for-like, as near-infrared scattered light observations only trace the surface layers of discs. However, Dipierro *et al.* (2015) have shown that the GI can create strong enough surface density perturbations that could be detected in near-infrared scattered light, so this agreement with Dong *et al.* (2015) is noteworthy.

The results of the aforementioned studies, and the results presented in this chapter, disagree somewhat with the results of Hall *et al.* (2016), who use a 1D analytical model (Clarke, 2009) extended to 2D and 3D, and find that spiral structure is only detectable across a narrow parameter space; specifically only at 680 GHz when adopting a distance of 140 pc. This may be because Hall *et al.* (2016) neglect hydrodynamic heating in their radiative transfer, so the spirals are 'cold' and only illuminated by the central star. Moreover, Hall *et al.* (2016) use a viscosity prescription that assumes local angular momentum transport, which means the spiral amplitudes are much smaller than in reality. As the results in this chapter are produced from a simulation with non-local angular momentum transport, and by radiative transfer calculations that accurately account for the shock-heating, I therefore argue that GI-induced structure should be easier to detect than Hall *et al.* (2016) conclude.

The aforementioned studies in the literature roughly follow the nomenclature that $m \approx 1/q$ (see Cossins *et al.*, 2009, Figure 8), where m is the number of spiral arms. Moreover, Dong *et al.* (2015) conclude that m will be a good diagnostic of the total disc mass. However, the disc model I use does not adhere to

this approximation as $m = 2$ whilst $q \approx 0.2$, but it is important to emphasise that the disc model used in this work is entirely consistent with the long-term behaviour of self-regulated, unstable, radiative discs, particularly considering the highly non-linear behaviour of the system (see the mode analyses in Mejía *et al.* (2005) and Boley & Durisen (2006), for example, or discussions in Durisen *et al.* (2007)). Therefore, whilst $m \approx 1/q$ can be a useful diagnostic, it is not part of a fundamental criterion for gravitationally unstable discs.

Comparison with RADMC-3D

In this chapter I have used LIME to produce continuum emission maps that have then been observed synthetically. However, there are numerous radiative transfer codes and it is imperative to compare results between them using consistent models in order to understand the strengths and limitations of each. One such alternative to LIME is RADMC-3D, which is a Monte Carlo radiative transfer code used to produce dust continuum emission images and gas line emission images in LTE regions (RADMC-3D can also model non-LTE line emission, but currently, only if local modes are adopted). The disc model is input into RADMC-3D using the pre-computed hydrodynamic dust temperatures and the 'ThinIceCoag' dust opacities, and a continuum flux image at $300\,\text{GHz}$ is produced to compare to the LIME optimal averaged image (produced using the average of eight runs using n_0 = $1 \times 10^{12}\,\text{cm}^{-3}$, $w = 0.5$, 2×10^5 points, $z \geq z_{\tau=3}$).

Figure 3.19 shows the residual flux between the optimal LIME image and the RADMC-3D image, and indicates that the two codes produce compatible images as there is a residual difference of < 10 per cent within the spiral arms. However there are large discrepancies, up to $\approx$,60 per cent, in the inter-arm and innermost disc regions that are most likely due to the difference in gridding employed by LIME and RADMC-3D. In RADMC-3D, the radiative transfer grid is the entire

3. CONTINUUM EMISSION AND MASS ESTIMATES
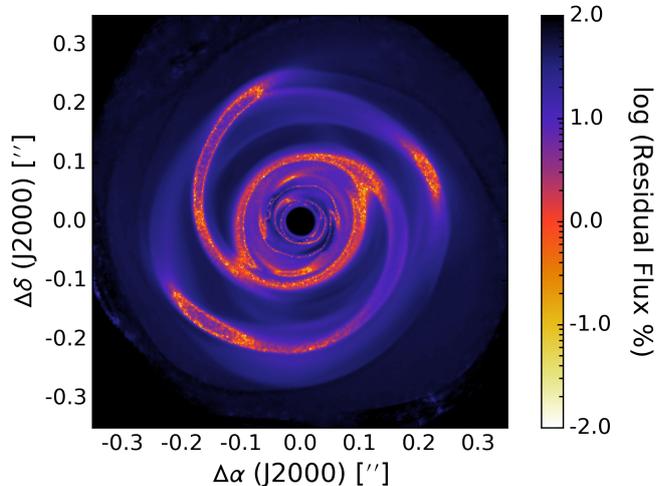
Figure 3.19: Residual flux between LIME runs using 2×10^6 grid points, f_L, and RADMC-3D, f_R, using the full hydrodynamic grid. This residual is defined as $(f_L\text{-}f_R)/(f_L\text{+}f_R)$, where f denotes flux per pixel.

hydrodynamic model grid, whereas in LIME the points are subsampled from this grid and density weighted. Therefore, in less dense regions, and hence optically thinner regions, the grid point spacing in RADMC-3D is much finer than in the LIME runs. For instance, in the inter-arm regions near the disc midplane, $l >$ 1.0 au, whereas the RADMC-3D grid resolution is 0.25 au; it is important to understand that the mean free path is a statistical average and hence a smaller grid point separation is always preferable if it is achievable. Conversely, in the innermost disc region, where the optical depth is considerably higher, the grid spacing in LIME becomes finer than that in RADMC-3D. This may explain why both the inter-arm and innermost disc flux is lower in the RADMC-3D continuum emission map, but for opposite reasons.

In order to determine if this discrepancy in inter-arm and innermost disc flux leads to observational differences, I produce synthetic observations of the LIME and RADMC-3D continuum emission maps, using a face-on inclination and the same observational setup as mentioned earlier. The results for ALMA Cycle 5 and
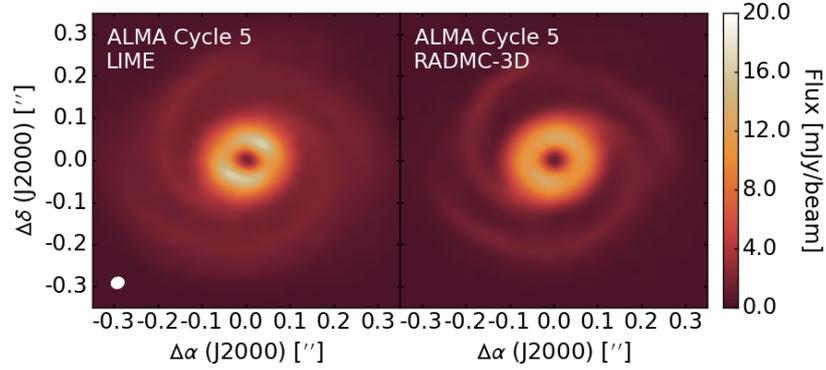
Figure 3.20: Continuum emission images of LIME (left) and RADMC-3D (right) radiative transfer calculations of the disc model at $300\,\mathrm{GHz}$ with 'ThinIceCoag' dust opacities, synthesised using the ALMA Cycle 5 antenna configuration. The white ellipse in the lower left indicates the size of the beam, which is $0.029 \times 0.031\,\mathrm{arcsec}^2$ and is constant across all panels. The noise is approximately $30\,\mathrm{\mu Jy\,beam}^{-1}$ across the parameter space.
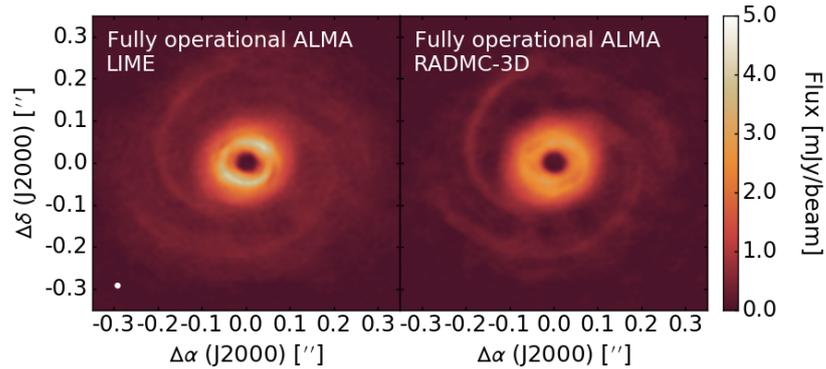
Figure 3.21: Same as Figure 3.20 but synthesised using the fully operational, maximally extended ALMA antenna configuration, with a beamsize of $0.016 \times 0.015\,\mathrm{arcsec}^2$ and a noise level of approximately $25\,\mathrm{\mu Jy\,beam}^{-1}$.

3. CONTINUUM EMISSION AND MASS ESTIMATES

a fully extended, maximally operational ALMA are shown in Figures 3.20 and 3.21 respectively, and demonstrate that, whilst the spiral fluxes are consistent between the two radiative transfer codes as expected, the innermost disc flux is lower in the RADMC-3D observations. More significantly, however, the contrast between arm and inter-arm regions is enhanced in the RADMC-3D observations, which results in a more easily detected spiral structure. As this is most likely a result of finer gridding in RADMC-3D, the conclusion is that one should perhaps use RADMC-3D to produce continuum emission maps when a high resolution model is available.

Whilst RADMC-3D likely produces more accurate continuum emission maps than LIME for the disc model I use, at least in the inter-arm regions, I have opted to show results for LIME throughout this chapter for a number of reasons. Firstly, the continuum emission maps I have produced only utilise ray tracing because the dust temperatures are known *a priori* from the radiative hydrodynamic model. As a result, the computational cost of using a high resolution, regularly spaced grid is low. However, if one were to compute the dust temperatures with a Monte Carlo radiative transfer code, then the computational time would increase significantly as enough photon packages need to be propagated to ensure a sufficient number enter each cell, which becomes especially problematic in the optically thick regions. In this case, using the optimal LIME grid may be more computationally efficient than using the high resolution, regularly spaced RADMC-3D grid. Secondly, LIME is one of the best available tools for producing line emission maps because LIME can calculate level populations self-consistently, without the assumption of LTE or optically thin line emission, or the use of LVG that RADMC-3D currently relies upon. Note, however, that whether these assumptions would result in large errors in emission maps is not clear. Nevertheless, when producing non-LTE line emission maps, the computational time no longer scales linearly

with the number of grid points as the level populations for each grid point must be calculated in an iterative sense until convergence is reached. Consequently, it becomes much more important in terms of efficiency to optimise the grid sampling. This can be achieved by, for example, restricting the grid points in relation to the continuum optical depth surface ($z \geq z_{\tau=3}$; see Section 3.2.5), which is explored in Chapter 4.

3.3.3 Observational mass estimates

Disc masses are typically estimated from continuum flux detections using

$$M_{\mathrm{disc}} = \frac{g S_\nu d^2}{\kappa_\nu B_\nu(T)}, \qquad (3.3)$$

where g is the gas-dust mass ratio, usually assumed to be the ISM value of 100, S_ν is the flux density, d is the distance to the source, κ_ν is an assumed dust opacity and $B_\nu(T_\nu)$ is the Planck function for an assumed dust temperature (Hildebrand, 1983). This method is based on the assumption that the temperature is uniform and the emission is optically thin. However, young, embedded systems are expected to be optically thick at the wavelengths typically used; for this reason results in the literature usually quote disc masses as lower limits.

Figure 3.22 shows the optical depth along the line-of-sight through the disc model I use when observed at the two extreme frequencies. Within this regime of the electromagnetic spectrum the dust opacity increases with frequency, as can be seen in Table 3.1 and Figure 3.10; hence the lowest optical depths are recovered at the lowest frequencies. Figure 3.22 clearly demonstrates that the disc spiral features are optically thick across the majority of the parameter space adopted in this chapter. To clarify, using the lowest dust opacity configuration (ThinIceNoCoag) at 90 GHz affords an average optical depth of approximately τ = 1 in the face-on spirals, but this increases with inclination, observing frequency
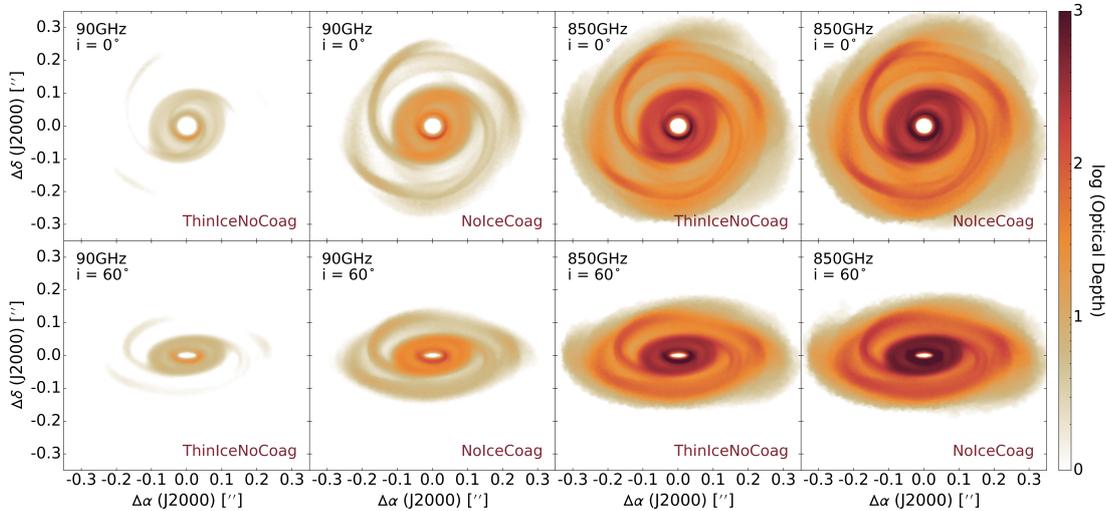
Figure 3.22: Optical depth along the line-of-sight of the disc model for two different frequencies, inclinations and dust opacity models.

and dust opacity. Note that the opacity of the inner disc, which is where most of the disc mass resides, is even higher than in the spirals. Therefore, young, gravitationally unstable discs are likely to be partially optically thick at millimetre wavelengths and substantially optically thick at submillimetre wavelengths, which could result in significantly underestimated disc masses. As the exact mass of the disc model is known I can explore how inaccurate such disc mass estimates can be.

I assume two different dust temperatures, $T_{\text{dust}} = 20\,\text{K}$ and $40\,\text{K}$, when calculating the disc mass. The former is chosen to mimic the calculations performed for observations of more evolved systems (e.g Ansdell *et al.*, 2016), based on the median temperature of Class II discs in Taurus-Auriga (Andrews & Williams, 2005). However, as the GI can lead to significant heating of young discs (see Chapter 2), I also adopt a higher dust temperature, $T_{\text{dust}} = 40\,\text{K}$. Incidentally, this is the dust temperature Tobin *et al.* (2016) use when deriving the mass of the recently formed fragment in L1448 IRS3B, as they argue the region around the fragment should be warmed by turbulence. Moreover, this is the peak brightness
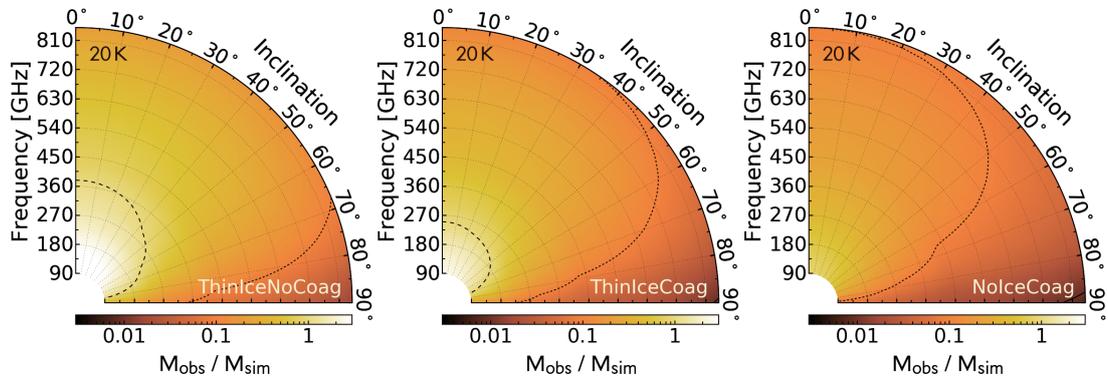
Figure 3.23: Fraction of actual disc mass derived from observations at various inclinations and frequencies, for three different dust grain models (see Table 3.1) and a constant dust temperature of 20 K. The contours denote fractions of 0.01 (solid line), 0.1 and 1.0 (longest-dashes line). Note that the face-on disc is inclined at 0°.
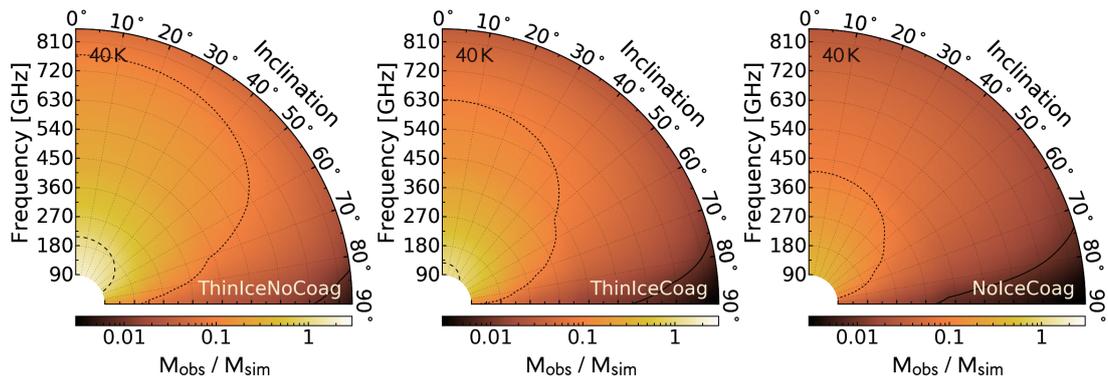
Figure 3.24: Same as Figure 3.23 but for a constant dust temperature of 40 K.

temperature, T_B, towards this fragment, and in optically thick regions $T_B \approx T_{\mathrm{dust}}$.

The flux density from the Cycle 5 ALMA synthetic observations (Figures 3.11–3.15) is estimated at each inclination and frequency. I then calculate disc masses for the observations produced when both the Cycle 5 antenna configuration and the fully extended, maximally operational antenna configuration are used. However, as the differences between the masses derived from the two antenna setups are minimal, the full ALMA results are omitted.

Figures 3.23 and 3.24 show how the ratio of the observationally derived mass,

127

M_{obs}, to the actual mass of the simulated disc model, M_{sim}, varies as a function of frequency, inclination, dust opacity and dust temperature. As the blackbody flux, B_ν, increases with temperature, a lower disc mass is recovered at a higher dust temperature. A lower disc mass is also recovered if use is made of a dust grain model that results in larger optical depths (see Table 3.1), because emission is observed from a smaller fraction of the disc. Similarly, observations at higher frequencies cannot peer as far through the disc, as can be seen in Figure 3.22, so a lower disc mass is also recovered. Finally, as the inclination of the disc increases, the recovered mass decreases because the morphology of the disc loses distinction and the line-of-sight column density increases. As a result, the recovered flux density, S_ν, decreases, particularly as the orientation approaches edge-on.

In summary, the derived disc mass is sensitive to the disc properties as well as the observational setup. However, some combinations of parameters are probably unrealistic for young, gravitationally unstable discs. For instance, when low opacity dust models (i.e. no coagulation has been assumed) are used, along with a low dust temperature, e.g. $T_{\mathrm{dust}} = 20\,\mathrm{K}$, the disc mass derived at low frequencies can be significantly larger than the actual mass. Indeed, observing the disc model close to face-on at $90\,\mathrm{GHz}$ results in an observed mass, $M_{\mathrm{obs}} = 4M_{\mathrm{sim}}$ when adopting these parameter values. These overestimates occur for two primary reasons. Firstly, using an underestimated dust temperature results in a lower Planck flux when far from the Rayleigh-Jeans limit, which increases the disc mass. As mentioned earlier, $T_{\mathrm{dust}} = 20\,\mathrm{K}$ is the median temperature of Class II discs and therefore, due to the shock-heating of GIs, is likely an underestimate for young, gravitationally unstable discs. Secondly, this dust model (ThinIceNo-Coag) differs from the underlying dust distribution in the hydrodynamic model across the observational frequency range implemented (see Figure 3.10); the latter assumes dust grains with sizes up to $1\,\mathrm{mm}$ are present. As observations indicate

that larger grains are already present in the envelopes of Class I objects (e.g. Miotello *et al.*, 2014), which are most likely explained by grain growth within the inner regions (Wong *et al.*, 2016), low dust opacities are likely inaccurate in young, gravitationally unstable discs. Note that whilst the assumption of grain growth perhaps contradicts the assumption of well mixed dust and gas, here it is supposed that there has not been sufficient time for the dust and gas to become decoupled because the disc model is very turbulent.

Now, as a higher dust opacity and dust temperature are most appropriate for the disc model, and the 'NoIceCoag' dust grain configuration is self-consistent with the disc simulation, I focus on the right panel of Figure 3.24. The maximum disc masses are recovered when considering a face-on disc, which results in: $M_\mathrm{obs} = 0.41 M_\mathrm{sim}$ at $90\,\mathrm{GHz}$; $M_\mathrm{obs} = 0.21 M_\mathrm{sim}$ at $230\,\mathrm{GHz}$; $M_\mathrm{obs} = 0.15 M_\mathrm{sim}$ at $300\,\mathrm{GHz}$; $M_\mathrm{obs} = 0.09 M_\mathrm{sim}$ at $430\,\mathrm{GHz}$; and $M_\mathrm{obs} = 0.03 M_\mathrm{sim}$ at $850\,\mathrm{GHz}$. Therefore, the derivations of disc masses from lower frequency data is preferable. However, as angular resolution is inversely proportional to frequency, currently the inference of accurate masses and spatially resolving spiral structure are likely mutually exclusive objectives. Overall, when what are understood to be realistic parameters are used, protoplanetary disc masses derived from continuum observations in the millimetre regime could underestimate the actual mass in a face-on disc by a factor of 2.5–30, depending on observing frequency, and this underestimate worsens as the disc inclination increases.

Comparison with other studies

The underestimated disc mass results presented in this chapter are consistent with the predictions of Forgan & Rice (2013), who use self-gravitating model discs to match observations of the Class 0 protostar L1527 IRS, and the continuum results of Douglas *et al.* (2013), who simulate a GI-driven disc with a

disc-to-star mass ratio nearly double that in the disc model I use. This result also appears consistent with the results of Dunham *et al.* (2014), who report a mass underestimate in a gravitationally unstable disc similar to the model I use, of a factor of 2–3 at millimetre wavelengths and a factor of 10 or more at sub-millimetre wavelengths. Dunham *et al.* (2014) calculate disc masses assuming a source distance of 250 pc, and so, as I adopt a source distance of 145 pc, less extreme underestimates are perhaps expected in Section 3.3.3 based on their results. However, this is not the case. A possible explanation is that the radiative transfer calculations performed by Dunham *et al.* (2014) are 2-dimensional and do not include the full, non-axisymmetric structure of the disc. As a result, spiral features, which are extremely optically thick at most wavelengths in the disc model I use (see Figure 3.22), are not represented accurately. Therefore, the underestimation of disc masses derived from observations of young, embedded discs may be even more pronounced than they predict. If this is the case then there are likely to be important consequences for the derived properties and classifications of young systems. In particular, discs that have been observed and determined not to contain enough mass to be gravitationally unstable could actually contain GI-driven features.

Accurate dust temperatures

It is important to acknowledge that the assumed dust temperature in Equation 3.3 is an estimated average of the optically thin emission temperature, which is typically not well constrained in young, embedded systems. Therefore, it is extremely worthwhile to assess the validity of the dust temperatures used in deriving the mass of the disc model thus far, and compare with typical assumptions made when deriving masses from observations.

The actual dust temperature of the optically thin emission varies as a function
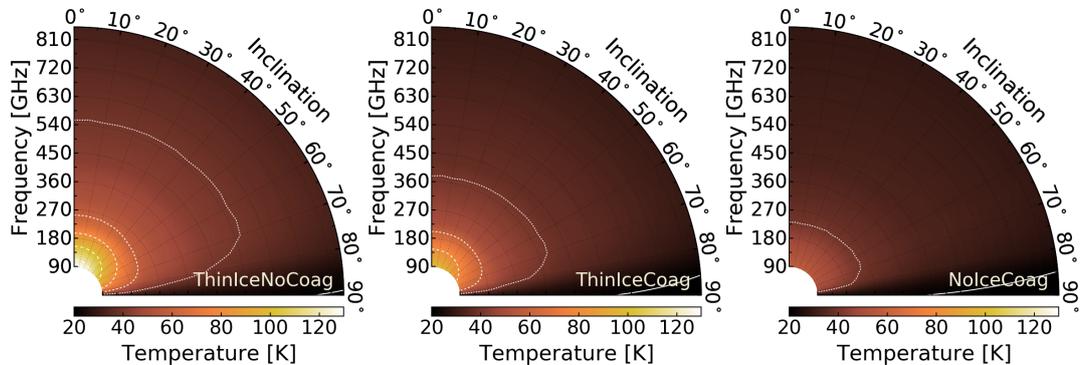
Figure 3.25: Mass-weighted average temperature of the optically thin emission at various inclinations and frequencies, for three different dust grain properties (see Table 3.1). The contours denote temperatures from 20 K (solid line) to 120 K (longest-dashes line) in 20 K increments.

of the optical depth. Hence, the appropriate average dust temperature to assume when using Equation 3.3 will change as a function of frequency, inclination and dust opacity. I explore this effect by calculating the mass-weighted average temperature of the emission above the $\tau = 1$ surface, which characterises the optically thin emission, in a similar method as described in Section 3.2.5. Figure 3.25 shows these results for the model disc and, as can be seen, for all dust opacities considered, the mass-weighted average temperature at 90 GHz is higher than at shorter wavelengths. This occurs due to the increase in optical depth with frequency, which is much more pronounced for low dust opacities (ThinIceNoCoag) than for high dust opacities (NoIceCoag). At 270 GHz and beyond, it becomes reasonable to adopt a constant dust temperature if $i < 80°$. At near-edge-on inclinations the morphology of the disc is obscured and the mass-weighted average temperature approaches the minimum value recovered, $T_{\text{dust}} \approx 20\,\text{K}$.

Beyond Band 3 of ALMA ($> 116\,\text{GHz}$), these results indicate that the average dust temperature is $T_{\text{dust}} \approx 30\text{--}40\,\text{K}$ in the GI-active, embedded protoplanetary disc, except when adopting low dust opacities (ThinIceNoCoag). If observations are performed at Band 3 (84–116 GHz), where the optical depth is lowest, the

assumed dust temperature should be increased significantly as more of the shock-heated regions can be observed; for the disc model I use, $T_{\text{dust}} \approx 55\text{--}120\,\text{K}$ at $90\,\text{GHz}$, depending on the dust opacity law adopted. These findings, which are representative of a late Class I/early Class 0 system, disagree with the recommendation of Dunham *et al.* (2014) to adopt $T_{\text{dust}} \approx 30\,\text{K}$ in a Class 0 source and $T_{\text{dust}} \approx 15\,\text{K}$ in a Class I source. This is most likely because, as mentioned previously, their radiative transfer modelling neglects the shock heating driven by the GI, and so their temperature estimates of the optically thin emission may be underestimated. This then implies that their derived masses are likely to be overestimated.

Overall, the method for deriving masses from continuum flux observations is questionable for two primary reasons. Firstly, the dust temperatures in a gravitationally unstable disc will cover a large range (approximately $20\text{--}250\,\text{K}$ in the disc model used in this work), and the reduction of this to a mass-weighted average dust temperature neglects the complex non-axisymmetric structure of the disc. Secondly, the dust temperature is an uncertain property as it is dependent on the dust opacity, which itself is poorly constrained due to the unconfirmed state of grain growth in young, embedded systems. Moreover, the use of a dust temperature that is inappropriately low for the system in question can inadvertently compensate for the large optical depths caused by large dust opacities. For example, a mass of $M_{\text{obs}} \approx M_{\text{sim}}$ can be recovered when large opacities (NoIceCoag) are adopted, if a low dust temperature of $T_{\text{dust}} = 20\,\text{K}$ is assumed. However, as has been demonstrated, this is an unrealistic dust temperature for the disc model I use. Therefore, even in this case, where the observational mass approaches the actual mass, the calculated disc mass is not accurate. Hence, mass estimates derived from continuum flux observations of embedded, gravitationally unstable discs are inherently unreliable.

3.4 Conclusions

3.4.1 LIME optimisations

Continuum emission maps of a model protoplanetary disc have been produced with LIME and in Section 3.2 methods for attaining accurate images have been explored in depth. The main results from this body of work, which focuses on continuum images, are as follows:

- The optimal grid point weighting function is dependent on the model used and features of interest within the model. When using number density weighting, which is the vanilla LIME default, $n_0 = 1 \times 10^{12}\,\mathrm{cm}^{-3}$ and $w = 0.5$ results in particularly prominent spiral features within the disc model.

- A convergence test should be used to find the number of grid points necessary to produce an accurate continuum emission image. This will depend on the model, but for the young, gravitationally unstable model protoplanetary disc featured in this chapter, a minimum of 2×10^5 grid points should be used. Note, however, that more grid points are always preferable if the computational cost can be afforded. This strategy should also be applied to line images.

- The contribution to emission intensity in high optical depth regions is negligible. Grid points can therefore be omitted where $\tau > 3$, which, as these are the densest regions, increases the number of grid points in the observed, less optically thick regions significantly. As a result, this method results in an improvement in the accuracy of the continuum images for the disc model when compared to vanilla LIME images produced using the same number of grid points. Hence, these findings demonstrate that specialised grid construction can improve the efficiency and accuracy of LIME images.

- The averaging of multiple LIME runs using identical inputs improves the

accuracy of the continuum emission image because the grid point coverage is effectively increased. As multiple instances of LIME can be run simultaneously, there is no strong argument against averaging consistent LIME images, barring strict computational or time constraints.

Although LIME is tailored for line emission studies, these findings are presented as an indicator that care should be taken even when using a radiative transfer code to produce continuum emission images, in order to ensure that these images are accurate. When line emission images are considered, the issues discussed in this chapter are amplified due to the complexity of the radiative transfer equation for molecular line transitions. Therefore, even more care should be taken in this scenario. The results regarding the continuum should be applicable to molecular line images, which is explored in the next chapter.

3.4.2 Continuum emission and mass estimates

I produced synthetic observations of the disc model in Section 3.3 across a large parameter space consisting of different frequencies, inclinations and dust opacities. The model represents a $0.17\,M_\odot$ protoplanetary disc that surrounds a $0.8\,M_\odot$ protostar likely to evolve into a Solar-like star. As a result this work may be indicative of observations of an object similar to our early Solar System. The main conclusions drawn from these synthetic observations are as follows:

- Using the antenna configuration for ALMA Cycle 5 and observing for 60 minutes reveals that, at 90–300 GHz, spiral features should be readily detected in a 0–60° inclined young, gravitationally unstable disc at a distance of 145 pc. Spiral features can also be distinguished in near-face-on discs at 430 GHz, but can only be identified at 850 GHz when the dust opacity is very low. For Cycle 5 the optimal frequency to observe non-axisymmetric structure in embedded objects is 230 GHz (1.3 mm).

- Using a fully extended, maximally operational ALMA affords similar results to Cycle 5 observations at lower frequencies as the angular resolution and sensitivity do not change significantly. However, at 430 GHz and 850 GHz the angular resolution is much improved; a minimum spatial resolution of 1.6 au and 0.8 au at 430 GHz and 850 GHz are obtained, respectively. Unfortunately, the spirals are still not distinguishable at these higher angular resolutions because the noise level increases with frequency. Nevertheless, the non-axisymmetric inner disc structure can be seen in extraordinary detail, particularly in inclined discs. Hence, once ALMA reaches maximum capacity, observations in Bands 8, 9 and 10 could be used to probe the innermost regions of embedded discs.

- The majority of the gravitationally unstable model disc featured in this work is very optically thick at frequencies beyond 90 GHz. This is because the spiral waves and inner disc contain a considerable amount of mass in vertically elongated regions. As a result, observations of embedded discs should be performed at long wavelengths where the optical depth is lowest.

- As the GI within a gravitationally unstable disc leads to the heating of the disc material on a global scale, the adoption of a dust temperature of 20 K, which is typically used for more evolved discs, is likely inaccurate. Instead, the mass-weighted average temperature of the optically thin regions within the disc model is $T_{\text{dust}} \approx 30\text{--}40$ K at high frequencies (≥ 230 GHz). At low frequencies (90 GHz), $T_{\text{dust}} \approx 55\text{--}90$ K as the disc is less optically thick, which means more of the shock-heated spiral structure is observed.

- Using the flux density of observations to estimate the mass of young, embedded discs is an inherently flawed procedure for two primary reasons. Firstly, condensing the 3-dimensional spiral structure into one value for the dust temperature and one value for the dust opacity across the entire disc is misrepresentative.

3. CONTINUUM EMISSION AND MASS ESTIMATES

Secondly, the dust temperature and dust opacity in optically thick objects are largely unknown quantities. Hence mass derivations are unreliable.

• The assumption of what are believed to be an appropriate dust temperature and a reasonable opacity within an embedded, gravitationally unstable disc can lead to the underestimation of mass by a a factor of 2.5–30 in a face-on disc, depending on frequency. Moreover, this underestimate worsens as the disc inclination increases. This could retrospectively validate the idea that the GI is active in discs previously thought not massive enough to be gravitationally unstable, which could have a significant impact on the understanding of the formation and evolution of protoplanetary discs.

The results of the synthetic observations presented here are encouraging for the future and suggest that spiral features in young, embedded, gravitationally unstable discs should be detectable in recent and future cycles of ALMA at millimetre wavelengths, and perhaps at submillimetre wavelengths given optimal conditions and long observing times. The synthetic observations support the recent detection of spiral structure in protoplanetary discs (e.g. Pérez *et al.*, 2016; Tobin *et al.*, 2016), which strengthens the argument that these non-axisymmetric features are driven by gravitational instabilities. However, as these objects are more complex than the disc model used in this work, this argument is still tentative. Therefore, more observations are needed to assess the prevalence of GI-induced structure in young, embedded objects. If such observations are performed across multiple wavelengths, unprecedented levels of detail of the disc morphology should be attainable, which will allow the importance of the gravitational instability on the formation and evolution of protoplanetary discs to be understood.

The synthetic observations of the disc model used in this chapter suggest that the mass of a young, gravitationally unstable disc cannot be accurately constrained as these objects are likely optically thick across a broad range of ALMA

frequencies; hence alternative approaches should be adopted. For example, efforts should be made to extract kinematic information from molecular line observations. Moreover, observing spiral structure in certain molecular lines could suggest that localised heating of the disc material is occurring (see Chapter 2), which would strengthen the argument for GI-driven spiral structure. Therefore, in the following chapter, I use LIME and the aforementioned gridding optimisations to explore the utility of ALMA for the extraction of spiral structure and kinematic information in commonly observed molecular line transitions. This will allow the assessment of the accuracy of disc masses derived from line images and will support the findings of the synthetic continuum observations presented in this chapter.

Chapter 4

Line absorption and protostellar mass estimates

4.1 Introduction

A young, embedded protoplanetary disc can have a mass similar to or greater than that of its host protostar at the epoch of protostellar formation. Consequently, the GI can develop within a disc and drive global spiral density waves that affect the chemical evolution of some molecular species via shock-heating, as shown in Chapter 2. Moreover, this temperature structure results in a large flux contrast between spiral and inter-spiral regions. Simulations have shown that this flux contrast can translate into observable spiral structure in the continuum (Cossins *et al.*, 2010; Dipierro *et al.*, 2014; Douglas *et al.*, 2013; Hall *et al.*, 2016, Chapter 3), and recent observations of Class 0 sources (e.g. Pérez *et al.*, 2016; Tobin *et al.*, 2016) support these findings.

As continuum observations of young, protoplanetary discs trace the dust emission exclusively, the information that can be extracted from continuum images is limited. Therefore, many observers probe specific molecular transitions in order to gain a more thorough understanding of the disc morphology and composition. Several molecules have been detected in protoplanetary discs to date. Whilst the

majority of molecular line detections have been made in more evolved discs (Class II/III), detections of CO (J = 2 → 1), ^{13}CO (J = 2 → 1), C^{18}O (J = 2 → 1), H$_2$CO (J = $3_{0,3}$ → $2_{0,2}$), SO (J$_N$ = 6_5 → 5_4), CS (J = 5 → 4), CCH (N = 3 → 2, J = 5/2 → 3/2, F = 3 → 2), CH$_3$OH (J$_N$ = $4_{0,4}$ → $3_{1,3}$, J$_N$ = $7_{-1,7}$ → $6_{1,6}$) have been made in younger (Class 0/I) systems (Ohashi *et al.*, 2014; Sakai *et al.*, 2014, 2016; Tobin *et al.*, 2012, 2016). However, in terms of the focus of this thesis, it is debatable whether the objects that have been observed thus far are gravitationally unstable. Moreover, the expected width of GI-driven spirals is on the order of au scales, but the smallest angular resolutions attained in these observations are $0.36 \times 0.25\,\mathrm{arcsec}^2$ for L1448 IRS3B at a distance of 230 pc (Tobin *et al.*, 2016) and $0.65 \times 0.37\,\mathrm{arcsec}^2$ for IRAS 04365+2535 at a distance of 140 pc (Sakai *et al.*, 2016), which correspond to physical scales of $80 \times 60\,\mathrm{au}^2$ and $90 \times 50\,\mathrm{au}^2$, respectively. Hence, the beamsizes of observations reported to date are far too large to resolve any GI-driven spiral structure if it exists. As ALMA is nearing its fully operational capacity, it is therefore timely and prudent to investigate whether spiral structure can be resolved with higher angular resolutions. The results can then be used to inform the selection of future observational targets, thus allowing the best observational strategy to be developed for determining if spiral features within young protoplanetary discs are GI-driven.

I explore methods to improve the default behaviour of LIME when producing line images in Section 4.2, and implement some of the optimisations found for continuum images (see Chapter 3) as a starting point. Calculations performed under the assumption of LTE are compared to non-LTE calculations, and I provide insight into which frequencies should be adopted for observations of embedded protoplanetary discs. In Section 4.3, perfect, noise-free synthetic observations of the model disc are produced across a large parameter space of molecular transitions, disc inclinations and angular resolutions. From this I produce charts
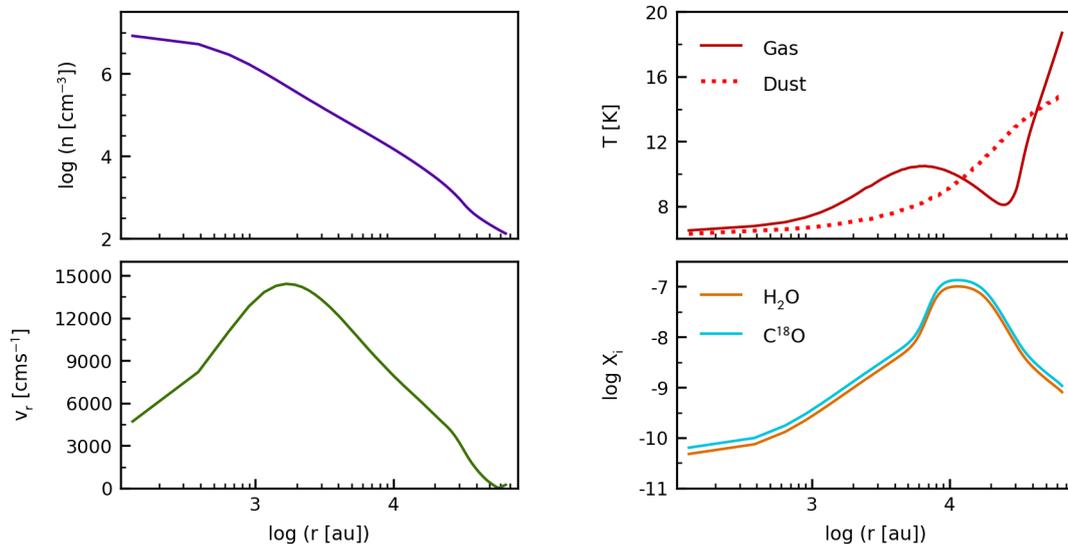
Figure 4.1: Spherically symmetrical envelope model used in the radiative transfer calculations (Keto *et al.*, 2015).

that depict the sensitivity required to detect flux originating within spiral features. I then investigate how feasible it is to spatially resolve the spiral structure from integrated intensity maps, and how feasible it is to spectrally resolve non-axisymmetric structure from line spectra and position-velocity (PV) diagrams. I then explore the accuracy and reliability of protostellar masses derived from PV diagrams. Finally, in Section 4.4 conclusions are presented.

4.2   Producing line image maps with LIME

4.2.1   Disc model

The disc model used in this paper is the same as used in Chapter 3, which is also described in detail in Chapter 2. An envelope is not included in the radiative hydrodynamic simulation as the disc is assumed to be well shielded, i.e. heating from external sources is neglected. The contribution of an envelope in the radiative transfer calculations is taken into account, however, through the

inclusion a $10\,M\odot$ Bonnor-Ebert sphere (see Keto *et al.*, 2015). The properties of this envelope model are shown in Figure 4.1 and whilst the velocities at the innermost radii are perhaps lower than expected in a young star-forming system, the rotational velocity is likely to be larger than the infall velocity at small radii (see e.g. Ohashi *et al.*, 2014). Consequently, the effect of underestimated envelope velocities should be minimal provided the disc and envelope flux can be separated.

4.2.2 Determining frequencies

Figure 4.2 shows the surface at which the optical depth in the disc is $\tau = 3$ at $90\,\mathrm{GHz}$ (top panel) and $850\,\mathrm{GHz}$ (bottom panel) respectively, superposed on y-axis slices of the number density. At $850\,\mathrm{GHz}$, the disc is largely optically thick, which means observations will only trace the surface layers of the disc. At $90\,\mathrm{GHz}$ however, which is near the lowest frequency ALMA is capable of observing, the disc is less optically thick and more of the disc material is probed. This has implications for extracting reliable information from the observations. Hence, hereafter line intensity maps are produced at relatively low frequencies (i.e. Band 3–7 of ALMA).

Whilst observing at low frequencies is necessary to trace the bulk of the disc material, it is also pivotal that abundance information is available in optically thin regions. Figure 4.2 shows the distribution of the fluid elements within the disc model, in white, collapsed to 2D along the y axis, and as can be seen, the fluid elements have a much coarser resolution than the underlying hydrodynamic grid. Consequently, at $850\,\mathrm{GHz}$, because the $\tau = 3$ boundary is near the surface of the disc, only regions devoid of fluid elements, and therefore devoid of abundances, are observed. At $90\,\mathrm{GHz}$ the disc is less optically thick as mentioned earlier, and so observations will be more reliable because more abundance-rich regions will be sampled. Therefore, Figure 4.2 demonstrates how important it
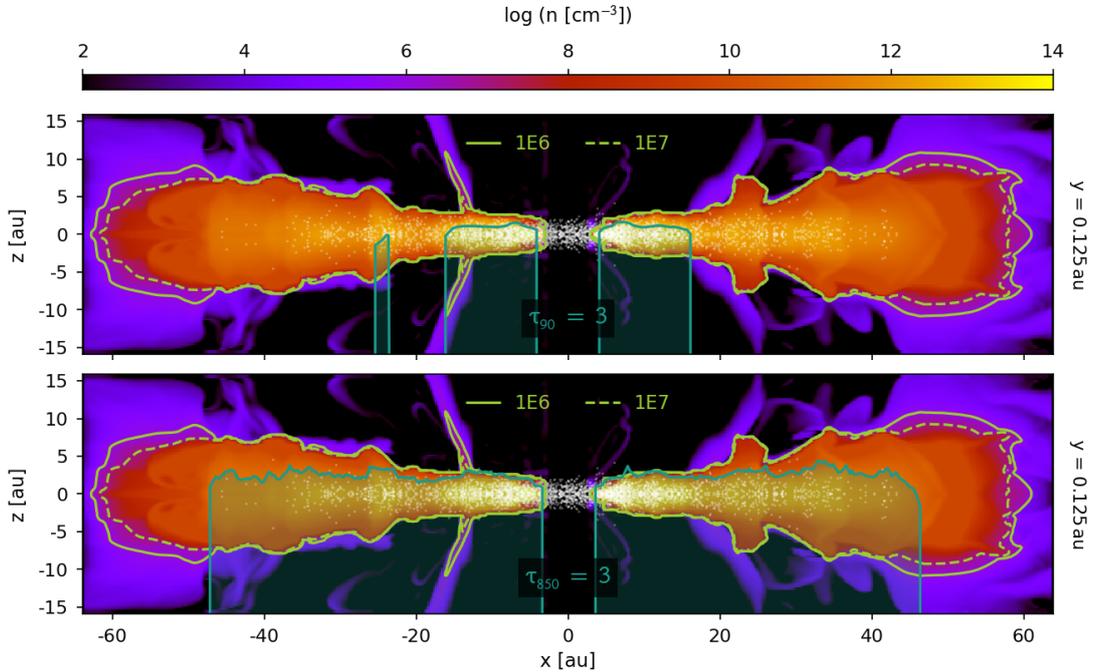
Figure 4.2: Nuclei number densities of the disc model along the $y = 0.125\,\mathrm{au}$ plane with solid and dashed green lines overplotted at number densities that approximately demarcate the boundary of LTE validity. The teal lines show the boundary where $\tau = 3$ at a frequency of $90\,\mathrm{GHz}$ (top) and $850\,\mathrm{GHz}$ (bottom); hence the shaded regions indicate the optically thick regions of the disc when viewed from above. The white dots indicate the x and z positions of all of the fluid elements (i.e. not only those constrained to $y = 0.125\,\mathrm{au}$) that are chemically processed (see Chapter 2).

is for chemical simulations of discs to ensure that the resolution of abundances is sufficient in optically thin regions. Note that for the disc model used in this work, the innermost disc is still sparsely populated by fluid elements even at low frequencies; hence the results for $r < 15\,\mathrm{au}$ are perhaps questionable. However, as the primary focus here is on the spiral features in the outer disc, this should not affect the results presented in this chapter.

4.2.3 LTE approximation

The complexity of line radiative transfer can be drastically simplified if LTE can
be assumed. In this case, instead of iterating towards a converged level population
distribution, the level populations can be assumed to follow a Maxwell-Boltzmann
distribution. The condition for LTE is $n_c{}^k > n_{crit}{}^k$, where $n_c{}^k$ and $n_{crit}{}^k$ are the
number density and critical density for the collisional partner k. The critical
density is defined as the ratio of radiative to collisional transitions, i.e.

$$n_{crit}{}^k = \frac{A_{ul} + B_{ul}\bar{J} - \frac{n_l}{n_u}B_{lu}}{\sum_{i \neq u} \gamma_{ui}{}^k} \, , \qquad (4.1)$$

where n_u and n_l are the level populations of the upper and lower levels and γ_{ui}
is the collisional rates of all transitions from the upper energy level. A_{ul}, B_{ul} and
B_{lu} are the Einstein coefficients for spontaneous emission, stimulated emission
and stimulated absorption, respectively, and $\bar{J}$ is the mean intensity.

Commonly, background radiation, stimulated emission and absorption are ne-
glected in the calculation of n_{crit}. However, in reality radiative trapping is impor-
tant for many line transitions, which can be incorporated through the inclusion
of a solid angle averaged escape fraction, $\bar{\beta}$. As $\bar{\beta}$ is dependent on the geometry
and kinematics of the region, its calculation is not trivial for a non-axisymmetric
disc model, although, for large optical depths, the general result is a reduction
in the critical density (see Shirley, 2015, and references within). An alternate
quantity, which naturally incorporates radiative trapping, is the number density
required to produce an integrated line intensity of $1\,\mathrm{km\,s^{-1}}$. This is known as
the effective excitation density, n_{eff}, and depends on the column density of the
observed molecule and the kinetic temperature of the collisional partner. Shirley
(2015) compared the optically thin critical density to the effective excitation den-
sity and found that, for most low-energy molecular transitions of observational

interest, $n_{\text{crit}} = 10^6$–$10^7\,\text{cm}^{-3}$. Moreover, Shirley (2015) found that n_{eff} is lower than n_{crit} by 1–2 orders of magnitude in nearly all cases.

One can assess the validity of LTE by comparing Table 1 of Shirley (2015) with the number density of the disc model I use, under the assumption that H_2 is the dominant collisional partner for all transitions. Figure 4.2 shows the number density in the $y = 0.125\,\text{au}$ plane with contours of density overplotted. I have used n_{crit} for comparison purposes because it presents a worst-case scenario for LTE validity, and because n_{eff} can be undefined if an integrated line intensity of $1\,\text{km}\,\text{s}^{-1}$ is not observed. As can be seen, the number density of the model disc exceeds the optically thin critical density in the emitting regions (i.e. $\tau <$ 3), meaning LTE should be appropriate for our disc model across a wide range of molecular transitions. This assumption is later verified in Section 4.2.7 by comparing the LTE results to full non-LTE calculations.

4.2.4 Weighting of grid points

I improve the density weighting algorithm in Chapter 3 because the default implementation is found to be inadequate for the model disc. Here however, *abundance* density weighting is utilised because the focus is on the line emission; hence the weighting function is amended to use abundance density, with a cutoff threshold of $0.001 \times \max(X_i)$, as only the strongest emission regions are of interest.

4.2.5 Number of grid points

In Chapter 3 I demonstrate that the number of grid points has a significant effect on the accuracy of the continuum flux image obtained. Line radiative transfer calculations add a level of complexity, even if LTE is assumed, and therefore more grid points are expected to be necessary than used in Chapter 3. In order to investigate this, I produce two $C^{17}O$ $1 \to 0$ images ($i = 30°$) using different
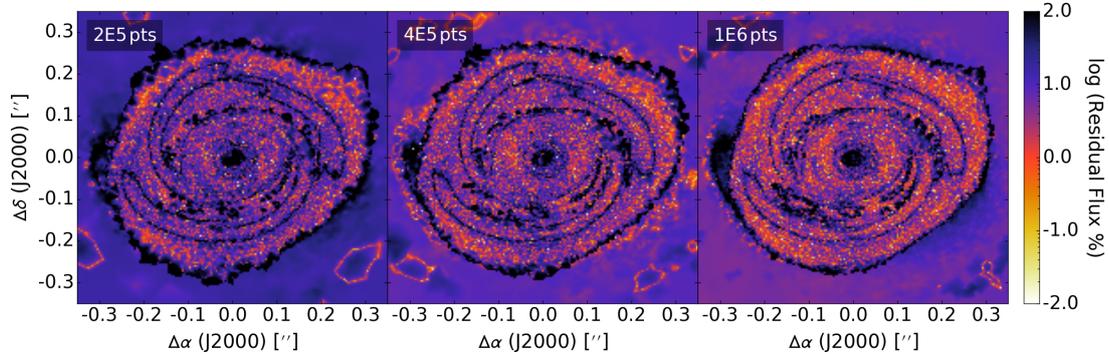
Figure 4.3: Residual integrated line flux for $C^{17}O$ $1 \rightarrow 0$, calculated under the assumption of LTE, between two LIME runs using the indicated number of grid points, with standard sampling. This residual is defined as $|(f_1 - f_2)|/(f_1 + f_2)$, where f denotes integrated flux per pixel.

numbers of grid points and then compare the residual integrated line fluxes. This method differs from that of Chapter 3, where a 'canonical' image for the residual is used, because the same level of consistency is not reached for the line images.

Figure 4.3 demonstrates that as the number of grid points is increased, the integrated flux maps become more consistent, suggesting that the line images are more accurate. This is expected, but, because of the complexity of line transfer, even when LTE is assumed, the residual at 1×10^6 points is much larger than for the continuum (see Chapter 3). Therefore, in order to achieve a residual flux that is less than the expected observational errors (≥ 10 per cent), more than 1×10^6 points are needed for the disc model when default sampling is used.

4.2.6   Sampling optimisations

Constructing a grid of more than 1×10^6 points is computationally expensive and time consuming. Consequently, it becomes advisable to investigate whether more accurate images can be obtained without increasing the number of grid points.

Model-specific sampling

The default behaviour of LIME is to implement either a random Cartesian sampling across the entire model, *par→sampling = 1*, or a radially logarithmic sampling routine across the entire model, *par→sampling = 2*. As of LIME v1.7 there is also the ability to use a completely separate tree-building sampling algorithm, but here the focus is on the original 'randoms-via-rejection' algorithm.

So far, including in Chapter 3, radially logarithmic sampling has been used, which I refer to as 'Sampling2', to ensure that, probabilistically, more points are positioned within the disc than the envelope. However, as a result more points are positioned in the innermost disc rather than the outer disc where the spiral features of particular interest are located. In order to improve upon this behaviour, I develop a new sampling routine that uses rectilinear sampling within the disc in order to ensure a more even distribution of points. Radially logarithmic sampling is still used to populate the envelope, but only with a small fraction of the total number of points because the mean free path in the envelope is much larger than in the disc (see Figure 3.7). I refer to this new sampling algorithm as 'Sampling3'[1].

The middle panel of Figure 4.4 shows the residual for $C^{17}O$ $1 \to 0$ ($i = 30°$) when 1×10^6 grid points are used and Sampling3 is adopted. When compared to Sampling2, one of the default LIME algorithms, the residual within the outer disc region is improved considerably. This is because, as mentioned earlier, Sampling3 affords a much more even distribution of grid points; hence a larger proportion of grid points are positioned beyond the inner disc, as Figure 4.5 demonstrates. Within the inner disc ($r < 15\,\mathrm{au}$) the difference in residual is minimal. This is because the natural consequence of a greater number of grid points in the outer disc is a smaller number of grid points in the inner disc. However, because the

---

[1]github.com/lolmevans/lime/tree/custom-sampling-routines
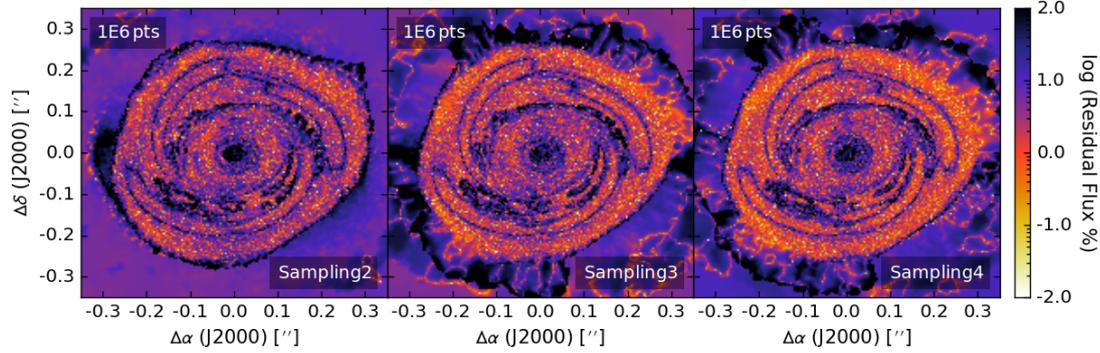
Figure 4.4: Residual integrated line flux for $C^{17}O$ $1 \rightarrow 0$, calculated under the assumption of LTE, between two LIME runs using the indicated number of grid points and standard sampling (left), a model-specific sampling routine (middle), or a model-specific sampling routine with an optical depth surface to constrain the positioning of grid points (right). This residual is defined as $|(f_1-f_2)|/(f_1+f_2)$, where f denotes integrated flux per pixel.
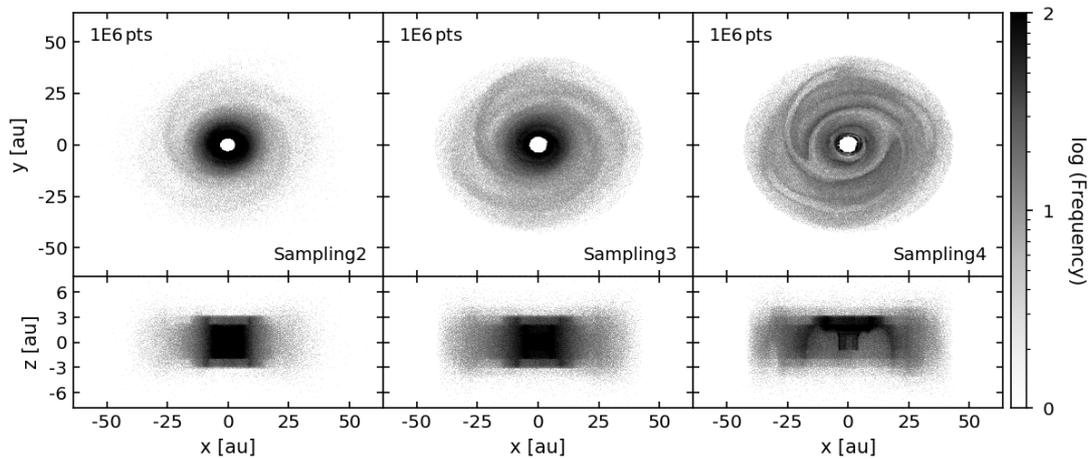

Figure 4.5: 2D histogram of grid point positions in the x-y plane (top) and x-z plane (bottom) when using standard sampling (left), a model-specific sampling routine (middle), or a model-specific sampling routine with an optical depth surface to constrain the positioning of grid points (right). The disc is being viewed from above.

inner disc is largely optically thick, emission from points near the midplane will be negligible. Therefore the grid point positioning can be optimised further by omitting negligibly-emitting regions.

Optical depth surface

In Chapter 3 I explore the notion of optimising grid point placement by restricting points to regions where $\tau < 3$, and find it to be a viable method. This is because the contribution to intensity is diminished by optically thick material, so that at $\tau > 3$ this contribution is negligible. As the continuum absorbs radiation at a particular frequency independent of its source, the same logic should apply for line emission.

I produce a new $C^{17}O$ $1 \rightarrow 0$ image ($i = 30°$) using the configuration in Section 4.2.6, whilst employing the optical depth surface method described in Chapter 3, with one adjustment: rather than relocate a point from $\tau > 3$ to $\tau < 3$ and then re-evaluate, instead, for the sake of simplicity, the point is rejected and another is selected randomly. I refer to this sampling algorithm as 'Sampling4'[1].

The right panel of Figure 4.4 shows the residual integrated line flux for Sampling4. Within the outer disc there is a small overall improvement in residual flux between Sampling3 and Sampling4, even though the x-y plane images in Figure 4.5 suggest the coverage within the spiral arms is more sparse for Sampling4. However, this is because the positioning of the grid points is more optimal as intended. Indeed, by restricting points to $\tau < 3$ the negligibly-emitting regions that lie at high optical depths are omitted. This also explains why there is a more marked improvement in the inner disc residual when using Sampling4; the point restriction is visually evident in the x-z plane images of Figure 4.5. Note that, whilst the residual beyond the disc boundary is considerably larger when using

---

[1]github.com/lolmevans/lime/tree/custom-sampling-routines

the custom sampling routines (Sampling3 and Sampling4), the focus of this work is on the disc itself and so this is not a concern for the results.

From this analysis it can be seen that Sampling4 offers the most convergent result for the disc model, when 1×10^6 grid points are used. However, it should be emphasised that convergence is not necessarily synonymous with accuracy, and where possible results should be compared to a 'canonical' result. In this case, I compare the LTE runs using the custom sampling algorithm to a full non-LTE run adopting the default sampling.

4.2.7 Non-LTE comparison

When calculating level populations under non-LTE conditions, the user must ensure that enough iterations are used to reach a satisfactory level of convergence. In LIME there is no convergence threshold that, once surpassed, terminates the calculation of level populations. Instead the user can set $par{\rightarrow}nSolveIters$ to dictate how many iterations will be performed. LIME does, however, calculate a signal-to-noise ratio for each grid point using the level population of the current iteration and the standard deviation of the level population mean over the past five iterations. This information could be used in future versions of LIME to develop a convergence criterion, e.g. iterating stops once 90 per cent of grid points have reached a SNR that exceeds 100. For now, however, I compare the SNR across iterations in order to determine how many iterations should be used for the disc model. As Figure 4.6 indicates, this convergence level appears to be reached by five iterations, but in order to err on the side of caution I use ten iterations for the non-LTE runs.

I generate two 'canonical' results by performing full non-LTE calculations for two grids with 1×10^6 points, selected with Sampling2. Sampling2 is used in order to avoid the possibility that the custom sampling algorithms are converging
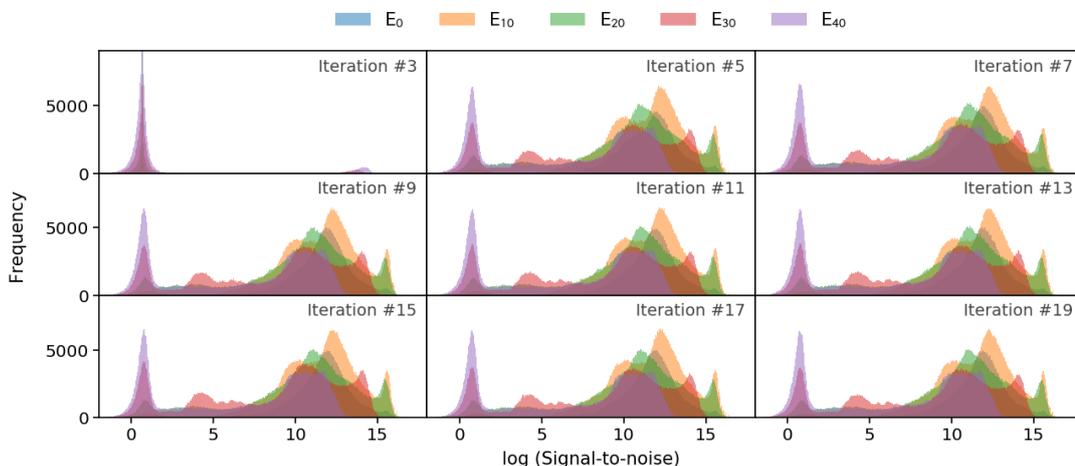
Figure 4.6: Histograms of the signal-to-noise ratios for different energy levels (i.e. J number) of $C^{17}O$ $1 \rightarrow 0$ as the amount of iterations of level population calculations increases. A converged distribution is reached by 5 iterations. The non-LTE LIME run shown here uses 1×10^6 grid points and Sampling2.

to a significantly different solution than the LIME default. I then calculate the residual between these two non-LTE runs, and compare to the residual of one non-LTE run and one LTE run from Section 4.2.6. To make this comparison easier to digest, in Figure 4.7 the regions where the residual flux is greater than 10 per cent (the expected observational errors) are demarcated in red/brown, and elsewhere in green. The purpose of this comparison is to assess whether using LTE is appropriate as we have predicted, and to establish the propinquity concerning the thermodynamic configurations.

Figure 4.7 shows that $C^{17}O$ $1 \rightarrow 0$ LIME images produced with LTE treatment are consistent with images produced with full non-LTE treatment, which is as expected. Moreover, as Figure 4.2 shows, this conclusion should hold across all low-energy transitions of the molecular species that are focused on in this chapter. Therefore, this result validates the use of LTE in Section 4.3, which is computationally beneficial because the assumption of LTE affords a considerable speedup in level population calculations. Consequently, hereafter Sampling4 is
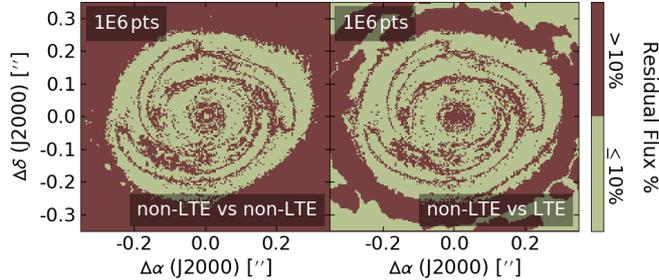
Figure 4.7: Residual integrated line flux for $C^{17}O$ $1 \to 0$ between two LIME runs using the indicated number of grid points. Regions exceeding 10 per cent are coloured red and elsewhere are coloured green. The left panel shows the result for two non-LTE runs, with standard sampling, and the right panel shows the result for one non-LTE run with standard sampling, and one LTE run with a custom sampling routine (see Section 4.2.6). This residual is defined as $|(f_1-f_2)|/(f_1+f_2)$, where f denotes integrated flux per pixel.

used and LTE is assumed.

Within all of the residual integrated line flux maps presented thus far, there is a particularly large difference that traces the outline of the non-axisymmetric structure, regardless of whether LTE is assumed or not. This is due to the large density gradients found at the boundaries between spiral and non-spiral material. A dedicated sampling routine would need to be implemented in order to accurately account for these rapid density variations, but, as these gradients only exist in very narrow regions, the effect on the observational results presented in this chapter should be negligible.

4.3 Noise-free synthetic observations

The inventory of molecules detected in protoplanetary discs at (sub)millimetre wavelengths includes CO, CN, CS, C_2H, CH^+, HCN, HNC, H_2O, HCO^+, NH_3, N_2H^+, N_2D^+, SO, DCO^+, DCN, H_2CO, c-C_3H_2 and some isotopologues of the listed species (e.g. Chapillon *et al.*, 2012; Dutrey *et al.*, 1997, 2011; Guilloteau *et al.*, 2016; Qi *et al.*, 2013; Salinas *et al.*, 2016, 2017; Thi *et al.*, 2011). ALMA is
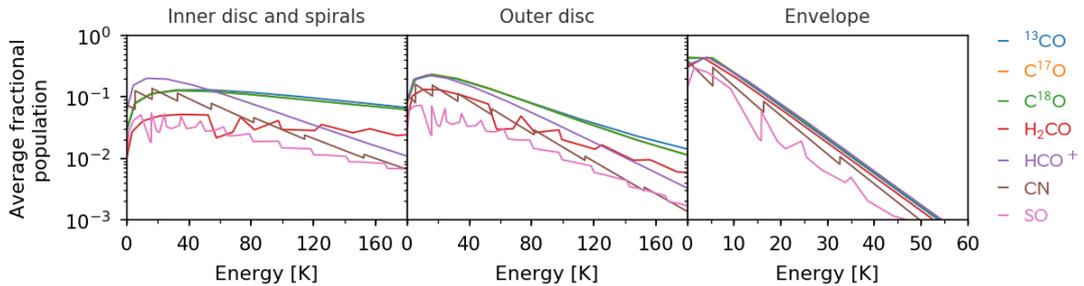
Figure 4.8: Fractional energy level populations averaged over grid points within the inner disc and spirals (left panel), the outer disc (middle panel) and the envelope (right panel). The disc regions are determined by density ranges.

now expanding this catalogue to include more complex organic molecules such as CH_3CN and CH_3OH (e.g. Öberg *et al.*, 2015; Walsh *et al.*, 2016). Therefore, it is timely to use simulations to investigate the observability of molecules in particularly young and embedded discs, so that the choices of targets and parameters for future observations can be informed, and also so that the chemical evolution from the protostellar to the protoplanetary disc phase can be studied.

I produce synthetic observations of ^{13}CO, $C^{18}O$, $C^{17}O$, H_2CO, HCO^+, CN and SO as these are species that play fundamental roles in disc chemistry and trace some aspect of the spiral structure in the disc model used (see Chapter 2). As shown in Section 4.2.2, only low frequency transitions of these molecules are viable; hence transitions in ALMA Band 3 (84–119 GHz), Band 6 (211–275 GHz) and Band 7 (275–370 GHz) are chosen. In order to narrow the possible transitions down further, I use LIME to calculate the level populations (in LTE) of each molecule considered and average these across different regions of the model disc. The results are shown in Figure 4.8 for the inner disc and spirals, the outer disc, and the envelope.

The focus of this work is on the spiral features. Hence, after identifying the energies of the most populated energy levels from Figure 4.8, whilst also considering the fact that lower frequency transitions are more reliable for the model used (see

Table 4.1: Molecular transitions used to produce synthetic observations of the model disc.

Molecule	Transition	Upper energy [K]	Lower energy [K]	Frequency [GHz]	Angular resolution [arcsec]	
					out02	out28
^{13}CO	$J = 3 \to 2$	22.055	11.028	330.588	0.993	0.014
$C^{17}O$	$J = 3 \to 2$	22.487	11.244	337.061	0.974	0.013
$C^{18}O$	$J = 3 \to 2$	21.971	10.986	329.331	0.997	0.014
H_2CO	$J_N = 3_{0,3} \to 2_{0,2}$	14.566	7.286	218.222	1.505	0.021
H_2CO	$J_N = 10_{2,8} \to 11_{0,11}$	167.304	158.689	258.296	1.271	0.018
HCO^+	$J = 3 \to 2$	17.850	8.925	267.558	1.227	0.017
CN	$N = 3 \to 2,\ J = 5/2 \to 3/2$	22.678	11.335	340.031	0.966	0.013
CN	$N = 2 \to 1,\ J = 3/2 \to 1/2$	11.335	3.786	226.333	1.449	0.020
CN	$N = 1 \to 0,\ J = 3/2 \to 1/2$	3.786	0.000	113.495	2.893	0.040
SO	$N = 6 \to 5,\ J = 7 \to 6$	33.050	24.316	261.844	1.254	0.017
SO	$N = 5 \to 4,\ J = 5 \to 4$	30.654	23.475	215.221	1.526	0.021
SO	$N = 2 \to 1,\ J = 1 \to 2$	10.987	3.100	236.452	1.389	0.019

Section 4.2.2), I select the transitions listed in Table 4.1. H_2CO ($10_{2,8} \rightarrow 11_{0,11}$) is included because Figure 4.8 shows that a transition between levels with relatively high energies should only be visible in the inner disc and spirals, and therefore may offer a clearer picture of the innermost density structure. CN ($1_{3/2} \rightarrow 0_{1/2}$) and CN ($3_{5/2} \rightarrow 2_{3/2}$) are included in order to investigate the effect of transition frequency on flux; CN is used for this because the fractional populations vary the least across low energies in the inner disc and spiral regions, as shown in Figure 4.8.

In the envelope the CO profile calculated by Keto *et al.* (2015) is used for ^{13}CO, $C^{17}O$ and $C^{18}O$, scaled by the appropriate isotopic abundances given by Wilson (1999). The HCO^+ profile follows the H_2O profile of L1544, scaled so that the maximum fractional abundance is 1×10^{-8}. H_2CO follows a step profile with a fractional abundance of 1.5×10^{-8} at $r \le 8000\,\mathrm{au}$ and 1.5×10^{-9} at $r > 8000\,\mathrm{au}$ (Young *et al.*, 2004). Finally, constant fractional abundances of 1×10^{-10} are adopted for SO and CN (Koumpia *et al.*, 2017; Miettinen, 2016). Whilst these abundance profiles in the envelope are primitive, the expectation is that isolation of the envelope flux will be straightforward. Therefore, as the focus of this work is on the disc spirals, the effect on the presented results should be minimal.

The model disc represents the same object as used in Chapter 3. It is assumed to be located at a distance of 145 pc, which is typical for the nearest star-forming regions (e.g. the Ophiuchus Molecular Cloud). Inclinations of 15°, 30°, 45°, 60° and 75° are adopted in order to span the range of inclinations between the individual sources in real systems such as IRAS 16243–2422, which is a protostellar binary with nearly face-on and nearly edge-on discs separated by 600 au. The observations are synthesised across different fully operational ALMA antenna configurations ('out02', 'out08', 'out13', 'out18', 'out21', 'out24' and 'out28'), for which a selection of angular resolutions are shown in Table 4.1; it is assumed

4. LINE ABSORPTION AND PROTOSTELLAR MASS ESTIMATES

Table 4.2: Spectral resolution and channel spacing in kHz for different correlator bandwidth modes and channel averaging factor, N. Adapted from the ALMA Technical Handbook[1].

Usable bandwidth [MHz]		Spectral resolution (channel spacing) [kHz]	
	N =	1	2
1875		977 (488)	1129 (977)
937.5		488 (244)	564 (488)
468.8		244 (122)	282 (244)
234.4		122 (61)	141 (122)
117.2		61 (31)	71 (61)
58.6		31 (15)	35 (31)

that each antenna configuration is applicable across all frequencies. The channel widths adopted are consistent with the spectral resolutions attainable for ALMA (see Table 4.2), for an assumed channel averaging factor $N = 1$. It is recommended to increase the averaging factor, and therefore decrease the number of channels, because this results in a smaller loss in final resolution. However, here $N = 1$ is used in order to provide the most optimistic results.

Perfect observations are produced with no sources of noise. This allows the constraint of the maximum attainable fluxes across the entire parameter space, which is accomplished by convolving the LIME images with a Gaussian beam using a fast Fourier transform module, `fft`, in PYTHON. The motivation for this is threefold. Firstly, a superior efficiency can be achieved with a fast Fourier transform algorithm compared to the production of realistic synthetic observations across the entire parameter space with software such as CASA (v4.5.0; McMullin *et al.*, 2007). Secondly, it is expected that a significant portion of the parameter space will simply be unobservable, implying that producing realistic observations in this scenario is superfluous. Finally, the image fidelity discrepancy between

---

[1]https://almascience.eso.org/documents-and-tools/cycle5/alma-technical-handbook

perfect and realistic observations is not a significant issue due to the extensive u-v coverage of ALMA. Rather than use a circular Gaussian beam, which is not entirely accurate, I use an elliptical Gaussian beam with a size determined by the `simobserve` task in CASA, for an on-source observation time of 12 hr and Briggs weighting with a robustness factor of 0.5.

4.3.1 Detecting spiral structure

Figure 4.9 shows flux maps integrated across a mostly envelope-free velocity range, for the indicated transition, narrowest channel spacing and highest angular resolution (see Table 4.1), at a disc inclination of 15°. This figure is presented in order to illustrate the extent of the spiral structure that is distinguishable for each species, under the condition of noise-free observations, but I emphasise that obtaining this level of detail is not currently possible with real observations. Nevertheless, Figure 4.9 allows the observable characteristics for various molecules to be determined, which can inform the preparation of observation proposals. For example, because CO is ubiquitous due to its highly volatile nature, the spirals are distinctly traced by each isotopologue. HCO^+ also traces the spirals but with a weaker flux primarily due to its lower abundance. There is an inner hole evident in the HCO^+ intensity map, and this results from the destruction of HCO^+ in the innermost disc due to high abundance of gas-phase H_2O; the extent of this hole could potentially offer insight into the disc mass as discussed in Chapter 2. H_2CO is mostly confined to the innermost disc due to its relatively high binding energy to dust grains, and hence could offer detailed views of the inner disc structure if the angular resolution is sufficient. However, H_2CO also traces the spiral structure somewhat in the outer disc, which is perhaps unexpected given the H_2CO column density map in Chapter 2. Equally noteworthy is the relatively weak reflection of the underlying spiral structure in the CN integrated intensity
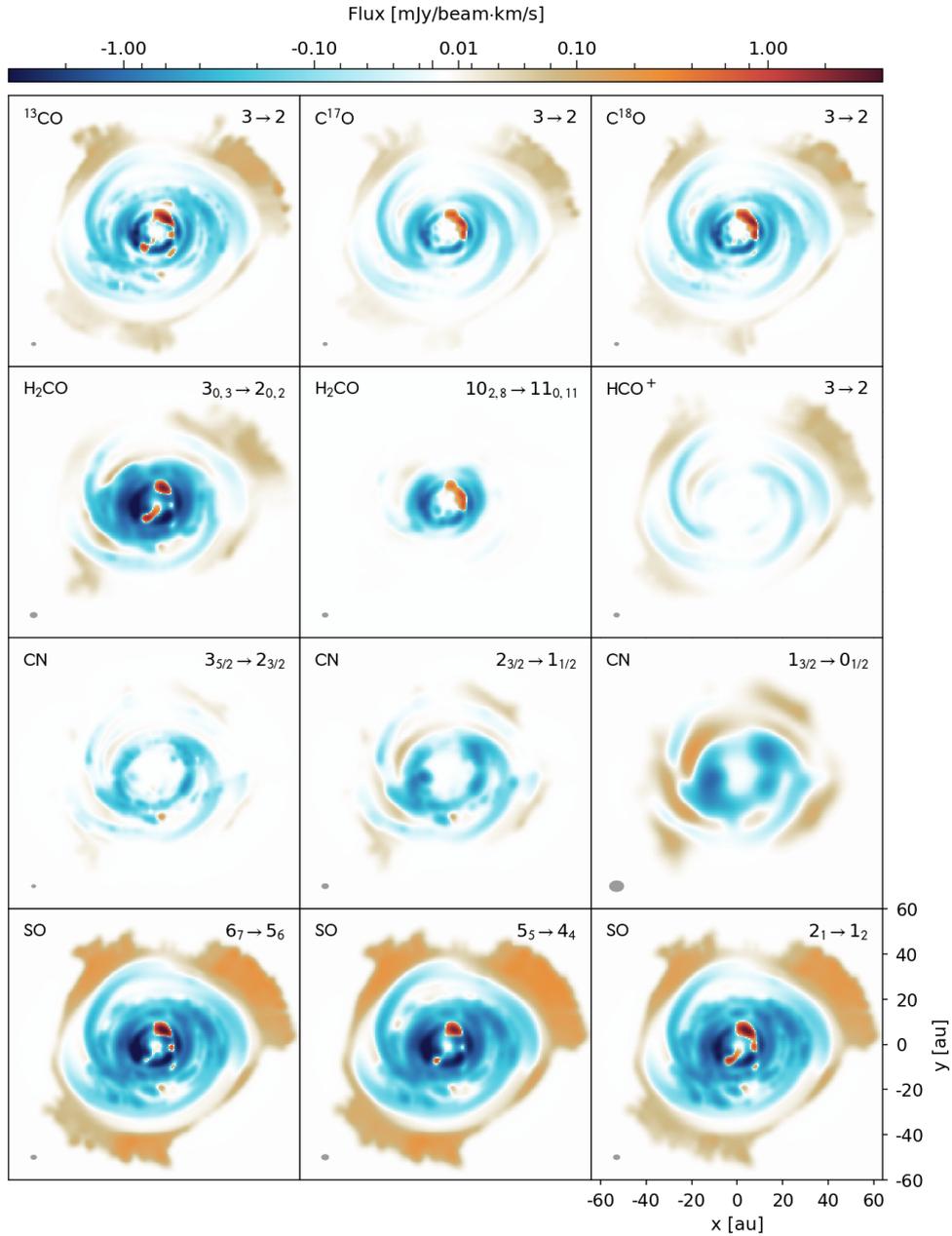
Figure 4.9: Integrated intensity maps (integrated from -5.0 to -0.8 km/s and 0.8 to 5.0 km/s) for each molecular transition, an inclination of 15°, a spectral resolution of 31 kHz and the 'out28' antenna configuration. The bottom right panel indicates the physical scale of the observed disc model, which is constant across all transitions shown. The grey circle in each panel shows the beamsize for the corresponding observation.

map given that I found that CN was one of the strongest candidates for tracing non-axisymmetric structure based on its abundance distribution in Chapter 2. Moreover, the column density map of SO is found to be limited in extent in Chapter 2, yet in the integrated flux maps here it traces as much of the disc as CO, albeit with slightly less contrast in the inner regions.

In essence, Figure 4.9 suggests that a high contrast in abundance density does not necessarily translate into a high contrast in flux because of the numerous interconnected processes that all contribute to line observability. As a result, it is necessary to perform radiative transfer calculations when one considers line flux imaging.

Required sensitivities

From the perfect observations (i.e. no noise included) I extract the flux attributable to a typical spiral feature in the disc model, and determine the sensitivity required to detect this flux at the 4σ level, which is taken as the threshold for a reliable detection. To accomplish this, a pixel position is identified within the spirals for a particular combination of molecular transition and disc inclination. I use the integrated intensity map with the smallest beamsize here because the spirals are the most distinguishable. I then extract the line spectra at this pixel and fit a Gaussian to the line feature originating from the spirals. From this Gaussian the full width at half-maximum (FWHM) and flux at half-maximum are calculated. The FWHM is compared to the channel width to determine if the line feature can be spectrally resolved, and I take the flux at half-maximum to ensure that enough of a peak can be detected and identified as line absorption (as is the case for spiral-originating flux). Using the same pixel position I then repeat this process as the beamsize and channel width are increased. The disc inclination is then changed and the pixel selection and Gaussian-fitting process
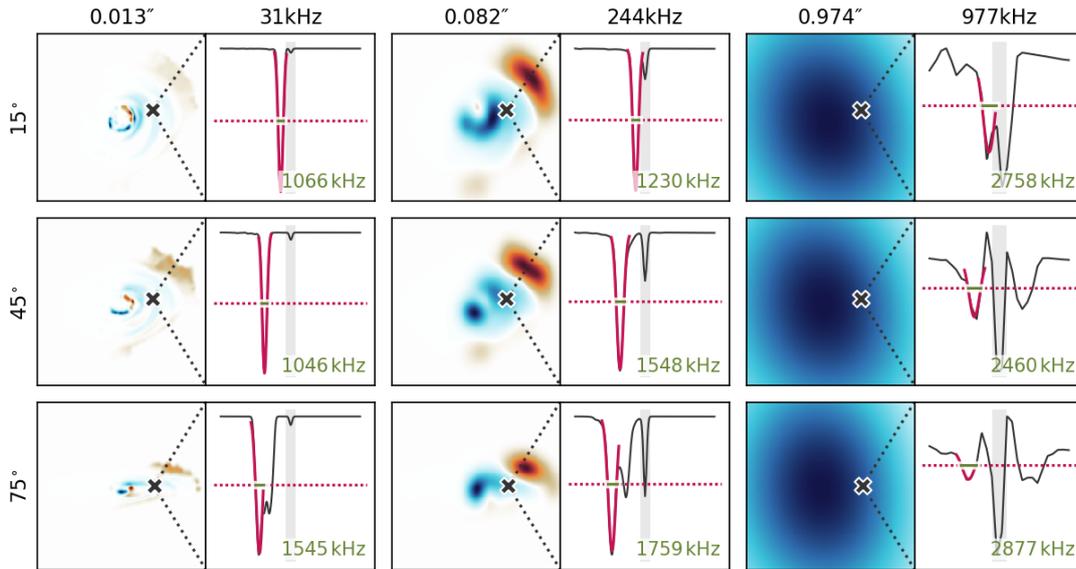
Figure 4.10: Depiction of the process undertaken to determine the sensitivity required for detection of line flux originating from spiral features in the disc model. Each panel shows, for a particular inclination, antenna configuration and channel width, the integrated intensity map with a pixel position within a spiral arm marked by a cross (left) and the line spectra extracted at this pixel position (right). In the spectra plots, the solid purple line indicates a Gaussian fit, the dashed purple line indicates the half-maximum amplitude of this fit and the green line and accompanying text detail the FWHM, which is compared to the frequency bandwidth in order to determine if the Gaussian fit can be resolved spectrally. The grey band indicates the envelope velocity range and if the Gaussian peak lies within this band then the line flux and envelope flux are treated as indistinguishable. The line transition used here as an example is $C^{17}O$ $3 \rightarrow 2$.

repeated. Finally, I move on to a different molecular transition and repeat the entire sequence. Figure 4.10 illustrates some steps of this process visually.

I condense the extracted sensitivities into charts that depict the sensitivity required for each molecular transition considered. These charts are shown in Figures 4.11–4.17 and within each is information pertaining to: whether the linewidth is unresolvable, i.e. whether the FWHM of the line is larger than the velocity resolution, indicated by a large black cross; whether the envelope substantially contaminates the line feature, indicated by a grey cross; and whether the spirals can be visually distinguished in an integrated intensity map, indicated by a white circle. Hence, wherever there is any type of cross in the charts, it means that detecting line flux from the disc spirals is unreliable for that particular combination of molecular transition, disc inclination, antenna configuration and channel width. Note that the particularly high sensitivities seen in some charts for the largest channel widths and beamsizes are because in those cases the envelope contribution can not be disentangled from the line flux (see the accompanying grey crosses), and so the Gaussian is fitted to a summation of line and envelope flux.

Figures 4.11 and 4.12 demonstrate that isotopologues of a species produce differing fluxes at similar frequencies. This is due to the difference in abundance of the isotopologues as a larger number of absorbing molecules results in a larger optical depth and hence a deeper absorption feature, as shown by the purple line spectra in Figure 4.23. However, the difference in peak flux recovered in the spiral regions is much less than the difference in abundance across the CO isotopologues; the change in abundance from ^{13}CO to C^{18}O is ≈ 8 and from C^{18}O to C^{17}O is ≈ 4, whereas the change in peak flux is ≈ 2 and ≈ 1.5, respectively. The reason for this is that the dependence of line flux on the column density of absorbers, known as the 'curve of growth', falls between $\sqrt{ln(N_i)}$ and $\sqrt{N_i}$ in the high optical depth
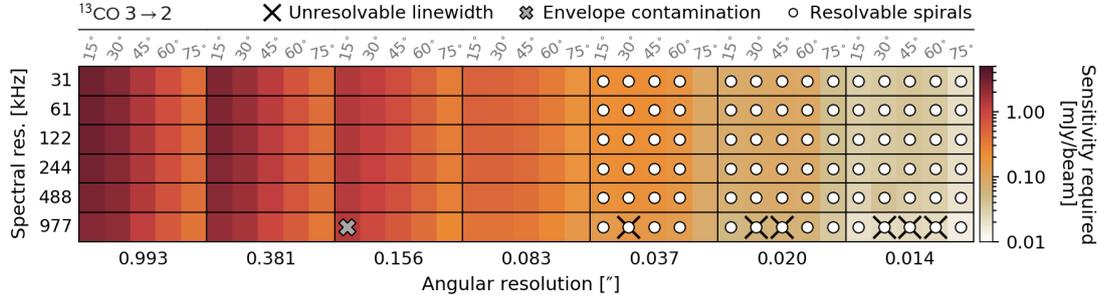
Figure 4.11: Sensitivity needed to detect ^{13}CO $3 \rightarrow 2$ line flux across different combinations of angular resolution, spectral resolution and disc inclination (grey labels). The white circles indicate combinations that result in spatially resolvable spiral features, which is determined by eye from integrated intensity maps such as Figure 4.9. The thick grey crosses indicate combinations that result in line spectra that are indistinguishable from the envelope. The thin black crosses indicate combinations where the Gaussian fitted to the line spectra (see Figure 4.10) is not spectrally resolvable.
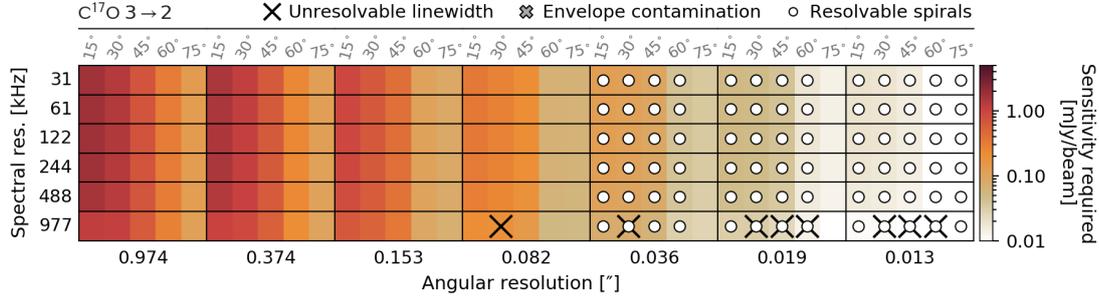

Figure 4.12: Same as Figure 4.11 but for C^{17}O $3 \rightarrow 2$.
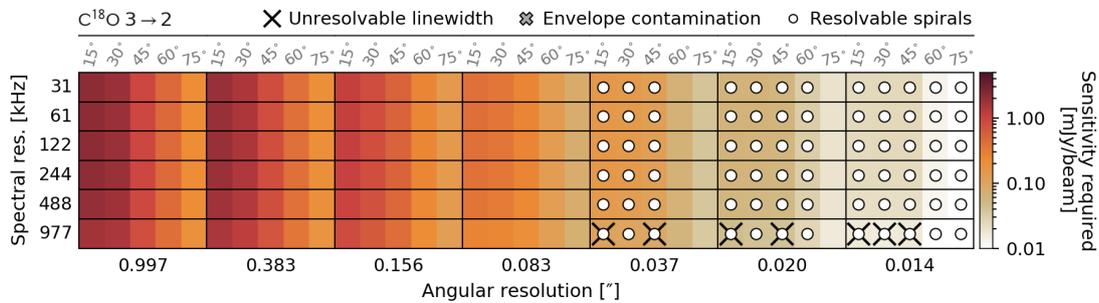

Figure 4.13: Same as Figure 4.11 but for C^{18}O $3 \rightarrow 2$.
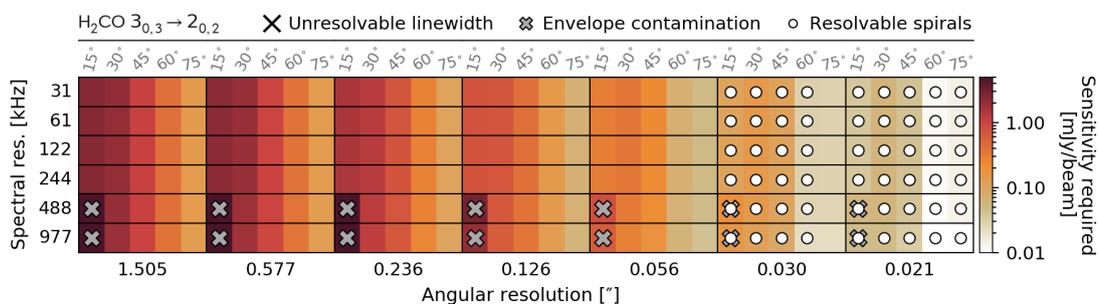
Figure 4.14: Same as Figure 4.11 but for H_2CO $3_{0,3} \rightarrow 2_{0,2}$.
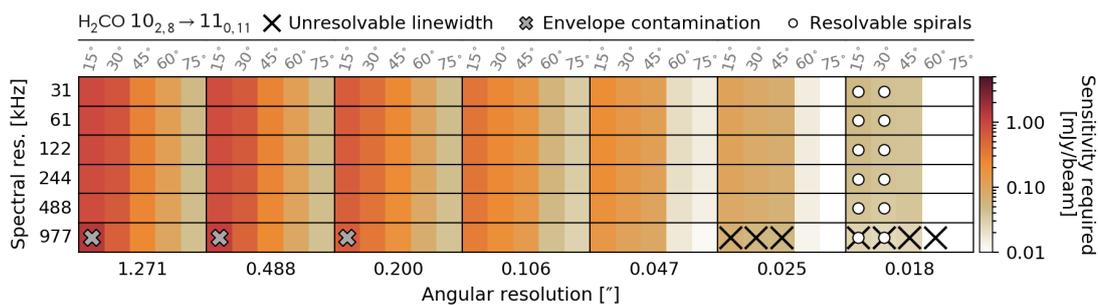


Figure 4.15: Same as Figure 4.11 but for H_2CO $10_{2,8} \rightarrow 11_{0,11}$.
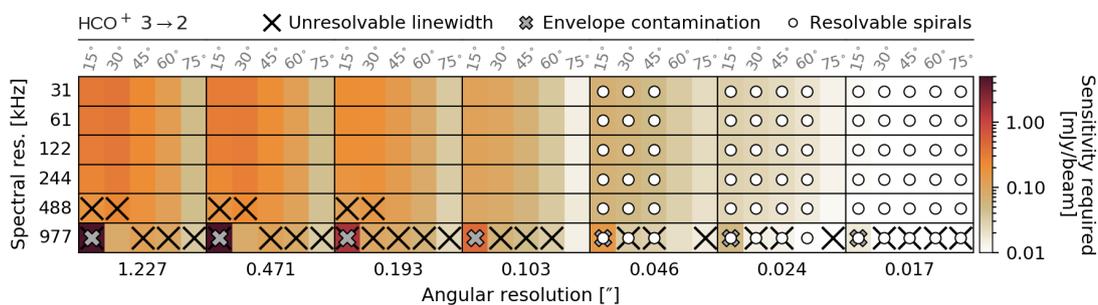
Figure 4.16: Same as Figure 4.11 but for HCO^+ $3 \rightarrow 2$.
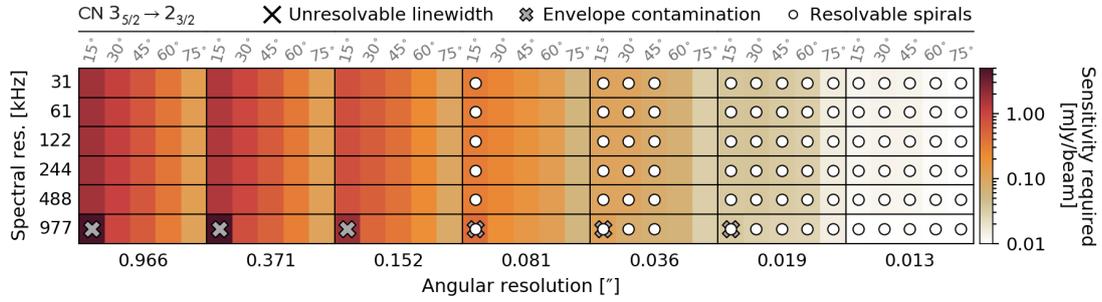
Figure 4.17: Same as Figure 4.11 but for CN $3_{5/2} \rightarrow 2_{3/2}$.
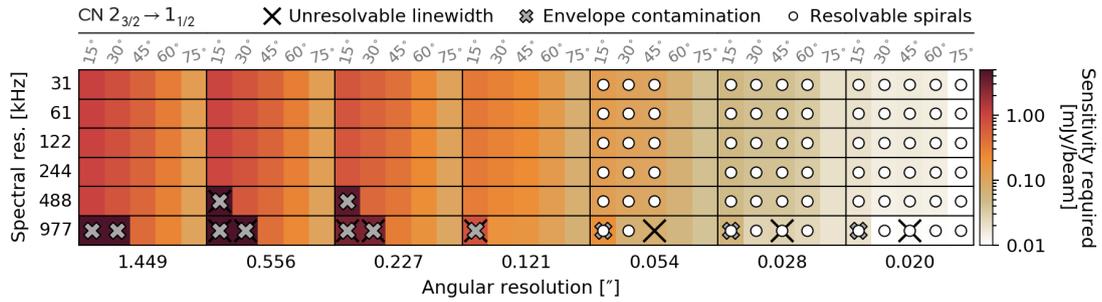

Figure 4.18: Same as Figure 4.11 but for CN $2_{3/2} \rightarrow 1_{1/2}$.
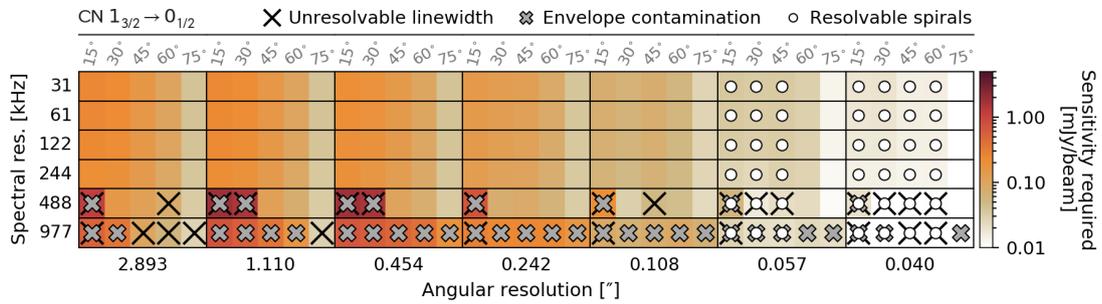
Figure 4.19: Same as Figure 4.11 but for CN $1_{3/2} \rightarrow 0_{1/2}$.
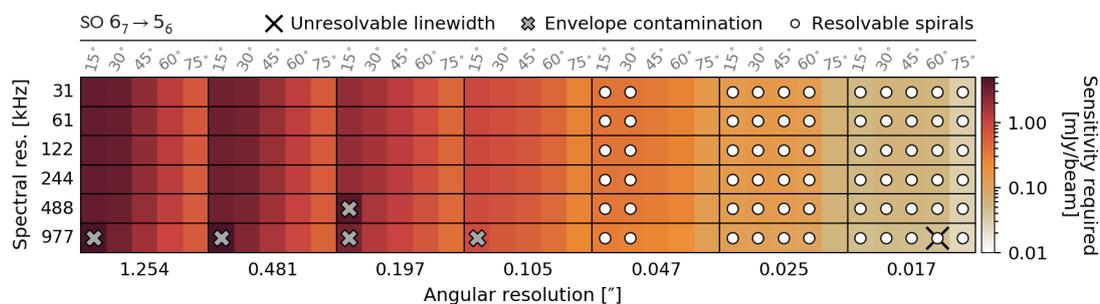
Figure 4.20: Same as Figure 4.11 but for SO $6_7 \to 5_6$.
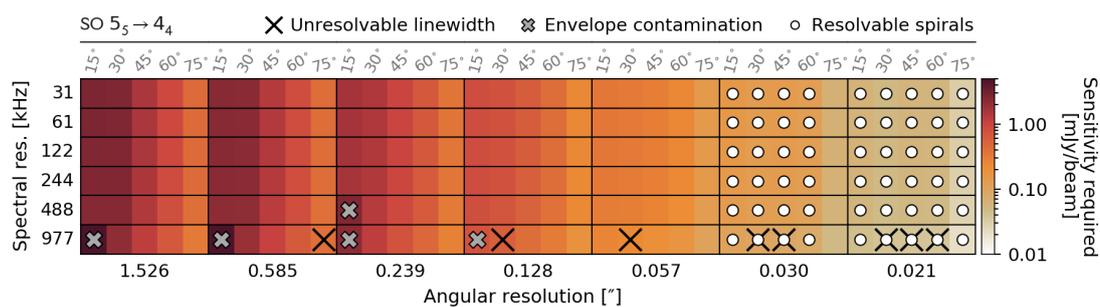

Figure 4.21: Same as Figure 4.11 but for SO $5_5 \to 4_4$.
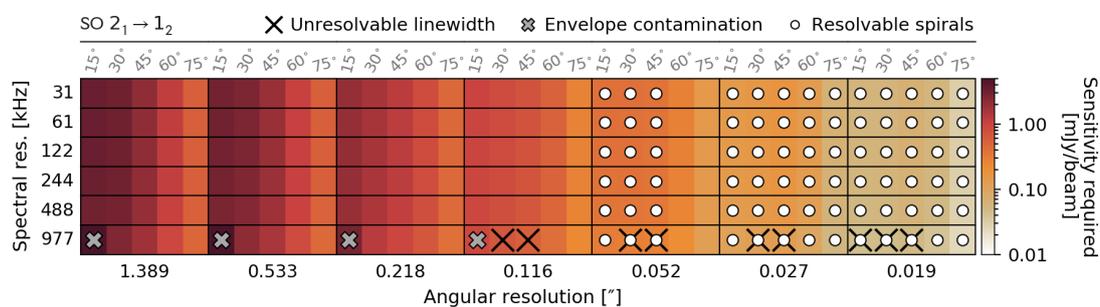
Figure 4.22: Same as Figure 4.11 but for SO $2_1 \to 1_2$.

regime. All of the CO isotopologues considered occupy this regime in the disc spirals, and hence the difference in flux lies within this dependence range. Strictly speaking, the curve of growth defines how the equivalent width of a line depends on the column density, but because the line shape is dominated by a Gaussian, i.e. the Lorentz damping wings are unimportant, it is the peak of the absorption feature that changes. However, at very high optical depths, such as occurs in the innermost disc in CO, the line becomes saturated. As a result, the FWHM of the line feature changes, rather than the peak, in order to maintain the curve of growth dependence. This phenomenon is illustrated by the orange line spectra in Figure 4.23.

Typically, for a particular temperature, the fractional population of levels decreases as the energy of the levels increases. This effect can broadly be seen across all molecules in Figure 4.8, albeit with some nuances due to the complex nature of the energy level structure of some species. One of these nuances is the roughly constant fractional population of CN from $N = 0$ to $N = 6$, which is used to investigate the effect of transition frequency on flux detected, somewhat independently of the energy level populations. Figures 4.19–4.17 show that, in this case, the sensitivity required increases with transition frequency, which is expected because the optical depth increases with frequency, resulting in a deeper absorption feature at the same position within the disc model. This phenomenon is illustrated in Figure 4.24.

Spatial resolution

The highest sensitivity required to spatially resolve spiral structure at a significant level (4σ) in the model disc is $0.38\,\mathrm{mJy\,beam^{-1}}$, which is recovered for SO $6_7 \rightarrow 5_6$ (see Figure 4.20). This is attained at an inclination of $i = 15°$ (i.e. close to face-on) when adopting the 'out21' antenna configuration (i.e. $0.047\,\mathrm{arcsec}$), but is
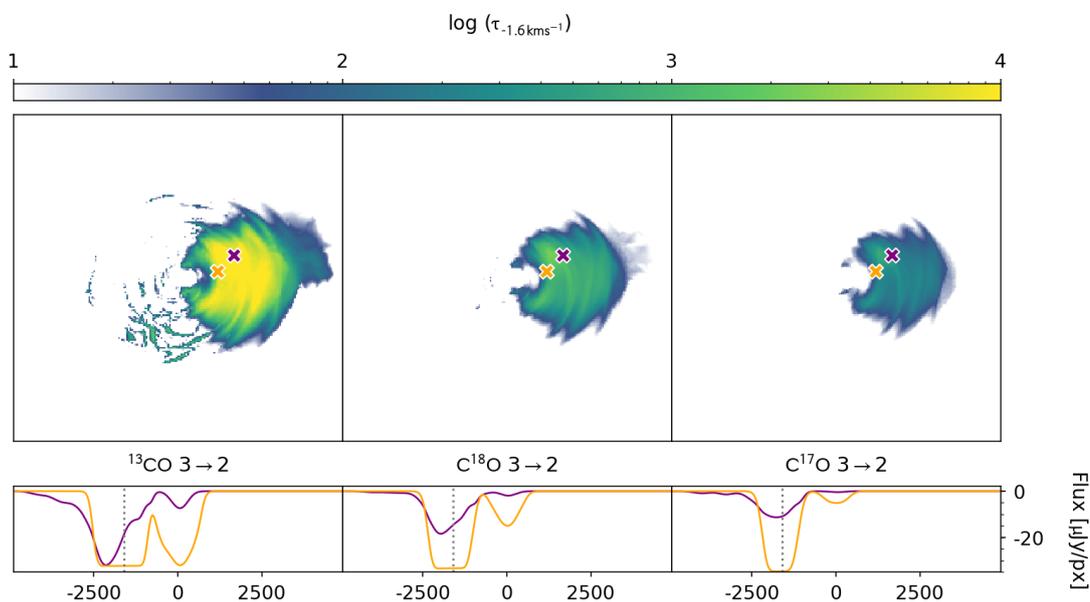
Figure 4.23: Comparison of CO absorption across different isotopologues. The top panels show the optical depth at $v = $ -1.6 km s^{-1} for each molecule and the bottom panels show the line spectra at the pixel positions shown in the top panel, which is the same across all transitions. The dotted gray line on the bottom panels marks $v = $ -1.6 km s^{-1}. These panels are produced for LIME images with no convolution applied.
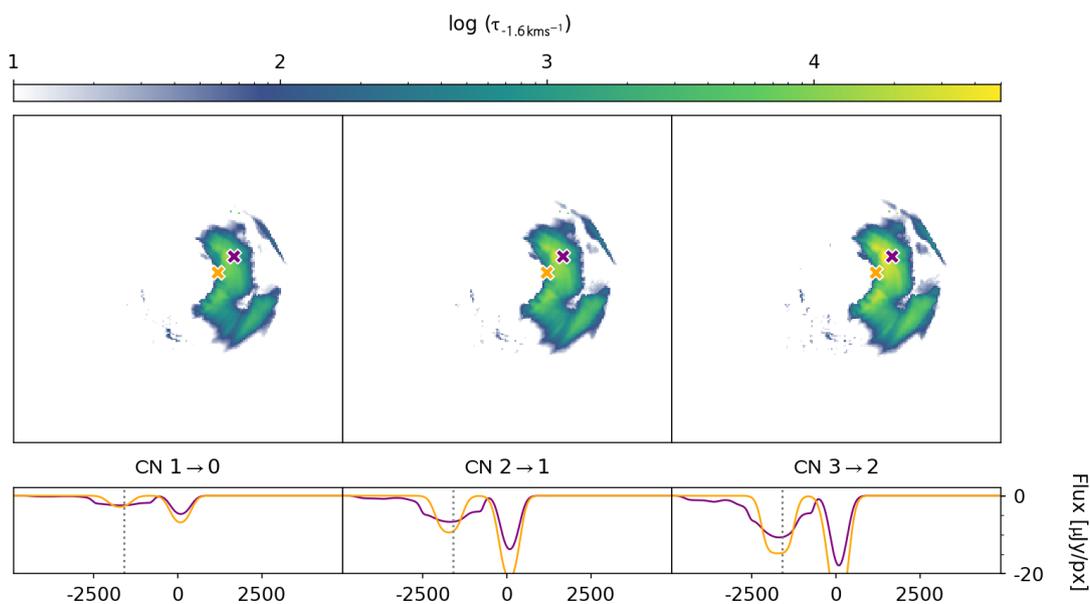
Figure 4.24: Same as 4.23 but across different low-energy CN line transitions.

approximately constant across all channel widths. Therefore, the largest spectral resolution (977 kHz) can be used in order to achieve the highest sensitivity. The ALMA Sensitivity Calculator, with automatic calculations of the precipitable water vapour and sky and system temperatures, indicates that, for a spectral resolution of 977 kHz, a sensitivity of $0.38\,\mathrm{mJy\,beam^{-1}}$ for SO $6_7 \rightarrow 5_6$ requires an on-source time of 11.9 hr. As this is the most optimistic case for the results presented in Figures 4.11 and 4.12, I find that in order to spatially resolve some form of spiral structure in a protosolar-like, Class 0 disc, a minimum of 12 hr of on-source time is required. Therefore, detecting spiral structure at a significant level in a relatively nearby, young, embedded system is feasible, but requires a dedicated observation.

Spectral resolution

Figures 4.11–4.17 indicate that if the condition of spatially resolving the spiral structure is relaxed, and instead the focus is on *spectrally* resolving the spiral structure, then much shorter observation times are permissible. For example, the sensitivity required for a 4σ detection of H_2CO $3_{0,3} \rightarrow 2_{0,2}$ in the spirals is approximately $2.3\,\mathrm{mJy\,beam^{-1}}$ when using a large beamsize. As a narrow channel spacing is preferable for spectral resolution, 31 kHz is used with the ALMA Sensitivity Calculator, again with automatic calculations of the precipitable water vapour and sky and system temperatures, to determine that this sensitivity requires an on-source observing time of ≈ 7.7 hr. If a coarser spectral resolution of 244 kHz is adopted, which is still sufficiently smaller than the linewidth across Figures 4.11–4.17, then an on-source observing time of ≈ 1.0 hr is sufficient. This is firmly within the capabilities of ALMA and is consistent with the recent detection of molecules within low resolution observations of young protoplanetary discs (e.g. Ohashi *et al.*, 2014; Sakai *et al.*, 2014, 2016; Tobin *et al.*, 2012, 2016).

The pressing question here is whether spiral structure can be distinguished spectrally from such observations. In order to investigate this I extract molecular line spectra for the species considered across the different antenna configurations, for a channel width of $244\,\text{kHz}$. I extract the spectra at pixel positions in pairs that are symmetric about $x = 0$, along the $y = 0$ axis, in order to ensure a range of the disc morphology and structure is sampled. I then compare spectra taken from the symmetrically positioned pixels in order to determine if non-axisymmetric disc structure can be distinguished. This process is completed across the range of different angular resolutions in order to assess if line features within the spectra are distinguishable for low angular resolution observations and, if so, whether these line features are faithful to the spectra from the high angular resolution observations, or instead are tainted by convolution. Figure 4.25 shows the integrated intensity maps with the pixel positions overplotted for ^{13}CO, at an inclination of 45°, along with line spectra plots. This is intended to serve as a representative example but the plots for all of the transitions are given in Appendix B.

As can be seen in Figure 4.25, at an inclination of 45° the line spectra convolved with large beamsizes are not necessarily faithful to the underlying spectral structure. This is because at the highest angular resolution, spectra taken from the left and right sides of the disc show a line feature at positive or negative velocities (excluding the envelope centered at $0\,\text{km}\,\text{s}^{-1}$) due to either being red or blue-shifted in respect to the observer. At the lowest angular resolutions, however, all spectra exhibit features at both positive and negative velocities. This finding applies to all of the transitions considered, which means that in order to achieve a compromise between flux and spectral accuracy, intermediate beamsizes (in terms of the beamsizes available for ALMA) are required.

At intermediate beamsizes, Figure 4.25 shows that overall the relations be-
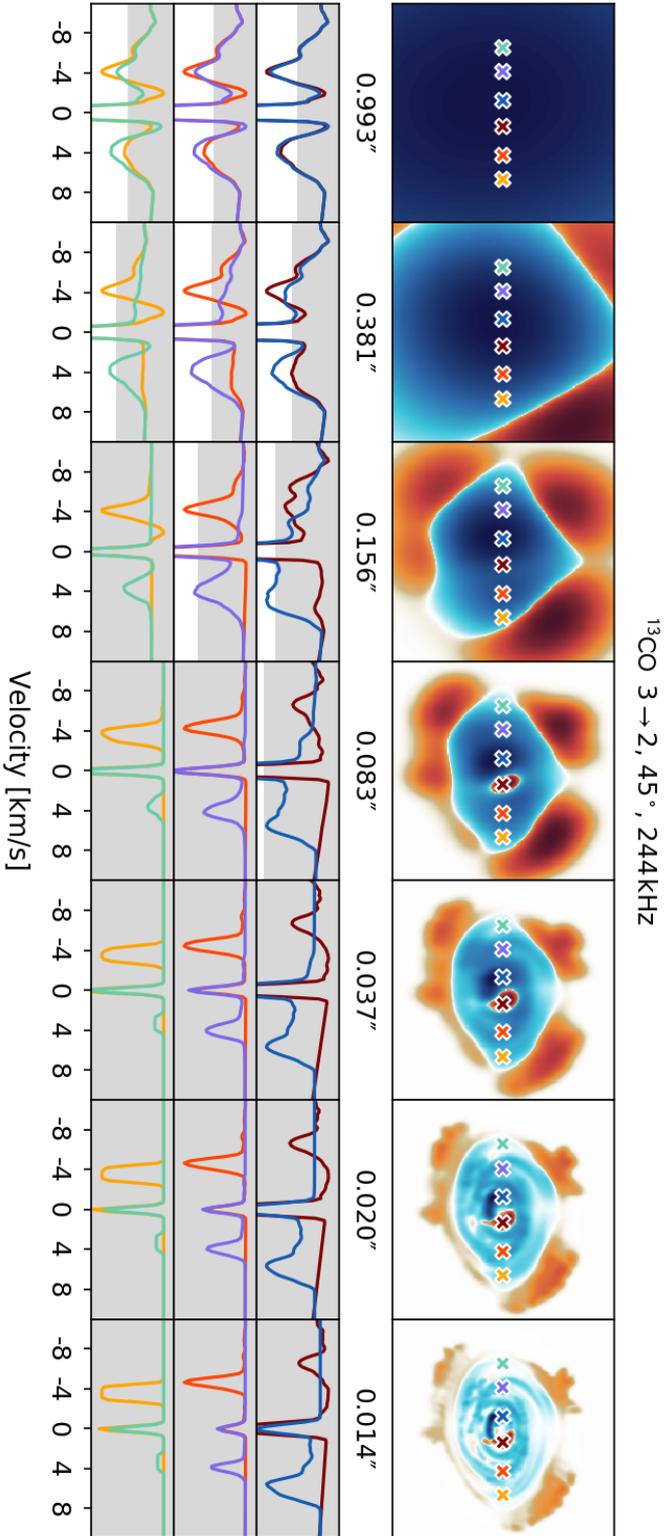
Figure 4.25: Integrated intensity maps of ^{13}CO $3 \rightarrow 2$ for an inclination of $45°$ and different antenna configurations (top panels). The integration is performed from -12 to $-1\,\mathrm{km\,s^{-1}}$ and 1 to $12\,\mathrm{km\,s^{-1}}$, in order to avoid the envelope contribution. Overlaid on the integrated intensity maps are crosses denoting the positions of molecular spectra extraction. These extracted molecular spectra are displayed below the intensity maps for a spectral resolution of $244\,\mathrm{kHz}$, normalised against the non-envelope minimum and maximum fluxes. The grey regions in the spectra plots denote 4σ for a $12\,\mathrm{hr}$ on-source observation, as calculated with the ALMA Sensitivity Calculator.

tween line peaks originating in the blue-shifted and red-shifted portions of the disc are maintained from the highest angular resolution observations. Again this is true for all of the molecular line transitions considered, and so intermediate angular resolution spectra could be used to infer the presence of non-axisymmetric structure in a young, embedded disc. This is, however, under the assumption that a sufficient noise level can be reached as Figure 4.25 indicates that 12 hr of on-source time only offers significant peak ^{13}CO detection for the largest angular resolutions. Note also that this determination becomes less reliable as the disc approaches an edge-on inclination because the complexity of the spectra increases due to the enhanced amount of material along the line-of-sight.

Position-velocity diagrams

Whilst it may be possible to infer non-axisymmetric structure from relatively low angular resolution observations via spectral analysis, concluding that this structure is spiral in nature, and therefore possibly driven by GIs, requires more evidence. A particularly strong indicator of spiral structure in Galactic simulations is the detection of finger-like features in a position-velocity diagram (see e.g. Bissantz *et al.*, 2003; Li *et al.*, 2016; Rodriguez-Fernandez & Combes, 2008), which can also be applied to GI-active protoplanetary discs (Douglas *et al.*, 2013). Therefore, I produce PV diagrams for all of the molecular transitions considered in this chapter, across the entire parameter space. These can be found in Appendix C, but here the PV diagram for ^{13}CO (without Keplerian fits) is shown as a representative example.

Figure 4.26 shows the position-velocity diagram for ^{13}CO across different inclinations and antenna configurations, for a channel width of 244 kHz. As can be seen, near edge-on (90°) inclinations are required to distinguish finger-like structure in the PV diagram. Moreover, in general high angular resolutions are also
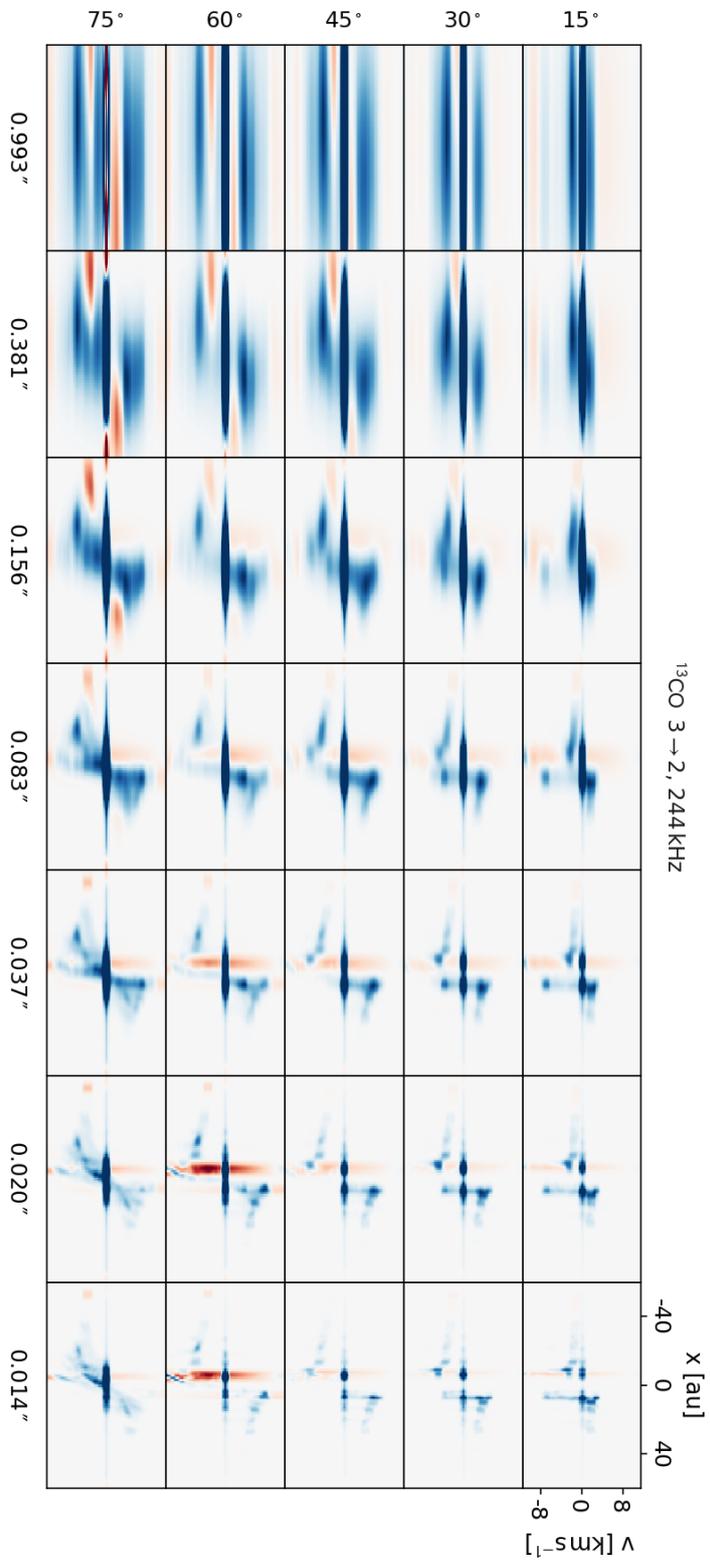
Figure 4.26: Position-velocity diagrams for ^{13}CO $3 \to 2$ across different disc inclinations and antenna configurations, for a spectral resolution of 244 kHz. The top right panel indicates the position and velocity ranges of the observed disc model, which are constant across all panels.

required, which, when cross-referencing with the sensitivity chart (Figure 4.11) suggests that if the spirals cannot be spatially resolved, then they cannot be identified in PV diagrams either. However, a caveat to this exists when considering intermediate angular resolutions and near edge-on inclinations. For 'out13' and 'out18' antenna configurations, the sensitivity charts indicate that distinguishing spiral structure in an integrated intensity map is not feasible for practically all of the molecular transitions considered, regardless of inclination. Contrastingly, on the basis of results shown in Figure 4.26, an argument can be made for the presence of non-axisymmetric structure for the same antenna configurations, when the disc is nearly edge-on. This is because the PV diagram showcases asymmetric features at positive and negative velocities. Furthermore, the high-contrast individual fingers seen at the highest angular resolutions, which directly trace the spiral structure, are essentially blurred together at lower angular resolution. These results hold true for all of the molecular transitions considered. Therefore, the presence of asymmetric absorption features extending to high positive and negative velocities from the center of a PV diagram could be indicative of GI-driven spiral structure in discs.

Determining the presence of non-axisymmetric structure from line spectra or PV diagrams requires intermediate beamsizes (≈ 0.1–0.2 arcsec for Band 6 and 7 of ALMA) in order to achieve a compromise between detected flux and convolution effects. However, beyond this criterion, each method has its strengths and weaknesses for identifying non-axisymmetric structure. For example, PV diagrams require nearly edge-on inclinations in order for clear finger-like structure to be seen, whereas asymmetric spectral line features favour orientations closer to face-on. Moreover, determining the presence of non-axisymmetric structure from line spectra is potentially possible at coarser angular resolutions, although concluding that the non-axisymmetric structure is spiral in nature is only possi-

ble with PV diagrams when considering the methods used in this chapter. An alternate method of confirming spiral structure may be to calculate the residuals between first moment maps and a Keplerian model (see e.g. Walsh *et al.*, 2017), if the deviations from Keplerian rotation in the disc are large enough, and the correct observational configurations are adopted. In summary, the information that can be extracted from spectral features in observations depends on the techniques used, and, regardless of technique, the transition observed, the system inclination and the angular resolution of the observation.

4.3.2   Significance of absorption features

All detected spectroscopic features of non-edge-on discs observed around T Tauri stars are emission features (e.g. Ansdell *et al.*, 2017; Williams & Cieza, 2011). This is because an irradiation-dominated disc has a surface temperature that is higher than its interior temperature, even when viscous heating is included in models via the α-disc prescription. Here, however, a disc model that is viscosity-dominated is used because the focus is on the earliest and most observationally challenging stages of disc formation. As a result, the vertical disc structure resembles cooler surface layers obscuring a hot midplane, rather than the warm surface layer seen in observations and simulations (see e.g. Henning & Semenov, 2013, and references within), which means the majority of the disc model is seen in absorption. Therefore, absorption could be a signature of a young, embedded protoplanetary disc dominated by viscous heating.

Because the temperature falls off as roughly $r^{-0.5}$ in the α-disc prescription, the detection of absorption across the majority of the extent of the disc would imply that this viscous heating is global in nature. As is shown in Chapter 2, gravitational instability can drive global shock heating throughout the disc that warms the midplane to large radii. Therefore, although confirming non-axisymmetric

structure is certainly a challenge in young, embedded discs, inferring the development of gravitational instability from low resolution absorption signatures may still be possible.

However, an unwanted consequence of absorption features is that, at low angular resolution, emitting and absorbing regions can be blended together, which will obfuscate the observed flux. Consequently, these opposing regions could destructively interfere, greatly reducing the flux that is received. This could then indicate that the observed system possesses a much weaker flux than it actually does, which could essentially mimic the effects of depletion. As this is a burgeoning field of research, ensuring reliable results are recovered from observations is of pivotal importance. Thus, care should be taken to account for this effect when analysing integrated line intensity maps and line spectra.

The absorption features recovered from the model disc used in this work originate in the surface layers of the disc. This is due to, firstly, the high optical depths of the continuum even at the lowest frequencies (see Chapter 3), and secondly, because the optical depths of all the transitions featured in this work, including less abundant CO isotopologues, are very large as shown in Figure 4.27. Consequently, it is important to emphasise that such high optical depths will lead to systematic underestimates of column densities and disc masses. Recently, Yu et $al.$ (2017) have found that high optical depths in a (gravitationally stable) $0.03\,\mathrm{M_\odot}$ protoplanetary disc model can lead to underestimated disc masses even for the most optically thin CO isotopologue they consider, $C^{17}O$. Moreover, Miotello et $al.$ (2017) find that the optical depth effects will be larger (and more complex) for more massive discs, and hence the disc mass will be more severely underestimated.
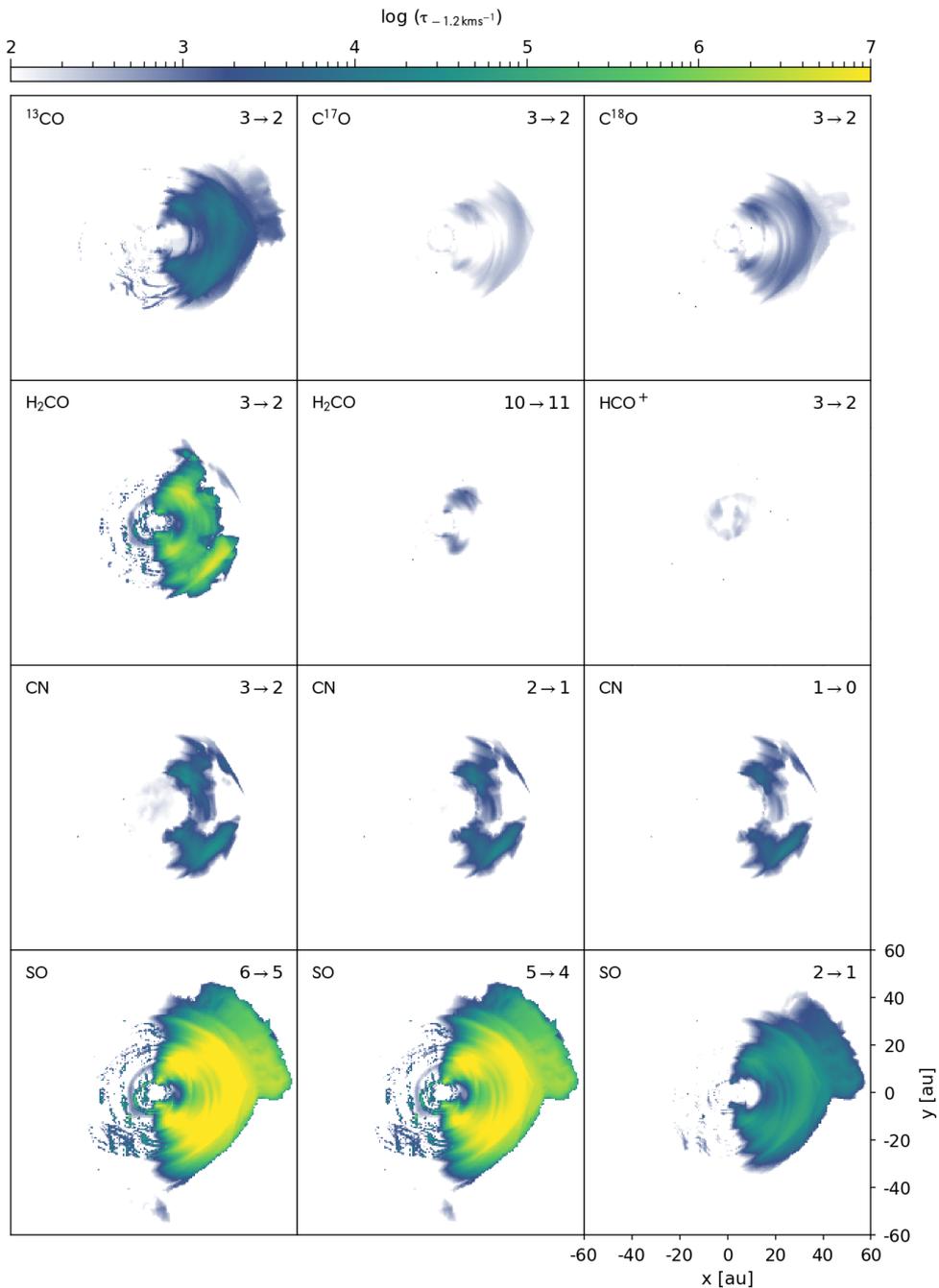
Figure 4.27: Optical depth at $v = $ -1.2 km s^{-1} for each molecular transition, at an inclination of 15°, calculated from the LIME images directly. The bottom right panel indicates the physical scale of the disc model, which is constant across all transitions shown.
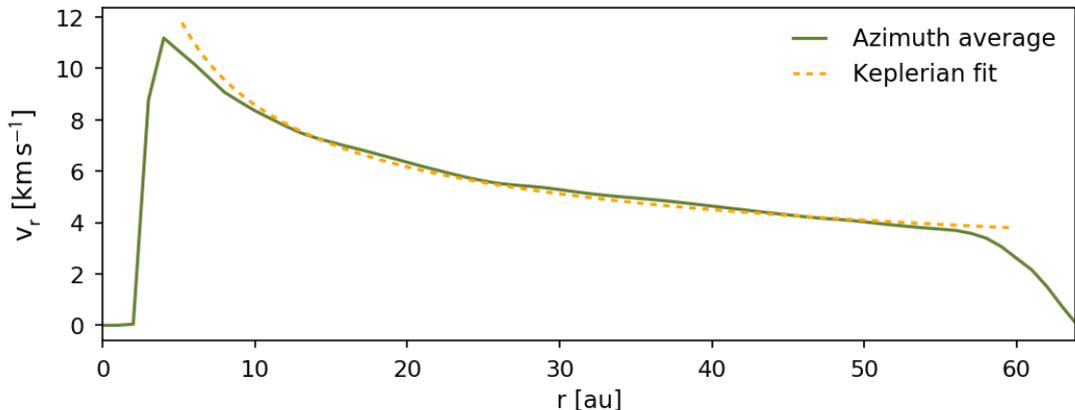
Figure 4.28: Azimuthally averaged rotational profile of the model disc showing that the disc rotation is Keplerian-like.

4.3.3   Protostellar mass estimates

The mass of the central protostar can be estimated by fitting a Keplerian curve to the position-velocity diagram of detected flux from the disc, as long as the disc rotational profile is sufficiently Keplerian. This may not be true for discs possessing non-axisymmetric structure, such as self-gravitating discs with spiral patterns. For the model disc used in this thesis, however, the assumption of Keplerian rotation is valid because the azimuthally averaged rotational profile can be closely approximated by a Keplerian curve across most of the disc, as shown in Figure 4.28. Out to 50 au, the Keplerian profile is given by

$$v_r = \sqrt{\frac{G\left(M_s + M_d\left(r/50\,au\right)\right)}{r}}, \tag{4.2}$$

where G is the Gravitational constant, M_s is the protostellar mass ($0.8\,\mathrm{M_\odot}$) and M_d is the protoplanetary disc mass ($0.17\,\mathrm{M_\odot}$). Note that the non-negligible mass of the protoplanetary disc is accounted for in the radial velocity, and is calculated as a function of radius using an exponent that is consistent with the azimuthally averaged surface density distribution of the model disc ($\Sigma \propto r^{-1.0}$).

4. LINE ABSORPTION AND PROTOSTELLAR MASS ESTIMATES

The aim of fitting the PV diagrams is to constrain the total protostellar and protoplanetary mass. Therefore, for this I use a slightly adjusted Keplerian profile

$$v_r = \sqrt{\frac{G\left(M_s + q * M_s\left(\left(r - 5\,au\right)/50\,au\right)\right)}{r}} \qquad (4.3)$$

where the inner disc hole ($r < 5\,au$) and outer most disc ($r > 55\,au$) are omitted in the fit, and q is the disc-to-star mass ratio. The value assumed for q is important to the fit and here I use $q = 0.21$, which is the disc-to-star mass ratio for the model disc used in this chapter, in order to present the most accurate results. However, deriving protostellar masses from real observations will require an estimate of this value. For a disc to be gravitationally unstable, typically $q > 0.1$. Hence, this can provide a lower limit for systems suspected to be self-gravitating. If the the disc-to-star mass ratio is underestimated then the derived protostellar mass will be overestimated. Similarly, if the disc-to-star mass ratio is overestimated then the protostellar mass will be underestimated. The disc-to-star mass ratio therefore introduces a systemic uncertainty that should be taken into account for young, embedded discs.

In order to fit Keplerian curves to the PV diagrams produced in Section 4.3.1, rotational profiles must first be extracted. I utilise two different methods for determining the rotational profiles. In the first method ('maximum') the maximum flux at each x-position is found. This gives a rotational profile, $v_{x,max}$. In the second method ('upper-edge'), as implemented by Seifried *et al.* (2016), at each x-position the y-axis is iterated through from high to low absolute velocity. The y-position is recorded for the corresponding x-position when the flux within a pixel first exceeds the sensitivity required (4σ, see Section 4.3.1). This gives a rotational profile, $v_{x,upper}$. For both methods the inner 5 au of the disc is omitted and only the upper right and lower left quadrants are fitted. Once the rotational profiles have been determined, Keplerian curves of the form given by Equation 4.3
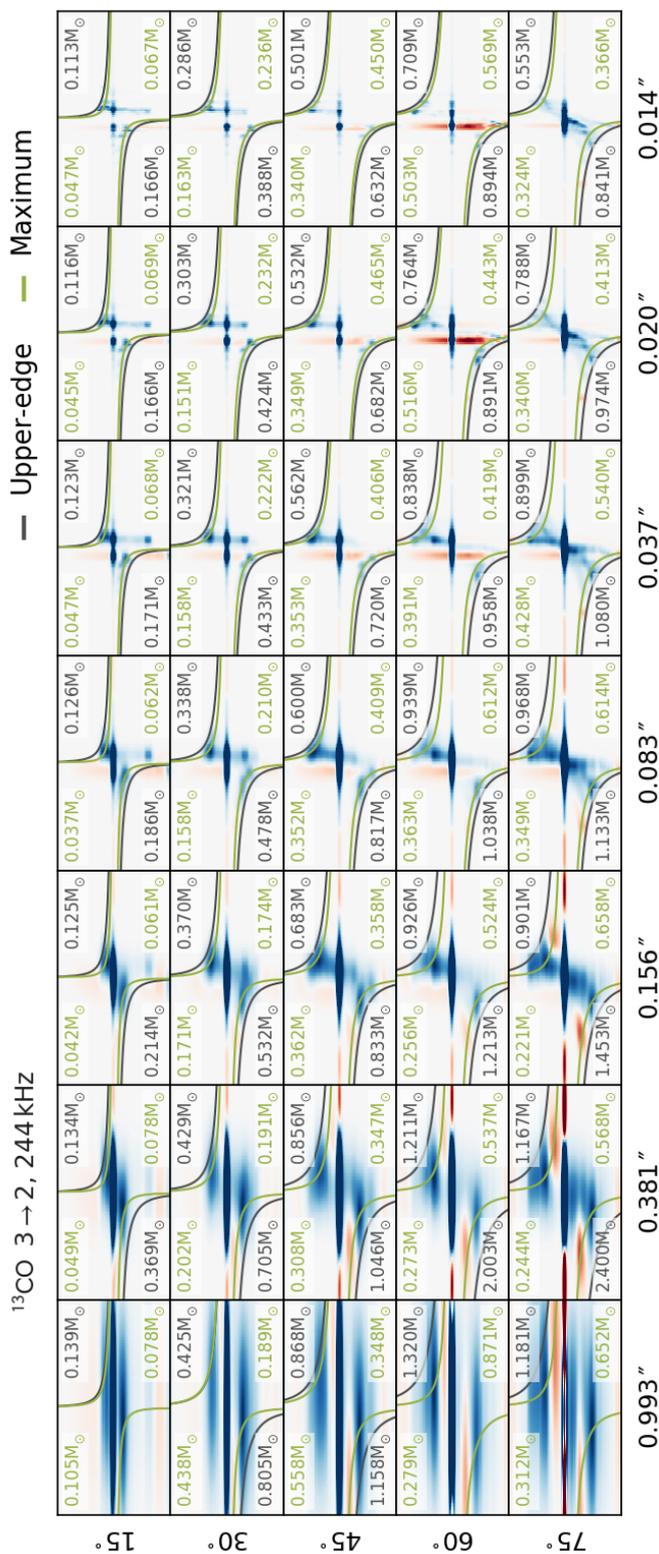
Figure 4.29: Position-velocity diagrams with Keplerian fits for $^{13}CO\ 3 \to 2$ across different disc inclinations and antenna configurations, for a spectral resolution of 244 kHz. The x-axis of each panel represents position and the y-axis of each panel represents velocity. Two different methods for fitting the Keplerian curves are used: in the first method ('maximum') the maximum flux at each x-position is found; and in the second method ('upper-edge') the location where the 4σ flux is first exceeded along the y-axis at each x-position is found.

4. LINE ABSORPTION AND PROTOSTELLAR MASS ESTIMATES

are fitted using the `curve_fit` routine in PYTHON. From these curves the protostellar mass, M_s, is derived. Figure 4.29 shows illustrative Keplerian fits and corresponding protostellar masses for each quadrant and fitting method, for ^{13}CO $3 \rightarrow 2$ at a spectral resolution of $244\,kHz$, across a range of angular resolutions and disc inclinations. Similar images for the other molecular transitions and spectral resolutions used in this chapter can be found at https://goo.gl/AVkHRj.

Figures 4.30 and 4.31 present the protostellar masses derived with Keplerian fitting, M_{kep} (equivalent to M_s above), averaged over both quadrants, as a fraction of the actual protostellar mass, M_{sim}. Note that the rotational velocity depends on the inclination as $v_r \propto \sin i$. Therefore, the recoverable protostellar mass also depends on the inclination, i, which is accounted for in the simulation mass as $M_{sim} = 0.8\,M_\odot \sin^2 i$. The spectral resolution used in Figures 4.30 and 4.31 is $244\,kHz$ as this offers the best compromise between on-source time required and distinction of the finger-like features in the PV diagrams. Figures showing the derived masses for the other spectral resolutions adopted in this chapter are shown in Appendix D. Generally, at higher spectral resolutions the mass estimates are relatively unchanged, particularly at small beamsizes, and at lower spectral resolution the protostellar mass values become increasingly unreliable as the Keplerian form is lost.

The derived protostellar masses vary considerably over the parameter space used, which is due to the large variability of the features seen in the PV diagrams (see Appendix C). For most molecules the derived protostellar mass fraction is slightly smaller for edge-on inclinations as compared to face-on inclinations. This is a result of a combination of two factors. Firstly, as the inclination approaches face-on, the radial motions within the disc can contribute to the apparent rotational velocity, thereby increasing the derived protostellar mass, M_{kep}. Secondly, as mentioned previously, the recoverable protostellar mass, M_{sim}, decreases as the
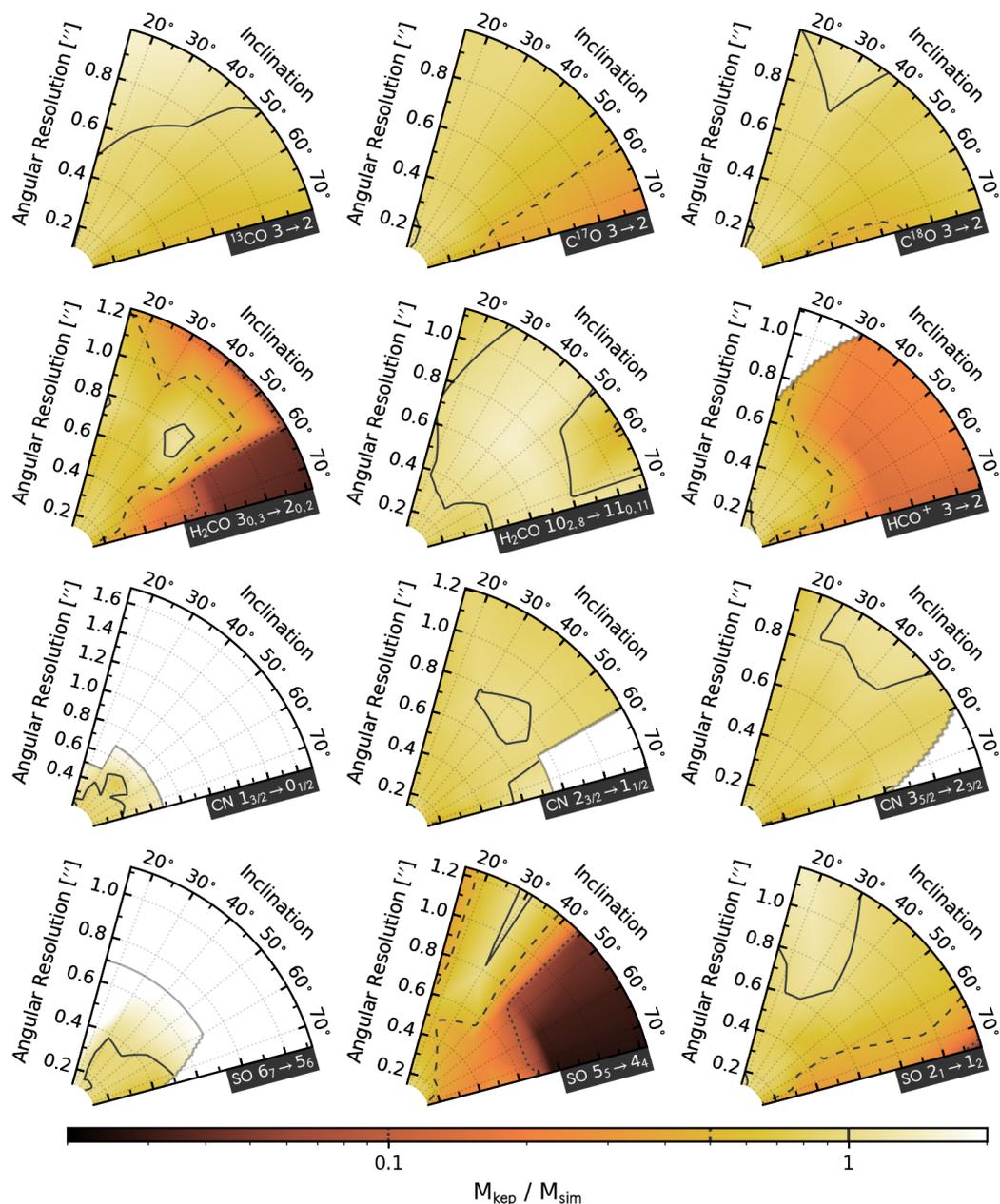
Figure 4.30: Fraction of actual protostellar mass derived by fitting Keplerian curves to the PV diagrams of various molecular transitions, across different disc inclinations and angular resolutions, for a spectral resolution of 244 kHz. In the 'maximum' method used here to fit the Keplerian curves, the maximum flux at each x-position is found. The contours denote fractions of 0.1 (smallest-dashes line), 0.5 and 1.0 (solid line).
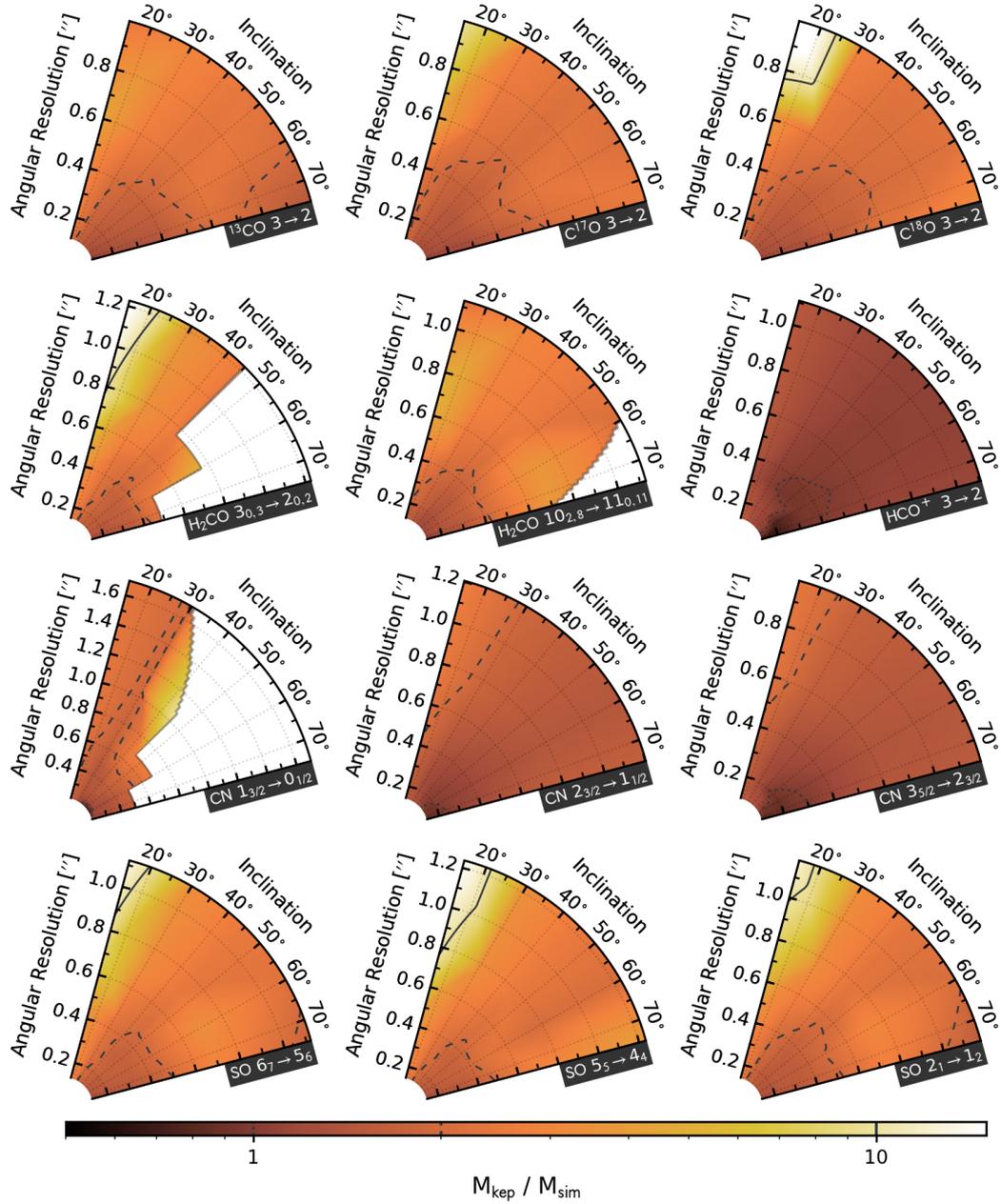
Figure 4.31: Same as Figure 4.30 but in the 'upper-edge' method used here to fit
the Keplerian curves, the location where the 4σ flux is first exceeded along the
y-axis at each x-position is found. The contours denote fractions of 1.0 (smallest-
dashes line), 2.0 and 10.0 (solid line).

inclination approaches face-on. Therefore, despite the fact that the derived mass varies considerably from edge-on to face-on, the fraction of the actual protostar mass recovered tends to only vary slightly with inclination.

Even though the fine structure is lost in the PV diagrams as angular resolution is decreased, the Keplerian fits remain relatively consistent. As a result, there is only a small change in the protostellar mass up to intermediate beamsizes (e.g. 0.086 arcsec for ^{13}CO $3 \rightarrow 2$). However, beyond these intermediate beamsizes, the Keplerian signature can be largely obscured. This is demonstrated by the lack of fit for several molecules, which incidentally does not occur for the smallest beamsizes, and, similarly, by the sudden drop in protostellar mass for H_2CO $3_{0,3} \rightarrow 2_{0,2}$ and SO $5_5 \rightarrow 4_4$ when using the 'maximum' method. Therefore, high angular resolution observations are preferable for the derivation of the protostellar mass from PV diagrams. Otherwise, caution is strongly advised.

In general terms, the 'upper-edge' method results in protostellar masses that are 2–10 times larger than the 'maximum' method. This is because, across the entire parameter space, the Keplerian curves fit to $v_{x,max}$ have lower linear eccentricities than the Keplerian curves fit to $v_{x,upper}$. Consequently, the use of the 'upper-edge' method generally overestimates the protostellar mass whereas the use of the 'maximum' method typically underestimates the protostellar mass in the model used.

The error in the mass is calculated as the standard deviation of the mean unless only one quadrant can be successfully fit, in which case the error of the derived protostellar mass is taken as the standard deviation of the fit. This results in typical errors of < 20 per cent (except at the lowest angular resolutions) for the former case, and < 10 per cent for the latter case. Hence, for both fitting methods there is only a very small region of the parameter space where masses that are accurate within errors are recovered. Due to this, and because

the underlying Keplerian structure is complicated by inclination and angular resolution effects, deriving the protostellar mass from PV diagrams of a GI-active disc is fraught with difficulty. Moreover, here I have fitted Keplerian curves to perfect PV diagrams (i.e. without noise). The introduction of realistic noise will most likely further complicate the extraction of protostellar mass.

4.3.4 Comparison with other studies

Douglas *et al.* (2013) explore the observability of spiral features in a more massive, gravitationally unstable, disc ($0.39 M_\odot$; see Ilee *et al.* 2011 and Chapter 2) than is considered in this thesis. The authors conclude that spiral features are detectable in absorption across a large parameter space. However, the sensitivities the authors adopt were calculated for a bandwidth of $1.875\,\mathrm{GHz}$, which is the available bandwidth of the basebands within the ALMA band receivers, rather than the expected linewidth of each transition as is appropriate (approximately 350–$450\,\mathrm{kHz}$ across the frequencies listed in their Table 1). Hence, their sensitivities are significantly higher than I find, meaning Douglas *et al.* (2013) report much shorter observation times are required than I report in this chapter. Nevertheless, the results in this chapter support the finding of Douglas *et al.* (2013) that a gravitationally unstable disc can be detected in absorption and confirm that, in principle, spiral features can be inferred from observations of protoplanetary discs both spatially and spectrally if the SNR is high enough.

Seifried *et al.* (2016) use 3D magnetohydrodynamics to simulate the collapsing of two different sized molecular cores into magnetically threaded protoplanetary discs systems: model 1, which is a $15.2\,M_\odot$ multi-protostar system with a disc that is most likely much more massive than the disc model used in this chapter; and model 2, which features a Bonnor-Ebert sphere envelope and evolves to form a single $0.62\,M_\odot$ protostar and a disc with an approximately $70\,\mathrm{au}$ radius, both

of which are comparable to the disc model used in this thesis. The authors use RADMC-3D to produce line images for different molecular transitions, and then use CASA to synthesise observations of these line images across different observing times, angular resolutions, disc inclinations and weather conditions. Overall, the authors conclude that Class 0 discs should be observable in numerous molecular transitions, across a wide range of observational parameters. However, no structural detail is apparent in the integrated intensity maps for their model 2, although this is partly due to the fact that this model remains gravitationally stable, and hence does not develop strong spiral features. On the other hand, their model 1 disc does contain non-axisymmetric structure, but this structure is only partially reflected in the integrated intensity maps. Therefore, this supports the findings of this chapter that spatially resolving spiral features is extremely challenging in protosolar-like discs.

The integrated intensity maps in Seifried *et al.* (2016) all show line flux in emission, whereas for the model disc used in this work the majority of line flux is seen in absorption as previously mentioned. A simple reason for this is that their model 2 is gravitationally stable and hence does not feature global heating of the midplane as in our model. However, this argument does not hold for their model 1 as it is gravitationally unstable. Therefore, an alternative explanation is that the authors assume constant abundances for all species they consider, whereas in Chapter 2 it is shown that spiral shocks have a significant effect on the abundances of many molecular species. However, this should only affect the contrast between the spiral and inter-spiral regions in their intensity maps, rather than convert emission to absorption. Moreover, the authors adopt lower abundances, which are more in-keeping with the peak abundances recovered for the disc model I use (see Chapter 2), and find similar results in emission. Dust temperatures that are significantly lower than the gas temperatures can potentially result in line fluxes

seen in emission rather than absorption, which can arise if the dust and gas temperature are thermally decoupled. Whilst Seifried *et al.* (2016) consider some degree of decoupling, in the regions of interest the dust and gas temperatures are equivalent, as is the case for the disc model used in this chapter. Therefore, I instead posit that the reason Seifried *et al.* (2016) see their disc models in emission is because the amplitudes of the spiral density waves in their disc models are lower than in the disc model used here. Hence, the midplane regions are likely not heated as significantly by global shocks. More simulations are certainly required to constrain the conditions under which young, embedded protoplanetary discs will be seen in absorption.

Seifried *et al.* (2016) also explore how feasible it is to extract protostellar masses from noisy synthesised PV diagrams of their disc models. In general they find that ALMA should be able to detect Keplerian rotation profiles in Class 0 systems across different molecular transitions, observational durations, observing conditions, angular resolutions and different disc inclinations. Given enough on-source time, the results in Section 4.3.1 tend to support this conclusion. The authors also find that the fraction of the protostellar mass recovered increases as the inclination approaches face-on, although the Keplerian profile loses distinction, which supports the results presented above. Moreover, the protostellar masses they derive increase with angular resolution, which I also find is true for the disc model used in this chapter. Whilst Seifried *et al.* (2016) find that the protostellar masses derived from Keplerian fits to the 'upper-edge' rotational profiles are generally accurate within a few 10 per cent across the majority of their parameter space, I find that this level of accuracy is only achieved for the disc model used here when the 'maximum' method is implemented to constrain the rotational profiles. Indeed, for the 'upper-edge' method I find that the protostellar mass is overestimated by a factor of at least 2 across most of the parameter space;

the accuracy threshold (4σ) is only met when I use the 'upper-edge' method for HCO^+ $3 \to 2$ seen in a non-face-on disc, and for the highest angular resolution observations of the CO isotopologues, the CN transitions and H_2CO $10_{2,8} \to 11_{0,11}$ seen in nearly edge-on discs. Therefore, the results presented in Section 4.3.1 disagree with Seifried *et al.* (2016) in this regard, which could be due to the increased complexity of fitting Keplerian curves to more pronounced finger-like structure seen in absorption. Hence, whereas Seifried *et al.* (2016) suggest using the 'upper-edge' method will result in the most accurate protostellar mass estimates, I find that a one-size-fits-all approach is perhaps inappropriate when considering gravitationally unstable discs.

4.4 Conclusions

4.4.1 Radiative transfer calculations

Line flux maps of a protoplanetary model disc have been produced using LIME and in Section 4.2 methods for obtaining accurate images have been explored. This involved making adjustments to the default sampling behaviour of LIME, comparing LTE treatment to non-LTE treatment, and determining the frequencies that reliably reflect the disc composition. The main results from this section are:

- A custom sampling routine affords the most convergent line flux images for the gravitationally unstable disc model. This custom routine combines rectilinear sampling of the disc with the restriction of grid points at $\tau > 3$. Therefore, specialised grid construction can improve the accuracy of molecular line images produced with LIME.

- A convergence test should be used to find the number of grid points necessary to produce an accurate line flux image. This is model dependent but for the young, gravitationally unstable disc model used in this chapter, a minimum of 1 $\times$ 10^6 points should be used. Note, however, that more grid points are always preferable if the computational cost can be afforded. Incidentally, this number of points is larger than is necessary in the continuum due to the increased complexity of radiative transfer calculations when considering line flux.

- Performing radiative transfer calculations for line fluxes can be extremely computationally expensive due to the coupled nature of the intensity, absorption and emission coefficients, and the level populations. A significant speed-up can be made if LTE is adopted, but the validity of this approximation should be checked by comparing the number density of the emitting regions to the critical

density (or effective excitation density). One can also compare the LTE run to a full non-LTE run in order to ensure the results are not significantly divergent; LTE is an accurate approximation for the disc model used in this work because non-LTE and LTE runs are found to be congruent.

- The frequency of a spectral feature can significantly affect the location of the observable emitting regions. At large frequencies the optical depth is higher, which means that less of the disc material is probed by observations. Consequently, the observed flux will originate from nearer the surface of the disc and hence closer to the critical density boundary, which degrades the applicability of LTE. Therefore, observing embedded protoplanetary discs at low frequencies is recommended.

- The resolution and extent of the abundances should be sufficient to encompass the emitting regions, as otherwise the reliability of line images can be questioned. This could have implications for simulations that distribute fluid elements by mass or density because the emitting regions can be located in low density regions, particularly at large frequencies, and hence may not be well sampled.

4.4.2 Synthetic observations

In Section 4.3 synthetic observations of the model disc were produced by convolving the LIME images with a 2D Gaussian beam across a large parameter space consisting of different molecular transitions, antenna configurations, spectral resolutions and disc inclinations. The observations were assumed to be perfect, i.e. no noise present, in order to determine the sensitivity that is required for a detection (as is typically requested by observation proposals). The model disc represents a $0.17M_\odot$ protoplanetary disc that surrounds a $0.8M_\odot$ protostar likely

to evolve into a Solar-like star. Hence, this work may be indicative of observations of an object similar to our early Solar System. The main results from this section are as follows:

- All transitions considered in this chapter trace spirals to an extent when observed at the highest angular resolution and no noise is present. However, reflection of spiral structure in integrated line intensity maps does not necessarily correlate with the underlying distribution of the species. Therefore, it is imperative that radiative transfer calculations are performed when considering line emission and absorption.

- The gravitational instability within the model disc drives spiral density waves that shock-heat the disc material globally. As a result, because the disc is assumed to be heavily embedded, it is comprised of cooler surface layers obscuring a hot midplane. Consequently, the disc is seen primarily in absorption across all transitions we consider. Therefore, absorption, which can be attributed to infalling material, could also be a signature of GI in Class 0 sources.

- The fact that the gravitationally unstable disc is seen in absorption could introduce complications for low angular resolution observations. This is because emitting and absorbing regions for a particular transition could blend together, reducing the overall flux that is detected. This could then affect further analysis and lead to erroneous conclusions such as the presence of significant depletion.

- All the molecular transitions considered are substantially optically thick ($\tau > 10^2$) in our disc model, even at the lowest frequency implemented (113 GHz; Band 3 of ALMA) and for the least abundant molecule (HCO^+). Therefore, the flux detected is only tracing the upper layers of the disc, which means that estimates of column densities and disc masses derived from line emission or absorption in young, embedded sources will most likely be significantly underestimated.

- The sensitivity required to detect absorption originating in spirals increases with frequency due to the increase in optical depth. The sensitivity also increases with abundance, albeit in a non-linear manner determined by the 'curve of growth'. Therefore, higher frequency transitions of more abundant isotopologues should afford easier absorption flux detections in young, embedded, gravitationally unstable discs. However, the increased optical depths mean that less of the disc material is probed, which will incidentally lead to larger systematic underestimates of column densities and disc masses.

- The sensitivity required for a spiral feature detection does not depend on the spectral resolution used, assuming the spectral resolution is smaller than the linewidth. The caveat to this is if the observed line spectrum is contaminated by the envelope flux contribution, which occurs for most species considered in this chapter when using large angular and spectral resolutions. Therefore, because on-source observing time increases as channel spacing decreases, observing young protoplanetary discs with a spectral resolution of 244–488 kHz is recommended.

- Spatially resolving the spiral structure in a GI-driven, protosolar-like disc should be possible if dedicated observations are performed. For the model disc used in this thesis, a minimum of 12 hr on-source time is required to enable a 4σ detection of SO ($7_6 \rightarrow 6_5$) at an angular resolution of 0.047 arcsec and a spectral resolution of 977 kHz. If a larger angular resolution is used then the on-source time for detection is reduced; an on-source time of 1 hr is required to detect H_2CO $3 \rightarrow 2$ for an angular resolution of 1.505 arcsec at a spectral resolution of 244 kHz.

- Spectrally resolving the spiral structure in a GI-driven, protosolar-like disc may be possible if intermediate beamsizes (e.g. 0.15 arcsec for ^{13}CO $3 \rightarrow 2$) are adopted; at lower angular resolutions the line spectra are altered too much by convolution. If line spectra that are extracted from symmetric positions within

4. LINE ABSORPTION AND PROTOSTELLAR MASS ESTIMATES

the disc show different peak amplitudes then this implies that the disc contains non-axisymmetric structure. However, it is not possible to reliably conclude from this that the structure is GI-driven.

- Direct confirmation of GI-driven spiral structure is achievable via PV diagrams if intermediate beamsizes are adopted. This is because finger-like features can be identified that directly correlate to spiral structure. However, this is only possible for nearly edge-on inclinations, which means that this technique would only work for a fraction of real protoplanetary discs. Nevertheless, with current instruments PV diagrams probably offer the most promising means for confirming the presence of GI-driven spiral structure in young, embedded protoplanetary discs.

- The protostellar mass can be obtained from PV diagrams if the rotation profiles are sufficiently Keplerian. For the disc model used in this chapter, the derived masses are only accurate for a small region of the parameter space. Observations with high angular and spectral resolutions are encouraged in order to best avoid smearing effects of the PV diagram features. However, even in this case the derived protostellar masses are very sensitive to the method used for fitting the rotational profiles. Therefore, caution is advised when deriving the protostellar mass from a GI-active disc that is likely to posses strong spiral features.

In this work the gas and dust temperatures are assumed to be equivalent within the model disc. If this assumption is inaccurate and the dust temperature is significantly lower than the gas temperature, then molecular line fluxes may be seen in emission rather than absorption as has been documented. However, this quandary essentially simplifies to whether the kinetic temperature is equivalent to the excitation temperature, which is the condition for LTE. As I have shown that LTE is appropriate for the model disc across the low energy transitions, the

assumption of thermal balance should be valid (see also Yu *et al.*, 2017, Appendix A). If, on the other hand, higher energy transitions are observed, or the disc is assumed to be less embedded, then the gas and dust temperatures may become decoupled and require recalculating.

A simplistic envelope model has been implemented in the radiative transfer calculations performed in this chapter. This has permitted the straightforward isolation of the envelope contribution in most line spectra. However, several molecular species have been observed to trace material flowing out from, and accreting onto, discs, which could contaminate the recovered line spectra in more complex manners. A method of combatting this is to use a high spectral resolution so that the different kinematic components can be disentangled, but, as the on-source observation time increases with spectral resolution, a compromise will most likely have to be made. An alternative method is to focus on species that do not typically trace envelope accretion or outflows, such as $C^{17}O$ and OCS. In terms of the effects on chemistry, accretion from the envelope can alter the disc composition, and hence synthesised line observations, but observations have indicated that variations are likely to only be significant near the centrifugal barrier (e.g. Sakai *et al.*, 2014; Sakai *et al.*, 2017). Moreover, outflows are known to harbour distinct chemical signatures, but their effects on the disc and envelope are likely to be insignificant. Indeed, Drozdovskaya *et al.* (2015) have shown that wide cavities are needed to directly irradiate the envelope and affect the composition. Therefore, the omission of outflows and envelope accretion should be appropriate for the gravitationally unstable disc model used in this thesis.

Chapter 5

Conclusions

5.1 Summary

This thesis contains work addressing the behaviour of discs surrounding young protostars. The topics discussed are the modelling of the dynamical and chemical evolution and the synthesis of continuum and line observations. The following sections present the most important findings of this thesis.

5.2 A simulation of dynamics and chemistry

Numerous simulations have shown that close to the formation epoch, a protoplanetary disc can have a mass comparable to that of the central protostar. As a result, the GI can develop and drive global spiral shocks throughout the disc, which leads to increases in temperature and density within shocked disc material. Most chemical simulations of protoplanetary discs to date have used the α prescription to describe the kinematic viscosity, but this is only strictly appropriate for local mass transport. Therefore, in Chapter 2 the chemical evolution of a 3D hydrodynamically simulated gravitationally unstable disc was investigated. The model disc in question has a mass of $0.17\,\mathrm{M_\odot}$ and surrounds a $0.8\,\mathrm{M_\odot}$ protostar. The system is representative of a Class 0 object and, moreover, its physical and

chemical evolution may be indicative of our early Solar System.

The chemical evolution of the model disc was considered to have no effect on the dynamics and was followed with a gas-grain chemical network code. It was found that the GI-driven shocks heat the disc material, which enhances the rates of desorption and the rates of some endothermic reactions for many species. Consequently, the gas-phase abundances of most species considered were found to be substantially increased in the spiral arms. Moreover, as the GI-driven spiral arms transport mass globally, and due to the high extinction assumed, the disc was found to have a chemically-rich midplane surrounded by cool surface layers. This is in stark contrast to the structure of a more evolved, axisymmetric disc, where photon-heated layers lie above a cold 'gas-phase desert' midplane. It was also found that the persistent shock heating caused permanent changes in the abundances of some species. In the inner disc the rapid succession of shocks quickly raises the temperature beyond the desorption energies of all neutral species, which leads to higher gas-phase abundances than would be expected in a more quiescent disc. In the outer disc, the effect of periodic shock heating was found to have significant effects on numerous species, such as the increases in the abundances of NH_3, HNO and CN by factors of $> 10^3$. Consequently, CN in particular was found to be a strong tracer of spiral structure in the model disc.

Essentially, the gravitational instability was found to induce significant transient and permanent changes in the chemical composition of a young protoplanetary disc model. An implication of this result is that observations of embedded discs could be used to characterise disc dynamics, even if the structure cannot be resolved spatially or spectrally. For example, a detection of CN in the outer regions of a disc is indicative of high temperatures, which could be produced by GI-driven shocks. Moreover, as the volatility of most COMs is comparable to water ice, shock heating in a GI-active disc may be preserved in the dust

grain ice mantle composition. For example, CH_3OH forms on dust grain surfaces in molecular clouds via sequential hydrogenation of CO; hence methanol ice is bound to CO. However, in the shock-heating regions of a gravitationally unstable disc, methanol ice will be desorbed and then, due to its relatively high desorption temperature, re-adsorb and be bound to H_2O ice rather than CO ice.

Simulations of more evolved protoplanetary discs should perhaps account for the GI phase of evolution when setting initial abundances, especially when considering more complex ices. Ideally, simulations should utilise a self-consistent treatment of molecular core collapse, followed by GI-active evolution (if the disc-to-star mass ratio is large enough) and then a later phase of more quiescent evolution, during which an axisymmetric α-disc prescription becomes appropriate.

5.3 Continuum observations and mass estimates

The recent advancements in observational technologies have led to the detection of non-axisymmetric structure in young protoplanetary discs. However, due to the inherent challenges of observing Class 0 sources, confirmation of GI has remained elusive. Therefore, synthetic continuum observations of gravitationally unstable discs have been used in order to assess the detectability of GI-driven spirals. Chapter 3 builds upon the available repository of results through the use of a model disc that may be analogous to our early Solar System.

In order to produce continuum images, LIME was used to solve the radiative transfer equation. A substantial number of points ($> 2 \times 10^5$) was found necessary to ensure that accurate continuum images of the model disc were produced. The accuracy of resultant images was found to be significantly affected by the weighting and sampling routines employed. In particular, restricting grid points to regions where $\tau < 3$ improved the reliability of the images because more points

were positioned in non-negligibly-emitting regions. Therefore, model-tailored grid construction was found to be important when producing LIME images.

Synthetic observations of the LIME images were produced with CASA across a large parameter space consisting of different frequencies, disc inclinations and dust opacities. It was found that an on-source time of 1 hr during Cycle 5 of ALMA should be sufficient to readily detect the GI-driven spiral structure in 0–60° inclined discs at 90–300 GHz. The optimal frequency for observing young, embedded protoplanetary discs was found to be 230 GHz because this frequency affords the best compromise between angular resolution and sensitivity. Moreover, lower frequencies were found preferable because the disc is substantially optically thick at frequencies beyond 90 GHz. Observations synthesised with a fully extended, maximally operational ALMA antenna configuration were found to be largely congruent with the Cycle 5 observations, implying that the results found will remain relevant throughout the operational lifetime of ALMA.

Continuum observations of protoplanetary discs are routinely used to estimate the masses based on the detected fluxes. However, this method proved to be inherently flawed for gravitationally unstable discs for two primary reasons. Firstly, collapsing the 3D distributions of dust temperature and dust opacity into 1D values for the entire disc is misrepresentative, particularly due to the non-axisymmetric structure. Secondly, the dust temperature and dust opacities in young, embedded discs are largely unknown quantities, and moreover, the often-assumed value of the dust temperature (20 K) was found to be inaccurate for the model disc. When what are believed to be appropriate values of the dust temperature and dust opacity are adopted, the mass was found to be underestimated by a factor of 2.5–30 in a face-on disc, depending on frequency; this underestimate worsens as the disc inclination is increased. Therefore, GI could be active in discs previously not thought to be massive enough to be gravitationally unstable,

which could have significant implications for the understanding of protoplanetary disc formation and early evolution mechanisms.

5.4 Line absorption and protostellar mass estimates

Numerous molecules have been detected in protoplanetary discs, and, recently, detections of simple molecules have been made in Class 0/I sources. However, due to the difficulties inherent in observing the youngest protostellar systems, the angular resolutions are much larger than the expected width of GI-driven spirals ($\approx 5\,\mathrm{au}$). Therefore, synthetic line images of a protosolar-like gravitationally unstable disc have been produced in order to determine if instruments like ALMA can sufficiently resolve the non-axisymmetric disc structure.

LIME was used to perform the radiative transfer calculations. In order to produce congruent images, a model-specific sampling routine was found to be necessary. This sampling algorithm entailed: at least 1×10^6 grid points; an abundance density weighting scheme; rectilinear sampling within the disc and radially logarithmic sampling within the envelope; and grid points being restricted to regions where $\tau < 3$. Therefore, as with continuum images, the construction of a model-tailored grid was found to be important for efficiency and accuracy, although the importance is emphasised in this case due to the relative complexity of line transfer. Care should also be taken in the choice of the frequency for line images because, due to the increase in optical depth with frequency, and hence more obscuration of disc material, observations at lower frequencies are preferred. The radiative transfer calculations were performed under the assumption of LTE, which was found to be valid for the adopted model disc because of the high number densities when compared to the critical densities, and because LTE runs were found to be consistent with full non-LTE runs. However, it is worth emphasising

that this assumption should be checked and validated for all instances of line radiative transfer calculations.

Synthetic observations were produced, without noise, with a PYTHON script that convolved the LIME images with a 2D Gaussian beam via a fast Fourier transform algorithm. A large parameter space was used that consisted of different molecular transitions (and thereby frequencies), angular resolutions (antenna configurations), disc inclinations and spectral resolutions. It was found that the spiral structure is traced to an extent for all transitions considered, although the integrated intensity maps do not necessarily coincide with the underlying distribution of the species. Hence, a correct treatment of radiative transfer must be performed when line fluxes are considered. For all molecular transitions, the disc is seen in absorption, and this is because of the substantial viscous heating (when compared to the irradiation heating) in the gravitationally unstable disc model. Therefore, absorption, which can be attributed to infall, could also be a signature of GI in a young, embedded protoplanetary disc.

Spatially resolving the spiral structure in a protosolar-like gravitationally unstable disc was found to be possible if a dedicated observation is performed. For the model disc, a minimum of 12 hr on-source time was found to be sufficient to allow a 4σ detection of flux originating in spiral features, at an angular resolution comparable to the width of the spiral features (≈ 7 au). Decreasing the angular resolution was found to reduce the on-source time required, but at the cost of discerning spiral structure. Spectrally resolving the spiral structure was found to be less challenging, as non-axisymmetric structure can be identified in line spectra of intermediate angular resolution (in terms of ALMA capabilities) observations, although concluding the presence of GI from asymmetric line spectra is questionable. It was found, however, that PV diagrams can directly prove the existence of spiral structure in intermediate angular resolution observations,

if the disc is nearly edge-on. Therefore, with current technologies, unambiguous line flux detection of spiral structure in a Class 0 source should be achievable.

PV diagrams can also be used to estimate the protostellar mass by fitting Keplerian curves to the rotational profiles. Observations with high angular and spectral resolutions were found to produce more reliable protostellar mass estimates because of the smearing effect of PV diagram features at poorer resolutions. Higher frequency observations were generally also found to be preferable due to the narrower velocity widths, and hence higher resolutions of the velocity axis in the PV diagrams. Overall, deriving the protostellar mass from PV diagrams was found to be unreliable even for optimal observations because the method used to fit the rotational profiles introduces a large source of uncertainty. Moreover, as the mass of a self-gravitating disc is appreciable to the protostellar mass, the inclusion of a necessary disc-to-star mass ratio in the Keplerian fitting introduces an additional source of uncertainty. Therefore, caution is certainly advised when estimating the protostellar mass from observations of gravitationally unstable discs, especially those that may possess particularly distinct spiral features.

5.5   Future work

Recent advancements in observational instrumentation have allowed structures within protoplanetary discs to be spatially resolved for the first time. Most of these observations have been of more evolved discs (see e.g. Casassus, 2016), but as the capabilities of ALMA are continually improving, detections of structure in younger, more embedded discs are surfacing (e.g. Pérez *et al.*, 2016; Tobin *et al.*, 2016). More than ever, simulations of protoplanetary discs are crucial for facilitating accurate interpretations of the observed features, which will guide our understanding of disc formation and evolution mechanisms, including the connection to planet formation processes. The complexity of these simulations
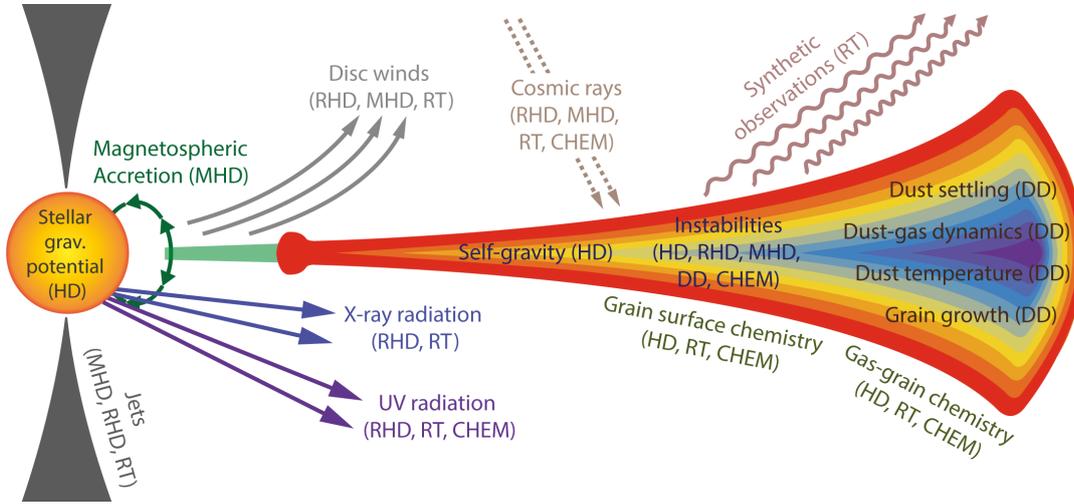
Figure 5.1: Illustration of some of the main processes that must be accounted for in order to accurately model a protoplanetary disc. The type of modelling required is indicated in parentheses and consists of hydrodynamics (HD), magneto-hydrodynamics (MHD), radiation-hydrodynamics (RHD), dust dynamics (DD), radiative transfer (RT) and chemistry (CHEM). Adapted from Haworth *et al.* (2016).

has increased in recent years, but there is still considerable room for improvement.

Modelling protoplanetary discs accurately is extremely challenging because discs span conditions ranging from cold, dense and molecular, through to hot, tenuous and ionised. Moreover, as Figure 5.1 illustrates, simulations must treat dynamic, magnetic, radiative and chemical processes, most of which are inter-linked. For example, the magnetic field is governed by the ion density, which in turn depends on the radiation field through the processes of photoionsiation, photodissociation of molecules and line and continuum cooling. Another example of linked processes occurs if the gas is turbulent (due to mechanisms like GI) and the dust is coupled to the gas, because in this case turbulent motion can be transferred to the dust grains, thereby affecting grain growth and fragmentation. Finally, the radiation and magnetic fields affect the gravitational instability (and fragmentation) within discs, which, as I have shown in this thesis, govern

the chemical composition of the disc. The ultimate end goal, then, is to be able to model these interlinked processes simultaneously. Currently, and in the near future, however, this is not possible as the computational costs are too high. Moreover, a simulation that accurately represents real objects should be achievable without a complete modelling of the entire set of dynamics. Therefore, it is prudent to identify key areas that can be addressed in the coming years, which I present here in relation to the work in this thesis.

The 3D radiative hydrodynamic simulation used in this thesis combines flux-limited diffusion (FLD) radially, where the radiative transfer equation is approximated by a diffusion equation, with ray-tracing vertically. However, FLD does not capture the long-range effects of radiative transfer (and also shadowing effects) within discs, and typically is based on the assumption that opacity is frequency independent. Therefore, significant improvements could be made by including multi-frequency rays to account for radiation transport in all directions. A Monte Carlo approach, as used in Chapters 3 and 4, could be used for this, although the computational cost is high. Incidentally this is the primary reason most Monte Carlo codes use simplistic models or snapshots of dynamical models when producing synthetic observations.

Over the lifetime of a protoplanetary disc, dust grains grow from ISM sizes to planetary body sizes, although the exact mechanisms are still not fully understood. The simulation in this thesis does not treat large dust grains, but this is appropriate because the Stokes number ≤ 1 except at the edges of the model disc (see Figure 3.1). However, there is observational evidence to suggest that grain growth may occur as early as the Class 0 stage (e.g. Chiang *et al.*, 2012; Liu *et al.*, 2016). In this case, larger dust grains become decoupled from the gas. For solid particles less than $\approx 100\,\mathrm{m}$ in size, the dominant interaction between dust and gas is via mutual drag force, which reduces the relative velocity between

the particles and the gas. This reduction is characterised by a stopping time. Hence, in order to avoid numerical instability, the simulation timestep must be shorter than the stopping time. A smaller particle size or higher concentration of particles reduces the stopping time, so the issue of numerical instability can become problematic in protoplanetary discs. It can be circumvented using a fluid approach, where the dust grains are treated as part of a 'mixture', because the stiff terms in the drag force can be operator-split, leading to a system of ODEs without any spatial coupling that can be integrated relatively straightforwardly. A 'hybrid' approach, in which the dust grains are treated as solid Lagrangian particles, can also be used for modelling a particle-gas system. The issue here, though, is that the inclusion of particles can make the system of equations globally coupled, in a similar fashion to a diffusion equation. Unlike diffusion equations, however, the numerical techniques for efficiently treating the global propagation of information don't currently exist for simulations that treat Lagrangian dust with Eulerian gas. Therefore, operator splitting the drag force on the gas is currently neglected, which means that the stopping time remains problematic for strong concentrations of solids. Nevertheless, the 'hybrid' approach does allow a much more accurate sampling of the particle velocity distribution than the fluid approximation, which therefore allows a more accurate treatment of dust grain collisions. As a result, the 'hybrid' model should be preferentially adopted for simulations of segregated dust dynamics, alongside studies dedicated to improving the reliability of the numerical methods implemented.

The hydrodynamic simulation featured in this thesis does not include a magnetic field. However, magnetic fields are known to thread at least an appreciable fraction of observed discs. Therefore, a significant number of MHD simulations have been performed in order to investigate the formation of magnetic protoplanetary discs, and have provided evidence that non-ideal MHD effects are necessary

to circumvent the magnetic braking catastrophe (see Tsukamoto, 2016, for a review). This has led to the general picture of a 'dead zone' in the shielded interiors of discs, where non-ideal effects suppress the MRI, surrounded by turbulent surface layers driven by the MRI. However, recent simulations are challenging this consensus (e.g. Gressel *et al.*, 2015) and so how these non-ideal effects interact with each other and with magnetorotational instabilities is not currently fully understood. Moreover, in relation to this thesis, how MRI turbulence interacts with GI turbulence is particularly unexplored. 'Gravito-magneto' studies of accretion outbursts in discs have been performed, where material piles up in a magnetically decoupled 'dead zone' until GI is initiated, followed by the development of MRI and subsequent accretion of excess mass. However, the contribution of GIs and MRIs to more prolonged phases of disc evolution, and how their relative importance changes with time, is still unclear. Very recently, Riols & Latter (2018) performed 3D shearing-box simulations of gravito-turbulent accretion discs with magnetic fields and found that GIs can either suppress MRIs or amplify magnetic fields via spiral wave dynamos. This could imply that GI develops an accompanying magnetic field, which then enables material to accrete in 'dead zones' via magnetic torques driven by GI rather than MRI, thereby leading to less violent outburst phases. However, it should be noted that this is a preliminary study that lacks an accurate vertical structure and realistic treatment of processes such as cooling. Therefore, more work is certainly required in order to establish the importance of GIs and MRIs throughout the formation and evolution of young protoplanetary discs.

The chemical network used in this thesis, whilst simplistic, should be appropriate for the results presented because the abundances of simple molecules are found to be consistent with those calculated with a more complex network (Quénard et al., in prep). Hence, reduced chemical networks, which are usually

more efficient to run, are of merit for investigations of simple molecular chemistry. Recently, there have been recent detections of CH_3CN and CH_3OH in more evolved discs (Öberg *et al.*, 2015; Walsh *et al.*, 2016), which suggest that complex organic molecules could also be present in young discs if these molecules are inherited from earlier epochs of disc evolution. Moreover, the recent detections of glycolaldehyde and other related molecules in the hot inner envelope of a Class 0 object (Jørgensen *et al.*, 2016) imply that COMs could be present in discs with temperatures exceeding $100\,K$, such as can occur within a gravitationally unstable disc. Therefore, the inclusion of COMs in a chemical network is most likely required in order to accurately treat GI-active disc composition. This also requires a sophisticated treatment of grain-surface chemistry because Walsh *et al.* (2014) find that grain-surface reactions lead to the efficient formation of COMs. However, as Walsh *et al.* (2014) use an α prescription to model a $10^6\,yr$ old protoplanetary disc, which possesses the typical cold midplane and warm surface layers structure, a similar chemical modelling is necessary for a gravitationally unstable disc in order to isolate the effects of the GI on COM formation and evolution. Moreover, such modelling is necessary in order to identify the complex molecules best suited for observations of GI-active discs, especially as COMs are weak emitters due to their complex rotational structures. In particular, GI-driven shocks may increase the gas-phase abundances of certain COMs due to the enhanced thermal desorption and generation of grain-surface radicals (which are then available for further molecular synthesis). Indeed, an exploration of a protoplanetary disc from the molecular core phase through to the instability phase should offer an insight into the production of species important for prebiotic chemistry, such as amino acids, thereby shedding light on the origin of chemical complexity in planetary systems.

Whilst the chemical modelling of Class 0 discs is relatively understudied, sev-

eral authors have used MHD simulations to investigate the evolution of the disc composition (e.g. Hincelin *et al.*, 2013, 2016; Yu *et al.*, 2016). To date, though, a 3D, global simulation where all of the key dynamics described above have been accounted for has yet to be performed. Therefore, the focus of future chemical simulations of young protoplanetary discs should be directed towards uniting these important dynamics into a sophisticated 3D radiation-magnetohydrodyamics code, which is then post-processed with an extended chemical network. A coupling of disc dynamics and complex chemistry would provide the most accurate treatment of disc evolution, but would be extremely computationally expensive. In reality, a simplistic in-situ chemical network should be sufficient because chemical effects on the disc dynamics are only likely to be significant for a few species and processes, such as CO ro-vibrational cooling and gas heating by PAHs. Grain-charging should also be included in this simplistic network so that the time-dependent ionisation structure, which is crucial for correctly modelling the magnetic field structure, can be determined accurately. In relation to this, outflows and jets should also be incorporated because jets and winds driven by magnetic fields can feed back into the disc, thereby altering the ionisation structure. A 'hybrid' particle-gas model should be adopted so that segregated dust dynamics can be modelled appropriately. The actual growth of dust grains can be justifiably omitted for short-term simulations, like the one used in this thesis, because the typical growth timescale ($> 10^4$ yr) is longer than the dynamic timescale. However, simulations of longer durations should include grain growth in order to accurately model dust traps, and the potential formation of planets within them.

Ideally, the dynamical criteria introduced above should be implemented gradually so that the importance of processes such as MRI, GI, grain collisions and ionisation can be separated and constrained. Once the hydrodynamic calculations have been performed, the physical evolution of the disc should be processed

by the extended chemical network, which should contain COMs and grain-surface reactions. This would allow radiative transfer calculations to be performed, likely under the assumption of LTE, which would allow synthetic observations to be produced that accurately reflect the underlying non-axisymmetric disc structure in the continuum and a variety of simple and complex molecular line species. These synthetic observations could then be compared to real observations of Class 0 sources in order to constrain future observational targets and enhance our understanding of the earliest phases of protoplanetary disc evolution.

5.6   Final remarks

Understanding the chemical evolution of protoplanetary discs around low mass stars is pivotal as it will shape the knowledge of planet formation and the production of pre-biotic molecules that are direct descendants of life. Most observations and simulations to date do not probe the earliest stages of disc evolution, and hence there is a scarcity of information concerning the youngest, most embedded discs- especially in terms of the chemistry. Therefore, in this thesis a simulation of a gravitationally unstable disc within a Class 0 system, which may be analogous to our early Solar System, has been investigated.

In this thesis I have shown that GI-driven shocks have a transient and permanent effect on disc structure and disc chemistry. The spiral features can be readily detected by ALMA in the continuum, although these dust features are ambiguous; hence the conclusion of GI as the driving mechanism is dubious. However, if continuum observations can be corroborated with line images that reveal similar non-axisymmetric structure, then this implies that both the dust temperatures and molecular abundances are locally enhanced. In this case, a much stronger argument can be made for the existence of global-scale turbulence, possibly driven by GI. In the near future, the continual advancement in angular resolution and

sensitivity of submillimetre interferometers such as ALMA, and the introduction of new near/mid-infrared instrumentation such as MIRI (Mid-InfraRed Instrument) on JWST (James Webb Space Telescope, to be launched in 2019) and the proposed European Extremely Large Telescope (E-ELT, first light planned for 2024), and new radio instrumentation like the proposed SKA (Square Kilometer Array, phase one operations scheduled for 2020) will increase the likelihood of unequivocally confirming the presence of gravitational instabilities in young and embedded protoplanetary discs.

Appendix A

Disc spiral evolution

Figure A.1 shows column density maps at different snapshots in time that illustrate how the disc evolves during the simulation. Low-order spiral waves, which are present in the model disc because of the initialisation conditions, drive spiral shocks and an increase in mass flux throughout the disc. The amplitude of the non-linear GI dampens due to the shock-heating and work done by gravity so that, by the end of the simulation, the disc is in a thermally self-regulating state.
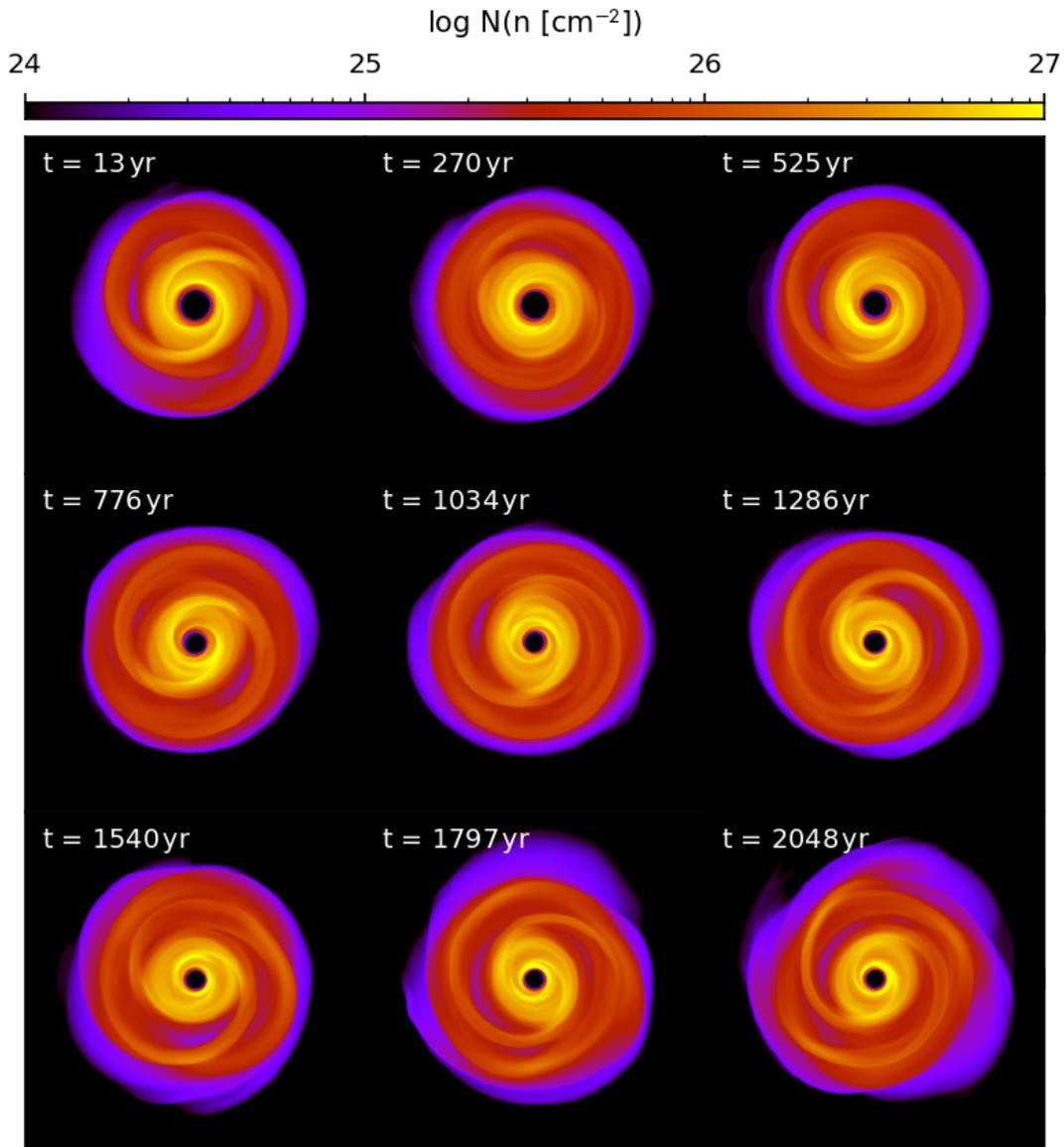
Figure A.1: Nuclei column density maps at different snapshots that illustrate how the spiral structure develops during the disc evolution.

Appendix B

Integrated line intensity maps and line spectra

Figures B.1–B.11 show integrated intensity maps at an inclination of 45° for the molecular transitions used in Chapter 4 (except ^{13}CO which is shown in Figure 4.25), across different angular resolutions. The line spectra extracted at symmetric pixel positions within the disc are plotted alongside, for a spectral resolution of 244 kHz. The line spectra for higher spectral resolutions are nearly indistinguishable for all transitions and hence are not shown here. For lower spectral resolutions the lineshape is significantly simplified because the velocity width approaches that of the linewidth. However, the overall structure of the line spectra is maintained. The integrated intensity maps and line spectra for all disc inclinations and spectral resolutions can be found at https://goo.gl/AVkHRj.

At high angular resolutions the peak amplitudes of the line spectra are different for equidistant blue-shifted and red-shifted positions within the disc. This phenomenon, which is evident for all molecular transitions considered, indicates that the disc contains non-axisymmetric structure. As the angular resolution is reduced, the ability to distinguish the actual structure of the disc worsens. Therefore, in order to achieve a compromise between flux and spectral accuracy, intermediate beamsizes (in terms of the beamsizes available for ALMA) are

B. INTEGRATED LINE INTENSITY MAPS AND LINE SPECTRA
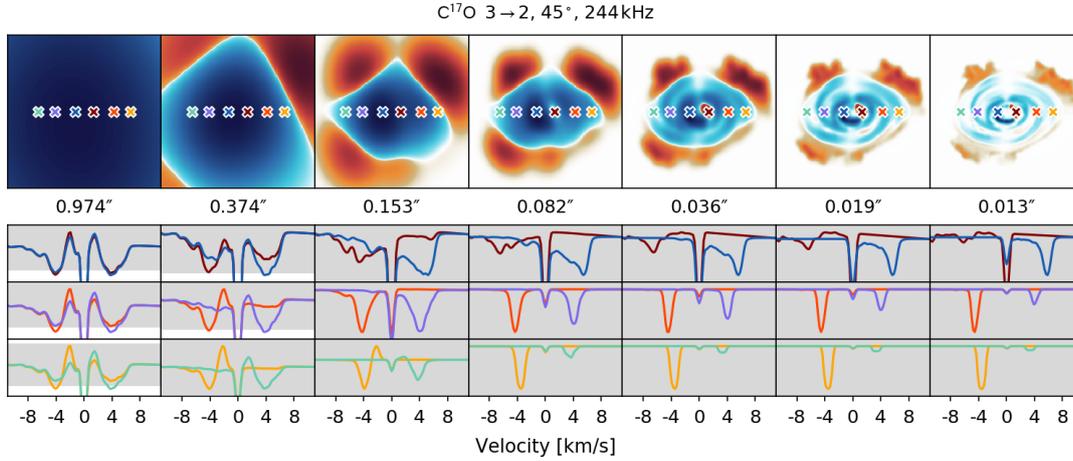
Figure B.1: Integrated intensity maps of $C^{17}O$ $3 \to 2$ for different antenna configurations (top panels). The integration is performed from -12 to -1 $\mathrm{km s}^{-1}$ and 1 to 12 $\mathrm{km s}^{-1}$, in order to avoid the envelope contribution. Overlayed on the integrated intensity maps are crosses denoting the positions of molecular spectra extraction. These extracted molecular spectra are displayed below the intensity maps for a spectral resolution of 244 kHz, normalised against the non-envelope flux minima and maxima. The grey regions in the spectra plots denote 4σ for a 12 hr on-source observation, as calculated with the ALMA Sensitivity Calculator.

required. Note, however, that this spectral analysis can not distinguish spiral structure specifically, and therefore can not be used to justify the GI directly.
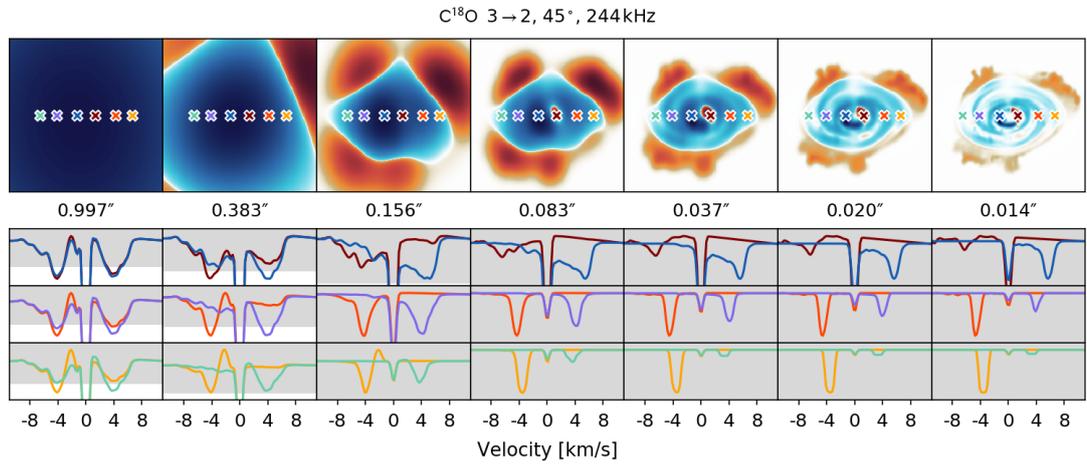
Figure B.2: Same as Figure B.1 but for $C^{18}O$ $3 \rightarrow 2$.
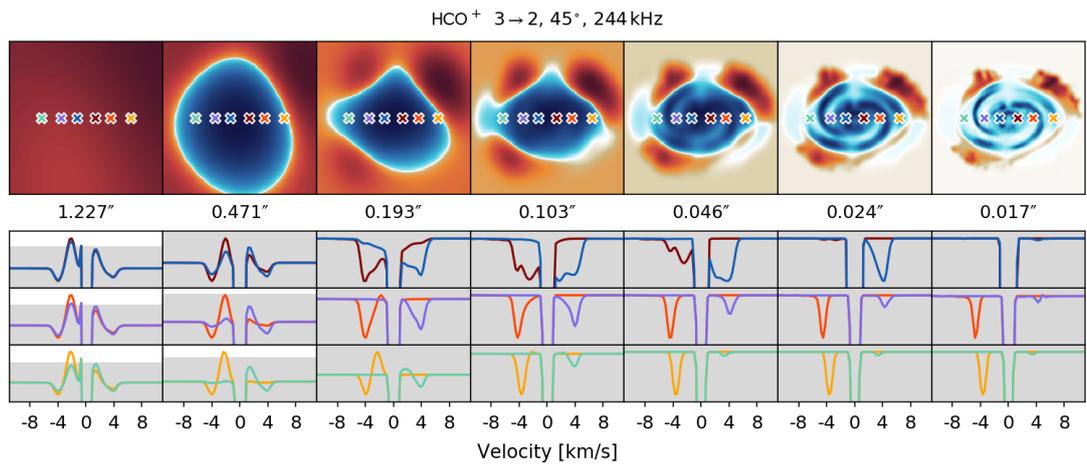
Figure B.3: Same as Figure B.1 but for HCO^+ $3 \rightarrow 2$.
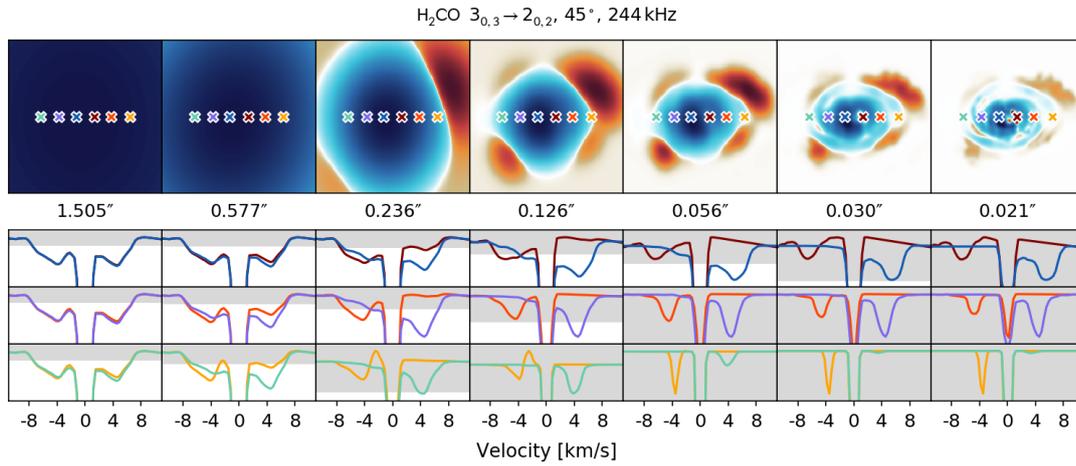
Figure B.4: Same as Figure B.1 but for H_2CO $3_{0,3} \rightarrow 2_{0,2}$.
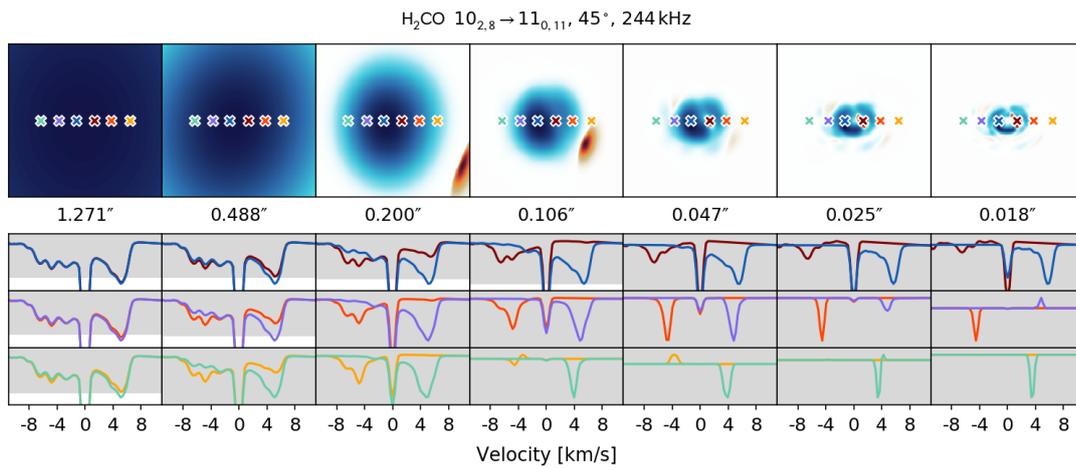
Figure B.5: Same as Figure B.1 but for H_2CO $10_{2,8} \rightarrow 11_{0,11}$.
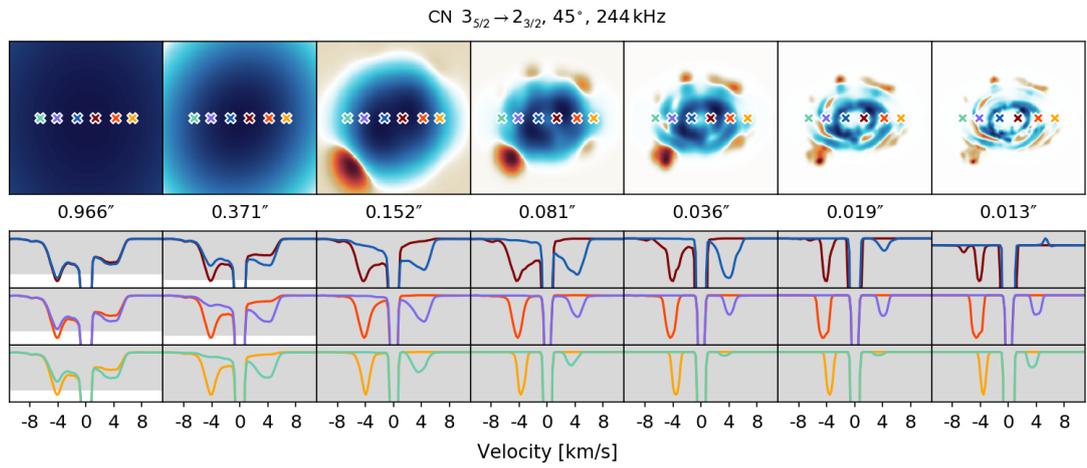
Figure B.6: Same as Figure B.1 but for CN $3_{5/2} \rightarrow 2_{3/2}$.
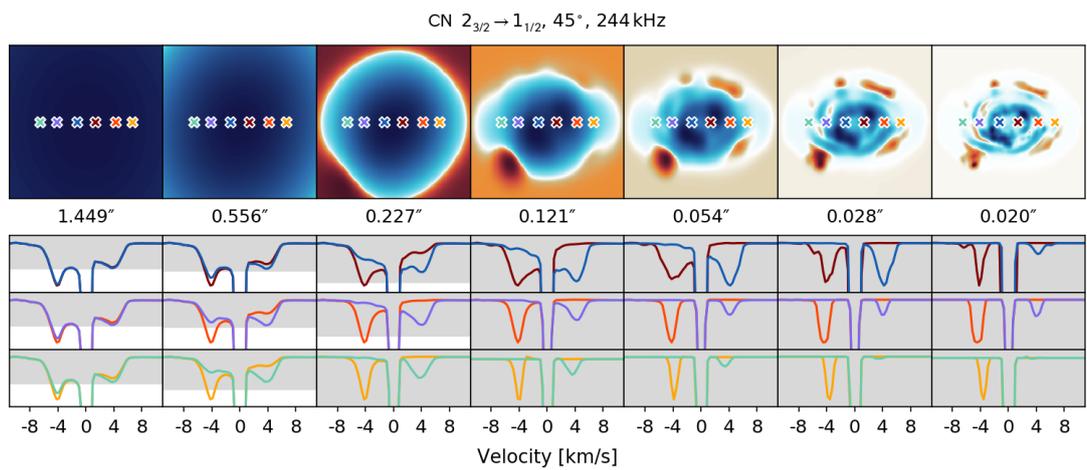
Figure B.7: Same as Figure B.1 but for CN $2_{3/2} \rightarrow 1_{1/2}$.
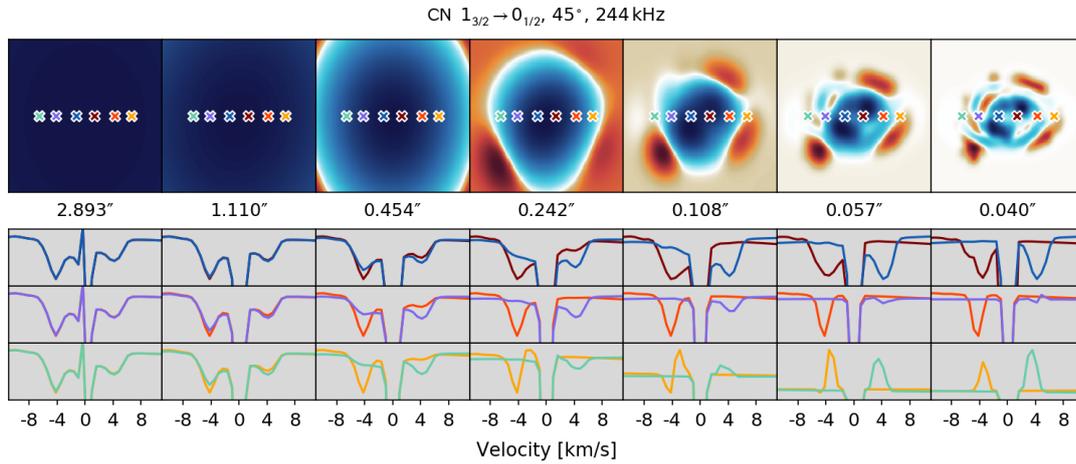
Figure B.8: Same as Figure B.1 but for CN $1_{3/2} \to 0_{1/2}$.
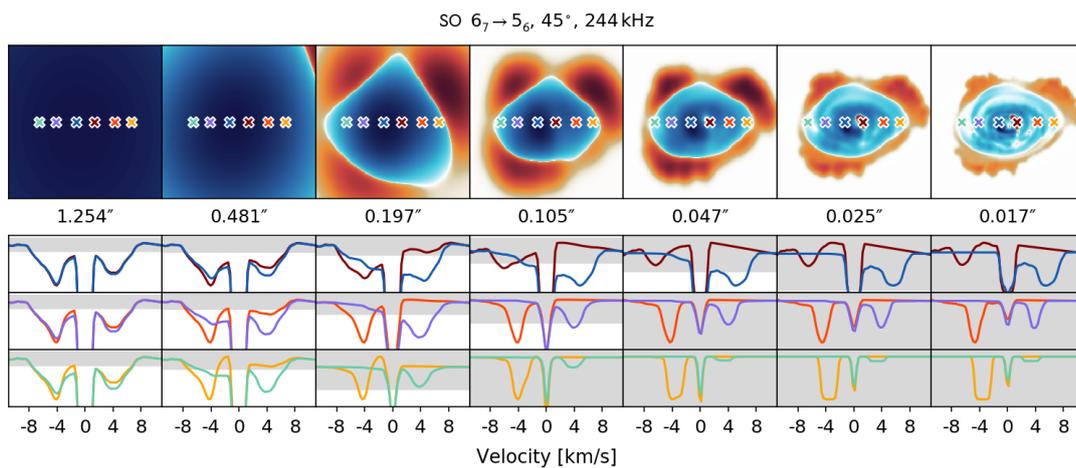
Figure B.9: Same as Figure B.1 but for SO $6_7 \to 5_6$.
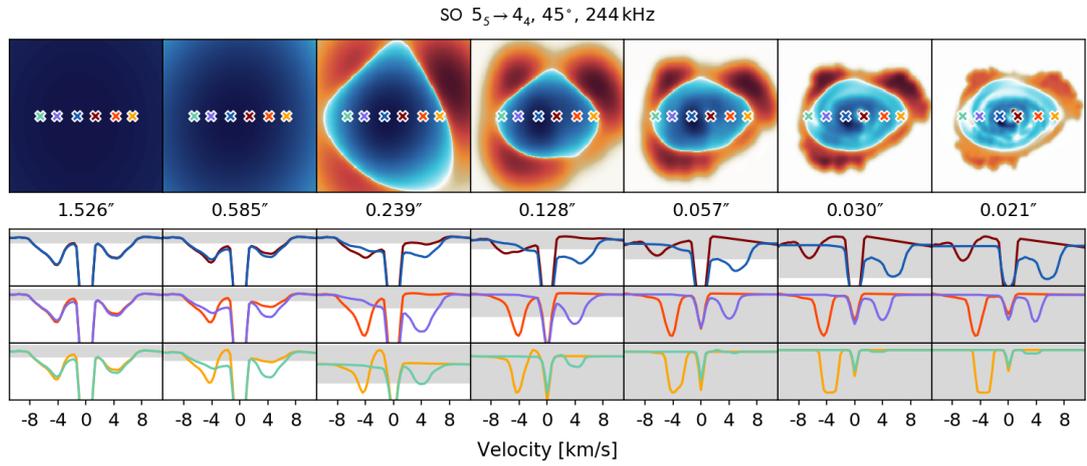
Figure B.10: Same as Figure B.1 but for SO $5_5 \rightarrow 4_4$.
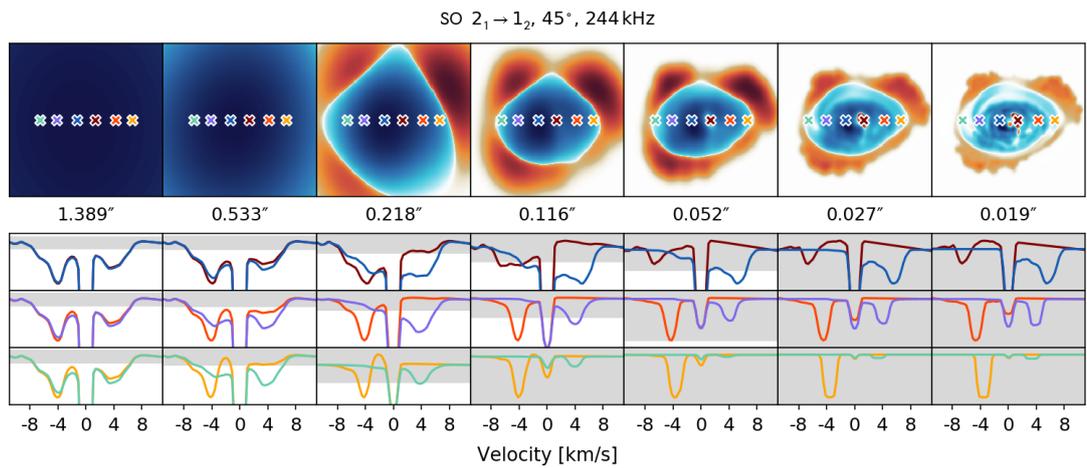
Figure B.11: Same as Figure B.1 but for SO $2_1 \rightarrow 1_2$.

Appendix C

Position-velocity diagrams

Figures C.1–C.11 show the position-velocity diagrams for the molecular transitions used in Chapter 4 (except ^{13}CO which is shown in Figure 4.26), across different disc inclinations and angular resolutions, for a spectral resolution of 244 kHz. For higher spectral resolutions, the differences in the PV diagrams are largely indistinguishable at velocities larger than $1\,\mathrm{km s^{-1}}$. When lower spectral resolutions are used the velocity structure within the PV diagram remains consistent for all but the lowest frequencies (i.e. CN $1_{3/2} \rightarrow 0_{1/2}$). Therefore PV diagrams are not presented here for other spectral resolutions but they can be found at https://goo.gl/AVkHRj.

At intermediate to high angular resolutions, and nearly edge-on inclinations, all molecular transitions show absorption features that extend from large positive and negative velocities towards the center of the PV diagram. This is indicative of non-Keplerian rotation, which, due to the asymmetric nature of some PV diagrams, may suggest the presence of spirals. Moreover, the PV diagrams of certain molecules, such as CO isotopologues and HCO^+, possess distinct finger-like structure, which has been used as a direct indicator of spirals in galaxies. Therefore, PV diagrams produced from observations of nearly edge-on young, embedded discs could be used to infer the presence of GI-driven spirals.
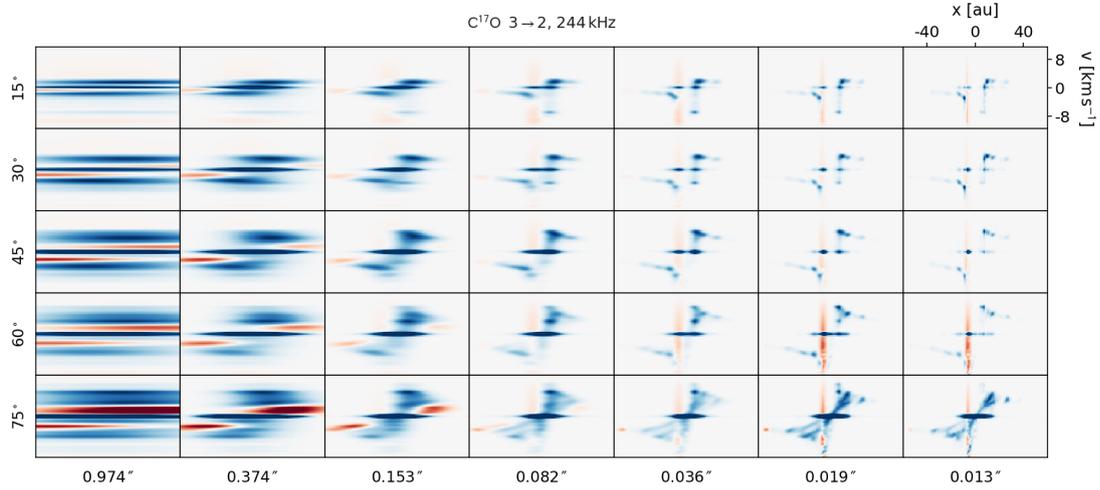
Figure C.1: Position-velocity diagram for C^{17}O $3 \to 2$ across different disc inclinations and antenna configurations, for a spectral resolution of 244 kHz. The top right panel indicates the position and velocity ranges of the observed disc model, which are constant across all panels.
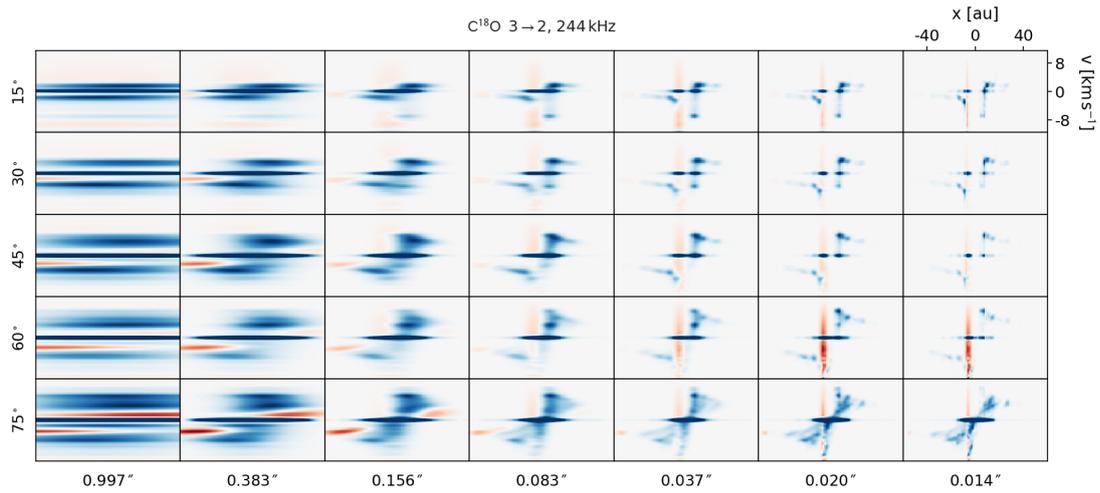

Figure C.2: Same as Figure C.1 but for C^{18}O $3 \to 2$.
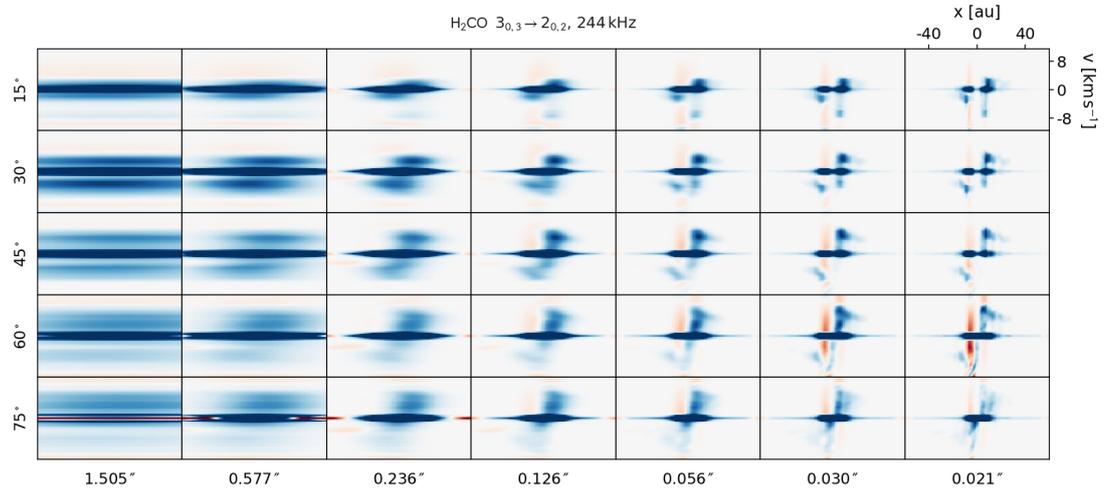
Figure C.3: Same as Figure C.1 but for H_2CO $3_{0,3} \rightarrow 2_{0,2}$.
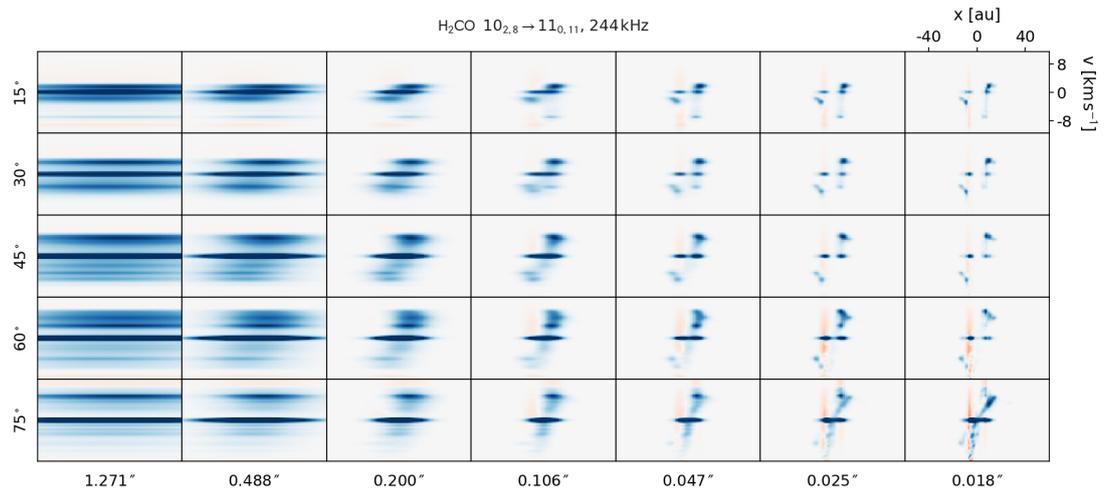
Figure C.4: Same as Figure C.1 but for H_2CO $3_{2,8} \rightarrow 2_{0,11}$.
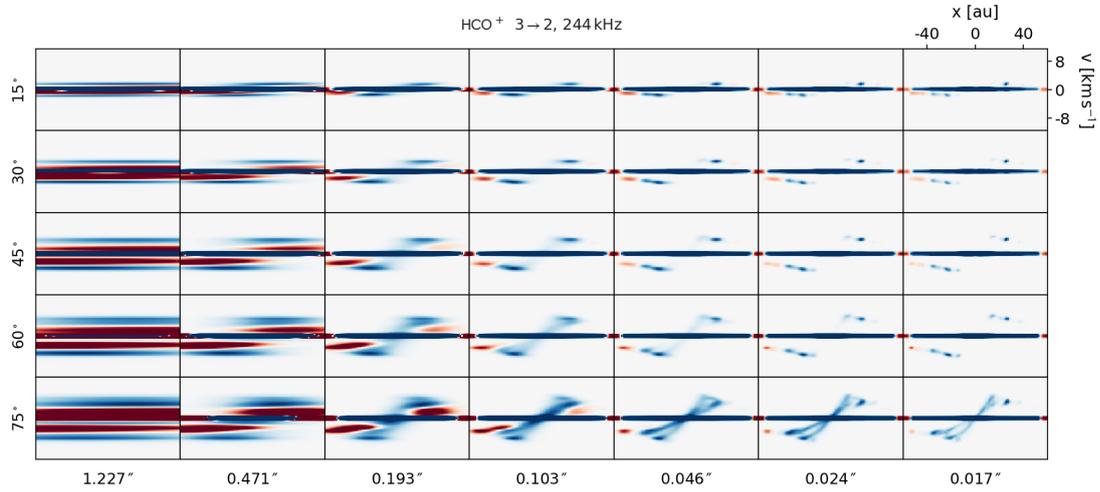
Figure C.5: Same as Figure C.1 but for HCO$^+$ 3 $\rightarrow$ 2.
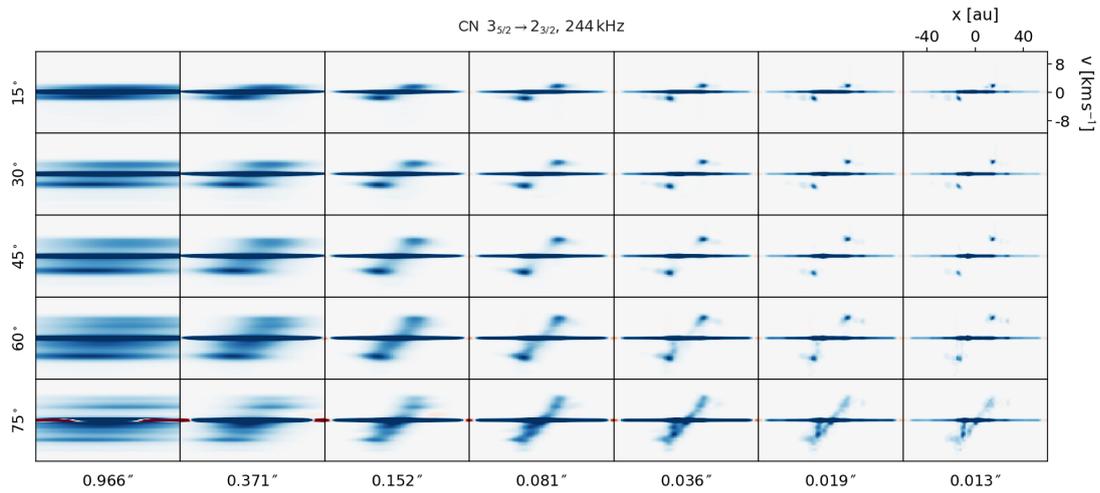

Figure C.6: Same as Figure C.1 but for CN $3_{5/2} \rightarrow 2_{3/2}$.
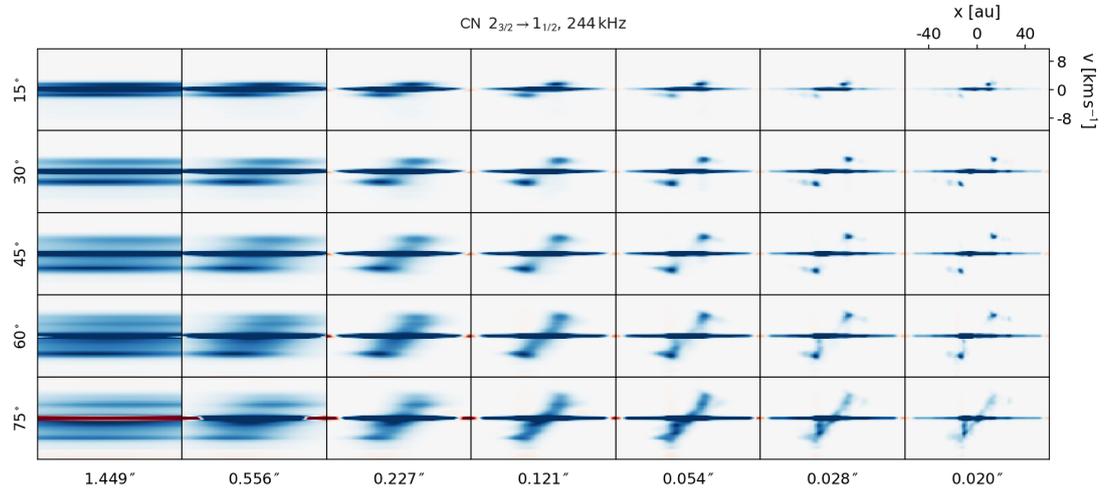
Figure C.7: Same as Figure C.1 but for CN $2_{3/2} \to 1_{1/2}$.
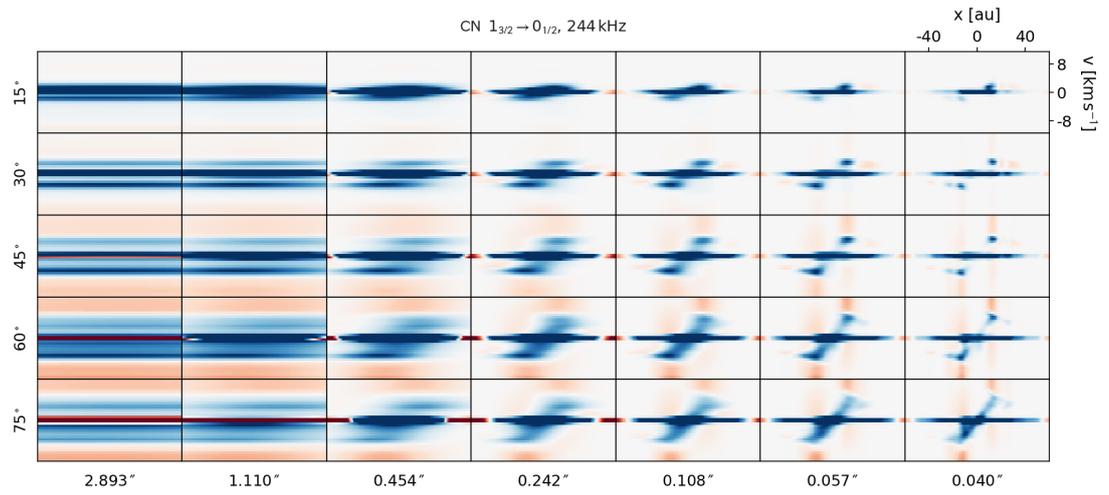
Figure C.8: Same as Figure C.1 but for CN $1_{3/2} \to 0_{1/2}$.
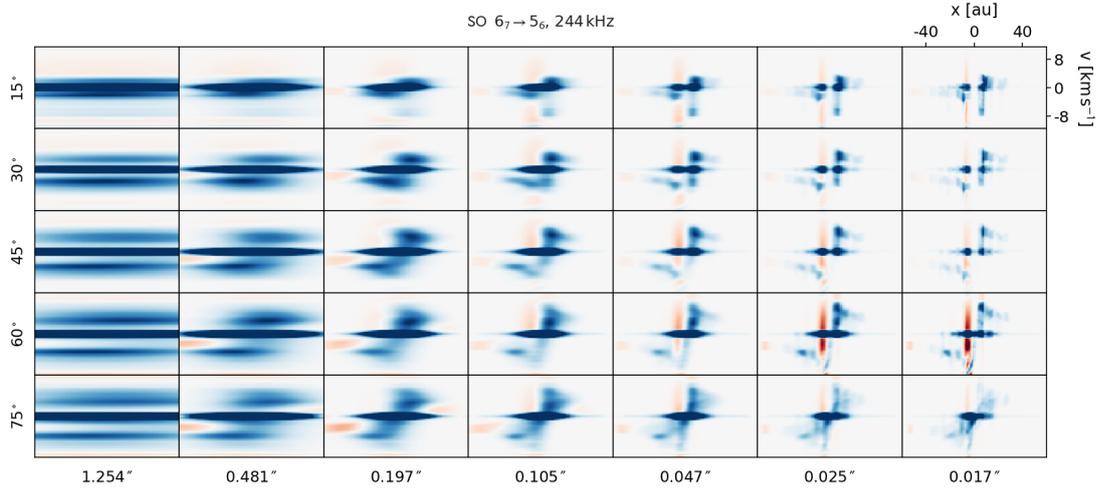
Figure C.9: Same as Figure C.1 but for SO $6_7 \to 5_6$.
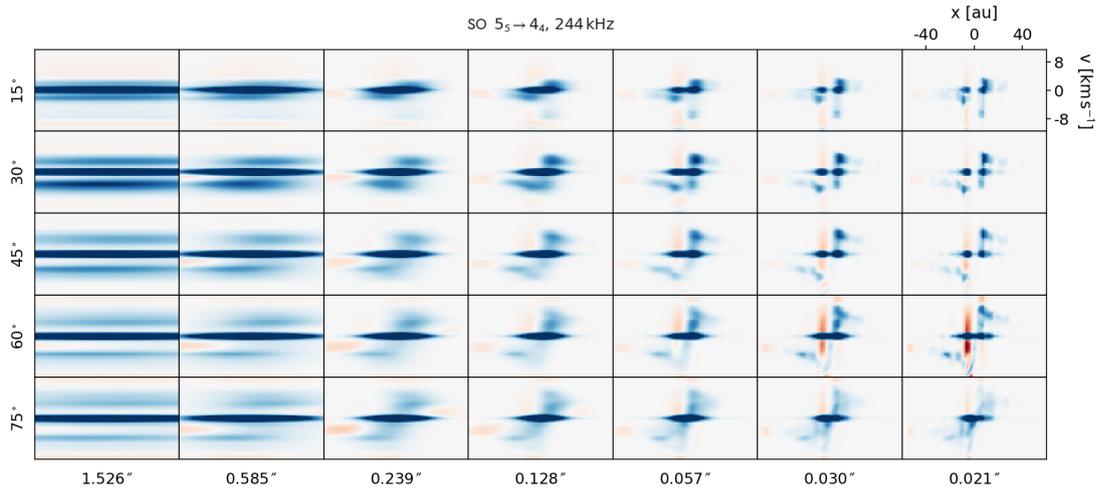

Figure C.10: Same as Figure C.1 but for SO $5_5 \to 4_4$.
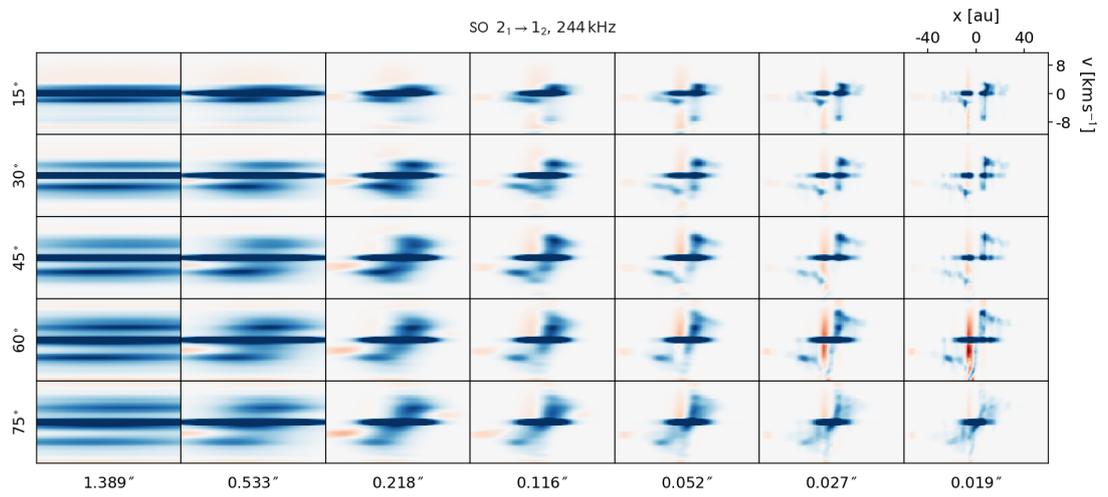
Figure C.11: Same as Figure C.1 but for SO $2_1 \rightarrow 1_2$.

Appendix D

Protostellar mass estimates

Figures D.1–D.10 show the protostellar masses derived from Keplerian curves fitted to position-velocity diagrams (see Figure 4.26 and Appendix C), across the entire parameter space used in Chapter 4 (except for a spectral resolution of 244 kHz which is shown in Figures 4.30 and 4.31). The results for two different fitting methods are shown for each spectral resolution: in the first method ('maximum') the maximum flux at each x-position is found; and in the second method ('upper-edge') the location where the 4σ flux is first exceeded along the y-axis at each x-position is found.

At higher spectral resolutions than 244 kHz the mass estimates are relatively unchanged, especially when the mass is derived using the 'upper-edge' method. For some transitions, such as H_2CO $3_{2,8} \rightarrow 2_{0,11}$ and SO $5_5 \rightarrow 4_4$, less of the parameter space is successfully fitted as the spectral resolution is increased. However, this occurs for large beamsizes where the fit isn't particularly reliable due to the smearing of the PV diagram structure. At the smallest beamsizes the protostellar mass estimates are generally consistent across spectral resolutions regardless of the fitting method used, because the features of the PV diagram, such as the finger-like structures in nearly edge-on discs, are generally maintained. The main exception to this is for the lower frequency transitions of CN, where

significantly lower protostellar mass fractions are recovered as the spectral resolution is reduced. This is primarily due to the velocity width being larger at lower frequencies; hence the velocity axis of the PV diagram has a lower resolution. Moreover, the flux originating from spiral regions for CN $1_{3/2} \to 0_{1/2}$ is particularly low (see Figure 4.19). As a result, the Keplerian fit becomes less reliable in this region of the parameter space.
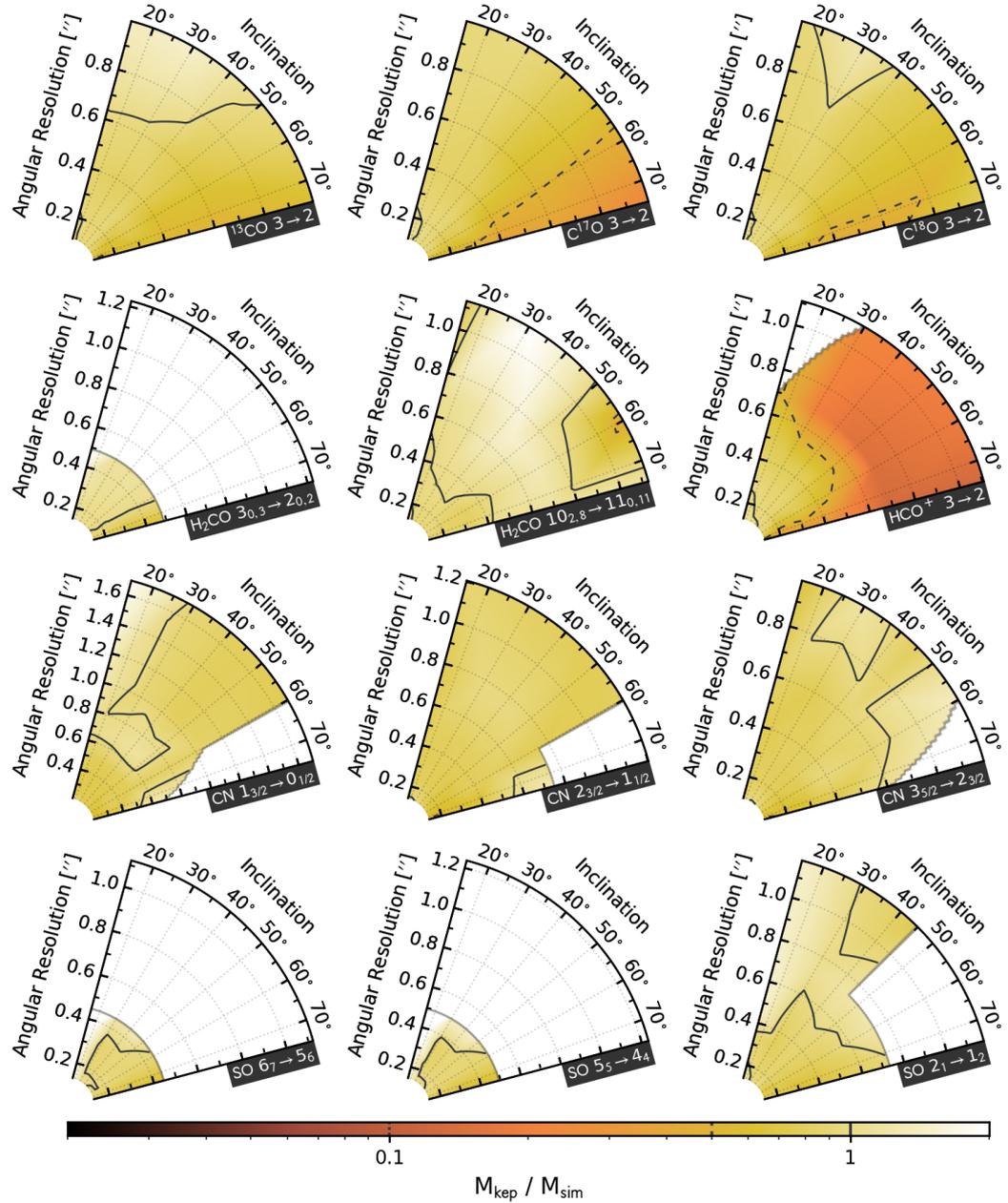
Figure D.1: Fraction of actual protostellar mass derived by fitting Keplerian curves to the PV diagrams of various molecular transitions, across different disc inclinations and angular resolutions, for a spectral resolution of 31 kHz. In the 'maximum' method used here to fit the Keplerian curves, the maximum flux at each x-position is found. The contours denote fractions of 1.0 (smallest-dashes line), 2.0 and 10.0 (solid line).
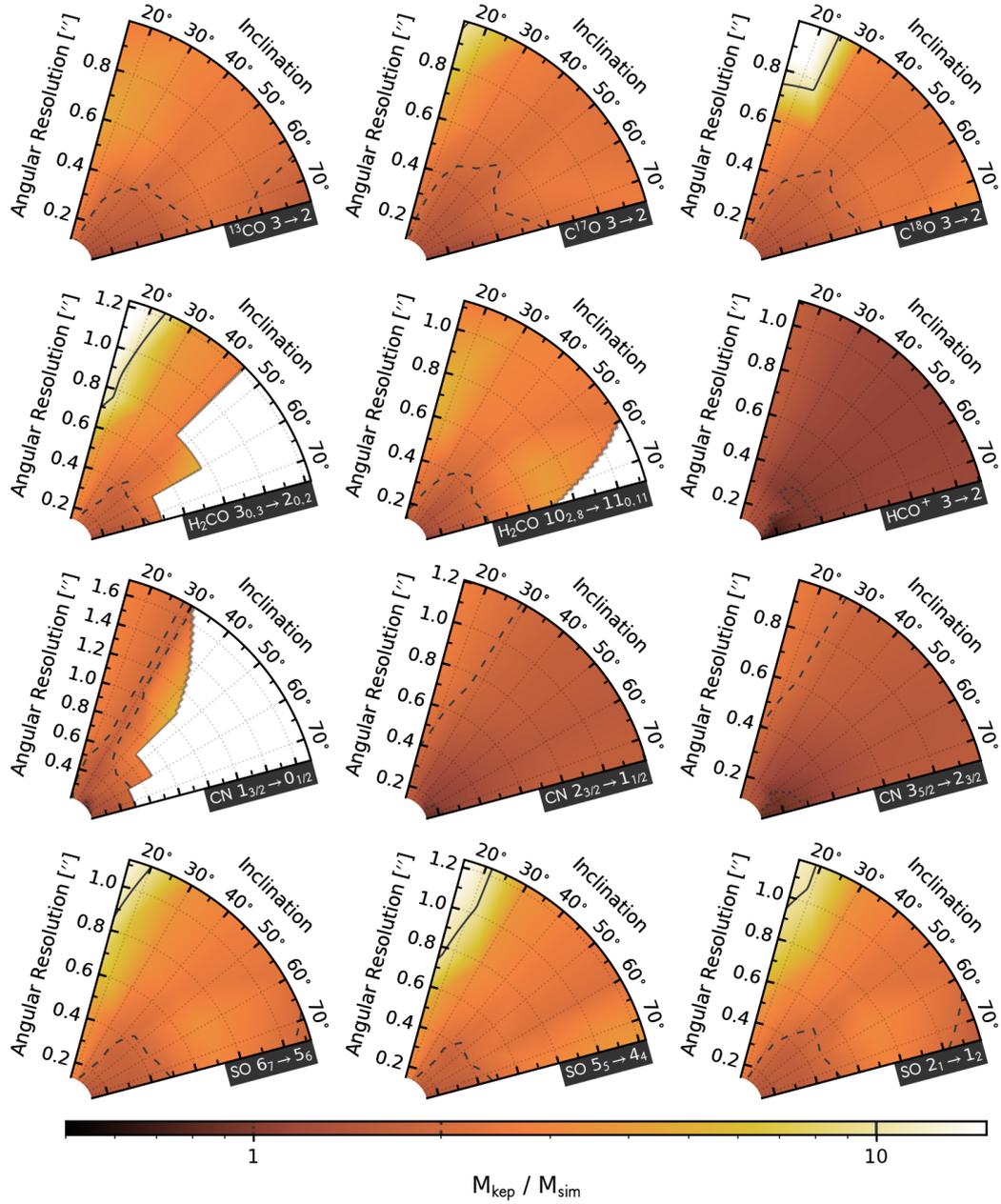
Figure D.2: Same as Figure D.1 but in the 'upper-edge' method used here to fit the Keplerian curves, the location where the 4σ flux is first exceeded along the y-axis at each x-position is found. The contours denote fractions of 1.0 (smallest-dashes line), 2.0 and 10.0 (solid line).
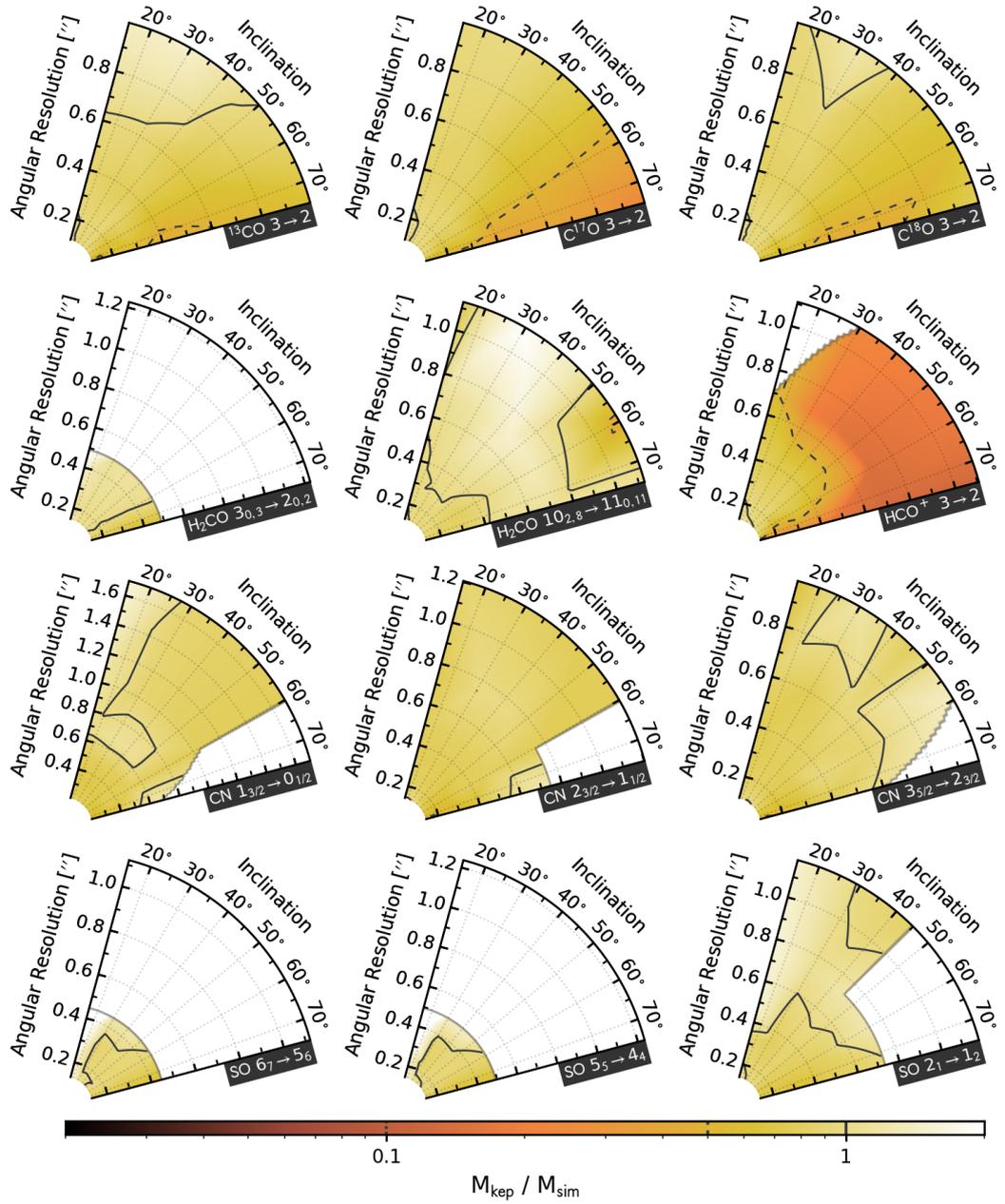
Figure D.3: Same as Figure D.1 but for a spectral resolution of 61 kHz.
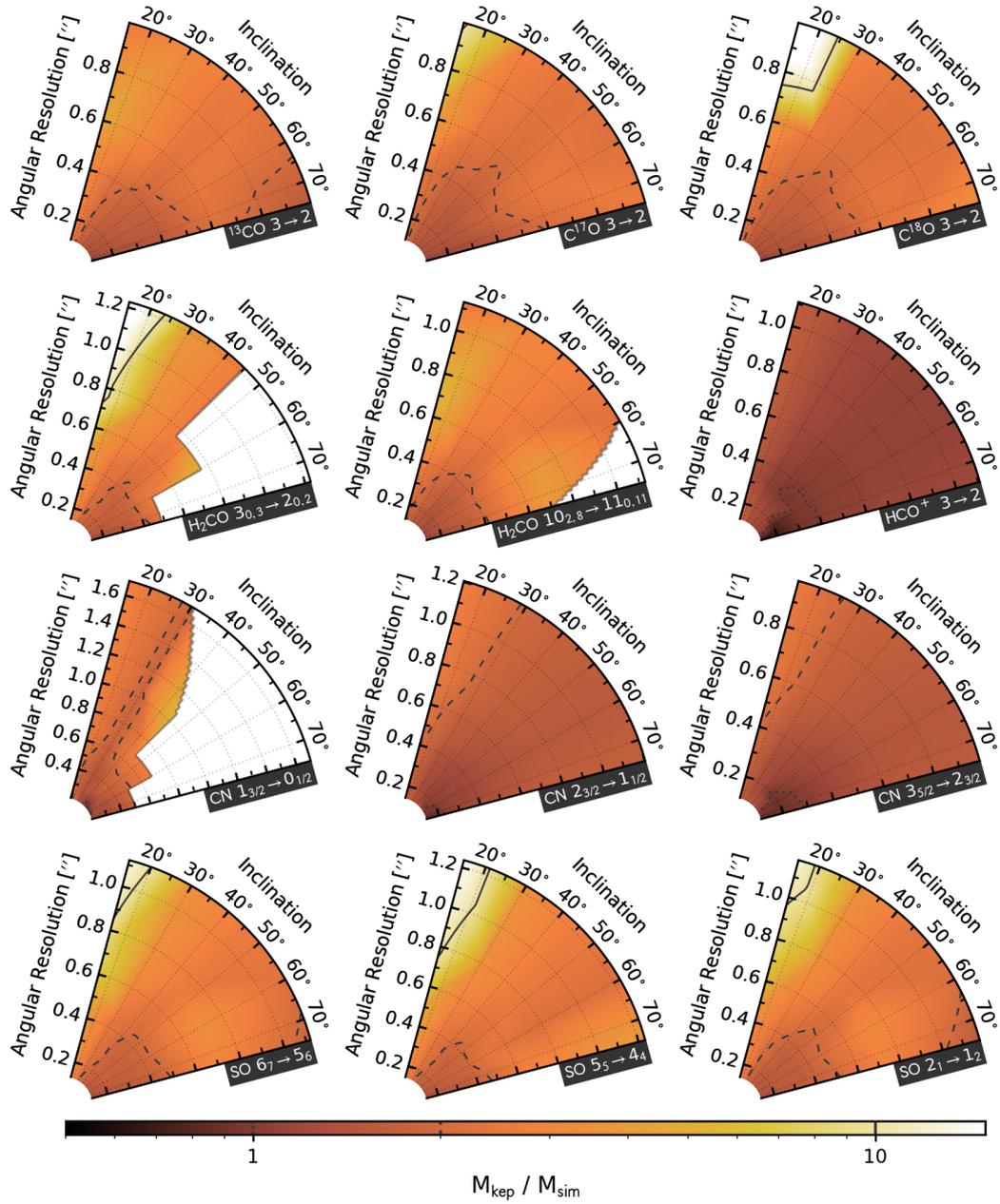
Figure D.4: Same as Figure D.2 but for a spectral resolution of 61 kHz.
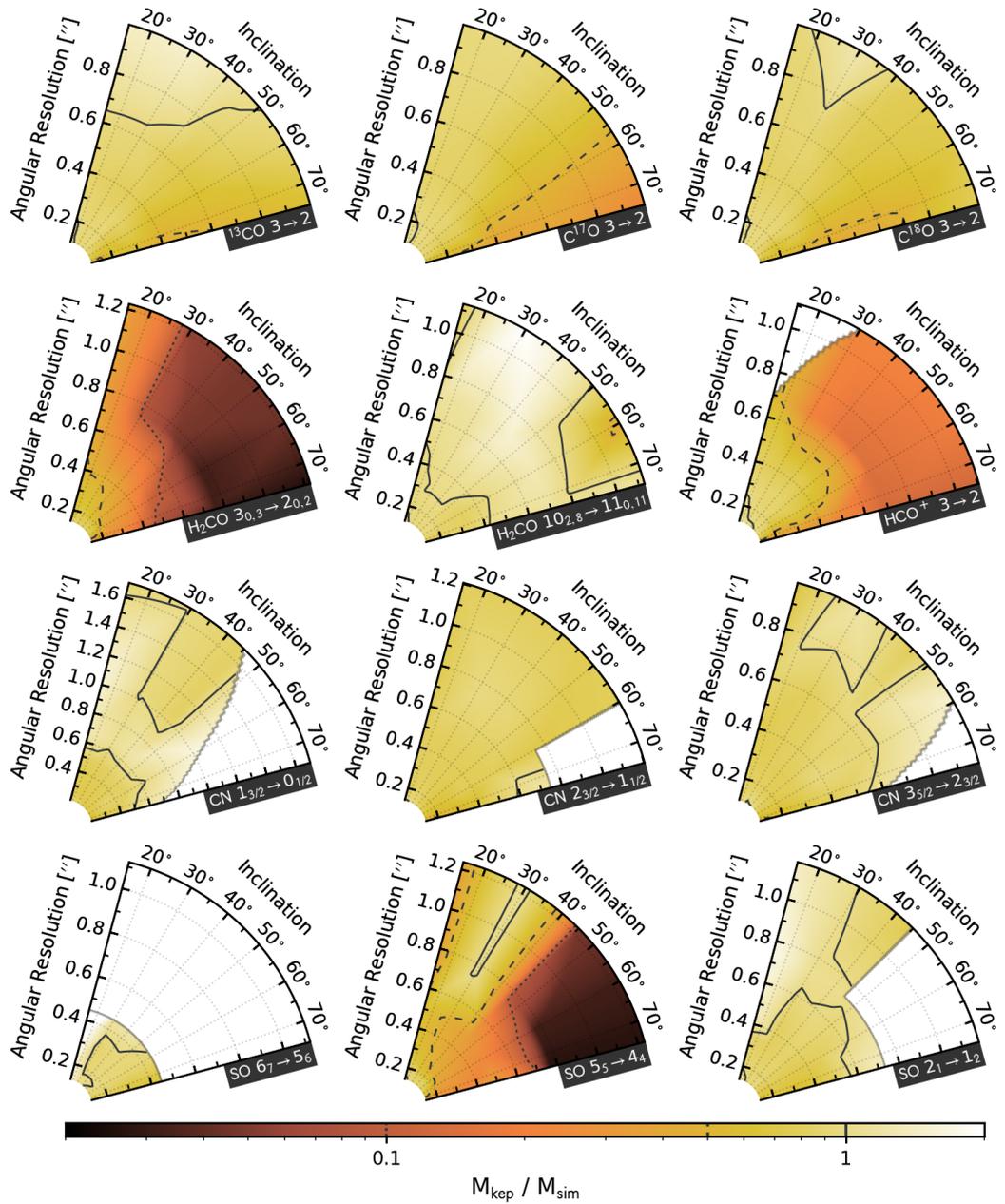
Figure D.5: Same as Figure D.1 but for a spectral resolution of 122 kHz.
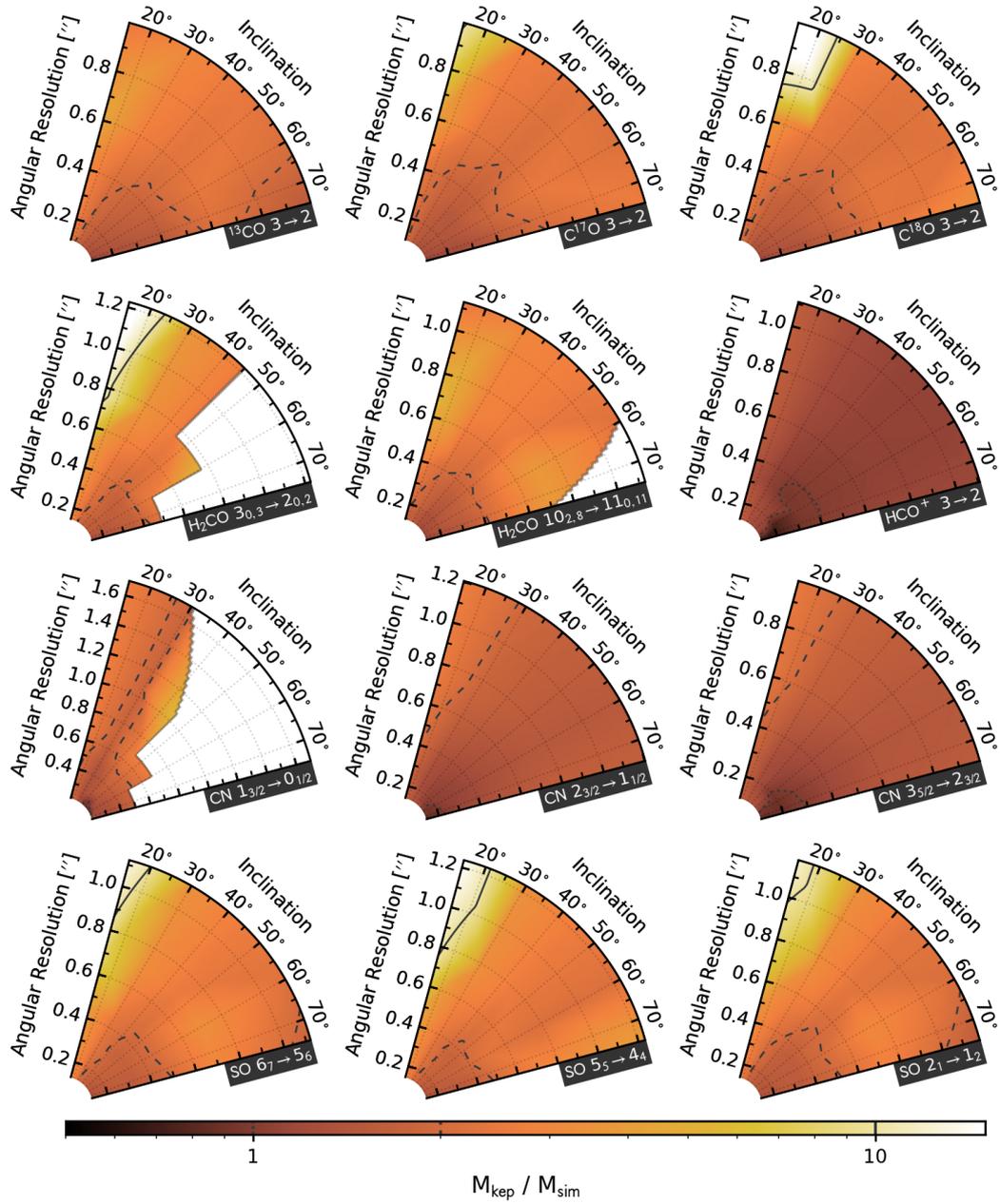
Figure D.6: Same as Figure D.2 but for a spectral resolution of 122 kHz.
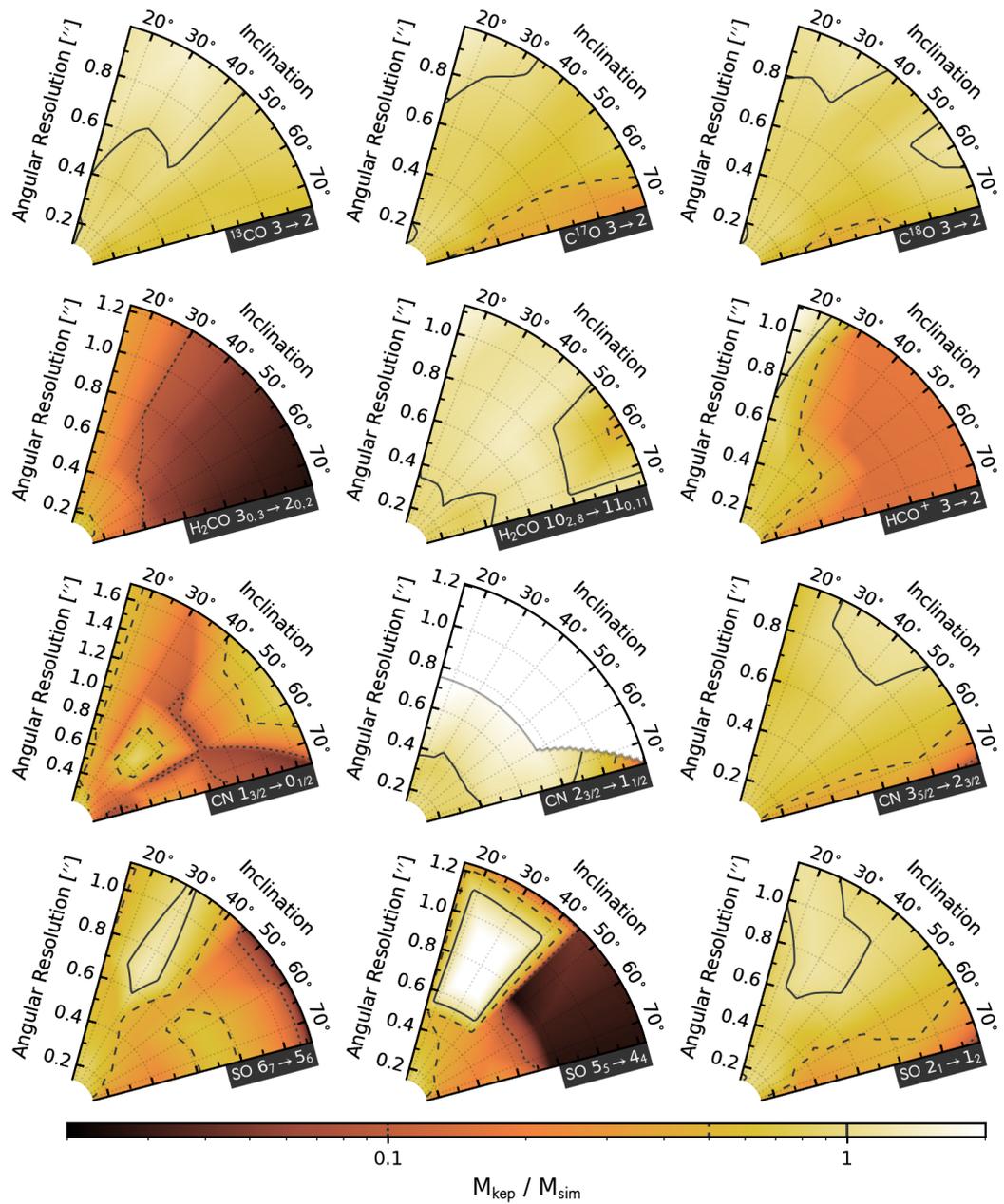
Figure D.7: Same as Figure D.1 but for a spectral resolution of 488 kHz.
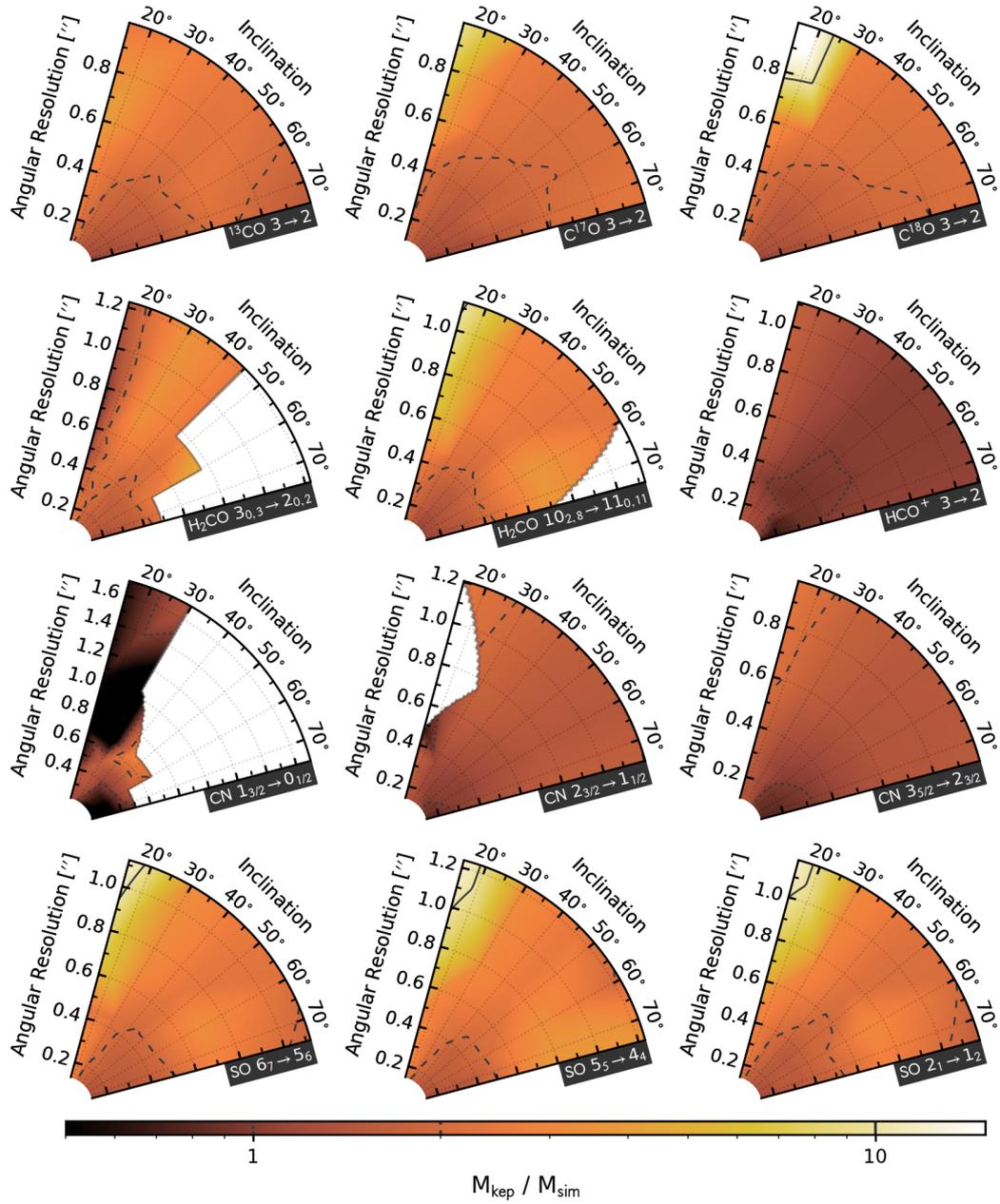
Figure D.8: Same as Figure D.2 but for a spectral resolution of 488 kHz.
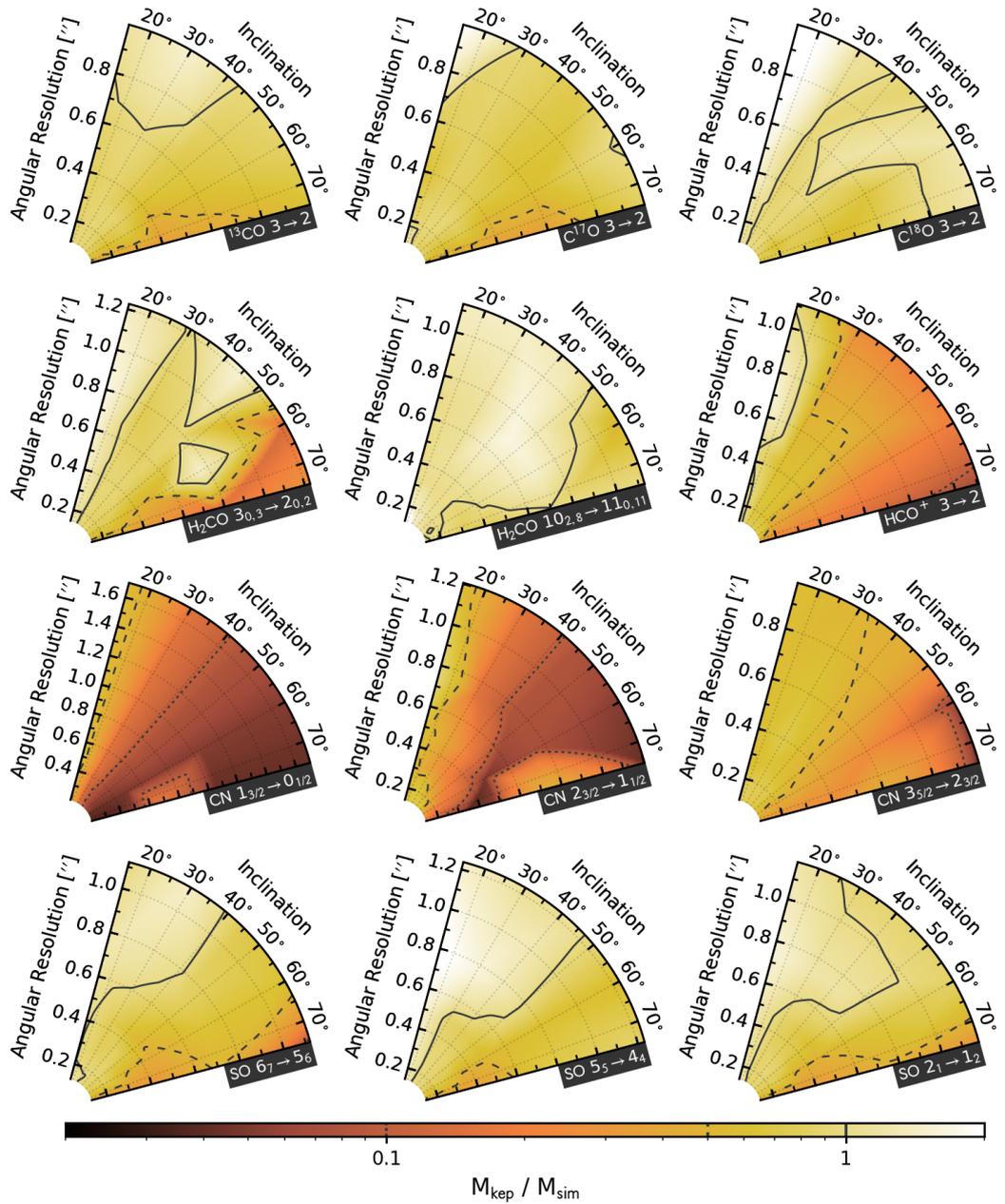
Figure D.9: Same as Figure D.1 but for a spectral resolution of 977 kHz.
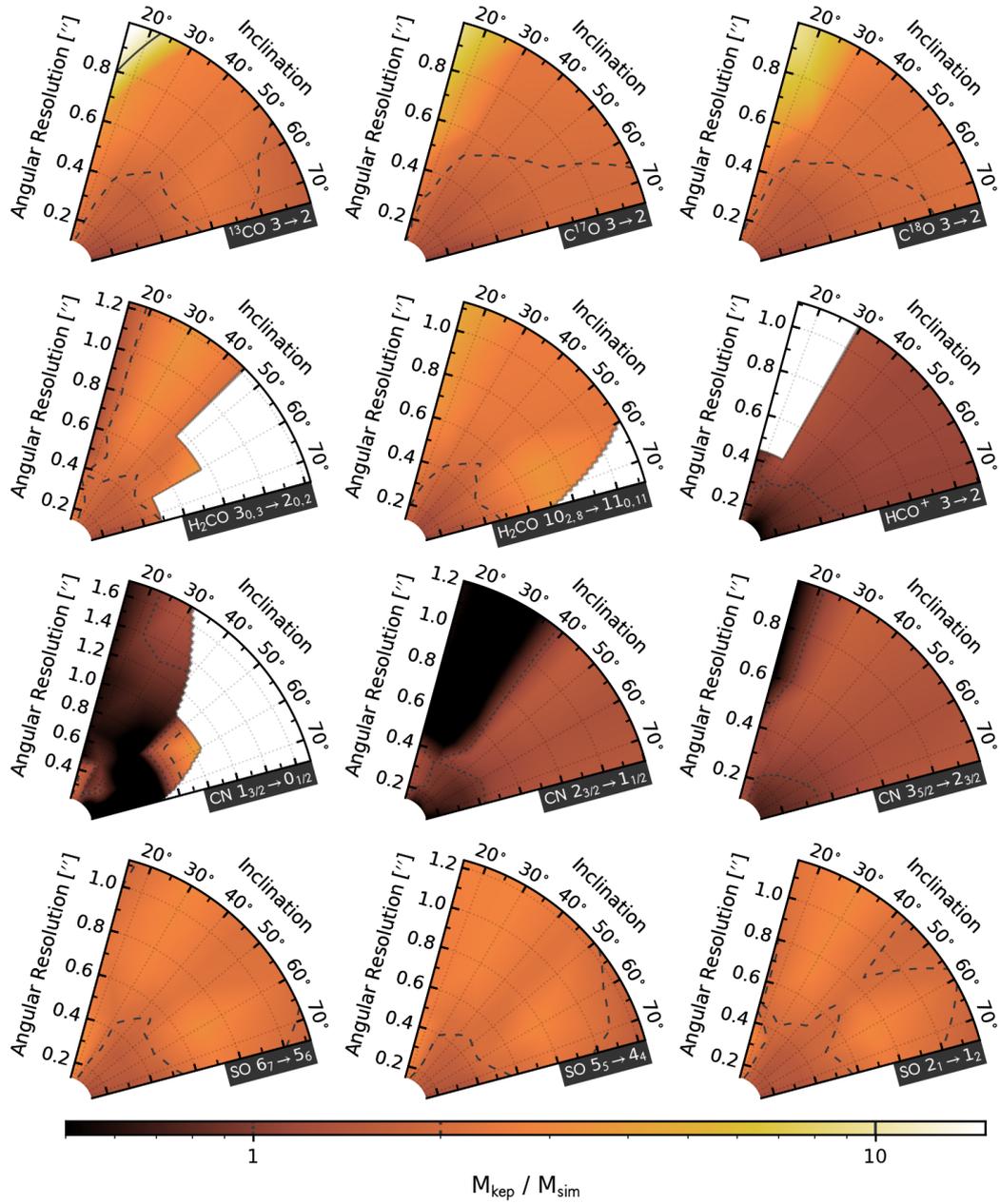
Figure D.10: Same as Figure D.2 but for a spectral resolution of 977 kHz.

References

Agúndez, M., Marcelino, N., Cernicharo, J. & Tafalla, M. (2018). Detection of interstellar HCS and its metastable isomer HSC: new pieces in the puzzle of sulfur chemistry. *A&A*, **611**, L1. 66

Akimkin, V., Zhukovska, S., Wiebe, D., Semenov, D., Pavlyuchenkov, Y., Vasyunin, A., Birnstiel, T. & Henning, T. (2013). Protoplanetary Disk Structure with Grain Evolution: The ANDES Model. *ApJ*, **766**, 8. 36, 78

Akiyama, E., Momose, M., Kitamura, Y., Tsukagoshi, T., Shimada, S., Koyamatsu, S. & Hayashi, M. (2013). An Observational Study of the Temperature and Surface Density Structures of a Typical Full Disk around MWC480. *PASJ*, **65**, 123. 34

Allen, A., Li, Z.Y. & Shu, F.H. (2003). Collapse of Magnetized Singular Isothermal Toroids. II. Rotation and Magnetic Braking. *ApJ*, **599**, 363. 12

ALMA Partnership, Brogan, C.L., Pérez, L.M., Hunter, T.R., Dent, W.R.F., Hales, A.S., Hills, R.E., Corder, S., Fomalont, E.B., Vlahakis, C., Asaki, Y., Barkats, D., Hirota, A., Hodge, J.A., Impellizzeri, C.M.V., Kneissl, R., Liuzzo, E., Lucas, R., Marcelino, N., Matsushita, S., Nakanishi, K., Phillips, N., Richards, A.M.S., Toledo, I., Aladro, R., Broguiere, D., Cortes, J.R., Cortes, P.C.,

REFERENCES

ESPADA, D., GALARZA, F., GARCIA-APPADOO, D., GUZMAN-RAMIREZ, L., HUMPHREYS, E.M., JUNG, T., KAMENO, S., LAING, R.A., LEON, S., MARCONI, G., MIGNANO, A., NIKOLIC, B., NYMAN, L.A., RADISZCZ, M., REMIJAN, A., RODÓN, J.A., SAWADA, T., TAKAHASHI, S., TILANUS, R.P.J., VILA VILARO, B., WATSON, L.C., WIKLIND, T., AKIYAMA, E., CHAPILLON, E., DE GREGORIO-MONSALVO, I., DI FRANCESCO, J., GUETH, F., KAWAMURA, A., LEE, C.F., NGUYEN LUONG, Q., MANGUM, J., PIETU, V., SANHUEZA, P., SAIGO, K., TAKAKUWA, S., UBACH, C., VAN KEMPEN, T., WOOTTEN, A., CASTRO-CARRIZO, A., FRANCKE, H., GALLARDO, J., GARCIA, J., GONZALEZ, S., HILL, T., KAMINSKI, T., KURONO, Y., LIU, H.Y., LOPEZ, C., MORALES, F., PLARRE, K., SCHIEVEN, G., TESTI, L., VIDELA, L., VILLARD, E., ANDREANI, P., HIBBARD, J.E. & TATEMATSU, K. (2015). The 2014 ALMA Long Baseline Campaign: First Results from High Angular Resolution Observations toward the HL Tau Region. *ApJ*, **808**, L3. 33

ANDRÉ, P., WARD-THOMPSON, D. & BARSONY, M. (1993). Submillimeter continuum observations of Rho Ophiuchi A - The candidate protostar VLA 1623 and prestellar clumps. *ApJ*, **406**, 122. 6, 7

ANDRÉ, P., DI FRANCESCO, J., WARD-THOMPSON, D., INUTSUKA, S.I., PUDRITZ, R.E. & PINEDA, J.E. (2014). From Filamentary Networks to Dense Cores in Molecular Clouds: Toward a New Paradigm for Star Formation. *Protostars and Planets VI*, 27. 2, 7

ANDREWS, S.M. & WILLIAMS, J.P. (2005). Circumstellar Dust Disks in Taurus-Auriga: The Submillimeter Perspective. *ApJ*, **631**, 1134. 126

ANDREWS, S.M., WILNER, D.J., HUGHES, A.M., QI, C. & DULLEMOND, C.P. (2010). Protoplanetary Disk Structures in Ophiuchus. II. Extension to Fainter Sources. *ApJ*, **723**, 1241. 17

ANDREWS, S.M., ROSENFELD, K.A., KRAUS, A.L. & WILNER, D.J. (2013). The Mass Dependence between Protoplanetary Disks and their Stellar Hosts. *ApJ*, **771**, 129. 87

ANSDELL, M., WILLIAMS, J.P., VAN DER MAREL, N., CARPENTER, J.M., GUIDI, G., HOGERHEIJDE, M., MATHEWS, G.S., MANARA, C.F., MIOTELLO, A., NATTA, A., OLIVEIRA, I., TAZZARI, M., TESTI, L., VAN DISHOECK, E.F. & VAN TERWISGA, S.E. (2016). ALMA Survey of Lupus Protoplanetary Disks. I. Dust and Gas Masses. *ApJ*, **828**, 46. 126

ANSDELL, M., WILLIAMS, J.P., MANARA, C.F., MIOTELLO, A., FACCHINI, S., VAN DER MAREL, N., TESTI, L. & VAN DISHOECK, E.F. (2017). An ALMA Survey of Protoplanetary Disks in the σ Orionis Cluster. *AJ*, **153**, 240. 174

ARMITAGE, P.J., LIVIO, M. & PRINGLE, J.E. (2001). Episodic accretion in magnetically layered protoplanetary discs. *MNRAS*, **324**, 705–711. 19

ARRHENIUS, S. (1889). Úber die Dissociationswrme und den Einfluss der Temperatur auf den Dissociationsgrad der Elektrolyte. *ZPC*, **96**, 4. 25

BAE, J., HARTMANN, L., ZHU, Z. & NELSON, R.P. (2014). Accretion Outbursts in Self-gravitating Protoplanetary Disks. *ApJ*, **795**, 61. 35, 85

BALBUS, S.A. (2003). Enhanced Angular Momentum Transport in Accretion Disks. *ARA&A*, **41**, 555. 10

REFERENCES

BALBUS, S.A. & HAWLEY, J.F. (1991). A powerful local shear instability in weakly magnetized disks. I - Linear analysis. II - Nonlinear evolution. *ApJ*, **376**, 214. 11

BALLESTEROS-PAREDES, J., KLESSEN, R.S., MAC LOW, M.M. & VAZQUEZ-SEMADENI, E. (2007). Molecular Cloud Turbulence and Star Formation. *Protostars and Planets V*, 63. 2

BALLY, J., REIPURTH, B. & DAVIS, C.J. (2007). Observations of Jets and Outflows from Young Stars. *Protostars and Planets V*, 215. 8

BAST, J.E., LAHUIS, F., VAN DISHOECK, E.F. & TIELENS, A.G.G.M. (2013). Exploring organic chemistry in planet-forming zones. *A&A*, **551**, A118. 54

BATE, M.R. (2010). Collapse of a molecular cloud core to stellar densities: the radiative impact of stellar core formation on the circumstellar disc. *MNRAS*, **404**, L79. 17

BATE, M.R., BONNELL, I.A. & BROMM, V. (2003). The formation of a star cluster: predicting the properties of stars and brown dwarfs. *MNRAS*, **339**, 577. 18

BATE, M.R., TRICCO, T.S. & PRICE, D.J. (2014). Collapse of a molecular cloud core to stellar densities: stellar-core and outflow formation in radiation magnetohydrodynamic simulations. *MNRAS*, **437**, 77. 4

BENISTY, M., JUHASZ, A., BOCCALETTI, A., AVENHAUS, H., MILLI, J., THALMANN, C., DOMINIK, C., PINILLA, P., BUENZLI, E., POHL, A., BEUZIT, J.L., BIRNSTIEL, T., DE BOER, J., BONNEFOY, M., CHAUVIN, G., CHRISTIAENS, V., GARUFI, A., GRADY, C., HENNING, T., HUELAMO, N., ISELLA, A., LANGLOIS, M., MÉNARD, F., MOUILLET, D., OLOFSSON,

J., PANTIN, E., PINTE, C. & PUEYO, L. (2015). Asymmetric features in the protoplanetary disk MWC 758. *A&A*, **578**, L6. 86

BERGIN, E.A. (2014). Astrobiology: An astronomer's perspective. In *American Institute of Physics Conference Series*, vol. 1638 of *American Institute of Physics Conference Series*, 5. 22

BERGIN, E.A., MELNICK, G.J. & NEUFELD, D.A. (1998). The Postshock Chemical Lifetimes of Outflow Tracers and a Possible New Mechanism to Produce Water Ice Mantles. *ApJ*, **499**, 777. 36

BERGIN, E.A., CLEEVES, L.I., GORTI, U., ZHANG, K., BLAKE, G.A., GREEN, J.D., ANDREWS, S.M., EVANS, N.J., II, HENNING, T., ÖBERG, K., PONTOPPIDAN, K., QI, C., SALYK, C. & VAN DISHOECK, E.F. (2013). An old disk still capable of forming a planetary system. *Nature*, **493**, 644. 34

BIRNSTIEL, T., DULLEMOND, C.P. & BRAUER, F. (2010). Gas-and dust evolution in protoplanetary disks. *A&A*, **513**, A79. 90

BISSANTZ, N., ENGLMAIER, P. & GERHARD, O. (2003). Gas dynamics in the Milky Way: second pattern speed and large-scale morphology. *MNRAS*, **340**, 949. 171

BOLEY, A.C. (2007). *The three-dimensional behavior of spiral shocks in protoplanetary disks*. Ph.D. thesis, Indiana University. 16, 38

BOLEY, A.C. & DURISEN, R.H. (2006). Hydraulic/Shock Jumps in Protoplanetary Disks. *ApJ*, **641**, 534. 15, 17, 39, 43, 45, 87, 103, 121

BOLEY, A.C. & DURISEN, R.H. (2008). Gravitational Instabilities, Chondrule Formation, and the FU Orionis Phenomenon. *ApJ*, **685**, 1193. 19, 35, 45, 85

REFERENCES

BOLEY, A.C., DURISEN, R.H., NORDLUND, Å. & LORD, J. (2007a). Three-Dimensional Radiative Hydrodynamics for Disk Stability Simulations: A Proposed Testing Standard and New Results. *ApJ*, **665**, 1254. 17, 38

BOLEY, A.C., HARTQUIST, T.W., DURISEN, R.H. & MICHAEL, S. (2007b). The Internal Energy for Molecular Hydrogen in Gravitationally Unstable Protoplanetary Disks. *ApJL*, **656**, L89. 38

BOSS, A.P. (2004). On the fragmentation of magnetized cloud cores. *MNRAS*, **350**, L57. 17

BOURKE, T.L., CRAPSI, A., MYERS, P.C., EVANS, N.J., II, WILNER, D.J., HUARD, T.L., JØRGENSEN, J.K. & YOUNG, C.H. (2005). Discovery of a Low-Mass Bipolar Molecular Outflow from L1014-IRS with the Submillimeter Array. *ApJ*, **633**, L129. 6

BRINCH, C. & HOGERHEIJDE, M.R. (2010). LIME - a flexible, non-LTE line excitation and radiation transfer method for millimeter and far-infrared wavelengths. *A&A*, **523**, A25. 91

BROWN, P.N., BYRNE, G.D. & HINDMARSH, A.C. (1989). VODE: A variable-coefficient ODE solver. *SIAM Journal on Scientific and Statistical Computing*, **10**, 1038. 49

CAI, K., DURISEN, R.H., MICHAEL, S., BOLEY, A.C., MEJÍA, A.C., PICKETT, M.K. & D'ALESSIO, P. (2006). The Effects of Metallicity and Grain Size on Gravitational Instabilities in Protoplanetary Disks. *ApJ*, **636**, L149. 17

CAI, K., DURISEN, R.H., BOLEY, A.C., PICKETT, M.K. & MEJÍA, A.C. (2008). The Thermal Regulation of Gravitational Instabilities in Protoplanetary Disks. IV. Simulations with Envelope Irradiation. *ApJ*, **673**, 1138. 90

CARRASCO-GONZÁLEZ, C., HENNING, T., CHANDLER, C.J., LINZ, H., PÉREZ, L., RODRÍGUEZ, L.F., GALVÁN-MADRID, R., ANGLADA, G., BIRNSTIEL, T., VAN BOEKEL, R., FLOCK, M., KLAHR, H., MACIAS, E., MENTEN, K., OSORIO, M., TESTI, L., TORRELLES, J.M. & ZHU, Z. (2016). The VLA View of the HL Tau Disk: Disk Mass, Grain Evolution, and Early Planet Formation. *ApJ*, **821**, L16. 8

CASASSUS, S. (2016). Resolved Observations of Transition Disks. *PASA*, **33**, e013. 201

CASELLI, P. (2005). Chemical Processes in Star Forming Regions. In *Astrophysics and Space Science Library*, vol. 324 of *Astrophysics and Space Science Library*, 47. 20, 22

CASELLI, P. & CECCARELLI, C. (2012). Our astrochemical heritage. *A&ARv*, **20**, 56. 52

CASELLI, P., HARTQUIST, T.W. & HAVNES, O. (1997). Grain-grain collisions and sputtering in oblique C-type shocks. *A&A*, **322**, 296. 52

CASELLI, P., BENSON, P.J., MYERS, P.C. & TAFALLA, M. (2002). Dense Cores in Dark Clouds. XIV. N_2H^+ (1-0) Maps of Dense Cloud Cores. *ApJ*, **572**, 238. 9

CHAPILLON, E., GUILLOTEAU, S., DUTREY, A., PIÉTU, V. & GUÉLIN, M. (2012). Chemistry in disks. VI. CN and HCN in protoplanetary disks. *A&A*, **537**, A60. 54, 152

CHARNLEY, S.B., TIELENS, A.G.G.M. & RODGERS, S.D. (1997). Deuterated Methanol in the Orion Compact Ridge. *ApJ*, **482**, L203. 23

REFERENCES

CHARNLEY, S.B., RODGERS, S.D. & EHRENFREUND, P. (2001). Gas-grain chemical models of star-forming molecular clouds as constrained by ISO and SWAS observations. *A&A*, **378**, 1024. 23

CHEN, H., MYERS, P.C., LADD, E.F. & WOOD, D.O.S. (1995). Bolometric temperature and young stars in the Taurus and Ophiuchus complexes. *ApJ*, **445**, 377. 6

CHIANG, H.F., LOONEY, L.W. & TOBIN, J.J. (2012). The Envelope and Embedded Disk around the Class 0 Protostar L1157-mm: Dual-wavelength Interferometric Observations and Modeling. *ApJ*, **756**, 168. 203

CLARKE, C.J. (2009). Pseudo-viscous modelling of self-gravitating discs and the formation of low mass ratio binaries. *MNRAS*, **396**, 1066. 120

CLEEVES, L.I., BERGIN, E.A. & HARRIES, T.J. (2015). Indirect Detection of Forming Protoplanets via Chemical Asymmetries in Disks. *ApJ*, **807**, 2. 36

COSSINS, P., LODATO, G. & CLARKE, C.J. (2009). Characterizing the gravitational instability in cooling accretion discs. *MNRAS*, **393**, 1157. 109, 120

COSSINS, P., LODATO, G. & TESTI, L. (2010). Resolved images of self-gravitating circumstellar discs with ALMA. *MNRAS*, **407**, 181. 87, 119, 139

CRUTCHER, R.M. (1999). Magnetic Fields in Molecular Clouds: Observations Confront Theory. *ApJ*, **520**, 706. 11

D'ALESSIO, P., CALVET, N. & HARTMANN, L. (1997). The Structure and Emission of Accretion Disks Irradiated by Infalling Envelopes. *ApJ*, **474**, 397. 15

D'ALESSIO, P., CALVET, N. & HARTMANN, L. (2001). Accretion Disks around Young Objects. III. Grain Growth. *ApJ*, **553**, 321. 89, 108, 109, 110

D'Alessio, P., Calvet, N., Hartmann, L., Franco-Hernández, R. & Servín, H. (2006). Effects of Dust Growth and Settling in T Tauri Disks. *ApJ*, **638**, 314. 89

Delgado-Donate, E.J., Clarke, C.J., Bate, M.R. & Hodgkin, S.T. (2004). On the properties of young multiple stars. *MNRAS*, **351**, 617. 18

Dipierro, G., Lodato, G., Testi, L. & de Gregorio Monsalvo, I. (2014). How to detect the signatures of self-gravitating circumstellar discs with the Atacama Large Millimeter/sub-millimeter Array. *MNRAS*, **444**, 1919. 37, 87, 119, 139

Dipierro, G., Pinilla, P., Lodato, G. & Testi, L. (2015). Dust trapping by spiral arms in gravitationally unstable protostellar discs. *MNRAS*, **451**, 5493. 118, 120

Dobbs, C.L., Krumholz, M.R., Ballesteros-Paredes, J., Bolatto, A.D., Fukui, Y., Heyer, M., Low, M.M.M., Ostriker, E.C. & Vázquez-Semadeni, E. (2014). Formation of Molecular Clouds and Global Conditions for Star Formation. *Protostars and Planets VI*, 3. 2

Dong, R., Hall, C., Rice, K. & Chiang, E. (2015). Spiral Arms in Gravitationally Unstable Protoplanetary Disks as Imaged in Scattered Light. *ApJ*, **812**, L32. 86, 119, 120

Dong, R., Vorobyov, E., Pavlyuchenkov, Y., Chiang, E. & Liu, H.B. (2016). Signatures of Gravitational Instability in Resolved Images of Protostellar Disks. *ApJ*, **823**, 141. 17

Douglas, T.A., Caselli, P., Ilee, J.D., Boley, A.C., Hartquist, T.W., Durisen, R.H. & Rawlings, J.M.C. (2013). Simulated observations of

REFERENCES

young gravitationally unstable protoplanetary discs. *MNRAS*, **433**, 2064. 37, 87, 93, 106, 129, 139, 171, 184

DRAINE, B.T. (2011). *Physics of the Interstellar and Intergalactic Medium*. Princeton University Press. 29

DROZDOVSKAYA, M.N., WALSH, C., VISSER, R., HARSONO, D. & VAN DISHOECK, E.F. (2014). Methanol along the path from envelope to protoplanetary disc. *MNRAS*, **445**, 913. 36

DROZDOVSKAYA, M.N., WALSH, C., VISSER, R., HARSONO, D. & VAN DISHOECK, E.F. (2015). The complex chemistry of outflow cavity walls exposed: the case of low-mass protostars. *MNRAS*, **451**, 3836. 193

DROZDOVSKAYA, M.N., WALSH, C., VAN DISHOECK, E.F., FURUYA, K., MARBOEUF, U., THIABAUD, A., HARSONO, D. & VISSER, R. (2016). Cometary ices in forming protoplanetary disc midplanes. *MNRAS*, **462**, 977. 36

DULLEMOND, C.P., JUHASZ, A., POHL, A., SERESHTI, F., SHETTY, R., PETERS, T., COMMERCON, B. & FLOCK, M. (2012). RADMC-3D: A multipurpose radiative transfer tool. Astrophysics Source Code Library. 88

DUNHAM, M.M., EVANS, N.J., II, TEREBEY, S., DULLEMOND, C.P. & YOUNG, C.H. (2010). Evolutionary Signatures in the Formation of Low-Mass Protostars. II. Toward Reconciling Models and Observations. *ApJ*, **710**, 470. 6

DUNHAM, M.M., VOROBYOV, E.I. & ARCE, H.G. (2014). On the reliability of protostellar disc mass measurements and the existence of fragmenting discs. *MNRAS*, **444**, 887. 117, 130, 132

DURISEN, R.H., MEJIA, A.C. & PICKETT, B.K. (2003). Gravitational Instabilities in Protostellar and Protoplanetary Disks. *Recent Research Developments in Applied Physics*, **1**, 173. 15

DURISEN, R.H., BOSS, A.P., MAYER, L., NELSON, A.F., QUINN, T. & RICE, W.K.M. (2007). Gravitational Instabilities in Gaseous Protoplanetary Disks and Implications for Giant Planet Formation. *Protostars and Planets V*, 607. 15, 121

DUTREY, A., GUILLOTEAU, S. & GUELIN, M. (1997). Chemistry of protosolar-like nebulae: The molecular content of the DM Tau and GG Tau disks. *A&A*, **317**, L55. 152

DUTREY, A., WAKELAM, V., BOEHLER, Y., GUILLOTEAU, S., HERSANT, F., SEMENOV, D., CHAPILLON, E., HENNING, T., PIÉTU, V., LAUNHARDT, R., GUETH, F. & SCHREYER, K. (2011). Chemistry in disks. V. Sulfur-bearing molecules in the protoplanetary disks surrounding LkCa15, MWC480, DM Tauri, and GO Tauri. *A&A*, **535**, A104. 152

EHRENFREUND, P. & CHARNLEY, S.B. (2000). Organic molecules in the interstellar medium, comets, and meteorites: a voyage from dark clouds to the early Earth. *A&ARv*, **38**, 427. 51

FEDELE, D., BRUDERER, S., VAN DISHOECK, E.F., HERCZEG, G.J., EVANS, N.J., BOUWMAN, J., HENNING, T. & GREEN, J. (2012). Warm H_2O and OH in the disk around the Herbig star HD 163296. *ApJ*, **544**, L9. 69

FEDELE, D., BRUDERER, S., VAN DISHOECK, E.F., CARR, J., HERCZEG, G.J., SALYK, C., EVANS, I., NEAL, J., BOUWMAN, J., MEEUS, G. *et al.* (2013). DIGIT survey of far-infrared lines from protoplanetary disks. I. [O i], [C ii], OH, H_2O, and CH^+. *ApJ*, **559**, A77. 69

REFERENCES

FORGAN, D. & RICE, K. (2013). The possibility of a self-gravitating disc around L1527 IRS? *MNRAS*, **433**, 1796. 129

FORGAN, D., RICE, K., STAMATELLOS, D. & WHITWORTH, A. (2009). Introducing a hybrid radiative transfer method for smoothed particle hydrodynamics. *MNRAS*, **394**, 882. 119

FROMANG, S., TERQUEM, C. & BALBUS, S.A. (2002). The ionization fraction in α models of protoplanetary discs. *MNRAS*, **329**, 18. 19

GALLI, D., LIZANO, S., SHU, F.H. & ALLEN, A. (2006). Gravitational Collapse of Magnetized Clouds. I. Ideal Magnetohydrodynamic Accretion Flow. *ApJ*, **647**, 374. 12

GAMMIE, C.F. (1996). Layered Accretion in T Tauri Disks. *ApJ*, **457**, 355. 19

GAMMIE, C.F. (2001). Nonlinear Outcome of Gravitational Instability in Cooling, Gaseous Disks. *ApJ*, **553**, 174. 17

GERIN, M., PETY, J., COMMERÇON, B., FUENTE, A., CERNICHARO, J., MARCELINO, N., CIARDI, A., LIS, D.C., ROUEFF, E., WOOTTEN, H.A. & CHAPILLON, E. (2017). Evidence for disks at an early stage in class 0 protostars? *A&A*, **606**, A35. 17

GÓMEZ, G.C. & VÁZQUEZ-SEMADENI, E. (2014). Filaments in Simulations of Molecular Cloud Formation. *ApJ*, **791**, 124. 2

GOULD, R.J. & SALPETER, E.E. (1963). The Interstellar Abundance of the Hydrogen Molecule. I. Basic Processes. *ApJ*, **138**, 393. 22

GRAEDEL, T.E., LANGER, W.D. & FRERKING, M.A. (1982). The kinetic chemistry of dense interstellar clouds. *ApJS*, **48**, 321. 52

GREAVES, J.S. & RICE, W.K.M. (2011). Do all Sun-like stars have planets? Inferences from the disc mass reservoirs of Class 0 protostars. *MNRAS*, **412**, L88. 87

GREDEL, R., LEPP, S., DALGARNO, A. & HERBST, E. (1989). Cosmic-ray-induced photodissociation and photoionization rates of interstellar molecules. *ApJ*, **347**, 289. 63

GREENE, T.P., WILKING, B.A., ANDRE, P., YOUNG, E.T. & LADA, C.J. (1994). Further mid-infrared study of the rho Ophiuchi cloud young stellar population: Luminosities and masses of pre-main-sequence stars. *ApJ*, **434**, 614. 8

GRESSEL, O., TURNER, N.J., NELSON, R.P. & McNALLY, C.P. (2015). Global Simulations of Protoplanetary Disks With Ohmic Resistivity and Ambipolar Diffusion. *ApJ*, **801**, 84. 205

GUILLOTEAU, S., REBOUSSIN, L., DUTREY, A., CHAPILLON, E., WAKELAM, V., PIÉTU, V., DI FOLCO, E., SEMENOV, D. & HENNING, T. (2016). Chemistry in disks. X. The molecular content of protoplanetary disks in Taurus. *A&A*, **592**, A124. 152

HALL, C., FORGAN, D., RICE, K., HARRIES, T.J., KLAASSEN, P.D. & BILLER, B. (2016). Directly observing continuum emission from self-gravitating spiral waves. *MNRAS*, **458**, 306. 120, 139

HARKER, D.E. & DESCH, S.J. (2002). Annealing of Silicate Dust by Nebular Shocks at 10 AU. *ApJ*, **565**, L109. 35, 85

HARSONO, D., ALEXANDER, R.D. & LEVIN, Y. (2011). Global gravitational instabilities in discs with infall. *MNRAS*, **413**, 423. 90

REFERENCES

HARTMANN, L. & KENYON, S.J. (1996). The FU Orionis Phenomenon. *ARA&A*, **34**, 207. 37

HASEGAWA, T.I., HERBST, E. & LEUNG, C.M. (1992). Models of gas-grain chemistry in dense interstellar clouds with complex organic molecules. *ApJS*, **82**, 167. 51

HASEGAWA, Y., I-HSIU LI, J. & OKUZUMI, S. (2017). Dust Growth and Magnetic Fields: from Cores to Disks (even down to Planets). *ArXiv e-prints*, arXiv:1707.04110. 34

HAWLEY, J.F., BALBUS, S.A. & WINTERS, W.F. (1999). Local Hydrodynamic Stability of Accretion Disks. *ApJ*, **518**, 394. 11

HAWORTH, T.J., ILEE, J.D., FORGAN, D.H., FACCHINI, S., PRICE, D.J., BONEBERG, D.M., BOOTH, R.A., CLARKE, C.J., GONZALEZ, J.F., HUTCHISON, M.A., KAMP, I., LAIBE, G., LYRA, W., MERU, F., MO-HANTY, S., PANIĆ, O., RICE, K., SUZUKI, T., TEAGUE, R., WALSH, C., WOITKE, P. & COMMUNITY AUTHORS (2016). Grand Challenges in Protoplanetary Disc Modelling. *PASA*, **33**, e053. 202

HENNEBELLE, P. & FROMANG, S. (2008). Magnetic processes in a collapsing dense core. I. Accretion and ejection. *A&A*, **477**, 9. 12, 13

HENNING, T. & SEMENOV, D. (2013). Chemistry in Protoplanetary Disks. *Chemical Reviews*, **113**, 9016. 33, 35, 36, 174

HERBST, E. & VAN DISHOECK, E.F. (2009). Complex Organic Interstellar Molecules. *ARA&A*, **47**, 427. 22, 23

HILDEBRAND, R.H. (1983). The Determination of Cloud Masses and Dust Characteristics from Submillimetre Thermal Emission. *QJRAS*, **24**, 267. 125

Hincelin, U., Wakelam, V., Commerçon, B., Hersant, F. & Guilloteau, S. (2013). Survival of Interstellar Molecules to Prestellar Dense Core Collapse and Early Phases of Disk Formation. *ApJ*, **775**, 44. 77, 207

Hincelin, U., Commerçon, B., Wakelam, V., Hersant, F., Guilloteau, S. & Herbst, E. (2016). Chemical and Physical Characterization of Collapsing Low-mass Prestellar Dense Cores. *ApJ*, **822**, 12. 207

Hirano, N., Ho, P.P.T., Liu, S.Y., Shang, H., Lee, C.F. & Bourke, T.L. (2010). Extreme Active Molecular Jets in L1448C. *ApJ*, **717**, 58. 6

Hollenbach, D., Kaufman, M.J., Bergin, E.A. & Melnick, G.J. (2009). Water, O2, and ice in molecular clouds. *ApJ*, **690**, 1497. 50

Ilee, J.D. (2013). *Modelling and observations of molecules in discs around young stars*. Ph.D. thesis, University of Leeds. 21

Ilee, J.D., Boley, A.C., Caselli, P., Durisen, R.H., Hartquist, T.W. & Rawlings, J.M.C. (2011). Chemistry in a gravitationally unstable protoplanetary disc. *MNRAS*, **417**, 2950. 36, 37, 39, 41, 48, 49, 52, 54, 59, 64, 65, 184

Ilee, J.D., Forgan, D.H., Evans, M.G., Hall, C., Booth, R., Clarke, C.J., Rice, W.K.M., Boley, A.C., Caselli, P., Hartquist, T.W. & Rawlings, J.M.C. (2017). The chemistry of protoplanetary fragments formed via gravitational instabilities. *MNRAS*, **472**, 189. 77

Ioppolo, S. (2010). *Surface formation routes of interstellar molecules*. Ph.D. thesis, Ph. D. thesis, University of Leiden (2010). 22

REFERENCES

JI, H., BURIN, M., SCHARTMAN, E. & GOODMAN, J. (2006). Hydrodynamic turbulence cannot transport angular momentum effectively in astrophysical disks. *Nature*, **444**, 343. 11

JONKHEID, B.J. (2006). *Chemistry in evolving protoplanetary disks*. Ph.D. thesis, Leiden University. 7

JOOS, M., HENNEBELLE, P. & CIARDI, A. (2012). Protostellar disk formation and transport of angular momentum during magnetized core collapse. *A&A*, **543**, A128. 14

JOOS, M., HENNEBELLE, P., CIARDI, A. & FROMANG, S. (2013). The influence of turbulence during magnetized core collapse and its consequences on low-mass star formation. *A&A*, **554**, A17. 4

JØRGENSEN, J.K., VAN DER WIEL, M.H.D., COUTENS, A., LYKKE, J.M., MÜLLER, H.S.P., VAN DISHOECK, E.F., CALCUTT, H., BJERKELI, P., BOURKE, T.L., DROZDOVSKAYA, M.N., FAVRE, C., FAYOLLE, E.C., GARROD, R.T., JACOBSEN, S.K., ÖBERG, K.I., PERSSON, M.V. & WAMPFLER, S.F. (2016). The ALMA Protostellar Interferometric Line Survey (PILS). First results from an unbiased submillimeter wavelength line survey of the Class 0 protostellar binary IRAS 16293-2422 with ALMA. *A&A*, **595**, A117. 206

KATAOKA, R. & SATO, T. (2016). Ionization of protoplanetary disks by galactic cosmic rays, solar protons, and by supernova remnants. *ArXiv e-prints*, arXiv:1606.05714. 50

KAUFMAN, M.J. & NEUFELD, D.A. (1996). Far-Infrared Water Emission from Magnetohydrodynamic Shock Waves. *ApJ*, **456**, 611. 36

KAZES, I. & CRUTCHER, R.M. (1986). Measurement of magnetic-field strengths in molecular clouds Detection of OH-line Zeeman splitting. *A&A*, **164**, 328. 3

KETO, E., RAWLINGS, J. & CASELLI, P. (2014). Chemistry and radiative transfer of water in cold, dense clouds. *MNRAS*, **440**, 2616. 91

KETO, E., CASELLI, P. & RAWLINGS, J. (2015). The dynamics of collapsing cores and star formation. *MNRAS*, **446**, 3731. 141, 142, 155

KLESSEN, R.S. & GLOVER, S.C.O. (2016). Physical processes in the interstellar medium. In Y. Revaz, P. Jablonka, R. Teyssier & L. Mayer, eds., *Star Formation in Galaxy Evolution: Connecting Numerical Models to Reality: Saas-Fee Advanced Course 43. Swiss Society for Astrophysics and Astronomy*, 85–249, Springer Berlin Heidelberg, Berlin, Heidelberg. 29

KOOIJ, D.M. (1893). *ZPC*, **12**, 155. 25

KOUMPIA, E., SEMENOV, D.A., VAN DER TAK, F.F.S., BOOGERT, A.C.A. & CAUX, E. (2017). The chemical structure of the Class 0 protostellar envelope NGC 1333 IRAS 4A. *A&A*, **603**, A88. 155

KRASNOPOLSKY, R., LI, Z.Y. & SHANG, H. (2011). Disk Formation in Magnetized Clouds Enabled by the Hall Effect. *ApJ*, **733**, 54. 14

KRASNOPOLSKY, R., LI, Z.Y., SHANG, H. & ZHAO, B. (2012). Protostellar Accretion Flows Destabilized by Magnetic Flux Redistribution. *ApJ*, **757**, 77. 14

KRATTER, K. & LODATO, G. (2016). Gravitational Instabilities in Circumstellar Disks. *ARA&A*, **54**, 271. 109

KRATTER, K.M. & MURRAY-CLAY, R.A. (2011). Fragment Production and Survival in Irradiated Disks: A Comprehensive Cooling Criterion. *ApJ*, **740**, 1. 90

REFERENCES

LADA, C.J. (1987). Star formation - From OB associations to protostars. In M. Peimbert & J. Jugaku, eds., *Star Forming Regions*, vol. 115 of *IAU Symposium*, 1. 6

LADA, C.J. & KYLAFIS, N.D. (1999). The Origin of Stars and Planetary Systems. In *NATO Advanced Science Institutes (ASI) Series C*, vol. 540 of *NATO Advanced Science Institutes (ASI) Series C*. 2

LARSON, R.B. (1969). Numerical calculations of the dynamics of collapsing proto-star. *MNRAS*, **145**, 271. 4

LARSON, R.B. (1973). The Evolution of Protostars - Theory. *Fundamentals Cosmic Phys.*, **1**, 1. 4

LARSON, R.B. (2002). The role of tidal interactions in star formation. *MNRAS*, **332**, 155. 18

LARSON, R.B. (2003). The physics of star formation. *Reports on Progress in Physics*, **66**, 1651. 2

LEE, C.F., MUNDY, L.G., REIPURTH, B., OSTRIKER, E.C. & STONE, J.M. (2000). CO Outflows from Young Stars: Confronting the Jet and Wind Models. *ApJ*, **542**, 925. 6

LEE, C.F., HO, P.T.P., LI, Z.Y., HIRANO, N., ZHANG, Q. & SHANG, H. (2017). A rotating protostellar jet launched from the innermost disk of HH 212. *Nature Astronomy*, **1**, 0152. 18

LI, Z., GERHARD, O., SHEN, J., PORTAIL, M. & WEGG, C. (2016). Gas Dynamics in the Milky Way: A Low Pattern Speed Model. *ApJ*, **824**, 13. 171

LI, Z.Y., KRASNOPOLSKY, R. & SHANG, H. (2011). Non-ideal MHD Effects and Magnetic Braking Catastrophe in Protostellar Disk Formation. *ApJ*, **738**, 180. 14

LIU, H.B., LAI, S.P., HASEGAWA, Y., HIRANO, N., RAO, R., LI, I.H., FUKAGAWA, M., GIRART, J.M., CARRASCO-GONZÁLEZ, C. & RODRÍGUEZ, L.F. (2016). Detection of Linearly Polarized 6.9 mm Continuum Emission from the Class 0 Young Stellar Object NGC 1333 IRAS4A. *ApJ*, **821**, 41. 203

LODATO, G. (2008). Classical disc physics. *New Astron. Rev.*, **52**, 21. 9

LODATO, G. & RICE, W.K.M. (2004). Testing the locality of transport in self-gravitating accretion discs. *MNRAS*, **351**, 630. 17, 119

LOINARD, L., ZAPATA, L.A., RODRÍGUEZ, L.F., PECH, G., CHANDLER, C.J., BROGAN, C.L., WILNER, D.J., HO, P.T.P., PARISE, B., HARTMANN, L.W., ZHU, Z., TAKAHASHI, S. & TREJO, A. (2013). ALMA and VLA observations of the outflows in IRAS 16293-2422. *MNRAS*, **430**, L10. 6

MACHIDA, M.N. & HOSOKAWA, T. (2013). Evolution of protostellar outflow around low-mass protostar. *MNRAS*, **431**, 1719. 50

MACHIDA, M.N. & MATSUMOTO, T. (2011). The origin and formation of the circumstellar disc. *MNRAS*, **413**, 2767. 14, 17

MATSUMOTO, T. & HANAWA, T. (2011). Protostellar Collapse of Magneto-turbulent Cloud Cores: Shape During Collapse and Outflow Formation. *ApJ*, **728**, 47. 5

MAUREIRA, M.J., ARCE, H.G., DUNHAM, M.M., PINEDA, J.E., FERNÁNDEZ-LÓPEZ, M., CHEN, X. & MARDONES, D. (2017). Kinemat-

REFERENCES

ics of a Young Low-mass Star-forming Core: Understanding the Evolutionary State of the First-core Candidate L1451-mm. *ApJ*, **838**, 60. 5

MAYER, L., LUFKIN, G., QUINN, T. & WADSLEY, J. (2007). Fragmentation of Gravitationally Unstable Gaseous Protoplanetary Disks with Radiative Transfer. *ApJ*, **661**, L77. 17

McELROY, D., WALSH, C., MARKWICK, A.J., CORDINER, M.A., SMITH, K. & MILLAR, T.J. (2013). The UMIST database for astrochemistry 2012. *A&A*, **550**, A36. 24

McKEE, C.F. (1989). Photoionization-regulated star formation and the structure of molecular clouds. *ApJ*, **345**, 782. 50

McMULLIN, J.P., WATERS, B., SCHIEBEL, D., YOUNG, W. & GOLAP, K. (2007). CASA Architecture and Applications. In R.A. Shaw, F. Hill & D.J. Bell, eds., *Astronomical Data Analysis Software and Systems XVI*, vol. 376 of *Astronomical Society of the Pacific Conference Series*, 127. 110, 156

MEEUS, G., MONTESINOS, B., MENDIGUTÍA, I., KAMP, I., THI, W.F., EIROA, C., GRADY, C.A., MATHEWS, G., SANDELL, G., MARTIN-ZAÏDI, C. *et al.* (2012). Observations of Herbig Ae/Be stars with Herschel/PACS. *A&A*, **544**, A78. 69

MEJÍA, A.C., DURISEN, R.H., PICKETT, M.K. & CAI, K. (2005). The Thermal Regulation of Gravitational Instabilities in Protoplanetary Disks. II. Extended Simulations with Varied Cooling Rates. *ApJ*, **619**, 1098. 39, 121

MELLON, R.R. & LI, Z.Y. (2009). Magnetic Braking and Protostellar Disk Formation: Ambipolar Diffusion. *ApJ*, **698**, 922. 14

MERU, F., JUHÁSZ, A., ILEE, J.D., CLARKE, C.J., ROSOTTI, G.P. & BOOTH, R.A. (2017). On the Origin of the Spiral Morphology in the Elias 2-27 Circumstellar Disk. *ApJ*, **839**, L24. 86, 107

MICHAEL, S. & DURISEN, R.H. (2010). Stellar motion induced by gravitational instabilities in protoplanetary discs. *MNRAS*, **406**, 279. 38

MIETTINEN, O. (2016). Characterising the physical and chemical properties of a young Class 0 protostellar core embedded in the Orion B9 filament. *Ap&SS*, **361**, 248. 155

MILLAR, T.J. (2015). Astrochemistry. *Plasma Sources Science Technology*, **24**, 043001. 23, 25

MILLAR, T.J., FARQUHAR, P.R.A. & WILLACY, K. (1997). The UMIST Database for Astrochemistry 1995. *A&A*, **121**, 139. 24, 48

MIOTELLO, A., TESTI, L., LODATO, G., RICCI, L., ROSOTTI, G., BROOKS, K., MAURY, A. & NATTA, A. (2014). Grain growth in the envelopes and disks of Class I protostars. *A&A*, **567**, A32. 34, 87, 110, 129

MIOTELLO, A., VAN DISHOECK, E.F., WILLIAMS, J.P., ANSDELL, M., GUIDI, G., HOGERHEIJDE, M., MANARA, C.F., TAZZARI, M., TESTI, L., VAN DER MAREL, N. & VAN TERWISGA, S. (2017). Lupus disks with faint CO isotopologues: low gas/dust or high carbon depletion? *A&A*, **599**, A113. 175

MOLYAROVA, T., AKIMKIN, V., SEMENOV, D., HENNING, T., VASYUNIN, A. & WIEBE, D. (2017). Gas mass tracers in protoplanetary disks: CO is still the best. *ArXiv e-prints*, arXiv:1710.02993. 36

MURRAY, N. (2011). Star Formation Efficiencies and Lifetimes of Giant Molecular Clouds in the Milky Way. *ApJ*, **729**, 133. 1

REFERENCES

MUSIOLIK, G., TEISER, J., JANKOWSKI, T. & WURM, G. (2016). Ice Grain Collisions in Comparison: CO2, H2O, and Their Mixtures. *ApJ*, **827**, 63. 23

MUTO, T., GRADY, C.A., HASHIMOTO, J., FUKAGAWA, M., HORNBECK, J.B., SITKO, M., RUSSELL, R., WERREN, C., CURÉ, M., CURRIE, T., OHASHI, N., OKAMOTO, Y., MOMOSE, M., HONDA, M., INUTSUKA, S., TAKEUCHI, T., DONG, R., ABE, L., BRANDNER, W., BRANDT, T., CARSON, J., EGNER, S., FELDT, M., FUKUE, T., GOTO, M., GUYON, O., HAYANO, Y., HAYASHI, M., HAYASHI, S., HENNING, T., HODAPP, K.W., ISHII, M., IYE, M., JANSON, M., KANDORI, R., KNAPP, G.R., KUDO, T., KUSAKABE, N., KUZUHARA, M., MATSUO, T., MAYAMA, S., MCELWAIN, M.W., MIYAMA, S., MORINO, J.I., MORO-MARTIN, A., NISHIMURA, T., PYO, T.S., SERABYN, E., SUTO, H., SUZUKI, R., TAKAMI, M., TAKATO, N., TERADA, H., THALMANN, C., TOMONO, D., TURNER, E.L., WATANABE, M., WISNIEWSKI, J.P., YAMADA, T., TAKAMI, H., USUDA, T. & TAMURA, M. (2012). Discovery of Small-scale Spiral Structures in the Disk of SAO 206462 (HD 135344B): Implications for the Physical State of the Disk from Spiral Density Wave Theory. *ApJ*, **748**, L22. 86

MYERS, P.C. & GOODMAN, A.A. (1988). Magnetic molecular clouds - Indirect evidence for magnetic support and ambipolar diffusion. *ApJ*, **329**, 392. 3

ÖBERG, K.I., GUZMÁN, V.V., FURUYA, K., QI, C., AIKAWA, Y., ANDREWS, S.M., LOOMIS, R. & WILNER, D.J. (2015). The comet-like composition of a protoplanetary disk as revealed by complex cyanides. *Nature*, **520**, 198. 153, 206

OHASHI, N., SAIGO, K., ASO, Y., AIKAWA, Y., KOYAMATSU, S., MACHIDA, M.N., SAITO, M., TAKAHASHI, S.Z., TAKAKUWA, S., TOMIDA, K., TOMISAKA, K. & YEN, H.W. (2014). Formation of a Keplerian Disk in the

Infalling Envelope around L1527 IRS: Transformation from Infalling Motions to Kepler Motions. *ApJ*, **796**, 131. 140, 142, 168

OSSENKOPF, V. (1997). The Sobolev approximation in molecular clouds. *New Astron.*, **2**, 365. 30

OSSENKOPF, V. (2002). Molecular line emission from turbulent clouds. *A&A*, **391**, 295. 30

OSSENKOPF, V. & HENNING, T. (1994). Dust opacities for protostellar cores. *A&A*, **291**, 943. 108

PAPALOIZOU, J.C. & SAVONIJE, G.J. (1991). Angular Momentum Transport in Self-Gravitating Gaseous Disks. In C. Bertout, S. Collin-Souffrin & J.P. Lasota, eds., *IAU Colloq. 129: The 6th Institute d'Astrophysique de Paris (IAP) Meeting: Structure and Emission Properties of Accretion Disks*, 99. 15

PÉREZ, L.M., CARPENTER, J.M., CHANDLER, C.J., ISELLA, A., ANDREWS, S.M., RICCI, L., CALVET, N., CORDER, S.A., DELLER, A.T., DULLEMOND, C.P., GREAVES, J.S., HARRIS, R.J., HENNING, T., KWON, W., LAZIO, J., LINZ, H., MUNDY, L.G., SARGENT, A.I., STORM, S., TESTI, L. & WILNER, D.J. (2012). Constraints on the Radial Variation of Grain Growth in the AS 209 Circumstellar Disk. *ApJ*, **760**, L17. 118

PÉREZ, L.M., CARPENTER, J.M., ANDREWS, S.M., RICCI, L., ISELLA, A., LINZ, H., SARGENT, A.I., WILNER, D.J., HENNING, T., DELLER, A.T., CHANDLER, C.J., DULLEMOND, C.P., LAZIO, J., MENTEN, K.M., CORDER, S.A., STORM, S., TESTI, L., TAZZARI, M., KWON, W., CALVET, N., GREAVES, J.S., HARRIS, R.J. & MUNDY, L.G. (2016). Spiral density waves in a young protoplanetary disk. *Science*, **353**, 1519. 86, 107, 136, 139, 201

REFERENCES

PHILLIPS, J.P. (1999). Rotation in molecular clouds. *A&AS*, **134**, 241. 9

PICKETT, B.K., CASSEN, P., DURISEN, R.H. & LINK, R. (1998). The Effects of Thermal Energetics on Three-dimensional Hydrodynamic Instabilities in Massive Protostellar Disks. *ApJ*, **504**, 468. 15

PRZYBILLA, N., NIEVA, M.F. & BUTLER, K. (2008). A Cosmic Abundance Standard: Chemical Homogeneity of the Solar Neighborhood and the ISM Dust-Phase Composition. *ApJ*, **688**, L103. 52

QI, C., ÖBERG, K.I. & WILNER, D.J. (2013). H2CO and N2H+ in Protoplanetary Disks: Evidence for a CO-ice Regulated Chemistry. *ApJ*, **765**, 34. 54

QI, C., ÖBERG, K.I., WILNER, D.J. & ROSENFELD, K.A. (2013). First Detection of c-C_3H_2 in a Circumstellar Disk. *ApJ*, **765**, L14. 152

QUANZ, S.P., AMARA, A., MEYER, M.R., GIRARD, J.H., KENWORTHY, M.A. & KASPER, M. (2015). Confirmation and Characterization of the Protoplanet HD 100546 b - Direct Evidence for Gas Giant Planet Formation at 50 AU. *ApJ*, **807**, 64. 8

QUATAERT, E. & CHIANG, E.I. (2000). Angular Momentum Transport in Particle and Fluid Disks. *ApJ*, **543**, 432. 11

RAY, T. (2012). Losing spin: the angular momentum problem. *Astronomy and Geophysics*, **53**, 5.19. 18

RICCI, L., TESTI, L., NATTA, A. & BROOKS, K.J. (2010). Dust grain growth in ρ-Ophiuchi protoplanetary disks. *A&A*, **521**, A66. 34

RICHERT, A.J.W., LYRA, W., BOLEY, A., MAC LOW, M.M. & TURNER, N. (2015). On Shocks Driven by High-mass Planets in Radiatively Inefficient Disks. I. Two-dimensional Global Disk Simulations. *ApJ*, **804**, 95. 86

RIOLS, A. & LATTER, H. (2018). Magnetorotational instability and dynamo action in gravito-turbulent astrophysical discs. *MNRAS*, **474**, 2212. 205

ROBITAILLE, T.P., WHITNEY, B.A., INDEBETOUW, R., WOOD, K. & DENZMORE, P. (2006). Interpreting Spectral Energy Distributions from Young Stellar Objects. I. A Grid of 200,000 YSO Model SEDs. *ApJS*, **167**, 256. 6

RODRIGUEZ-FERNANDEZ, N.J. & COMBES, F. (2008). Gas flow models in the Milky Way embedded bars. *A&A*, **489**, 115. 171

SAKAI, N., OYA, Y., SAKAI, T., WATANABE, Y., HIROTA, T., CECCARELLI, C., KAHANE, C., LOPEZ-SEPULCRE, A., LEFLOCH, B., VASTEL, C., BOTTINELLI, S., CAUX, E., COUTENS, A., AIKAWA, Y., TAKAKUWA, S., OHASHI, N., YEN, H.W. & YAMAMOTO, S. (2014). A Chemical View of Protostellar-disk Formation in L1527. *ApJ*, **791**, L38. 140, 168

SAKAI, N., SAKAI, T., HIROTA, T., WATANABE, Y., CECCARELLI, C., KAHANE, C., BOTTINELLI, S., CAUX, E., DEMYK, K., VASTEL, C. *et al.* (2014). Change in the chemical composition of infalling gas forming a disk around a protostar. *Nature*, **507**, 78. 83, 193

SAKAI, N., OYA, Y., LÓPEZ-SEPULCRE, A., WATANABE, Y., SAKAI, T., HIROTA, T., AIKAWA, Y., CECCARELLI, C., LEFLOCH, B., CAUX, E., VASTEL, C., KAHANE, C. & YAMAMOTO, S. (2016). Subarcsecond Analysis of the Infalling-Rotating Envelope around the Class I Protostar IRAS 04365+2535. *ApJ*, **820**, L34. 140, 168

REFERENCES

Sakai, N., Oya, Y., Higuchi, A.E., Aikawa, Y., Hanawa, T., Ceccarelli, C., Lefloch, B., López-Sepulcre, A., Watanabe, Y., Sakai, T., Hirota, T., Caux, E., Vastel, C., Kahane, C. & Yamamoto, S. (2017). Vertical structure of the transition zone from infalling rotating envelope to disc in the Class 0 protostar, IRAS 04368+2557. *MNRAS*, **467**, L76. 33, 193

Salinas, V.N., Hogerheijde, M.R., Bergin, E.A., Cleeves, L.I., Brinch, C., Blake, G.A., Lis, D.C., Melnick, G.J., Panić, O., Pearson, J.C., Kristensen, L., Yildiz, U.A. & van Dishoeck, E.F. (2016). First detection of gas-phase ammonia in a planet-forming disk. NH_3, N_2H^+, and H_2O in the disk around TW Hydrae. *A&A*, **591**, A122. 152

Salinas, V.N., Hogerheijde, M.R., Mathews, G.S., Öberg, K.I., Qi, C., Williams, J.P. & Wilner, D.J. (2017). DCO^+, DCN, and N_2D^+ reveal three different deuteration regimes in the disk around the Herbig Ae star HD 163296. *A&A*, **606**, A125. 152

Seifried, D., Sánchez-Monge, Á., Walch, S. & Banerjee, R. (2016). Revealing the dynamics of Class 0 protostellar discs with ALMA. *MNRAS*, **459**, 1892. 178, 184, 185, 186, 187

Semenov, D. & Wiebe, D. (2011). Chemical evolution of turbulent protoplanetary disks and the Solar nebula. *ApJS*, **196**, 25. 35

Shakura, N.I. & Sunyaev, R.A. (1973). Black holes in binary systems. Observational appearance. *A&A*, **24**, 337. 10

Shirley, Y.L. (2015). The Critical Density and the Effective Excitation Density of Commonly Observed Molecular Dense Gas Tracers. *PASP*, **127**, 299. 144, 145

SHU, F.H., ADAMS, F.C. & LIZANO, S. (1987). Star formation in molecular clouds - Observation and theory. *ARA&A*, **25**, 23. 1, 7

SOBOLEV, V.V. (1957). The Diffusion of Lα Radiation in Nebulae and Stellar Envelopes. *Soviet Ast.*, **1**, 678. 30

SPITZER, L. & ARNY, T.T. (1978). Physical Processes in the Interstellar Medium. *American Journal of Physics*, **46**, 1201. 4

STAHLER, S.W. & PALLA, F. (2005). *The Formation of Stars*. Weinheim: Wiley-VCH. 27

STONE, J.M. & BALBUS, S.A. (1996). Angular Momentum Transport in Accretion Disks via Convection. *ApJ*, **464**, 364. 11

STONE, J.M., GAMMIE, C.F., BALBUS, S.A. & HAWLEY, J.F. (2000). Transport Processes in Protostellar Disks. *Protostars and Planets IV*, 589. 11

THI, W.F., MÉNARD, F., MEEUS, G., MARTIN-ZAÏDI, C., WOITKE, P., TATULLI, E., BENISTY, M., KAMP, I., PASCUCCI, I., PINTE, C., GRADY, C.A., BRITTAIN, S., WHITE, G.J., HOWARD, C.D., SANDELL, G. & EIROA, C. (2011). Detection of CH$^+$ emission from the disc around HD 100546. *A&A*, **530**, L2. 152

TIELENS, A.G.G.M. & ALLAMANDOLA, L.J. (1987). Composition, structure, and chemistry of interstellar dust. In D.J. Hollenbach & H.A. Thronson Jr., eds., *Interstellar Processes*, vol. 134 of *Astrophysics and Space Science Library*, 397. 51

TOBIN, J.J., HARTMANN, L., CHIANG, H.F., WILNER, D.J., LOONEY, L.W., LOINARD, L., CALVET, N. & D'ALESSIO, P. (2012). A ∼0.2-solar-mass pro-

tostar with a Keplerian disk in the very young L1527 IRS system. *Nature*, **492**, 83. 140, 168

TOBIN, J.J., KRATTER, K.M., PERSSON, M.V., LOONEY, L.W., DUNHAM, M.M., SEGURA-COX, D., LI, Z.Y., CHANDLER, C.J., SADAVOY, S.I., HARRIS, R.J., MELIS, C. & PÉREZ, L.M. (2016). A triple protostar system formed via fragmentation of a gravitationally unstable disk. *Nature*, **538**, 483. 33, 86, 107, 126, 136, 139, 140, 168, 201

TOHLINE, J.E. (1982). Hydrodynamic collapse. *Fundamentals Cosmic Phys.*, **8**, 1. 4

TOMIDA, K., OKUZUMI, S. & MACHIDA, M.N. (2015). Radiation Magnetohydrodynamic Simulations of Protostellar Collapse: Nonideal Magnetohydrodynamic Effects and Early Formation of Circumstellar Disks. *ApJ*, **801**, 117. 5, 14

TOMIDA, K., MACHIDA, M.N., HOSOKAWA, T., SAKURAI, Y. & LIN, C.H. (2017). Grand-design Spiral Arms in a Young Forming Circumstellar Disk. *ApJ*, **835**, L11. 86, 107

TOOMRE, A. (1964). On the gravitational stability of a disk of stars. *ApJ*, **139**, 1217. 15

TSUKAMOTO, Y. (2016). Magnetic Field and Early Evolution of Circumstellar Disks. *PASA*, **33**, e010. 205

TSUKAMOTO, Y., MACHIDA, M.N. & INUTSUKA, S.I. (2013). Formation, orbital and thermal evolution, and survival of planetary-mass clumps in the early phase of circumstellar disc evolution. *MNRAS*, **436**, 1667. 17

van der Tak, F.F.S. & van Dishoeck, E.F. (2000). Limits on the cosmic-ray ionization rate toward massive young stars. *A&A*, **358**, L79. 19

Van Loo, S., Ashmore, I., Caselli, P., Falle, S.A.E.G. & Hartquist, T.W. (2013). Sputtering in oblique C-type shocks. *MNRAS*, **428**, 381. 52

Visser, R., Van Dishoeck, E.F., Doty, S.D. & Dullemond, C.P. (2009). The chemical history of molecules in circumstellar disks. I. Ices. *A&A*, **495**, 881. 50

Visser, R., Doty, S.D. & van Dishoeck, E.F. (2011). The chemical history of molecules in circumstellar disks. II. Gas-phase species. *A&A*, **534**, A132. 77

Vorobyov, E.I. & Basu, S. (2005). The Origin of Episodic Accretion Bursts in the Early Stages of Star Formation. *ApJ*, **633**, L137. 17

Vorobyov, E.I. & Pavlyuchenkov, Y.N. (2017). Improving the thin-disk models of circumstellar disk evolution. The 2+1-dimensional model. *A&A*, **606**, A5. 17

Wakelam, V., Herbst, E., Loison, J.C., Smith, I.W.M., Chandrasekaran, V., Pavone, B., Adams, N.G., Bacchus-Montabonel, M.C., Bergeat, A., Béroff, K., Bierbaum, V.M., Chabot, M., Dalgarno, A., van Dishoeck, E.F., Faure, A., Geppert, W.D., Gerlich, D., Galli, D., Hébrard, E., Hersant, F., Hickson, K.M., Honvault, P., Klippenstein, S.J., Le Picard, S., Nyman, G., Pernot, P., Schlemmer, S., Selsis, F., Sims, I.R., Talbi, D., Tennyson, J., Troe, J., Wester, R. & Wiesenfeld, L. (2012). A KInetic Database for Astrochemistry (KIDA). *ApJS*, **199**, 21. 24, 48

Walsh, C., Millar, T.J. & Nomura, H. (2010). Chemical Processes in Protoplanetary Disks. *ApJ*, **722**, 1607. 34, 78

REFERENCES

WALSH, C., NOMURA, H., MILLAR, T.J. & AIKAWA, Y. (2012). Chemical Processes in Protoplanetary Disks. II. On the Importance of Photochemistry and X-Ray Ionization. *ApJ*, **747**, 114. 34

WALSH, C., MILLAR, T.J., NOMURA, H., HERBST, E., WIDICUS WEAVER, S., AIKAWA, Y., LAAS, J.C. & VASYUNIN, A.I. (2014). Complex organic molecules in protoplanetary disks. *A&A*, **563**, A33. 34, 36, 206

WALSH, C., LOOMIS, R.A., ÖBERG, K.I., KAMA, M., VAN 'T HOFF, M.L.R., MILLAR, T.J., AIKAWA, Y., HERBST, E., WIDICUS WEAVER, S.L. & NOMURA, H. (2016). First Detection of Gas-phase Methanol in a Protoplanetary Disk. *ApJ*, **823**, L10. 153, 206

WALSH, C., DALEY, C., FACCHINI, S. & JUHÁSZ, A. (2017). CO emission tracing a warp or radial flow within ≲100 au in the HD 100546 protoplanetary disk. *A&A*, **607**, A114. 174

WARD-THOMPSON, D., KIRK, J.M., CRUTCHER, R.M., GREAVES, J.S., HOLLAND, W.S. & ANDRÉ, P. (2000). First Observations of the Magnetic Field Geometry in Prestellar Cores. *ApJ*, **537**, L135. 11

WARD-THOMPSON, D., KIRK, J.M., ANDRÉ, P., SARACENO, P., DIDELON, P., KÖNYVES, V., SCHNEIDER, N., ABERGEL, A., BALUTEAU, J.P., BERNARD, J.P., BONTEMPS, S., CAMBRÉSY, L., COX, P., DI FRANCESCO, J., DI GIORGIO, A.M., GRIFFIN, M., HARGRAVE, P., HUANG, M., LI, J.Z., MARTIN, P., MEN'SHCHIKOV, A., MINIER, V., MOLINARI, S., MOTTE, F., OLOFSSON, G., PEZZUTO, S., RUSSEIL, D., SAUVAGE, M., SIBTHORPE, B., SPINOGLIO, L., TESTI, L., WHITE, G., WILSON, C., WOODCRAFT, A. & ZAVAGNO, A. (2010). A Herschel study of the properties of starless cores in

the Polaris Flare dark cloud region using PACS and SPIRE. *A&A*, **518**, L92. 2

WILLIAMS, J.P. & CIEZA, L.A. (2011). Protoplanetary Disks and Their Evolution. *ARA&A*, **49**, 67. 174

WILSON, T.L. (1999). Isotopes in the interstellar medium and circumstellar envelopes. *Reports on Progress in Physics*, **62**, 143. 155

WONG, Y.H.V., HIRASHITA, H. & LI, Z.Y. (2016). Millimeter-sized grains in the protostellar envelopes: Where do they come from? *PASJ*, **68**, 67. 129

WOODALL, J., AGÚNDEZ, M., MARKWICK-KEMPER, A.J. & MILLAR, T.J. (2007). The UMIST database for astrochemistry 2006. *A&A*, **466**, 1197. 24

YOUNG, K.E., LEE, J.E., EVANS, N.J., II, GOLDSMITH, P.F. & DOTY, S.D. (2004). Probing Pre-Protostellar Cores with Formaldehyde. *ApJ*, **614**, 252. 155

YU, M., WILLACY, K., DODSON-ROBINSON, S.E., TURNER, N.J. & EVANS, N.J., II (2016). Probing Planet Forming Zones with Rare CO Isotopologues. *ApJ*, **822**, 53. 207

YU, M., EVANS, N.J., II, DODSON-ROBINSON, S.E., WILLACY, K. & TURNER, N.J. (2017). Disk Masses around Solar-mass Stars are Underestimated by CO Observations. *ApJ*, **841**, 39. 175, 193

ZHAO, B., CASELLI, P., LI, Z.Y., KRASNOPOLSKY, R., SHANG, H. & NAKAMURA, F. (2016). Protostellar disc formation enabled by removal of small dust grains. *MNRAS*, **460**, 2050. 14

ZHAO, B., CASELLI, P., LI, Z.Y. & KRASNOPOLSKY, R. (2018). Decoupling of magnetic fields in collapsing protostellar envelopes and disc formation and fragmentation. *MNRAS*, **473**, 4868. 14